Control of multicellular power converters for microgrids and renewable energies applications

Khaled Tamizi

université PARIS-SACLAY

NNT = 2018SACLS212

Thèse de doctorat

UNIVERSITÉ PARIS SUD
Comprendre le monde, construire l'avenir

Control of Multicellular Power Converters for Microgrids and Renewable Energies Applications

Thèse de doctorat de l'Université Paris-Saclay
préparée à Université Paris-Sud

École doctorale n°575 electrical, optical, bio : physics and engineering (EOBE)
Spécialité de doctorat: génie électrique

Thèse présentée et soutenue à Gif sur Yvette, le 12 Juillet 2018, par

M Khaled TAMIZI

Composition du Jury :

Eric MONMASSON Professeur des Universités de Cergy Pontoise (SATIE)	Président
Guillaume GATEAU Professeur, ENSEEIHT (- LAPLACE)	Rapporteur
Mickaël HILAIRET Professeur des Universités Franche-Comte (–FEMTO-ST)	Rapporteur
Cyrille GAUTIER Doctor, site SAFRAN Paris-Saclay (SAFRAN TECH)	Examinateur
Eric LABOURE Professeur des Universités Paris-Sud (– GeePs)	Directeur de thèse
Olivier BETHOUX Professeur des Universités Sorbonne Université (– GeePs)	Co-Directeur de thèse

université PARIS-SACLAY

ÉCOLE DOCTORALE
Physique et ingénierie : électrons, photons, sciences du vivant (EOBE)

Titre : Commande de convertisseurs multicellulaires destinés aux microgrids et aux systèmes d'énergies renouvelables

Mots clés : Electronique de puissance, commande, Energie renouvelable, Microgrids, MPC

Résumé Les convertisseurs multicellulaires DC-DC sont utilisés dans de nombreuses applications et de nombreux systèmes électriques. Ils présentent un intérêt particulier pour des applications spécifiques liées aux énergies renouvelables et aux Microgrids. Leur principal avantage provient de leur capacité intrinsèque à réduire les ondulations liées au découpage des grandeurs électriques en entrée et en sortie du système de conversion. Cette propriété intéressante au niveau système peut être étendue au fonctionnement interne du convertisseur en adjoignant à ce dernier un élément de filtrage par inductances couplées magnétiquement. Ce composant permet d'étendre les propriétés externes de réduction des ondulations au fonctionnement de chaque cellule du convertisseur. Il permet également d'augmenter la dynamique propre du système de conversion. Ces propriétés permettent de réduire significativement le niveau et le volume de filtrage en entrée et sortie du convertisseur et donc d'augmenter de manière importante sa compacité et son rendement énergétique. Cependant, l'ajout de ce dispositif magnétique induit, de par le couplage des équations du système qu'il provoque, une complexification du contrôle de la structure associée également à la nécessité d'augmenter le nombre de capteurs.

Ce travail de thèse a pour objectif d'établir et d'évaluer différents modes de contrôle pour les convertisseurs multicellulaires DC-DC. Le point commun aux méthodes proposées est de permettre la gestion aussi bien des grandeurs externes au convertisseur que des grandeurs internes constituées par les courants de circulation entre cellules connectées en parallèle. Ces composantes de courant sont également nommées « courants différentiels ». Trois types de contrôle sont étudiés : Pour le premier, des correcteurs linéaires classiques sont utilisés conjointement avec des techniques de découplage des équations du système. La robustesse de ces méthodes de contrôle vis-à-vis des incertitudes sur la connaissance des paramètres du système fait l'objet d'un focus particulier dans cette partie du travail. Pour le second, une version modifiée de la technique de commande connue sous le nom Model Predictive Control est proposée. Celle-ci permet d'assurer le contrôle de la fréquence de commutation et l'entrelacement des commandes PWM des cellules. Pour le troisième mode, nous étudions une méthode basée sur le contrôle vectoriel direct des courants différentiels.

Une implantation sur un système numérique équipé d'un micro-processeur et d'un FPGA est proposée et permet de valider les résultats de l'étude théorique.

Title : Control of multicellular power converters for microgrids and renewable energies applications

Keywords : Power Electronics, Control, Renewable Energy, Microgrids, MPC

Abstract : The interleaved multicell DC-DC power converters are broadly used in many applications and systems especially in renewable energy systems and microgrids. They reduce the current ripple at the input and output side. Also, an implemented magnetic coupling between cells leads to reduce the current ripple in each of them and to improve the dynamical electrical behavior. These properties involve a reduction on the filtering requirements and so, allow to improve the converter compactness as well as its conversion efficiency. Nevertheless, for such power converters, the control complexity is also increased as well as the number of required sensors.

The thesis aims to establish different mode of control of interleaved multicell DC-DC converters. The common point of these methods is to control the external quantities at the output of the converter but also the internal quantities, constituted by the circulating currents between parallel cells or in other words the differential currents. Three main strategies are investigated: the first one uses classical linear controllers with different decoupling technics and focuses on the robustness regarding the system parameters variations. The second one uses a Model Predictive Control technic which is designed to provide a fix switching frequency and interleaving of the cells PWM commands. The last one presents a space vector direct control of the differential currents.

In a last part, these control principles are tested on a prototype and implemented on a Microcontroller and FPGA board in order to carry out an experimental verification.

Table of Contents

Table of Tables

Table of Figures

Abbreviations

µC	Microcontrollers
AC	Alternating Current
ADC	Analog to Digital Converters
ASIC	Applied-Specific Integrated Circuit
A-W	Anti-Windup
CC-MPC	Continuous Control - Model Predictive Control
CT	Conversion Ratio
DC	Direct Current
DPC	direct power control
DSP	Digital Signal Processor
DTC	Direct Torque Control
FCS-MPC	Finite Control Set -Model Predictive Control
FFT	Fast Fourier Transform
FPGA	Field-Programmable Gate Array
I/O	Input/Output
ICTs	Inter Cell Transformers
IGBT	Insulated-Gate Bipolar Transistor
IIR	Infinite Impulse Response
LP	Linear Programing
LQR	Linear Quadratic Regulator
MIMO	Multi Inputs Multi Outputs
MPC	Model Predictive Control
MPP	Maximum Power Point
Op-Amp	Operational Amplifiers
P	Active Power
PI	proportional–integral
PV	Photovoltaic
PWM	Pulse Width Modulation
Q	Reactive Power
QP	Quadratic Programing
RAM	Random Access Memory
RMS	Root Mean Square
seg	Time segment
SISO	Single Input Single Output
SVD	Space Vector Direct Control
SVM	Space Vector Modulation
SVP	space vector placement
VF	Virtual Flux
VOC	Voltage Oriented Control
VSC	Voltage Source Converters
XSG	Xilinx System Generator

Résumé

Description du contexte et travaux réalisés

Les convertisseurs DC-DC multicellulaires entrelacés sont d'excellents candidats pour les microgrids et les systèmes de production électrique à base de renouvelable en raison de leur comportement électrique et de leur possible dynamique élevée. En effet, l'une des principales caractéristiques de ces convertisseurs est de réduire les ondulations des grandeurs électriques à leur entrée et à leur sortie. Ils constituent donc une bonne option pour les convertisseurs destinés aux applications solaires en raison de la réduction des contraintes électriques sur la chaine de conversion photovoltaïque tout en réduisant les exigences de filtrage et donc la taille des filtres entrainant, de ce fait, une augmentation de la compacité du convertisseur. De plus, la nature multicellulaire de cette famille de convertisseurs offre la possibilité d'obtenir un rendement énergétique très élevé sur une très large plage de puissance en permettant de choisir le nombre de cellules à mettre en service. Là encore, ceci constitue un avantage indiscutable pour les applications de conversion pour les systèmes de production électrique à base de renouvelable par essence de nature très fluctuante.

Ces avantages sont contrebalancés par la difficulté de contrôle due à l'augmentation significative du nombre de grandeurs à contrôler. Le couplage magnétique entre cellules qui conduit à une amélioration supplémentaire des performances du système ajoute à cette complexité en introduisant des relations croisées entre les commandes de chacune des cellules et les grandeurs à contrôler.

Le travail présenté dans ce document porte sur le contrôle de telles structures. Nous présentons trois approches différentes pour contrôler les convertisseurs DC-DC multicellulaires entrelacés couplés. La première utilise des contrôleurs linéaires appliqués à une représentation modale du système. Un modèle de contrôle prédictif (MPC) est utilisé dans la seconde et une approche basée sur un contrôle vectoriel direct avec prédiction de modèle est utilisée pour la troisième.

Il existe plusieurs publications sur le contrôle des convertisseurs de puissance multicellulaires. Dans [1-6] les auteurs proposent des solutions basées sur le contrôle linéaire, certaines d'entre eux travaillent sur des contrôleurs PI indépendants et les autres sur le contrôle d'état. Dans [7-9], des techniques du type MPC (Model Predictive Control) sont utilisées mais dans les implémentations proposées, la fréquence de commutation est variable. Ce problème est traité dans [10-16], où les auteurs proposent des méthodes pour limiter les variations ou pour régler la fréquence de commutation. Dans [17-27], les méthodes de contrôle direct de la puissance et de placement vectoriel des commandes sont étudiées. Nous pouvons noter que la plupart de ces travaux ont été réalisés sur des convertisseurs DC-AC ou AC multicellulaires, mais le problème des convertisseurs DC-DC multicellulaires entrelacés couplés n'a pas été traité de manière significative.

L'objectif principal de cette thèse est de concevoir le système de contrôle dédié à de tels convertisseurs. Les stratégies de contrôle proposées devraient permettre d'équilibrer et

de stabiliser les convertisseurs de puissance multicellulaires entrelacés couplés et de surmonter les effets de couplage. Le fort couplage magnétique entre les cellules du convertisseur rend en effet l'équilibrage du courant difficile et augmente la complexité du contrôle. Quels sont les effets du couplage sur l'équilibrage ? Quelle est l'influence des variations des paramètres du convertisseur sur la stabilité ? Quelles sont les limites de mise en œuvre du contrôleur en temps réel ?

Nous tentons dans ce document de répondre à ces questions. Nous nous concentrons pour cela sur l'équilibrage des courants dans les cellules, sur la stabilité et sur la robustesse du contrôleur vis-à-vis des variations de la charge ou des paramètres du convertisseur. La mise en œuvre en temps réel est également un axe important de ce travail.

Ce document est constitué de six chapitres :

- En introduction, nous avons formulé le problème, la portée, les motivations et les objectifs de ce travail.

- Le deuxième chapitre donne un bref état des lieux des différents sujets abordés dans la thèse.

- Le troisième chapitre présente une première approche basée sur la commande linéaire des convertisseurs de puissance multicellulaires entrelacés couplés. Ce chapitre couvre la modélisation mathématique du convertisseur de puissance et présente différentes stratégies de contrôleurs linéaires et une analyse de chacune d'entre elles. Les méthodes de contrôle présentées sont successivement basées sur des contrôleurs PI appliqués avec une stratégie de découplage modale, sur un retour d'état découplant et un retour d'état réglé sur un critère quadratique (LQR : linear quadratic regulator).

- Le chapitre quatre présente une méthode basée sur le principe du contrôle prédictif du convertisseur par la méthode FCS-MPC (*Finite Control Set Model Predictive Control*). La méthode proposée est une évolution des méthodes utilisant ce principe de contrôle. Elle est conçue de telle manière à permettre de fixer la fréquence de découpage et à assurer un séquencement des commandes imitant l'entrelacement des commandes des cellules générées par les modulateurs à porteuses triangulaires généralement utilisés pour cette famille de convertisseurs. La conception et les performances d'un tel contrôleur sont analysées dans le cas de deux structures de type Boost et Buck et la robustesse du contrôleur est analysée vis-à-vis d'une modification de certains paramètres du système.

- Le chapitre cinq présente une stratégie de contrôle vectoriel des commandes des cellules (*Space Vector Control*) combinée à une stratégie MPC (*Model Predictive Control).* Les performances de la combinaison des deux méthodes de contrôle sont analysées et validées par simulation.

- Le dernier chapitre concerne la mise en œuvre expérimentale de différents contrôleurs proposés aux chapitres trois et quatre. Ce chapitre est divisé en trois parties. La première partie décrit le banc d'essai expérimental et ses composants. La deuxième partie traite de la mise en œuvre du contrôle linéaire et présente les résultats expérimentaux. La dernière partie est consacrée à la mise en œuvre de la méthode FCS-MPC et montre la stratégie d'implantation dans une cible FPGA et les difficultés de mise en œuvre.

Les principaux résultats

Contrôle linéaire des convertisseurs multicellulaires entrelacés

La structure servant de support à cette partie est un convertisseur multicellulaire à 3 cellules de type Buck dont le filtre de sortie est constitué par une inductance couplée.

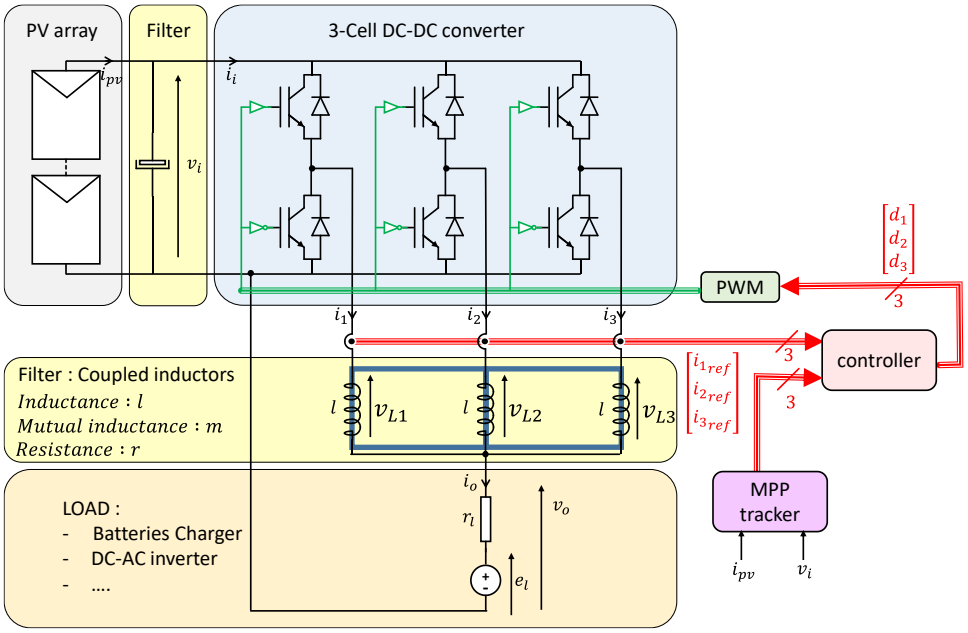

Le modèle moyen (à l'échelle de la fréquence de découpage) permet de construire le modèle d'état du convertisseur. Cette modélisation orientée contrôle montre qu'il existe un couplage significatif entre les différentes cellules.

$$\frac{d}{dt}\begin{bmatrix} i_1 \\ i_2 \\ i_3 \end{bmatrix} = -\begin{bmatrix} l & -m & -m \\ -m & l & -m \\ -m & -m & l \end{bmatrix}^{-1}\begin{bmatrix} r & 0 & 0 \\ 0 & r & 0 \\ 0 & 0 & r \end{bmatrix}\begin{bmatrix} i_1 \\ i_2 \\ i_3 \end{bmatrix} + \begin{bmatrix} l & -m & -m \\ -m & l & -m \\ -m & -m & l \end{bmatrix}^{-1}\left(\begin{bmatrix} d_1 \\ d_2 \\ d_3 \end{bmatrix} v_i - \begin{bmatrix} 1 \\ 1 \\ 1 \end{bmatrix} e_l\right)$$

Dans ce premier chapitre, on aborde la manière la plus simple et la plus robuste de mettre en œuvre un schéma de contrôleur dédié au contrôle des courants dans cette famille de convertisseur.

Pour faire face à ce problème, différentes approches sont évaluées.

- La première est basé sur un contrôle des courants dans chaque cellule par des contrôleurs indépendants classiques de type PI. Ce type de contrôleur est facile à mettre en œuvre et un anti-windup est facile à utiliser dans cette stratégie. Ce contrôleur donne de bons

résultats lorsque les courants dans les cellules ont des variations identiques, mais lorsqu'il y a variation individuelle des courants ou déséquilibre dans le convertisseur, il est démontré que ce type de contrôleur ne peut pas gérer correctement l'influence des voies les unes sur les autres.

- La seconde est basée sur une méthode modale. Elle est aisée à comprendre et à synthétiser d'un point de vue technique. Il est démontré qu'en fonctionnement en mode linéaire, cette méthode permet un très bon découplage entre les entrées de référence et les sorties associées. Cependant, un système anti-windup efficace ne peut pas être mis en œuvre pour prendre en compte de façon optimale la saturation des intégrateurs dans cette stratégie. Une stratégie équivalente sur le papier utilise une stratégie de contrôle d'état découplante, ce qui signifie que les coefficients du contrôleur sont définis de manière à assurer un découplage de la structure de commande. Les simulations montrent que le couplage est plus faible que dans le cas du contrôle modal et moins agressif en ce qui concerne les variations du rapport cyclique. Il est également montré que le comportement du système en boucle fermée est sensible aux paramètres magnétiques du coupleur. Or, ces derniers peuvent être difficiles à évaluer avec précision. Notons également que le contrôle des modes différentiels de cette structure met en œuvre des gains élevés pour compenser la dynamique naturellement lente associée à ces modes, ce qui peut entraîner une sensibilité au bruit et un risque de saturation des rapports cycliques.

- La dernière méthodologie est basée sur un retour d'état complet d'un modèle étendu dont les paramètres sont définis en minimisant une fonction de coût quadratique. Cette technique dite LQR permet de trouver un bon compromis entre les différents points clés du comportement du contrôleur, à savoir la stabilité, le temps de réponse, le découplage et la robustesse. Il est démontré que les réglages obtenus, maintiennent un couplage qui reste toutefois faible et acceptable. De plus ce contrôleur présente une structure quasi découplée du point de vue des intégrateurs permettant de mettre en œuvre aisément une technique anti-windup simple et efficace. De plus, le contrôleur actionne moins les rapports cycliques pendant les phases transitoires, ce qui réduit la sensibilité au bruit. Enfin, avec de tels réglages, ce contrôleur est également plus robuste aux changements de paramètres magnétiques des coupleurs, ce qui constitue un atout important.

En conclusion de ce chapitre, l'approche par retour d'état complet basée sur la méthode LQR présente un compromis très intéressant vis-à-vis des différentes exigences issues d'un cahier des charges. De plus ce type de contrôleur peut être aisément implanté dans un microcontrôleur ou un FPGA. Ces résultats très positifs encouragent à valider l'étude sur un banc d'essai de laboratoire. Ce qui sera fait dans le dernier chapitre.

Model Predictive Control des convertisseurs multicellulaires

Le principe est ici d'utiliser un algorithme basé sur le modèle de fonctionnement du convertisseur pour définir au sens d'un critère la séquence de commandes optimale des interrupteurs d'une structure multicellulaire à l'échelle d'une période de découpage. À la différence d'autre méthodes issues de la littérature la technique de commande proposée

permet de maitriser la fréquence de découpage tout en assurant un séquencement des commandes imitant l'entrelacement des commandes des cellules générées par les modulateurs à porteuses triangulaires entrelacées.

Il est démontré dans ce chapitre que la méthode de contrôle FCS-MPC peut être utilisée pour contrôler un convertisseur DC-DC multicellulaire couplé magnétiquement. Il offre la possibilité d'équilibrer le courant et de contrôler le courant global d'un tel convertisseur même s'il existe un fort couplage entre les cellules. La méthode proposée permettant de fixer la fréquence de commutation des interrupteurs est validée. Les avantages de la méthode proposée au-delà de la fréquence fixe sont les suivants :

- Une réduction du nombre de séquences à évaluer permettant une implémentation en temps réel avec une cible FPGA. De plus cette méthode ne nécessite pas de calcul hors ligne ;
- Une fréquence d'échantillonnage des grandeurs à contrôler faible (les mesures sont effectuées au début de la période de découpage) ;
- Une mise en œuvre possible pour un nombre élevé de cellules ou pour les convertisseurs multiniveaux.

Toutefois, le contrôle basé sur la méthode FCS-MPC a aussi beaucoup de limites :

- Le nombre de séquences à évaluer par période de découpage devient très vite très important. Ce nombre dépend en effet du nombre de points qui divise la période de de découpage définissant par ailleurs la résolution en rapport cyclique ;
- Un système numérique très rapide est donc nécessaire pour tester en temps réel toutes les séquences de commutation possibles et trouver la solution optimale ;
- Ce type de contrôleur est sensible aux paramètres du modèle. Il peut donc être nécessaire d'ajouter certaines fonctions pour compenser certaines déviations, comme par exemple des observateurs pour estimer certains paramètres.

En conclusion, en raison de ces limitations, la méthode FCS-MPC n'est pas vraiment satisfaisante. Pour lever ces limitations, une nouvelle méthodologie basée également sur le modèle du convertisseur mais avec beaucoup moins de limitations est proposée au chapitre suivant.

Contrôle vectoriel et Model Predictive Control des convertisseurs multicellulaires

La méthode mixte associant le contrôle vectoriel aux principes du MPC est une réelle amélioration par rapport au FCS-MPC présenté au chapitre précédent.

En effet, la connaissance du modèle permet de calculer directement la durée d'application des vecteurs d'une séquence de vecteurs prédéfinie avec une résolution possible élevée sans avoir à tester différentes possibilités de rapport cycliques. Ainsi, la limitation précédente disparaît. Cette méthode assure également une fréquence de commutation constante et permet, par le choix des séquences réalisées, d'assurer un entrelacement régulier des cellules en régime permanent. La méthode MPC appliquée ici

vise à déterminer la meilleure séquence à appliquer au convertisseur de puissance. Ceci conduit à évaluer une fonction coût pour seulement 12 séquences différentes par rapport à la méthode FCS-MPC précédente qui nécessitait 1000 évaluations pour seulement 9 points de prédiction sur la période de découpage. Cette méthode donne donc clairement de bien meilleurs résultats pour un coût d'implantation plus bas.

Dans la dernière partie de ce chapitre, la robustesse de la méthode est analysée par rapport aux erreurs dans la connaissance des paramètres du modèle. Les simulations montrent que le convertisseur reste stable même pour des erreurs de modèle significatives. Néanmoins, l'erreur du modèle sur l'inductance provoque un décalage significatif de la valeur moyenne du courant différentiel qui peut conduire à la saturation du composant magnétique. Cette sensibilité à l'inductance nécessite plus d'investigation afin d'être géré.

D'autres améliorations peuvent également être apportées en ce qui concerne la gestion des saturations des rapports cycliques. Ce type de problème survient surtout lorsque le mode commun moyen est proche du niveau 0 ou niveau 3 car certains rapports cycliques sont alors très petits ou très importants. Mais ce problème peut également survenir en cas de variation importante et rapide de la tension de mode commun.

Résultats expérimentaux

La structure générale du banc d'essai est présentée ci-dessous.

Ce banc d'essai est construit autour d'un convertisseur de puissance à trois cellules et d'une inductance couplée en sortie. On peut également voir sur cette figure, que le contrôleur utilise une implémentation mixte : la gestion des courants et l'élaboration des PWM sont implantées dans un FPGA (Xilinx® Kintex® -7 XC7K325T FPGA) et le contrôleur de tension de sortie est intégré dans un microcontrôleur (Freescale QorlQ P5020, double cœur, cache de données L1 de 2 GHz 32 Ko par cœur, 32 Ko de cache d'instructions L1 par cœur, 512 Ko de cache L2 par cœur, 2 Mo de cache L3 total, Freescale QorlQ P1011 800 MHz pour la communication avec le PC hôte). Tous ces périphériques sont inclus dans une MicroLabbox Dspace. La dernière partie correspond à la partie le logicielle implantée sous Controldesk (fonctionnant sur un PC) dédiée au contrôle du banc d'essai et fournissant des moyens de surveillance.

Dans ce chapitre, nous décrivons la mise en œuvre des stratégies de contrôle développées précédemment. Nous avons vu que les résultats expérimentaux obtenus sur le banc d'essai valident les résultats théoriques et les analyses des chapitres précédents pour le contrôleur PI indépendant, la stratégie de contrôle par découplage et le retour d'état réglé par la technique LQR. Toutes ces méthodes de contrôle ont été facilement implémentées sur la cible FPGA. En ce qui concerne la méthode de contrôle FCS-MPC, l'implantation sur FPGA n'a pas abouti même si nous avons proposé dans ce travail des descriptions partielles de sa mise en œuvre. Au moment de la rédaction du document, il n'y a pas de résultats expérimentaux pour cette méthode en raison de la difficulté à implanter la totalité de l'algorithme dans la cible FPGA.

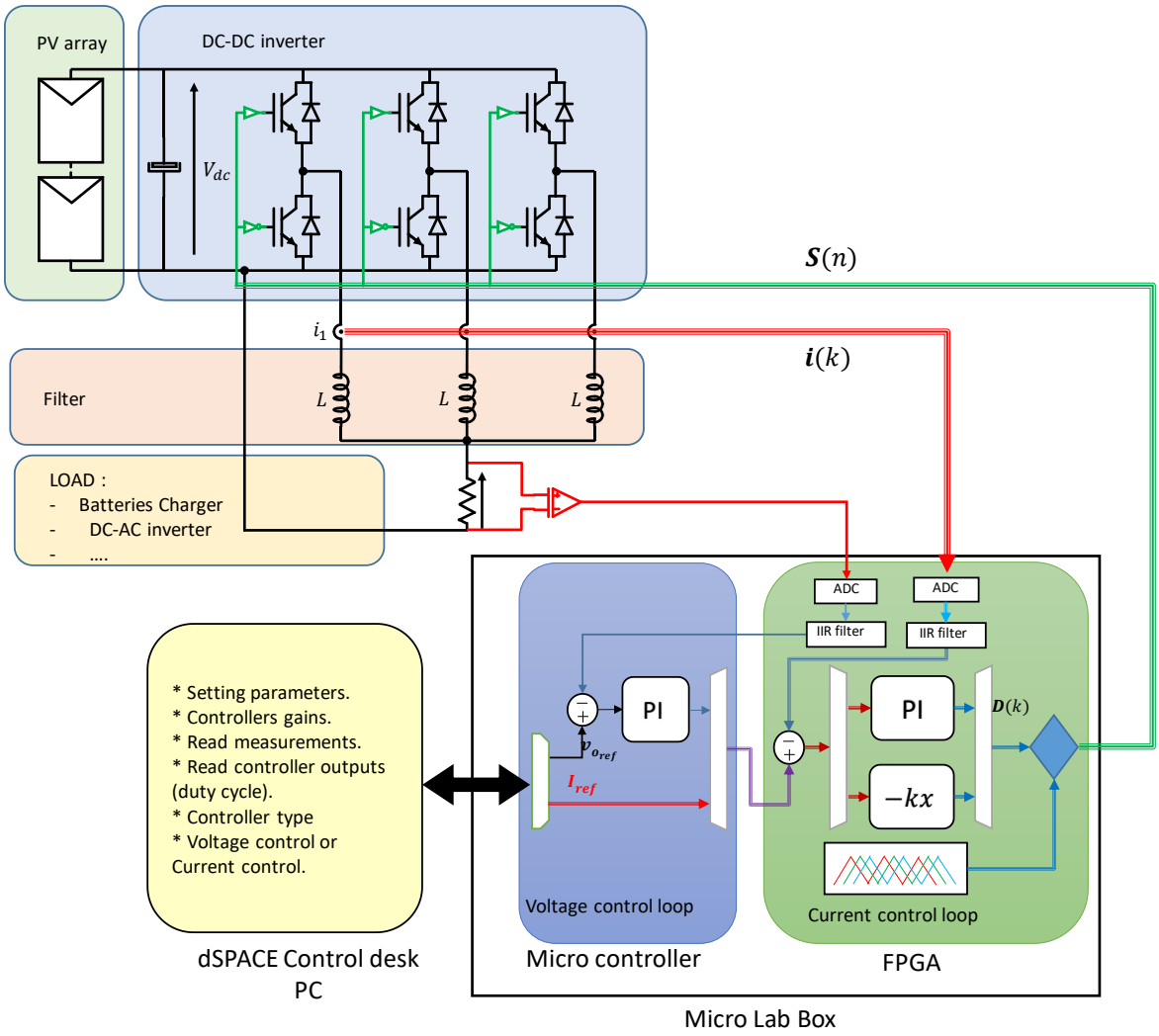
PV array
DC-DC inverter
V_{dc}
$S(n)$
i_1
$i(k)$
Filter
L
L
L
LOAD :
- Batteries Charger
- DC-AC inverter
- ....
ADC
ADC
IIR filter
IIR filter
PI
PI
$D(k)$
$V_{o_{ref}}$
I_{ref}
$-kx$
Voltage control loop
Current control loop
* Setting parameters.
* Controllers gains.
* Read measurements.
* Read controller outputs (duty cycle).
* Controller type
* Voltage control or Current control.
dSPACE Control desk PC
Micro controller
FPGA
Micro Lab Box

Chapter 1. Introduction

Interleaved multicell DC-DC converters are excellent candidates for microgrids and renewable energy systems due to their electrical behavior and their possible high dynamics. Indeed, one of the main characteristics of these converters is to improve the current ripples at their input and output. They are thus a good option for solar system due to the reduction of the electrical stress on the PV string while reducing the filtering requirements and thus the size of the filters and thereby leading to an increase of the converter compactness. Moreover, the multicellular nature of this family of converters offer the possibility of obtaining a very high energy efficiency over a very wide range of power by allowing to choose the number of cells to put into operation. Again, this is an indisputable advantage for conversion applications for renewable energy systems.

These advantages are counterbalanced by the control difficulty due the to the significant increase in the number of variables to be controlled in this type of complex system. The coupling between cells which leads to further improve of the performances of the system adds to this complexity. The work presented in this paper deals with the control of such structures.

The scope of this research is based on three different approaches to control coupled interleaved multicell DC-DC converters, the first one is based on linear control applied to a modal representation of the system, model predictive control (MPC) is used for the second and space vector direct control (SVD) with model prediction for the third.

There are several publications on the subject of multicell power converters control. In [1]–[4] authors propose solutions based on linear control, some of them are working on independent PI controllers and the others are working on state space control. In [5], [6] MPC is used but, in the proposed control implementations, the switching frequency is variable. In [7]–[13] authors propose methods to limit the variations or to set the switching frequency. In [14]–[23] direct power control and space vector placement methods are studied. We can note that most of these works were done on multicell DC-AC or AC inverters, but the problem of coupled interleaved multicell DC-DC converters has not been significantly addressed.

The main objective of this thesis is to design the control system dedicated to such converters. The proposed control strategies should allow to balance and stabilize coupled interleaved multicell power converters and to overcome the coupling effects. The strong magnetic coupling between the converter cells makes current balancing difficult and increase the complexity of control. What are the effects of coupling on the current balancing? What are the influence of the converter parameters variations on the stability? What are the implementation limitations of the real time controller?

From these main questions it is clear that our research will focus on current balancing, on stability and on robustness of the controller against the change into the load or converter parameters. The real-time implementation is also an important axis of this work.

The thesis is divided in six chapters. In introduction, we formulated the problem, the scope, the motivations and the objectives of this work.

- The second chapter gives a brief state of the art on the different topics covered in the thesis.

- The third chapter is about the first research approach, namely the linear control of coupled interleaved multicell power converters. This chapter covers the mathematical modeling of the power converter and presents different linear controller strategies and an analysis of each of them. These control methods are based on PI controllers applied with a decoupling strategy and on state feedback and linear quadratic regulator (LQR).
- Chapter four is related to Finite Control Set Model Predictive Control FCS-MPC. The proposed method for fixing the switching frequency is well studied and the design of the controller in the case of two structures boost and buck are presented. The robustness of the controller is analyzed.
- Chapter five presents a space vector control strategy (DSV) combined with MPC. The proposed method is analyzed and validated by simulation. Also, the combination between the proposed DSV and MPC is covered.
- The last chapter is about the experimental implementation of different controllers proposed in chapters three and four. This chapter is divided in three parts. The first part describes the experimental test bench and its components. The second part deals with the implementation of the classical linear control and the gives derived experimental results. The last part is dedicated to the implementation of FCS-MPC and shows the implementation difficulties.

Chapter 2. State of Art

2.1. Introduction

This chapter is divided in four sections. The first section is dedicated to multicell power converters and recall their topologies and their use, especially in the field of renewable energies with a particular focus on solar applications and DC microgrids. The next sections are related to control of power electronics converters. We recall first some main results on classical control strategies dedicated to power converters and earlier works related to control of interleaved multicell power converter. Then a brief description of a particular control strategy based on model predictive control is done. The last section is dedicated to the presentation of space vector placement strategies.

2.2. Multicell Power Converter

2.2.1. Topologies of Multilevel DC/DC Converters

There are a lot of different topologies of multilevel power converters reliant on the power range, kind of conversion, their applications etc. but they have the same basic properties. Such as apparent switching frequency and harmonic cancellation [24].

2.2.1.1 Series connections

There are more than one way to design a series multicell power converter depending on the nature of power source.

(1) Series connection with isolated power sources

Figure 2-1 shows a multicell DC-DC power converter with a series connections. In this structure where the power supplies are isolated, the delivered power from each power supply, the duty cycles and the switching frequencies can be different from each cell. This topology is used in DC-AC applications more than in DC-DC applications.

For DC applications they can be used with DC storage devices, such as batteries where each power converter manages the battery cell energy while providing, though the series connection, the capability to deliver high voltages [25]. The DC sources can also be low voltage generators such as fuel cells or PV panels [26]–[28]. For PV panels in a same string, all cells can have the same design, switching frequency and duty cycles. It is also possible to apply an interleaved PWM to this structure reduce the voltages and currents ripples at the input and output of the power converter[27].

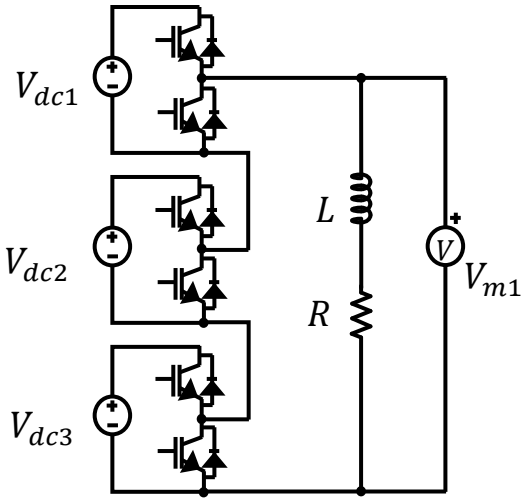

Figure 2-1 Multicell Power converter: series connection with isolated power supply

(2) Flying capacitor

This topology can be used with a single DC source and can be used either for AC or DC applications. In case of unidirectional output current some switches can be replaced by diodes as shown in Figure 2-2-a[29].

Such converters can be designed with any number of cells as shown in Figure 2-2-b [30]. For AC sources, reverse blocking devices can replace bidirectional switches of Figure 2-2-b to build the current source inverter shown in Figure 2-2-c. This can also be done by using a four-quadrant AC chopper as in [31]. In these to last configurations, the voltage source is AC, the flying capacitor voltages are AC too. The control of such AC topologies are more complex to realize as the dynamic of active balancing of the capacitor voltages should be fast I order to follow the AC voltage of the source. This involves a high switching frequency.

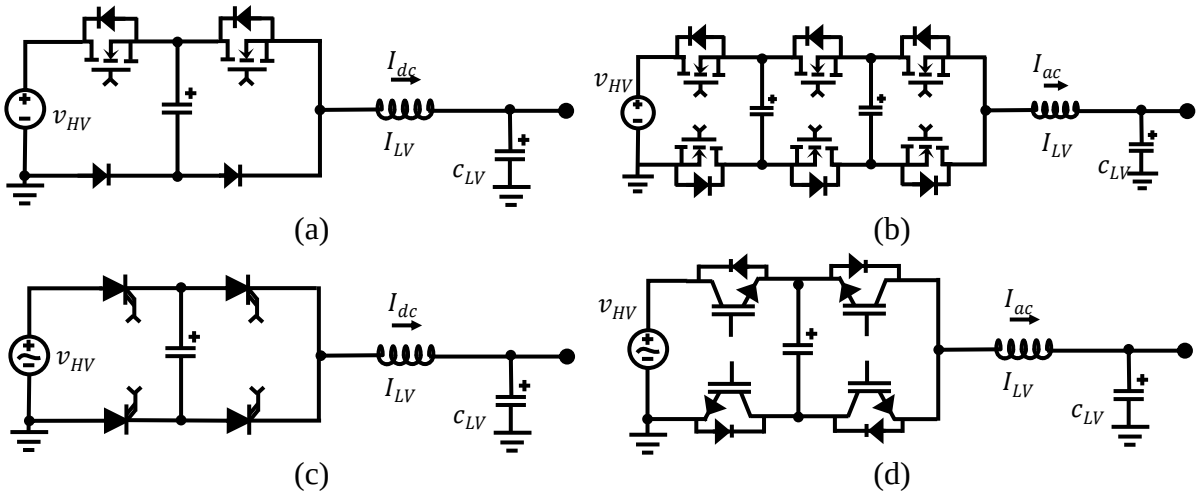

Figure 2-2 Different topology of flying capacitor converters

2.2.1.2 Parallel connections

(1) Star connection with interleaved PWM

Figure 2-3 shows a multicell boost converter with a star connection of inductors [32]. The three inductors in this structure have the same size and the supply current is divided in three equal parts through the three cells.

The main advantage of the interleaved multicell power converter with a star connection is the reduction of the voltages and current ripples at the input and output of the converter. This offer the possibility to reduce significantly the size of input and output filtering capacitors.

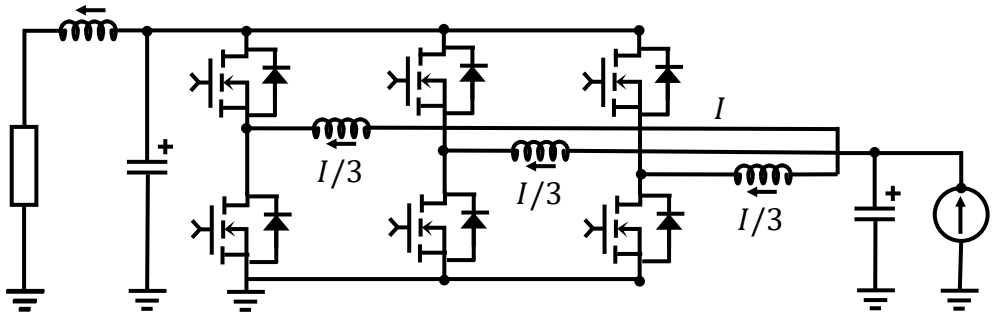

Figure 2-3 Parallel multicell converter with star-connected inductors

(2) Interleaved multicell power converter with InterCell Transformers (ICTs)

The current ripple reduction in interleaved parallel star connection using uncoupled inductors is only visible at the input and the output. There is no reduction of the rate of current ripple in the cells in such topologies. Such a solution is thus limited to a reduced number of cells (three or four). It is possible to solve this issue by using inductors magnetically coupled. The magnetic coupling can significantly reduce the ripples in the cells as shown in Figure 2-5. In this figure we can note that the cell-currents ripples are significantly reduced in Figure 2-5-b. These results can be compared with the cell-currents waveforms for uncoupled inductors in Figure 2-5-a. This property offers the opportunity of significantly reducing the size of inductors.

The cells of a multicell parallel power converter can be magnetically coupled in two ways. The cyclic cascade configuration, in which two windings transformers are used to link two adjacent cells as in Figure 2-4-a. The second possible configuration is to use a monolithic magnetic device as shown in Figure 2-4-b. In this structure, all the winding are wound on the same magnetic core in such a way cell are coupled with the others. Different design topologies for coupled inductors and ICT are shown in [33].

The subdivision of currents in multiple cells involves that such parallel topologies can be used for high current supply systems and very low voltage. The possible reduction of the global output inductance is also an interesting property as it provides to such converter the capability to drive a very dynamic load [24], [34].

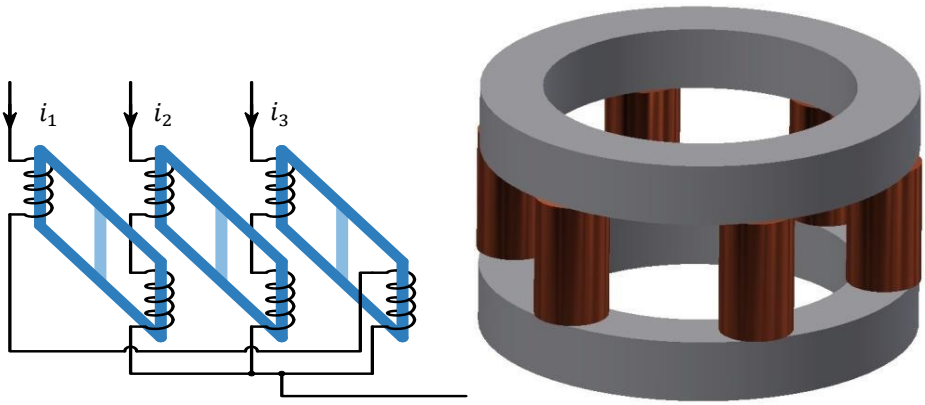

(a) (b)

Figure 2-4 InterCell Transformers. a) cyclic cascade configuration b) monolithic configuration

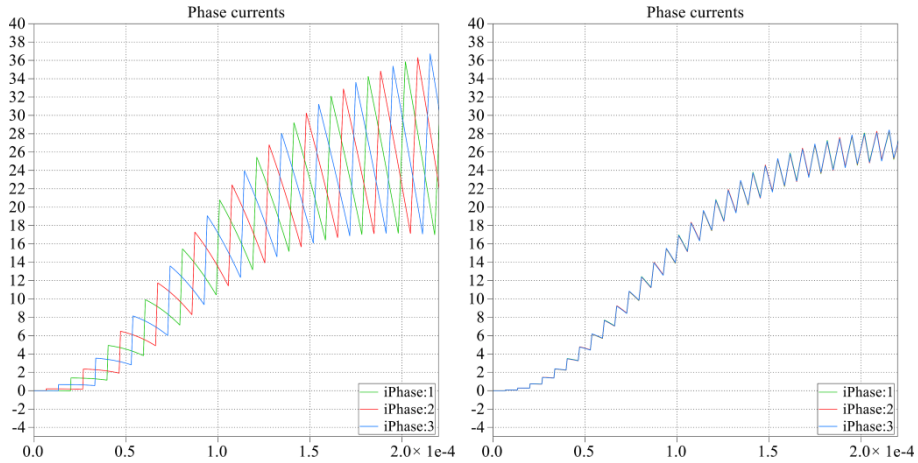

(a) (b)

Figure 2-5 phase currents of three cells parallel multicell converter: a) uncoupled b)coupled[6]

2.2.2. Multicell Power Converter in Solar application and microgrids

Parallel multi-cell converters using intercell transformers (ICTs) are an attractive technique in the field of low and medium voltage and high current power converters. These very versatile structures can be used in many types of power conversion structures such as Boost or Buck DC-to-DC power converters as well as in DC-to-AC inverters or AC-to-DC synchronized rectifiers. They are broadly used in various applications and are particularly useful in renewable energy systems such as in photovoltaic inverters [35], [36], storage management systems [37], fuel cell converters [38] as well as in electrical vehicle [39]. Notwithstanding this success, there is scope for further improvements, such as ICT design for fault-operation [33] and control enhancement [2], [3].

Figure 2-6 show a simple schematic of a microgrids structure. The main player in such

microgrids is the power converters. Power converters are used in microgrids for balancing the power, voltage and current. The multicell power converters are suitable to be used in renewable energy resources due to their features and advantages[40].

A photovoltaic array feeds a load which could be possibly a battery, directly some DC loads or a grid inverter. As both PV maximum power point and the load voltage can vary greatly, it is mandatory to interface a converter between the load and the source.

This can be done for low voltages and low power with a multicell interleaved power converter [25]. Compared to classic single buck converter, the main advantage of this power electronics structure is to ensure low current ripples at both input and output sides. In fact, regarding the input stage, the input current ripple is reduced by an n factor while the input current apparent frequency is increased by a factor of n. As a result, the C_i capacitance can be reduced by a significant n^2 factor leading to improve the system dynamics and namely its ability to track faster the maximum power point of the PV array. Similarly, the amplitude of phase current ripples are reduced by a n^2 factor compared to an uncoupled multi-cell converter (considering a similar filtering inductance value), which reduces the constraints on the power semi-conductors and the related losses. Moreover, the global power converter output current ripple is reduced by n compared to a classical one-cell Buck DC-DC converter, in the same way as for interleaved multi-cell DC-DC Buck converter with uncoupled inductors. This limits the need to filter the output voltage: in some cases, no additional output capacitor is required.

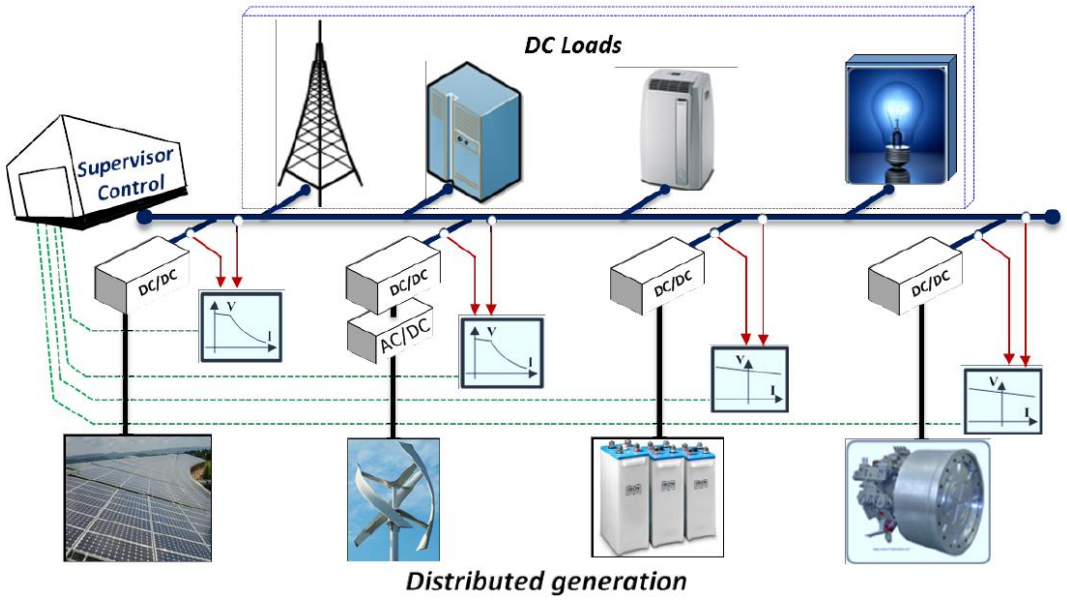

Figure 2-6 schematic diagram of DC microgrid structure (https://www.et.aau.dk/research-programmes/microgrids)

2.3. Classical control and LQR

There are a number of control methods to control power converters and drives. The most popular control strategies are shown in Figure 2-7. Some strategies are very well covered and

simple, such as the hysteresis control, whereas other control strategies are more complex and need higher calculation power but lead to higher system performances.

Current control in power converters is the main studied topic. For such control, there are two main classical approaches that have been widely studied in the last decades: specifically, hysteresis control and linear control using pulse width modulation (PWM).

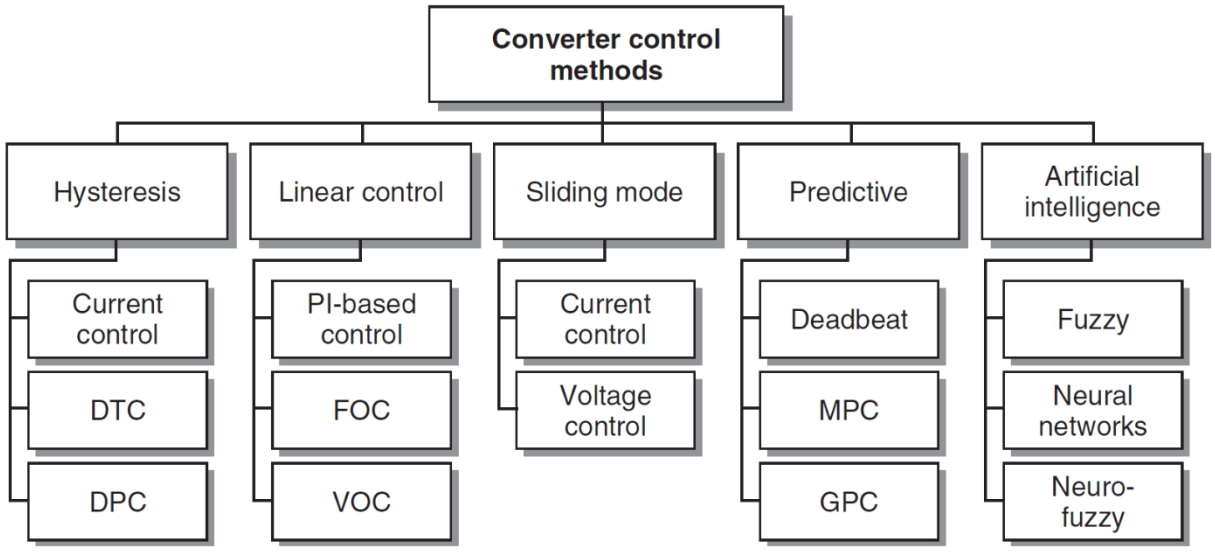

Figure 2-7 Different types of converter control for power converters and drives

2.3.1. Hysteresis control

Hysteresis control uses the nonlinearity of a power converters induced by the switching states of a power converter. The proper switching state can be defined in order to insure an oscillation of the controlled quantities around the required one with a given hysteresis width. It can be used in simple applications, for example in case of basic current control but can also be generalized to more complex systems like in direct power control (DPC) [41]. Usually this type of controller is implemented with analog electronic devices. Indeed, an implementation on a digital platform, required a very high sampling frequency to properly control variations of the controlled quantities. Moreover, the switching frequency is variable in such control for a fixed hysteresis width but note that there are some possible modifications of this control strategy to achieve a fixed switching frequency.

Figure 2-8 shows waveforms for an hysteresis current control applied to a single phase inverter. The controlled current is the load current (i_L). This value is compared to the reference (i_L^*). The calculated difference (error ε) pass through an hysteretic comparator. If the error reached the upper limit ($\delta/2$), the controller turns on T_1 and T_4 and turns off the other two switches. The opposite command is applied when the error is less than the lower limit ($-\delta/2$). It can be observed from. Figure 2-8-b that the load current follows its reference with a pick to pick oscillation equal to the hysteresis width.

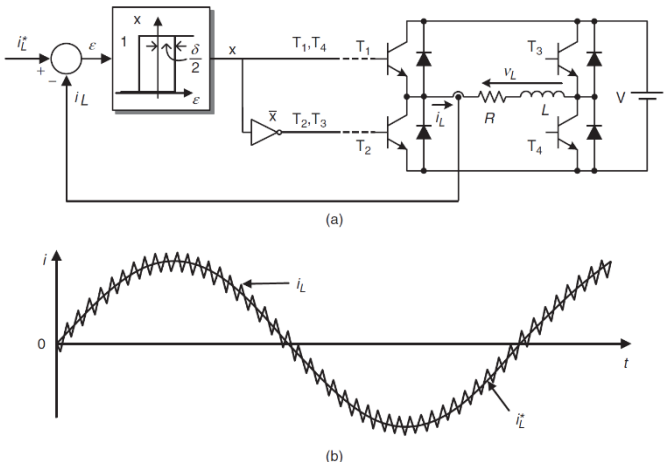

Figure 2-8 Hysteresis current control for a single-phase inverter. (a) Control scheme. (b) Load current

2.3.2. Linear control using PWM

The power converters are linear switched systems. From an average point of view, at the switching frequency scale, they can be linearized. With such approach, it is possible to use any linear controller with a PWM or a space vector modulator and proportional integral (PI) controllers are commonly used.

2.3.3. PI/IP control

Independent PI controllers are well suited to control uncoupled MIMO system quantities. This is natural for current control of uncoupled multicell power converters but for coupled ones, a decoupling strategy must be applied.

Authors in [1] use PI controllers to control a multicellular uncoupled parallel inverter in d,q axis in order to easily control the active and reactive power delivered to the grid. In these axis the system equations are coupled. Authors proposed a control strategy defined by elements of Figure 2-9 where we can see coupling effects between the two axis. Nevertheless, they used PI controllers for each axis without taking into account the coupling effects. They assumed these effects like disturbances. Note that effects of coupling are not studied and discussed in this reserch.

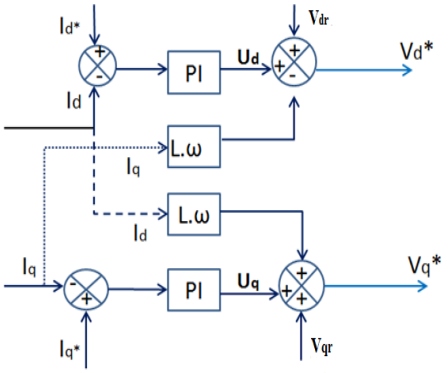

Figure 2-9 Diagram of the decoupled PQ Control

A current decoupling strategy is proposed in [2]. Authors use a classical PI controller to control the fictitious decoupled quantities of multicell power converter as shown in Figure 2-10. For this purpose, they diagonalized the inductance matrix (the mathematical representation of the coupled inductor) by using two transformations matrix (T) and its inverse (T^{-1}). These transforms lead to calculate fictitious currents for which an independent PI controller can be applied. This document does not deal with the problem of the sensitivity of the control with regard to uncertainties on the knowledge of the model.

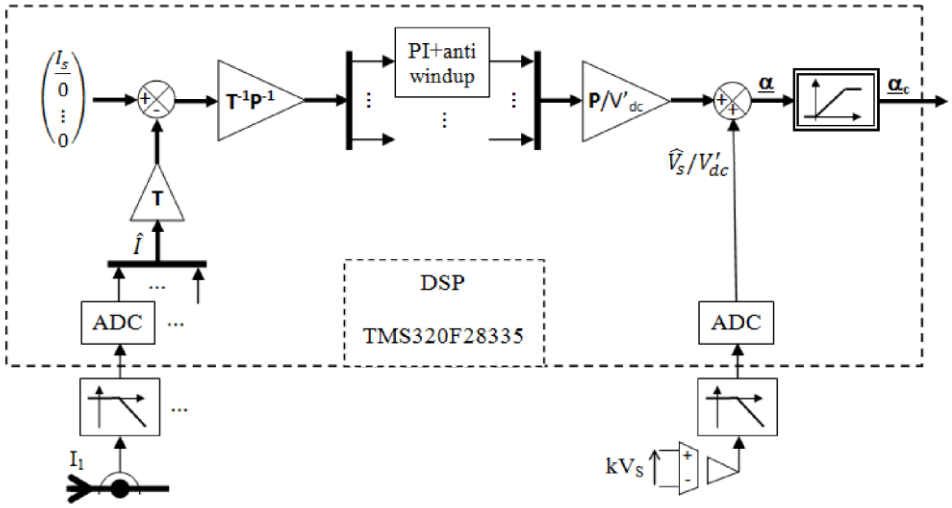

Figure 2-10 Block diagram of the decoupled control strategy of a multicell power converter

This control technique will be used in this PhD but an addition will be made concerning the sensitivity study to the parameters of the model.

2.3.4. State space control

The state space control is suitable for multi inputs multi outputs (MIMO) systems, and the multicell power converter is a MIMO system. Authors in [3] use state feedback to control the

sharing of currents between cells as shown in Figure 2-11. The idea behind the state feedback is to calculate the control input (u) by multiplying all the states (x) by a gains value ($\boldsymbol{u = -K\,x}$).

In this example all cells currents are measured and the difference with one-nth of the total required output current is calculated. Then, the gain matrix ($\boldsymbol{K_{i_i}}(s)$) is applied and give sharing correction component of the duty cycle (d_i). The output voltage control loop (duty cycle D) gives the global identical duty cycles D_i applied to each cell. In other words, the current loop is used to control the differential mode of the currents and the voltage loop is used to control the common mode. In this paper authors did not study neither the sensitivity to the parameters of the model neither the impact of the coupling effect on this control strategy.

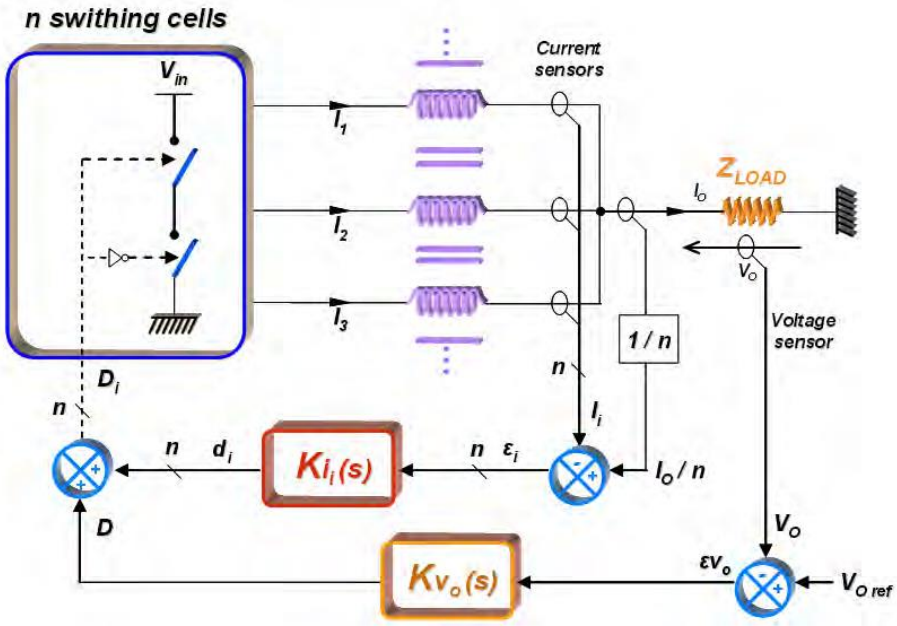

Figure 2-11 current sharing and voltage regulation for n-arm buck converter

The technique proposed in [4] is concerned with the control of a three level inverter (with no magnetic coupling) by state feedback. The control is designed for small signal in $d-q$ axis. In this paper authors used linear quadratic program (LQR) technique to find the controller gains.

Based on these works, we will use in this PhD two different ways to design the state space feedback controller. In the first method, we use pole placement with some constraints to deal with the high degree of freedom of our system. In the second approach, we use linear quadratic regulator (LQR) technique to find the optimal controller's gains. In addition, an in-depth analysis of the sensitivity to uncertainties on the knowledge of the system parameters will be conducted as well as an analysis of the coupling effects .

2.4. Model Predictive Control

Model predictive control (MPC) is playing a great role in the control of systems. It is used in many applications [42]–[45]. The main feature of MPC is to be able to deal with nonlinear, constrained and multi-input multi-outputs systems.

Mainly, in the field of power electronics, the MPC principles make it as a talented control substitute for power converters and machine drive [5], [46] because of its numerous advantages:

- Its concepts are spontaneous and easy to understand.
- It can deal the control of converters with multi inputs, multi output and states (currents, voltage, power, etc.)
- Nonlinearity and constrained can be included in MPC in an easy way

2.4.1. Basic principles of Model Predictive Control

The principle of MPC is illustrated in the Figure 2-12. At time-step k state-values are acquired. Based on the model and on the cost function the optimal switching vector sequence is calculated and the future states are predicted until the end of prediction horizon ($k + H_p$). At time-step k, the first calculated optimal control input $u(k)$ of the switching sequence (the output of the controller for a power converter) is applied to the system. This procedure is repeated at each time-steps with new measurements while moving the prediction horizon by one step to keep the same length of the horizon (H_p).

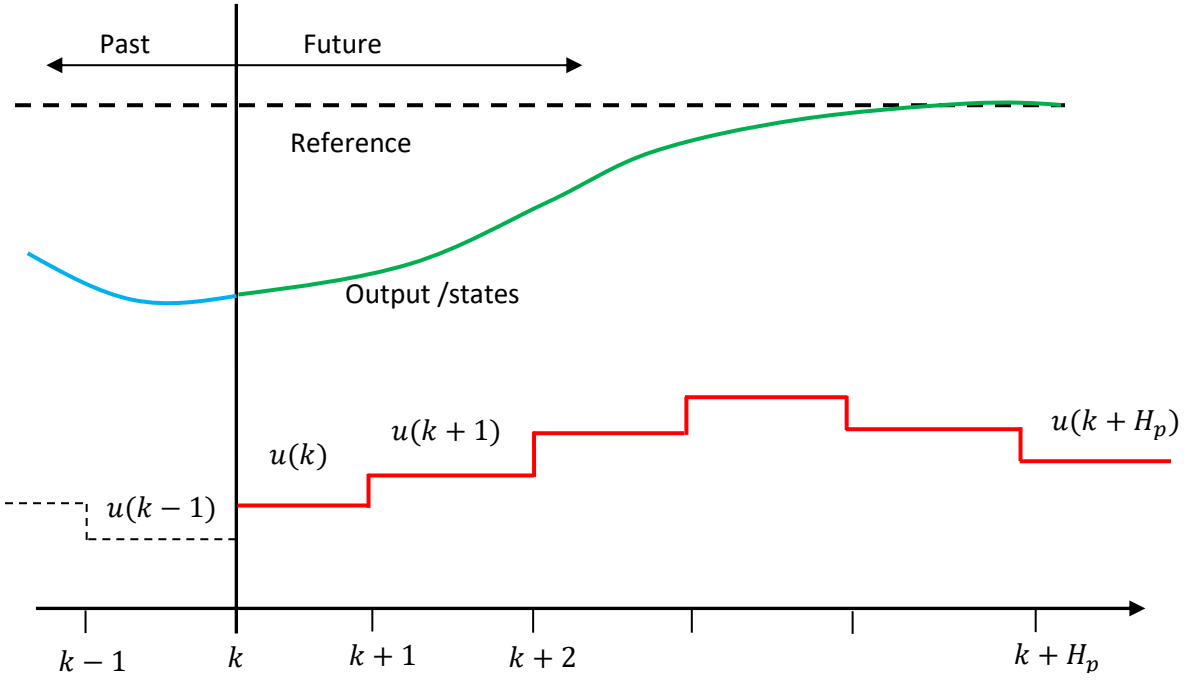

Figure 2-12 MPC principle

The principle of MPC is based on:

- The system model, to predict the future behavior of variables for a specific horizon called prediction horizon (H_p). A discrete model is needed for MPC and can take the form of a discrete state-space model. The model can be either linear or nonlinear.

$$\boldsymbol{x}(k+1) = f(\boldsymbol{x}(k), \boldsymbol{u}(k)) \qquad (2\text{-}1)$$

$$\boldsymbol{y}(k) = f(\boldsymbol{x}(k), \boldsymbol{u}(k)) \qquad (2\text{-}2)$$

- The cost function to specify the desired behavior of the system. The cost function can customize the behavior of the system, and can include the references, the states and the future control input as in equation (2-3). The cost function can be in quadratic programing (QP) or linear programing (LP).

$$J = f(\boldsymbol{x}(k), \boldsymbol{u}(k) \dots \dots \dots \boldsymbol{u}(k + H_p)) \qquad (2\text{-}3)$$

- The minimization of the cost function to find the optimal actuating signal. The optimization of the cost function along a specific horizon (H_p) subjected to the dynamic of the system (model) and a specific constraint will result in an optimal switching vectors (in power electronics applications) from instant k to $(k + H_p)$. Appling only the first optimal switching vector $\boldsymbol{S}(k)$ to the power converter.

$$\min_u J$$

subjected to:

$$\begin{gathered} x(k+1) = \boldsymbol{A}_d x(k) + \boldsymbol{B}_d u(k) \\ y(k) = \boldsymbol{C}_d x(k) + \boldsymbol{D}_d u(k) \\ 0 \leq x(k) \leq i_{up} \\ u(k) \in [0,1] \end{gathered} \qquad (2\text{-}4)$$

- The constraints that can be applied on control input ($u(k)$) and states ($x(k)$) represent the main advantage of MPC. In a power converter, the state constraints can be for example the voltage in a flying capacitor converter or the currents in the cell for a multicell converter. The control input can be a continuous quantity which represents the duty cycle if a PWM modulator is used. In this case, the constraint will be applied on the duty cycle ($u(k) = d(k) \in [0,1]$). For a finite number of control input, MPC becomes Finite control set MPC (FCS-MPC). In this case, the constraints will be on the cell states with only 2 possible values ($u(k) = S(k) \in \{0,1\}$)

The search for an optimal solution is carried out at each sampling instants, with new measurements and gives a new optimal switching vector. This is called *receding horizon* strategy.

2.4.2. Finite control set MPC

MPC with Continuous Control Set applied to a power converter requires a PWM modulator as shown in Figure 2-13-a. It has a high computational cost as control inputs are continuous functions. Conversely, FCS-MPC with a defined number of switch states combinations that can be applied to the converter and thus to the model does not need a PWM modulator as shown in Figure 2-13-b and has a lower computational cost. One advantage of FCS-MPC is that the switching actions are taken in the optimization problem and can be assumed as a constraints on the control input [46]. The other is the reduced number of control set. Nevertheless, this number depends on the prediction horizon and on the topology of the power converter. For example, for a one step prediction horizon and a one cell power converter the control set will be $S = 0\ or\ 1$. To predict the states at $k + 1$ we have thus two prediction states $x^p_{s=0}(k+1)$ and $x^p_{s=1}(k+1)$. But when the prediction horizon is

more than one for this one cell power converter the size of control set depends on the prediction horizon an is equal to 2^{Hp}. This mean that the complexity increases exponentially with the prediction horizon. Due to its properties only FCS-MPC will be study in this PhD.

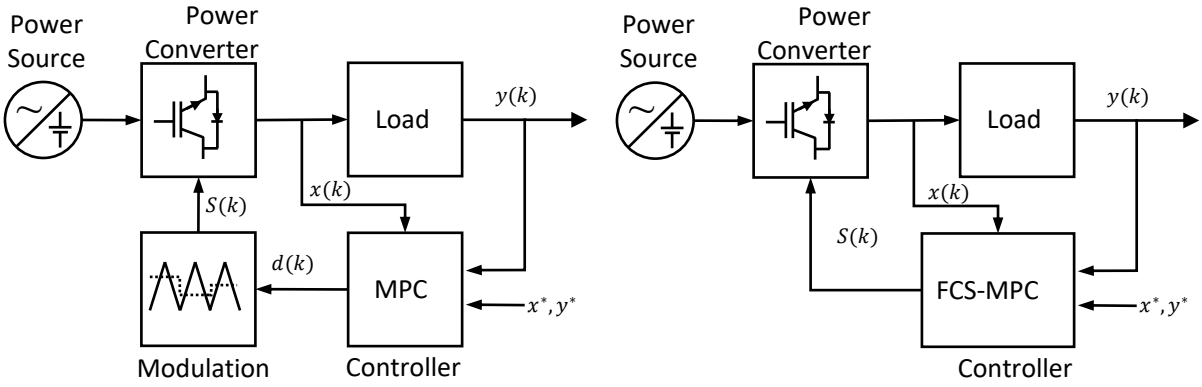

Figure 2-13 Model predictive control :a) with continuous control set, b)with finite control set

2.4.2.1 Working principle for one step prediction horizon

To explain the principle of FCS-MPC for one step prediction horizon we use here an example based on a 3-cell DC-DC power converter. Figure 2-14 shows the block diagram of this example. The discrete state space model of the multicell converter with a sampling period (T_s) is given by the following equations:

$$x(k+1) = \boldsymbol{A}_d x(k) + \boldsymbol{B}_d u(k)$$
$$y = \boldsymbol{C}_d x(k) \qquad (2\text{-}5)$$

Where :

$$\boldsymbol{A}_d = \begin{bmatrix}1 & 0 & 0\\ 0 & 1 & 0\\ 0 & 0 & 1\end{bmatrix} - T_s \begin{bmatrix} l & -\mathrm{m} & -\mathrm{m}\\ -\mathrm{m} & l & -\mathrm{m}\\ -\mathrm{m} & -\mathrm{m} & l\end{bmatrix}^{-1} \begin{bmatrix} r+r_L & r_L & r_L\\ r_L & r+r_L & r_L\\ r_L & r_L & r+r_L\end{bmatrix}, \boldsymbol{B} = V_{dc}T_s \begin{bmatrix} l & 0 & 0\\ 0 & l & 0\\ 0 & 0 & l\end{bmatrix}^{-1}$$

$$\boldsymbol{C} = \begin{bmatrix}1 & 0 & 0\\ 0 & 1 & 0\\ 0 & 0 & 1\end{bmatrix}, \quad \boldsymbol{x} = \begin{bmatrix} i_1\\ i_2\\ i_3\end{bmatrix}, \boldsymbol{u} = \begin{bmatrix} S_1\\ S_2\\ S_3\end{bmatrix}$$

If the purpose of FCS-MPC is to control the currents in each cell, the cost function can be based on the difference between the Cell currents and there references:

$$J = \left(i_{ref}(k) - i_{av}(k)\right)' \boldsymbol{Q} \left(i_{ref}(k) - i_{av}(k)\right) \qquad (2\text{-}6)$$

Where **Q** is a weighting matrix which is positive semi-definite. This matrix can be used to tradeoff between the terms of the cost function.

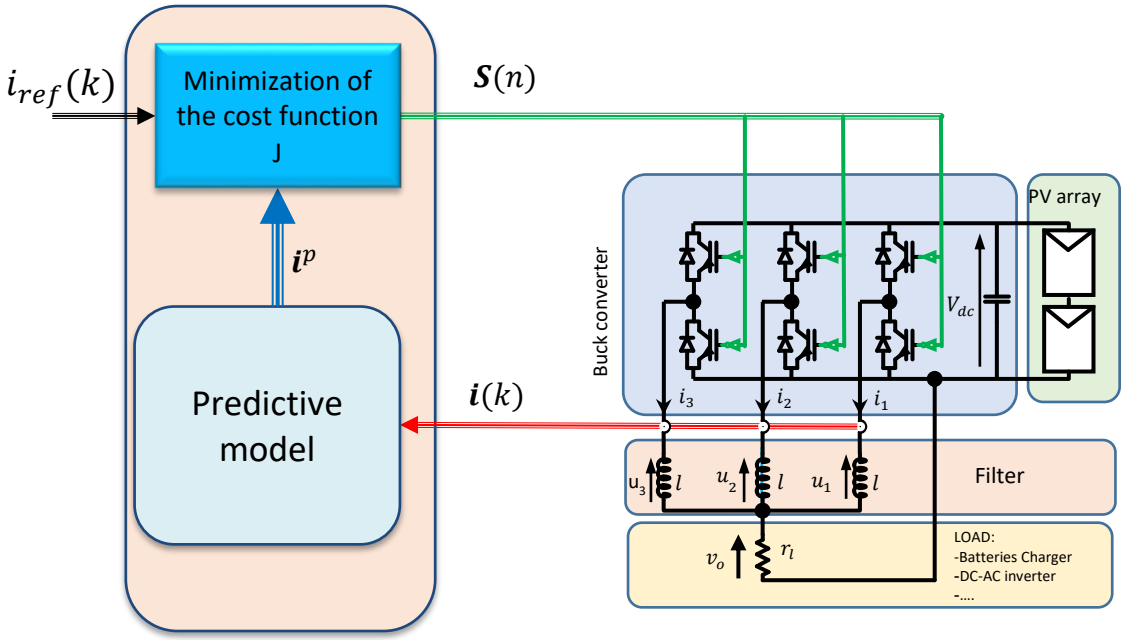

Figure 2-14 Block diagram of model predictive control of the currents of a 3-Cell buck converter

Constraints can be added on the states (here currents in the cells). For example, current should not be negative, this gives the lower limits for the current. The upper limits of currents can be defined based on the power converter characteristics (maximum delivered power). Such constraints are defined by two inequalities (2-7).

$$\begin{bmatrix}0\\0\\0\end{bmatrix} \leq \begin{bmatrix}i_1\\i_2\\i_3\end{bmatrix} \leq \begin{bmatrix}i_{1_{up}}\\i_{2_{up}}\\i_{3_{up}}\end{bmatrix} \tag{2-7}$$

The control set for a one step prediction horizon and a 3-cell power converter contains eight different combinations $S \in \{000,001,010,011,100,101,110,111\}$. This control set can be considered as constraints on the control input (it is only possible to apply one of the groups belonging to the control set).

To find the optimal switching vector S that minimizes the cost function, we have to minimize a quadratic function (quadratic programing QP) subject to constraints, given by equation (2-8).

$$\min_u \left(i_{ref}(k) - i_{av}(k)\right)' \boldsymbol{Q} \left(i_{ref}(k) - i_{av}(k)\right)$$

subjected to:

$$\begin{aligned} x(k+1) &= \boldsymbol{A}_d x(k) + \boldsymbol{B}_d u(k) \\ y(k) &= \boldsymbol{C}_d x(k) + \boldsymbol{D}_d u(k) \\ 0 &\leq x(k) \leq i_{up} \\ u(k) &\in S \end{aligned} \tag{2-8}$$

Figure 2-15 shows the current in the three cells for a step input of the references. In these simulations, the predicted currents $i^p(k+1)$ are calculated based on the current measurements $i(k)$ at time t_k, the state space model of equation (2-5) and all the possible switching vectors. Figure 2-15-b shows a zoom on one part of the figure and all the possible predicted currents at time 5.65. At this time, the values of the QP cost function (2-6) for each switching vector are shown in Table 2-1. From this table we can see that the minimum cost function is 0.018342 obtained for the switching vector S_0 applied at this time to the power converter.

Table 2-1 The values of QP cost function at $t = t_{k+1}$

	$S_0 = 000$	$S_1 = 001$	$S_2 = 010$	$S_3 = 011$	$S_4 = 100$	$S_5 = 101$	$S_6 = 110$	$S_7 = 111$
J	0.018342	0.044189	0.053625	0.243802	0.049677	0.239853	0.249289	0.603796

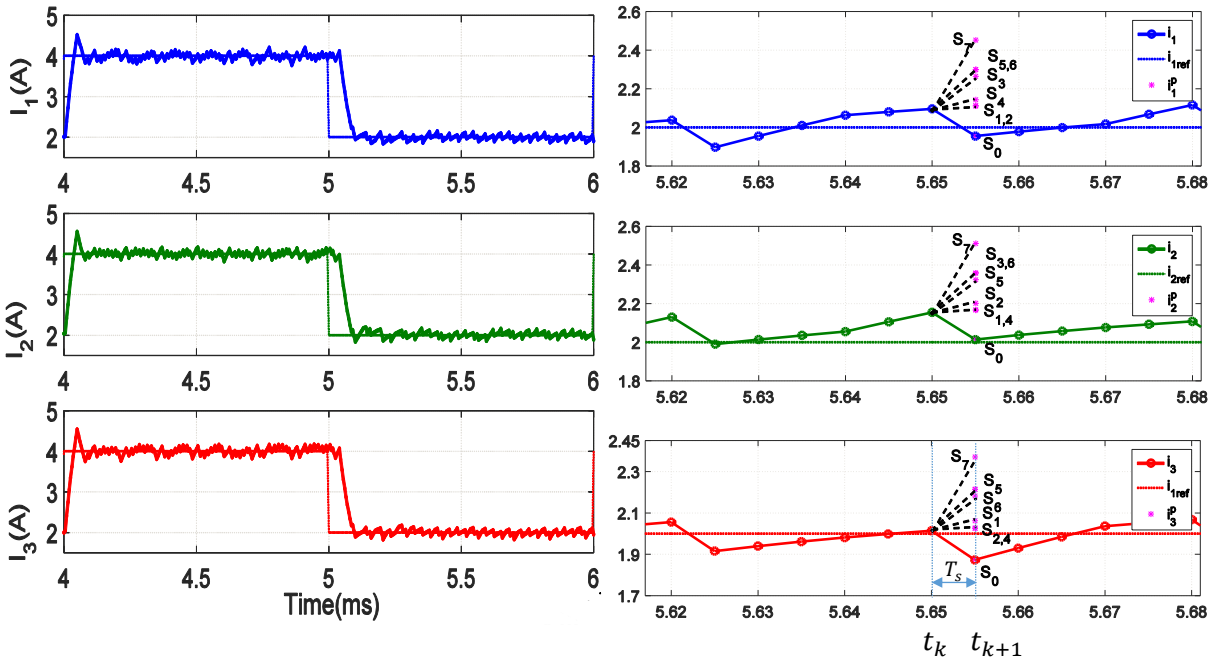

Figure 2-15 Current response :a)currents in the 3 cells , b) zoom and predicted currents

Note that the switching frequency is variable for this control principle. Its maximum is equal to half of the sampling frequency ($f_{sw_{max}} = f_s/2$), when using the FCS-MPC for one prediction horizon.

Some authors propose to control the variation of the switching frequency via the cost function as in [47]. In this paper they used (2-9) as a cost function to control the switching frequency of a DC-AC inverter. The first two term are dedicated to the error between the real and imaginary load currents in a complex representation and their references respectively. The third term is dedicated to the number of commutations that are requested to change the switching state. The switching state that leads to less commutations will lower this term . It has a straight relation with the switching frequency of the power converter. The control of switching frequency is a main issue when using FCS-MPC and many authors propose methods for this purpose [7]–[13] [14-20].

$$J = |i_\alpha^* - i_\alpha^{\boldsymbol{p}}| + |i_\beta^* - i_\beta^{\boldsymbol{p}}| + \lambda_n n_c \qquad (2\text{-}9)$$

Because of its interesting properties, many authors proposed to use MPC to control multilevel, or multicell power converters. In chapter 4 we will propose a new methodology to obtain with FCS-MPC an interleaved fixed switching frequency for a multicell coupled power converter.

2.5. Space vector Placement

The FCS-MPC is broadly used for current control and DPC of power converters [14]–[22], [48], because it matches the discrete nature of power converter but, as seen in the previous section, the switching frequency is variable and depends on the sampling frequency for classical FCS-MPC.

Some authors proposed a new method to have a fixed switching frequency by using a combination of FCS-MPC, DPC and Virtual flux (VF) [49] . The block diagram of their method is shown in Figure 2-16. Authors use the estimated VF, the switching table (that contains all the voltage space vectors of a voltage source converters (VSC)) and the estimated inductance to predict the future command of the power semiconductors for one switching period which is divided in six time interval as shown in Figure 2-17.

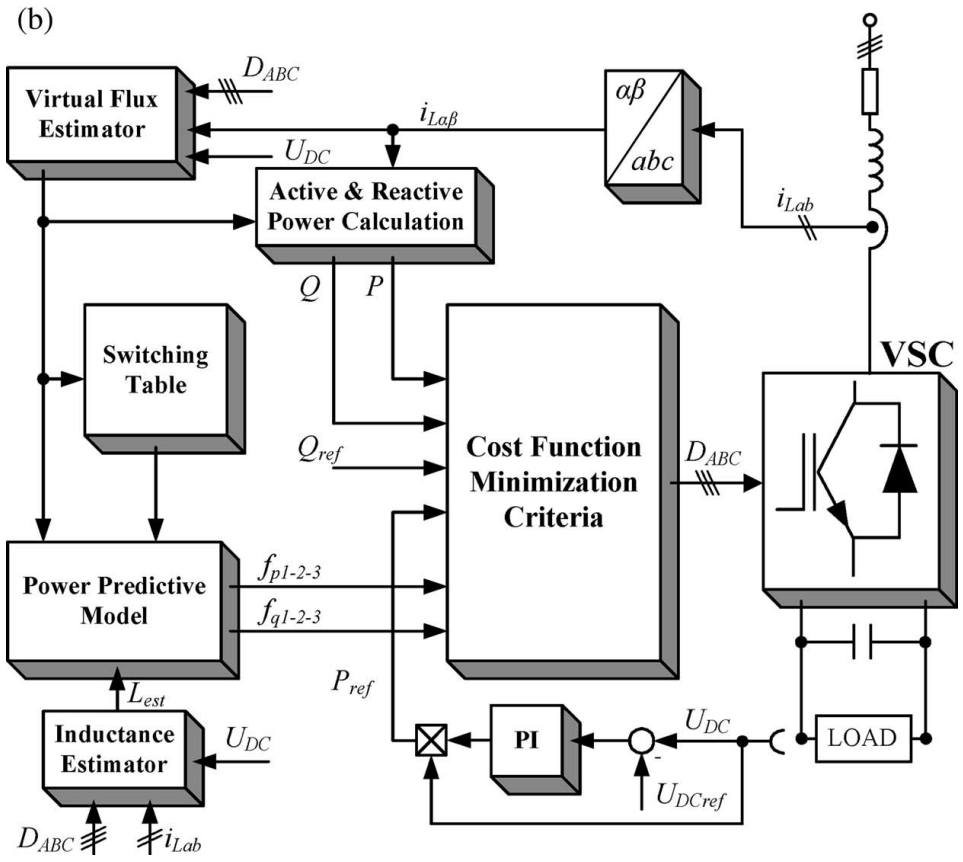

Figure 2-16 block diagram of DPC with VF control and choke inductance estimators for three phase ac/dc voltage source converters(VSCs)

From a given space vector sequence, the active and reactive power and the virtual flux can be estimated. From these estimations, the optimal (leading to the minimum cost function value) duration of application of each space vector of the sequence (t_1, t_2 and t_3) can be derived.

Such methods are mainly used in AC power converters such as AC-DC, DC-AC, AC-DC-AC or active filters but there is a lack of references related to such method applied to multicell DC-DC power converters. In this PhD, we propose in chapter 5 a strategy inspired by this type of methodology combining SV and FCS-MPC and dedicated to multicell DC-DC power converters.

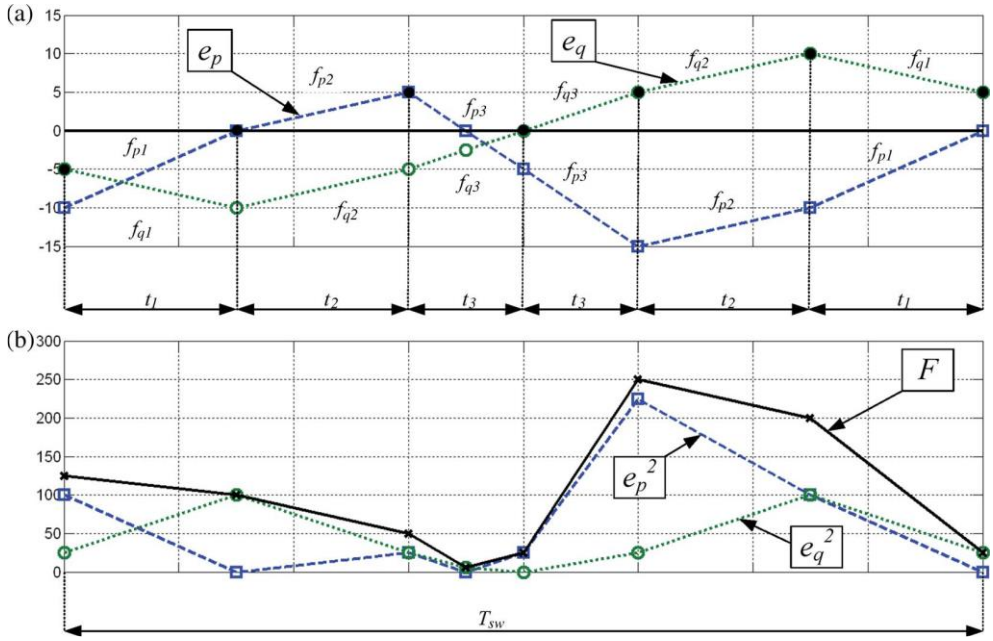

Figure 2-17 Example response of (a) derivatives of active and reactive powers, and (b) cost function and their components.

Chapter 3. Classical control of multicell interleaved power converter

3.1. Introduction

Parallel multi-cell converters using inter cell transformers (ICTs) are an attractive technique in the field of low and medium voltage and high current power converters. These very versatile structures can be used in many types of power conversion structures such as Boost or Buck DC-to-DC power converters as well as in DC-to-AC inverters or AC-to-DC synchronized rectifiers.

On a very broad basis, fractioning power shows many advantages. When interleaved generated PWM patterns are used, it enables to significantly reduce the switching stress due to interconnections leakage energy leading to voltage overshoot and electromagnetic interferences and the harmonic spectrum. This also allows a significant decrease of input and output filters size. The best performances are obtained in multi-cell converters when the converter is designed with one or several magnetic ICTs instead of individual inductors [50]. With respect to this final point, the ICT has to figure an important coupling effect to achieve good performances (compactness, power efficiency, current constraints). From a control point of view this magnetic coupling makes the power stage switch from several single input single output SISO systems to a unique multi input multi output MIMO system. Despite this change, the challenge is to keep the dedicated control algorithm as simple as possible, in terms of settings and implementation. It aims at providing an efficient control, both robust regarding system uncertainties and easy to implement in a classic microcontroller.

The literature shows that the study of the ICT multicell converter control has already been undertaken. First, Bolloch et al. have elaborated a strategy permitting a relevant steady state behavior without deeply studying the dynamic behavior of the control scheme [3]. Then, Gautier et al. have proposed a strategy based on decoupling matrixes which permits to control the natural modes of the converter with independent PI controller [2]. This unique solution based on a practical approach leads to a single solution which has not really been considered in a broader context permitting to assess its performances regarding other solutions. On a more specific issue, sensitivity analysis regarding parameters uncertainties are not assessed. Amghar et al. have explored another possible control technique based on a combination of PI controller and Petri nets method. It requires very high sampling rates to operate properly and, in the submitted work, the magnetic coupling effect has not yet been taken into account [51]. The proposed work focuses on ICT converters and intends to study control issue in the general framework a state representation. It enables to exhibit the available degrees of freedom and to argue on their best use. The control performance criteria are assessed regarding parameter uncertainties in order to address robustness key issue. In addition, the theoretical study is supplemented with a comprehensive analysis of the implementation issues.

This control issue is illustrated with a solar application. The system under consideration is based on a solar PV string feeding a DC-DC buck converter as a MPP tracker. Indeed, the two interesting points are that solar PV strings classically provide a medium voltage range completely adapted to parallel multi-cell converters and solar converters require a very high energy efficiency which parallel multi-cell converters can ensure by optimizing the number of active cells during operation [52]. As a matter of fact, PV current changes on a wide range due to the sunlight changes during the day; in this context power partitioning can achieve a very high power efficiency on a

wide power range [53].

A step-down voltage topology is commonly used in high efficiency grid connected transformer-less solar inverters to obtain a one-stage DC-to-AC [54] conversion but also in some multi-stages solar inverters[55]. A very versatile solution regarding the photovoltaic plant voltages can be built by using a two stages power converter. In this configuration, the first stage is a Buck converter, followed by a Boost converter. This solution is very versatile and is promoted in solar battery charging applications [TI product reference: Texas Instruments SM3320-BATT-EV/NOPB]. Therefore, this study considers such Buck-type first stage.

Current balancing in parallel multi-cell converters has been widely discussed in numerous articles for uncoupled (inductors) and coupled (ICTs) topologies. In these previous works the proposed control strategies are mainly based on classical PI controllers without any in-depth study of their performances under practical conditions of use. The present investigation is carrying out a comprehensive study which considers the different ways to tune the control settings with respect to system parameter sensitivity, decoupling behavior and the ease of implementation including control value saturation.

The chapter aims at providing a simple and efficient control strategy that can contribute to promote the development of parallel multi-cell converters using ICTs. To do so, the manuscript is organized as follows. After this short introduction, section II presents the control model of the interleaved multi-cell buck converter and the specifications related to the PV application under study; this part concludes on the importance to control not only the input voltage and output current but also the inner cell currents. The third section presents the independent PI controller, tuning the controller gains, simulate the system under deferent conditions to test the controller performance. The fourth section presents the need to extend the model using additional integrators in order to cancel the steady state error. This section considers the possibility of tuning the parameters of the state feedback. The section addresses the particular tuning choice which permits to cancel the interphase current coupling. This case is studied individually both with respect to its robustness regarding parameters uncertainties and in regard to implementation. As these performances can be further enhanced, the fifth section considers another design method based on the optimization of a quadratic optimization function, named LQR approach. This part shows first how to tune the cost function weighting coefficients in order to fit the initial requirements, second the good robustness property of this approach and third the simplicity of the implementation taking orders of magnitude into account. Finally, the chapter ends with conclusions.

3.2. Multi-cell interleaved buck converter and its control-oriented model

3.2.1. Multi-cell interleaved buck converter for solar application

Figure 3-1 depicts the system under study. A photovoltaic array feeds a load which could be possibly a battery directly powering DC loads or a grid inverter. As both PV maximum power point and the load voltage can vary greatly, it is mandatory to interface a converter between the load and the source: this is the multi-cell converter using a monolithic ICT formed by n windings wounded on the same magnetic circuit. For simplicity, it has three switching cells ($n = 3$) and a 3-phase-transformer acting as an output current filter. The input current is filtered by the input capacitor C_i.

Each switching cell is driven by a PWM control signal characterized by a constant switching frequency f and a duty cycle d_k, which represents a system control variable. The system parameters and the rated variables are listed in Table 3-1.

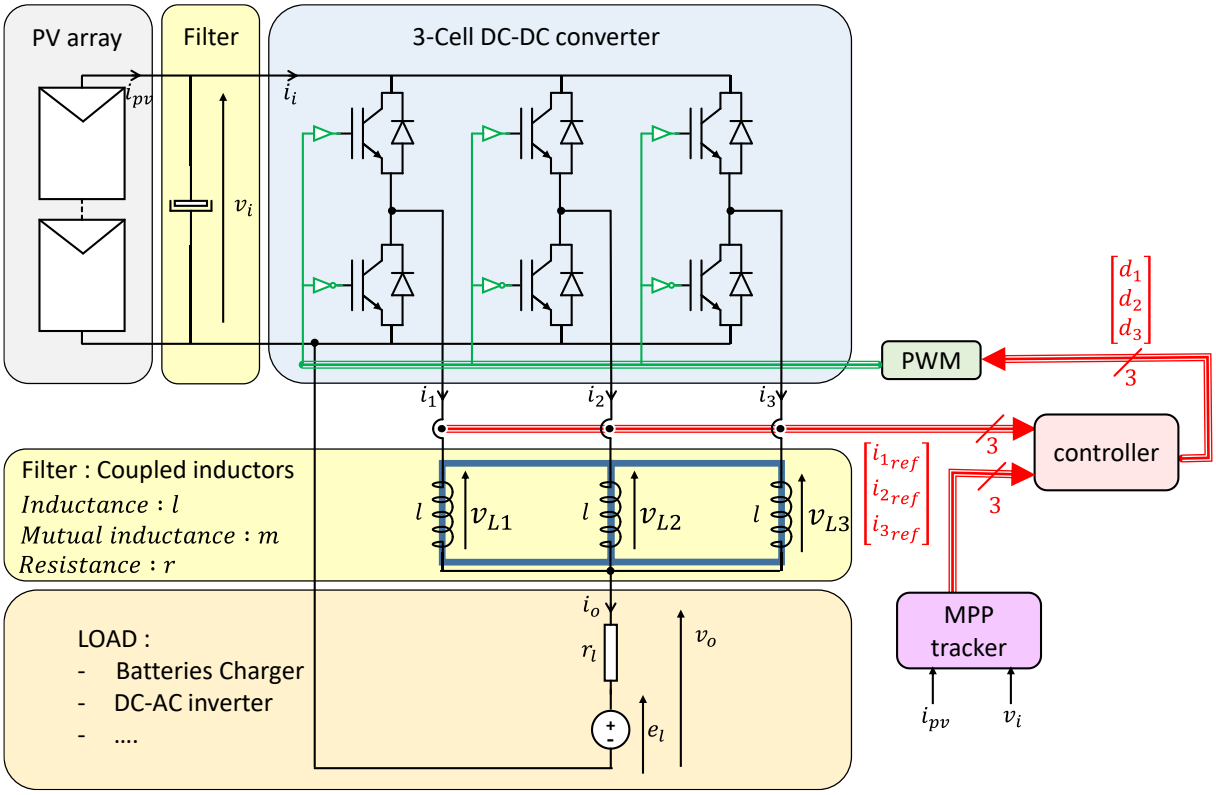

Figure 3-1 Multi-Cell coupled power converter architecture

Compared to classic single buck converter, the main advantage of this power electronics structure is to ensure low current ripples at both input and output sides. In fact, regarding the input stage, the input current ripple is reduced by an n factor while the input current apparent frequency is increased by a factor of n. As a result, the C_i capacitance can be reduced by a significant n^2 factor leading to improve the system dynamics and namely its ability to track faster the maximum power point of the PV array [24], [34], [56]. Similarly, the amplitude of phase current ripples are reduced by a n^2 factor compared to an uncoupled multi-cell converter (considering a similar filtering inductance value), which reduces the constraints on the power semi-conductors and the related losses. Moreover, the global power converter output current ripple is reduced by n compared to a classical one-cell Buck DC-DC converter, in the same way as for interleaved multi-cell DC-DC Buck converter with uncoupled inductors[24]. This limits the need to filter the output voltage: in some cases, no additional output capacitor is required.

These electrical and energetics advantages are counterbalanced by a rising difficulty to control the system in static and dynamic conditions. This is the reason why a control-orientated model is needed to study the feedback control.

Table 3-1 Multi-Cell coupled power converter parameters

Symbol	Quantity	Value
v_i	PV panel array voltage	400 V
$I_{i_{rated}}$	PV panel array current	9.25 A
f	Cell switching frequency	20 kHz
C_i	Input capacitance	2 mF
l	ICT self-inductance	20.0 mH
m	ICT mutual inductance	9.5 mH
r	ICT rated phase resistance	0.2 Ω
r_l	rated load resistance	0 Ω
$i_{l,max}$	short circuit current protect.	15 A
e_l	rated load voltage source	200 V
l_{min}	Minimum ICT self-induct.	19.7 mH
m_{max}	Maximum ICT mutual induct.	9.7 mH
r_{max}	maximum ICT phase resist.	0.5 Ω

3.2.2. The mathematical model of converter.

For general purpose, the power converter model uses the following assumptions:

- Regarding the closed loop response time of the controlled system, PV array behaves as a perfect voltage source. The input voltage of the power converter v_i is therefore imposed in the model.
- The load fed by the power converter can represent different types of loads and is assumed to be linear. It is considered as a Thévenin's equivalent circuit consisting of an equivalent voltage source e_l in series connection with an equivalent impedance Z_l. The following developments only consider the pure real case, namely: $Z_l = r_l$. Finally, the DC load is hence described by:

$$v_o = e_l + r_l\, i_o \qquad (3\text{-}1)$$

$$i_o = i_1 + i_2 + i_3 \qquad (3\text{-}2)$$

- The monolithic ICT is also considered as linear and is represented by three magnetically coupled electrical equations. For a 3-leg symmetrical monolithic ICT the mutual inductances are identical with a negative value and are denoted $-m$ in the following model while l is the winding self-inductance:

$$\begin{bmatrix} v_{L1} \\ v_{L2} \\ v_{L3} \end{bmatrix} = \begin{bmatrix} l & -m & -m \\ -m & l & -m \\ -m & -m & l \end{bmatrix} \frac{d}{dt} \begin{bmatrix} i_1 \\ i_2 \\ i_3 \end{bmatrix} + \begin{bmatrix} r & 0 & 0 \\ 0 & r & 0 \\ 0 & 0 & r \end{bmatrix} \begin{bmatrix} i_1 \\ i_2 \\ i_3 \end{bmatrix} \qquad (3\text{-}3)$$

- The 3 switching cells are controlled by 3 binary control variables. For the purpose of designing a control scheme, only the average cell behavior is considered as shown in Figure 3-2; the system control inputs are the 3 duty-cycles of each cell d_k which have a limited range from 0 to 1. Duty cycles saturation should therefore be managed by the

controller. This technical point has to be taken into account properly.

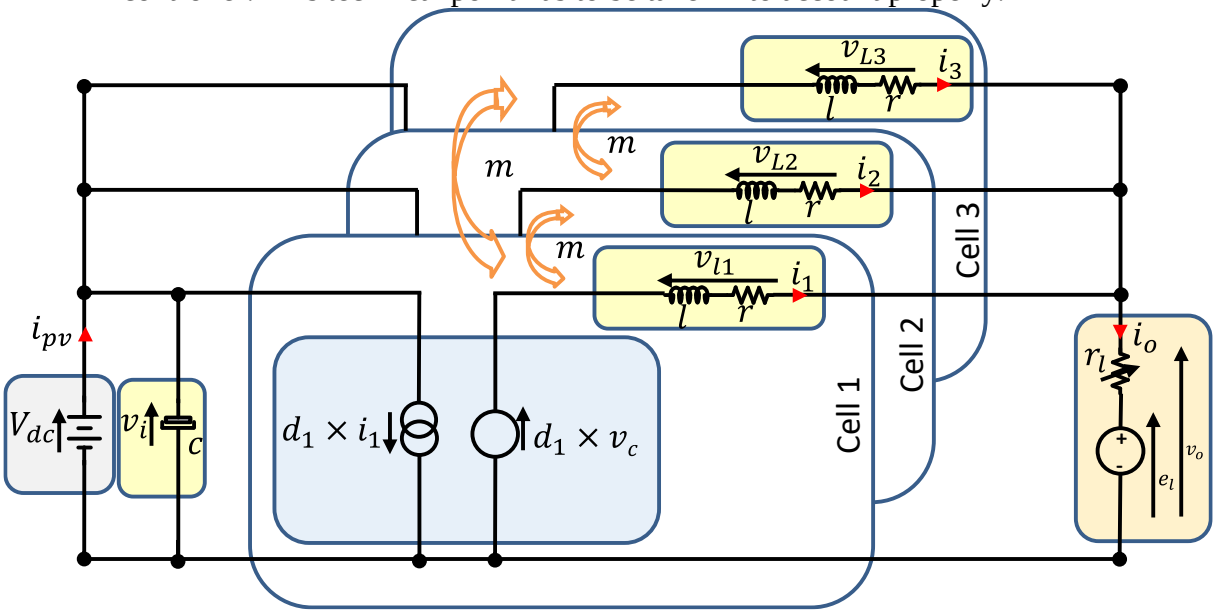

Figure 3-2 The equivalent average model of Multi-cell interleaved buck converter

With these assumptions and writing the three Kirchhoff's voltage laws of the converter enables to obtain the converter average model as in following equation:

The voltage equations are defined by taking the voltage loop between 1st - 2nd leg , 2nd - 3rd and 1st leg – load:

$$v_i \begin{bmatrix} d_1 - d_2 \\ d_2 - d_3 \\ d_1 \end{bmatrix} = \begin{bmatrix} v_{L1} - v_{L2} \\ v_{L2} - v_{L3} \\ v_{L1} + v_o \end{bmatrix} \tag{3-4}$$

Rearrangement of the voltage equation (3-4) yields:

$$v_i \left(\begin{bmatrix} 1 & -1 & 0 \\ 0 & 1 & -1 \\ 1 & 0 & 0 \end{bmatrix} \begin{bmatrix} d_1 \\ d_2 \\ d_3 \end{bmatrix} \right) = \left(\begin{bmatrix} 1 & -1 & 0 \\ 0 & 1 & -1 \\ 1 & 0 & 0 \end{bmatrix} \begin{bmatrix} v_{L1} \\ v_{L2} \\ v_{L3} \end{bmatrix} + \begin{bmatrix} 0 \\ 0 \\ v_o \end{bmatrix} \right) \tag{3-5}$$

The multi-cell converter duty cycles are thus given by equation (3-6):

Substituting for voltages from ((3-1), (3-2) and (3-3) in equation (3-6) yields:

$$v_i \begin{bmatrix} d_1 \\ d_2 \\ d_3 \end{bmatrix} = \left(\begin{bmatrix} v_{L1} \\ v_{L2} \\ v_{L3} \end{bmatrix} + \begin{bmatrix} 0 & 0 & 1 \\ -1 & 0 & 0 \\ -1 & -1 & 1 \end{bmatrix} \begin{bmatrix} 0 \\ 0 \\ v_o \end{bmatrix} \right) \tag{3-6}$$

$$v_i \begin{bmatrix} d_1 \\ d_2 \\ d_3 \end{bmatrix} = \left(\begin{bmatrix} l & -m & -m \\ -m & l & -m \\ -m & -m & l \end{bmatrix} \frac{d}{dt} \begin{bmatrix} i_1 \\ i_2 \\ i_3 \end{bmatrix} + \begin{bmatrix} r + r_l & r_l & r_l \\ r_l & r + r_l & r_l \\ r_l & r_l & r + r_L \end{bmatrix} \begin{bmatrix} i_1 \\ i_2 \\ i_3 \end{bmatrix} + \begin{bmatrix} 1 \\ 1 \\ 1 \end{bmatrix} e_l \right) \tag{3-7}$$

Equation (3-7) is written in the state-space representation as follows:

$$\frac{d}{dt}\begin{bmatrix} i_1 \\ i_2 \\ i_3 \end{bmatrix} = -\begin{bmatrix} l & -m & -m \\ -m & l & -m \\ -m & -m & l \end{bmatrix}^{-1}\begin{bmatrix} r+r_l & r_l & r_l \\ r_l & r+r_l & r_l \\ r_l & r_l & r+r_L \end{bmatrix}\begin{bmatrix} i_1 \\ i_2 \\ i_3 \end{bmatrix} + \begin{bmatrix} l & -m & -m \\ -m & l & -m \\ -m & -m & l \end{bmatrix}^{-1}\left(\begin{bmatrix} d_1 \\ d_2 \\ d_3 \end{bmatrix} v_i - \begin{bmatrix} 1 \\ 1 \\ 1 \end{bmatrix} e_l\right) \quad (3\text{-}8)$$

It is worth noting that the load voltage source represents a battery or the capacitive input filter of an inverter. This mean that the series resistance r_l is low and can be neglected in a first approach. With this assumption, the resulting state-space representation is:

$$\frac{d}{dt}\begin{bmatrix} i_1 \\ i_2 \\ i_3 \end{bmatrix} = -\begin{bmatrix} l & -m & -m \\ -m & l & -m \\ -m & -m & l \end{bmatrix}^{-1}\begin{bmatrix} r & 0 & 0 \\ 0 & r & 0 \\ 0 & 0 & r \end{bmatrix}\begin{bmatrix} i_1 \\ i_2 \\ i_3 \end{bmatrix} + \begin{bmatrix} l & -m & -m \\ -m & l & -m \\ -m & -m & l \end{bmatrix}^{-1}\left(\begin{bmatrix} d_1 \\ d_2 \\ d_3 \end{bmatrix} v_i - \begin{bmatrix} 1 \\ 1 \\ 1 \end{bmatrix} e_l\right) \quad (3\text{-}9)$$

Note that the term r is voluntary not factored into the state equation to underline that the forthcoming robustness analysis of each control strategy considers individual winding resistance variation.

Functionally, the output current i_o, sum of the three winding currents, is the only variable which should be controlled. In actual experience, the converter faces discrepancies at several level (winding and power semiconductors resistances due to temperature difference, actual duty cycle of a cell due to non-identical dead-time, as examples) which may generate large DC current mismatch between each winding. It is hence mandatory to control each individual current i_k. In this context, the output vector is the state vector.

3.2.3. Mode analysis of the state-space average model.

In an ideally balanced system, the state-space model should be written as:

$$\frac{d}{dt}\boldsymbol{I} = \boldsymbol{A}\boldsymbol{I} + \boldsymbol{B}\boldsymbol{D} - \frac{1}{(l-2m)}\begin{bmatrix} 1 \\ 1 \\ 1 \end{bmatrix} e_l \quad (3\text{-}10)$$

With $\boldsymbol{A}$ the state matrix and $\boldsymbol{B}$ the control matrix.

$$\boldsymbol{A} = -r\begin{bmatrix} l & -m & -m \\ -m & l & -m \\ -m & -m & l \end{bmatrix}^{-1} = \frac{-r}{(l-2m)(l+m)}\begin{bmatrix} l-m & m & m \\ m & l-m & m \\ m & m & l-m \end{bmatrix}$$

$$\boldsymbol{B} = v_i.\begin{bmatrix} l & -m & -m \\ -m & l & -m \\ -m & -m & l \end{bmatrix}^{-1} = \frac{v_i}{(l-2m)(l+m)}\begin{bmatrix} l-m & m & m \\ m & l-m & m \\ m & m & l-m \end{bmatrix}$$

and $\boldsymbol{I} = [i_1 \quad i_2 \quad i_3]^t$ the state vector, $\boldsymbol{D} = [d_1 \quad d_2 \quad d_3]^t$ the control vector and e_l the perturb input.

To better understand the system functioning, the modal analysis is an appropriate and effective

tool. In this case, the state matrix can be diagonalized based on the three eigen vectors:

- One, specifically $\Lambda_1 = [1 \quad 1 \quad 1]^t$ associated to a first eigen value $\lambda_1 = (l - 2m)^{-1}$
- And two others, namely $\Lambda_2 = [1 \quad -1 \quad 0]^t$ and $\Lambda_3 = [0 \quad 1 \quad -1]^t$ related to a second eigen value $\lambda_2 = (l + m)^{-1}$.

For the converter under study, the evaluation of the eigen values ratio is $\lambda_1/\lambda_2 = 2.95/0.1 = 29.5$. It is hence clear that the open-loop system has two very different dynamics, which requires a specific control design.

From an engineer point of view, these two individual dynamics corresponds to the common mode and the differential modes.

In the common mode, the three phase currents evolve similarly driven by the same duty cycles. Summing the three state equations and defining i_{cm} and d_{cm} the common mode phase current and the shared duty cycle, respectively leads to the following one-dimension equation:

$$\frac{d}{dt} i_{cm} = -\frac{r}{l - 2m} i_{cm} + \frac{v_i}{l - 2m} d_{cm} - \frac{1}{l - 2m} e_l \qquad (3\text{-}11)$$

In the first differential mode, the third duty cycle and the third current remain constant $d_3 = d_0$ $i_3 = i_0$ whereas the two others evolves symmetrically: $d_1 = d_0 + \delta d$ and $d_2 = d_0 - \delta d$. Subtracting the two first state equations and naming $i_{diff} = i_1 - i_2$ the circulation current between the two considered phases leads to the following one-dimension equation:

$$\frac{d}{dt} i_{diff} = -\frac{r}{l + m} i_{diff} + \frac{2v_i}{l + m} \delta d \qquad (3\text{-}12)$$

By nature, the circulating current can change slowly.

3.2.4. Simulink model of multicell interleaved DC-DC buck converter

Different models are built to simulate the Buck converter, a discrete model and an equivalent average model are created on Simulink-Matlab. The switched model was built in Matlab with Simpower tools. In this model, each cell is a two-IGBT, two-diodes half-bridge. The equivalent average model using controlled voltage and current sources is used to reduce the simulation time. The two models are shown in Figure 3-3.

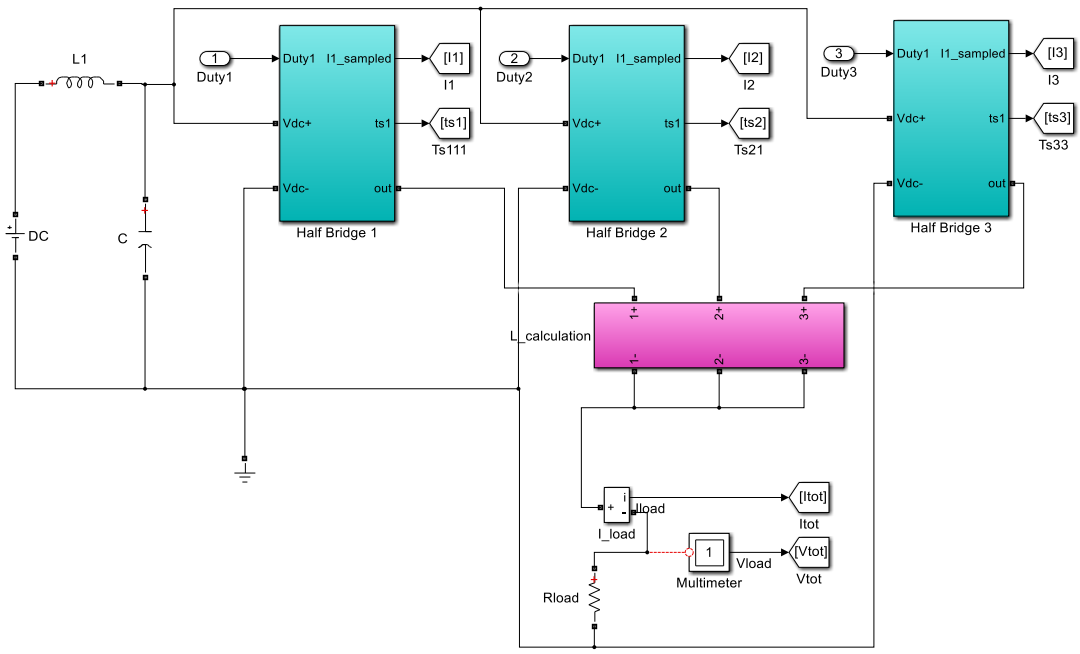

(a)

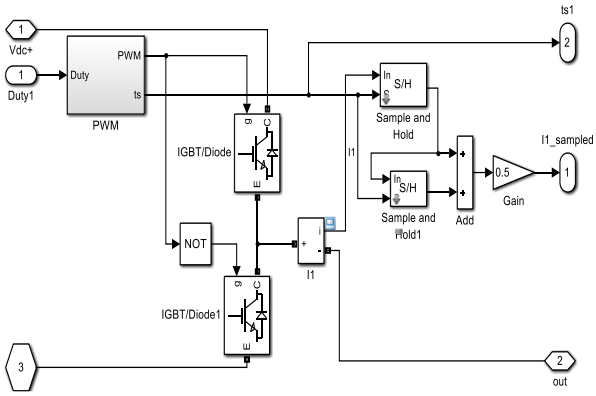

(b)

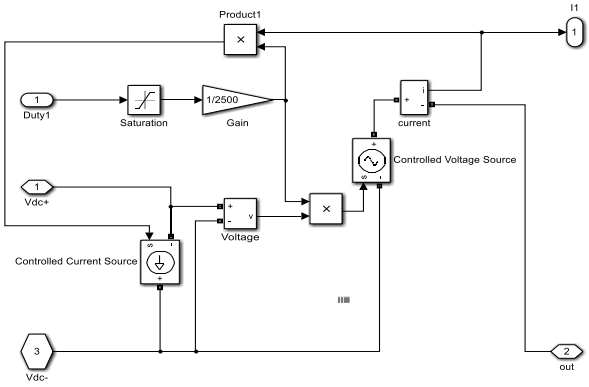

(c)

Figure 3-3 The Simulink model of a multicell interleaved DC-DC buck converter (a) The buck converter model with three half-bridges in parallel (b) One half bridge model using two IGBTs (c)The implemented equivalent average model of a half-bridge

The open loop response of the two models for a 3-cell Interleaved Buck-converter are shown in Figure 3-4. In these simulations the duty cycles of the 3 cells change from 45% to 55% with a resistive load equal to 15Ω . This simulation shows that it is possible to use the average model as tools for studying the dynamics of the converter rather than the switched one[57].

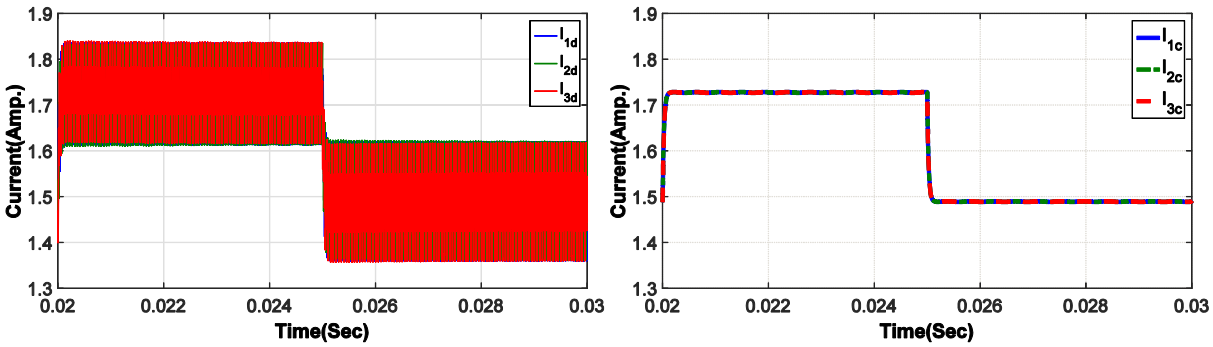

(a) (b)

Figure 3-4 Open loop simulation of multicell interleaved DC-DC converter : (a) Switched model (b)Average model

3.2.5. Simulation specifications

The control design must be done with relevant required dynamics. The present study considers the specifications summarized in Table 3-2. Indeed, the first requirement is to guarantee a good precision in steady state in order to fulfill the maximum power point tracker requirements. Second, the time taken for the response to reach the desired set point is also important for the system functionality. The solar converter needs to react to solar irradiance changes which in the worst case may occur in a 10 ms time period, which is not very challenging. However, there are obviously other scenarios to consider; short circuit limitation is one of the cases requiring a rapid action. For this demanding challenge the settling time is set to 500 µs which means ten switching periods. A third key point is to ensure a good stability margin of the closed loop system. This point is achieved by satisfying an overshoot criteria and decay ratio. The first criterion gives also a good indication on how duty cycles saturations are managed, while the latter gives a good performance index of the system stability. In addition, the minimization of the windings currents coupling permits to control independently each phase current which is essential to modify the phase power distribution in case of a local overheating; the limited overshoot while another current is changing is a way to take this fact into account.

Table 3-2 Closed loop system specification

Symbol	Quantity	Value
ε_i	Steady state offset	*0*
τ_{i_o}	Time-response (settling time)	$500\mu s$
$\Delta\%_{i_k/i_k}$	Percentage overshoot regarding i_k subject to $i_{k,ref}$ setpoint change	*10%*
$\Delta\%_{i_j/i_k}$	Percentage overshoot regarding $i_{j\neq k}$ subject to $i_{k,ref}$ setpoint change	*10%*
DR	Maximum decay ratio	*20%*

Finally, it is worth noting that the load voltage source represents a battery or the capacitive input filter of an inverter. Consequently, this voltage varies slowly and is measured for regulation purpose. Hence e_l represents a perturbation which can be simply cancelled by an additional feed forward term. That is the reason why the load voltage source will no longer be considered, as mentioned in Table 3-1.

3.3. Proportional-Integral Controller

PI or IP controllers are used to improve the transient response of the system, the steady state error and to improve the stability of the system [58].

In our application, the multicell interleaved buck DC-DC converter has three branches connected in star connection. The control model of the converter has three inputs (the duty cycles of each cell d_k) and three outputs (the currents in each branch i_k). With respect to control, the power converter is a multi-input-multi-output (MIMO) system.

PI/IP controllers are designed for single input single output (SISO) systems. A basic control strategy should be to assign one PI controller to each cell of the converter. In this strategy, each controller varies one duty cycle in order to control the current in the corresponding cell while considering the effects of magnetic couplings between cells (due to mutual inductances) as disturbances. This principle is shown in the Figure 3-5.

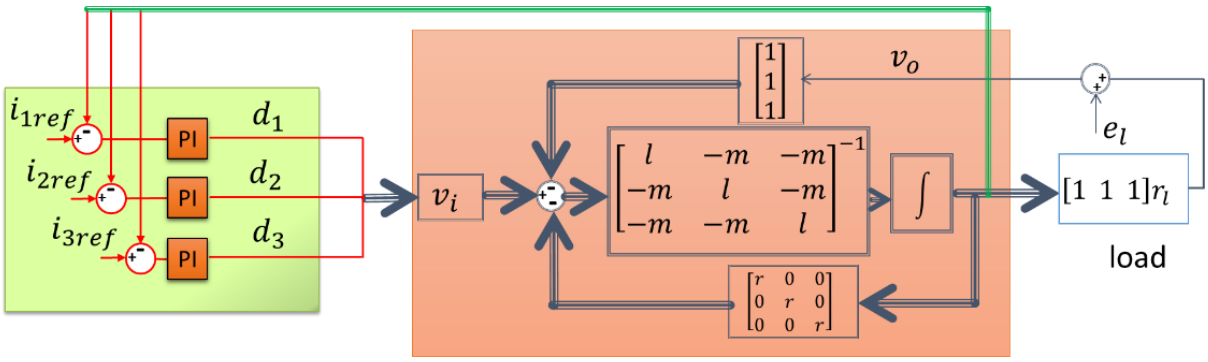

Figure 3-5 PI controller with system dynamics of multicell interleaved Buck DC-DC converter

Some of the advantages of using PI/IP controller are related to the facility of its design and implementation. Note that an anti-windup algorithm can and should be applied on each integrator in order to manage saturation of duty-cycles. In addition, in this control architecture, each controller can be tuned (K_i and K_p) independently. As the dynamic of each branch of the converter are the same, only a single tuning of the controller parameters for one branch is needed. The same parameters can be applied in the other branches.

Simulation results in Figure 3-6-a show the step responses of the closed loop system while references of the three currents are the same and are modified at the same time. For proper settings of the controllers parameters, the step responses are stable and shows no steady state remaining errors. The controller parameters are tuned in such a way that the transient response (settling time, rise time and the overshoot) meet the specifications: no overshoot and 500µs settling time.

Nevertheless, in case of different current variations in each branch, magnetic coupling effects between the converter branches must be investigated. Figure 3-6-b shows the step responses of the system while different step values are applied on each current references at the same time. This figure shows the huge effect of coupling on the currents response. We demonstrate here that individual PI/IP current controllers cannot easily manage the currents in a strongly coupled structure.

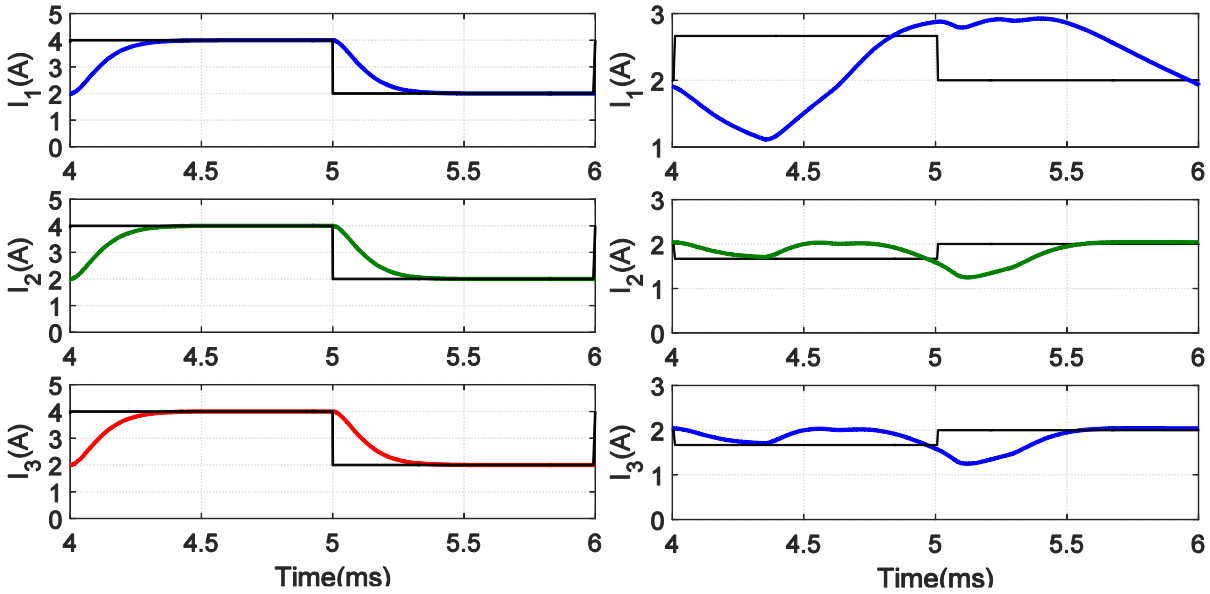

(a) *(b)*

Figure 3-6 PI and IP simulation result : (a)The same current command , (b)Coupling effect

3.4. State Feedback

In the previous section, the power converter behavior using a state representation was described. It allows to better understand the effects of the ICT magnetic coupling on the system. As it is easy to monitor each state variable using 3 current sensors, full state feedback seems to be a very appropriate control technique to adjust the characteristics of the closed loop system. A first step gives the overall control structure. Then the state feedback setting is considered showing a great number of possible tuning strategies.

3.4.1. Control structure and the related extended model

The basic principle of state feedback [59] is to place the closed loop system poles using the following linear control law:

$$\boldsymbol{D = -KI + FI_{ref}} \qquad \textit{(3-13)}$$

Where

- The $n \times n$ feedback matrix $\boldsymbol{K}$ enables to achieve the desired pole placement, which determines the system behavior.
- The $n \times n$ pre-filter matrix $\boldsymbol{F} = \boldsymbol{B}^{-1}(\boldsymbol{BK} - \boldsymbol{A})$ ensures a unit static gain between the reference values and the measured values. It is important to stress that this matrix is calculated with the state and control matrices ($\boldsymbol{A}$ and $\boldsymbol{B}$) and thus strongly depends on the system parameters.

Obviously, due to the mandatory pre-filter matrix, this first control structure is strongly dependent on system parameters uncertainties. The way to deal with this is to add integral terms to the feedback structure. It provides a suitable solution enabling to strengthen the overall feedback robustness and guarantee no static error in any case. The idea is first to integer the errors between the references and the related currents $\dot{\boldsymbol{e}}(t)$ and then consider the three integer outputs as three additional system states as in Consequently the extended state dimension is $n_e = 2n = 6$.

Similarly to the basic state feedback, the control values $\boldsymbol{D}$ are calculated using the full state knowledge as depicted in Figure 3-7. Note that the reference values $\boldsymbol{I_{ref}}$ no longer act directly on the control values but through an integral path which filters the set point variations which avoids temporal overshoots of output values during fast transient.

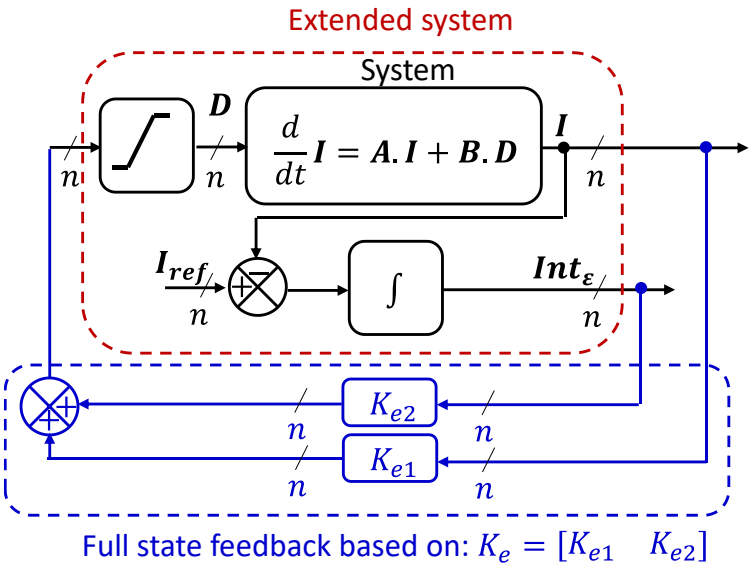

Figure 3-7 Extended system with full state feedback

The new added states due to integral action will be:

$$\dot{\boldsymbol{e}}(t) = \boldsymbol{I}(t)_{ref} - \boldsymbol{I}(t) \qquad (3\text{-}14)$$

By combining the state space equation (3-10) and the new states in equation (3-14), we get the resulting state space representation of the extended system:

$$\frac{d}{dt}\begin{bmatrix} \boldsymbol{I} \\ \boldsymbol{Int_\varepsilon} \end{bmatrix} = \begin{bmatrix} \boldsymbol{A} & \boldsymbol{0_{3\times3}} \\ -\boldsymbol{Id_{3\times3}} & \boldsymbol{0_{3\times3}} \end{bmatrix}\begin{bmatrix} \boldsymbol{I} \\ \boldsymbol{Int_\varepsilon} \end{bmatrix} + \begin{bmatrix} \boldsymbol{B} \\ \boldsymbol{0_{3\times3}} \end{bmatrix}\boldsymbol{D} + \begin{bmatrix} \boldsymbol{0_{3\times3}} \\ \boldsymbol{Id_3} \end{bmatrix}[\boldsymbol{I_{ref}}] \qquad (3\text{-}15)$$

The control input $\boldsymbol{D}$ is a combinations of two parts. The first part is related to the states of the dynamic system and the other part is related to the integral action:

$$\boldsymbol{D} = -\boldsymbol{K_e}\begin{bmatrix}\boldsymbol{I}\\ \boldsymbol{Int_\varepsilon}\end{bmatrix} = -[\boldsymbol{K}_{e1}\ \ \boldsymbol{K}_{e2}]\begin{bmatrix}\boldsymbol{I}\\ \boldsymbol{Int_\varepsilon}\end{bmatrix} \qquad (3\text{-}16)$$

The $n \times n_e$ feedback matrix $K_e = [K_{e1} \quad K_{e2}]$ has $n \times n_e = 18$ independent real parameters. Adjusting these latter permits to choose the $n_e = 6$ poles of the closed loop system which has a strong influence on the system's dynamics. It is thus evident that the $\boldsymbol{K_e}$ matrix meeting this pole criteria is not unique. To take advantage of the opportunities offered by these too many coefficients, it is important to add explicit additional criteria permitting to strictly define them.

3.4.2. Tuning of state feedback gain

Every control input (column b of the control input matrix $\boldsymbol{B}$) that produces a controllable pair ($\boldsymbol{A}$, b) allows to shift all n eigenvalues of the matrix $\boldsymbol{A}$ to the new location. So, only one input is needed to shift all eigenvalues, if the system is controllable with respect to that input. If each of the p-inputs can fully control the system, the system has more degrees of freedom than needed (there are p inputs and only one input is needed to assign all eigenvalues). It is well-known that for a single input system there is a unique state feedback gain solution $\boldsymbol{K_e}$ to any desired configuration of eigenvalues. However, for a system with more than one independent input there is no unique state gain solution (there are many $\boldsymbol{K_e}$ that can yield the same polynomial closed-loop characteristic) [60].

One of the solutions for tuning the gain of state feedback is to design a system to be dynamically decoupled. This involves breaking the link between current references and current responses. This can be achieved by setting the closed loop transition matrix to be diagonal.

Combining the extended state equation (3-15) and the full feedback control law (3-16) derives the close loop behavior described by:

$$\frac{d}{dt}\begin{bmatrix}\boldsymbol{I}\\ \boldsymbol{Int_\varepsilon}\end{bmatrix} = \begin{bmatrix}\boldsymbol{A} & \boldsymbol{0_{n\times q}}\\ -\boldsymbol{Id_{q\times n}} & \boldsymbol{0_{q\times q}}\end{bmatrix}\begin{bmatrix}\boldsymbol{I}\\ \boldsymbol{Int_\varepsilon}\end{bmatrix} - \begin{bmatrix}\boldsymbol{B}\\ \boldsymbol{0_{q\times p}}\end{bmatrix}[\boldsymbol{K}_{e1}\ \ \boldsymbol{K}_{e2}]\begin{bmatrix}\boldsymbol{I}\\ \boldsymbol{Int_\varepsilon}\end{bmatrix} + \begin{bmatrix}\boldsymbol{0_{n\times q}}\\ \boldsymbol{I_{d_{q\times q}}}\end{bmatrix}[\boldsymbol{I_{ref}}] \qquad (3\text{-}17)$$

Where:

n: the number of states

p: the number of input

q: the number of output

$\boldsymbol{K_{e1}}$ represents a $n \times n$ matrix made of the n first columns of $\boldsymbol{K_e}$ while $\boldsymbol{K_{e2}}$ is a similar matrix consisting of the last columns of $\boldsymbol{K_e}$.

For the three legs interleaved buck converter the closed loop state space model will be:

$$\frac{d}{dt}\begin{bmatrix}\boldsymbol{I}\\ \boldsymbol{Int_\varepsilon}\end{bmatrix} = \begin{bmatrix}\boldsymbol{A}-\boldsymbol{B}.\boldsymbol{K_{e1}} & -\boldsymbol{B}.\boldsymbol{K_{e2}}\\ -\boldsymbol{Id_{3x3}} & \boldsymbol{0_{3x3}}\end{bmatrix}\begin{bmatrix}\boldsymbol{I}\\ \boldsymbol{Int_\varepsilon}\end{bmatrix} + \begin{bmatrix}\boldsymbol{0_{3x3}}\\ \boldsymbol{Id_{3x3}}\end{bmatrix}[\boldsymbol{I_{ref}}] \qquad (3\text{-}18)$$

The characteristics of the system response is fully determined by the value of the $n \times n_e = 18$ adjustable terms of the closed-loop state matrix, namely the first n rows of this matrix. It is sought

to impose:

- First the $n_e = 6$ eigen values in order to settle the overall closed loop dynamics. Writing the characteristic equation and identifying it with its desire form leads to $n_e = 6$ non-linear equations as in equation (3-19).

$$\boldsymbol{det}(s\boldsymbol{I} - \boldsymbol{A}_{e,cl}) = \prod_{\boldsymbol{i=1}}^{\boldsymbol{6}}(s - \boldsymbol{\lambda}_i) \qquad (3\text{-}19)$$

Where:

$\boldsymbol{A}_{e,cl}$ is a closed loop transition matrix of the extended system.

$\boldsymbol{\lambda_i}$ is the desired eigenvalue.

The eigenvalue of the matrix $\boldsymbol{A}_{e,cl}$ are the poles of the closed loop that are needed to be placed at specified location to have the required response.

- Second a cancellation of the coupling effect between the three windings currents. For instance, i_2 and i_3, as well as $int_{\varepsilon 2}$ and $int_{\varepsilon 3}$, must no longer impact the time-derivative of the first current di_i/dt. In sum, the closed loop matrix must conform to the following structure:

$$\boldsymbol{A}_{e,CL} = \begin{bmatrix} a_{11} & 0 & 0 & a_{14} & 0 & 0 \\ 0 & a_{22} & 0 & 0 & a_{25} & 0 \\ 0 & 0 & a_{33} & 0 & 0 & a_{36} \\ -1 & 0 & 0 & 0 & 0 & 0 \\ 0 & -1 & 0 & 0 & 0 & 0 \\ 0 & 0 & -1 & 0 & 0 & 0 \end{bmatrix} \qquad (3\text{-}20)$$

Now, to determine the values of elements of the state transition matrix of the closed loop extended system $\boldsymbol{A}_{e,cl}$ the determent of the matrix $\boldsymbol{A}_{e,cl}$ and the desired polynomial of the closed loop poles must match as in equation (3-19). The determinant of $(s\boldsymbol{I} - \boldsymbol{A}_{e,cl})$ of a six states system will be a sixth degree polynomial function as in the equation (3-21) , and the polynomial of the desired closed loop eigenvalues will be a sixth degree polynomial as in equation (3-22). The result of matching the two equations gives six nonlinear equations. Matlab is used to solve those six non-linear equations by $fsolve\ function$. By doing so, we find the closed loop transition matrix's elements (3-20) of extended system.

$$\begin{aligned} &\boldsymbol{det}(s\boldsymbol{I} - \boldsymbol{A}_{e,cl}) \\ &\quad = S^6 + (-a_{11} - a_{22} - a_{33})S^5 \\ &\quad + (a_{14} + a_{25} + a_{36} + a_{11}a_{22} + a_{11}a_{33})S^4 \\ &\quad + (-a_{11}a_{25} - a_{14}a22 - a_{11}a_{36} - a_{14}a_{33} - a_{22}a_{36} - a_{25}a_{33} \\ &\quad - a_{11}a_{22}a_{33})S^3 \\ &\quad + (a_{14}a_{25} + a_{14}a_{36} + a_{25}a_{36} + a_{11}a_{22}a_{36} + a_{11}a_{25}a_{33} \\ &\quad + a_{14}a_{22}a_{33})S^2 + (-a_{11}a_{25}a_{36} - a_{14}a_{22}a_{36} - a_{14}a_{25}a_{33})S \\ &\quad + a_{14}a_{25}a_{36} \end{aligned} \qquad (3\text{-}21)$$

$$\prod_{i=1}^{6}(s-\boldsymbol{\lambda}_i) = S^6 + (-\lambda_1-\lambda_2-\lambda_3-\lambda_4-\lambda_5-\lambda_6)S^5 + (\lambda_1\lambda_2+\lambda_1\lambda_3+\lambda_1\lambda_4 + \lambda_2\lambda_3+\lambda_1\lambda_5+\lambda_2\lambda_4+\lambda_1\lambda_6+\lambda_2\lambda_5+\lambda_3\lambda_4+\lambda_2\lambda_6+\lambda_3\lambda_5+\lambda_3\lambda_6 + \lambda_4\lambda_5+\lambda_4\lambda_6+\lambda_5\lambda_6)S^4 + (-\lambda_1\lambda_2\lambda_3-\lambda_1\lambda_2\lambda_4-\lambda_1\lambda_2\lambda_5-\lambda_1\lambda_3\lambda_4-\lambda_1\lambda_2\lambda_6-\lambda_1\lambda_3\lambda_5 - \lambda_2\lambda_3\lambda_4-\lambda_1\lambda_3\lambda_6-\lambda_1\lambda_4\lambda_5-\lambda_2\lambda_3\lambda_5-\lambda_1\lambda_4\lambda_6-\lambda_2\lambda_3\lambda_6-\lambda_2\lambda_4\lambda_5 - \lambda_1\lambda_5\lambda_6-\lambda_2\lambda_4\lambda_6-\lambda_3\lambda_4\lambda_5-\lambda_2\lambda_5\lambda_6-\lambda_3\lambda_4\lambda_6-\lambda_3\lambda_5\lambda_6 - \lambda_4\lambda_5\lambda_6)S^3 + \left(\lambda_1\lambda_2\lambda_3\lambda_4+\lambda_1\lambda_2\lambda_3\lambda_5+\lambda_1\lambda_2\lambda_3\lambda_6+\lambda_1\lambda_2\lambda_4\lambda_5+\lambda_1\lambda_2\lambda_4\lambda_6 + \lambda_1\lambda_3\lambda_4\lambda_5+\lambda_1\lambda_2\lambda_5\lambda_6+\lambda_1\lambda_3\lambda_4\lambda_6+\lambda_2\lambda_3\lambda_4\lambda_5+\lambda_1\lambda_3\lambda_5\lambda_6 + \lambda_{2\lambda_3\lambda_4\lambda_6}+\lambda_1\lambda_4\lambda_5\lambda_6+\lambda_2\lambda_3\lambda_5\lambda_6+\lambda_2\lambda_4\lambda_5\lambda_6+\lambda_3\lambda_4\lambda_5\lambda_6\right)S^2 + (-\lambda_1\lambda_2\lambda_3\lambda_4\lambda_5-\lambda_1\lambda_2\lambda_3\lambda_4\lambda_6-\lambda_1\lambda_2\lambda_3\lambda_5\lambda_6-\lambda_1\lambda_2\lambda_4\lambda_5\lambda_6 - \lambda_1\lambda_3\lambda_4\lambda_5\lambda_6-\lambda_2\lambda_3\lambda_4\lambda_5\lambda_6)S + \lambda_1\lambda_2\lambda_3\lambda_4\lambda_5\lambda_6 \tag{3-22}$$

$$\boldsymbol{A}_{e,CL} = (\boldsymbol{A_e} - \boldsymbol{B}_e\boldsymbol{K_e}) \tag{3-23}$$

The next step is to find the gain matrix $\boldsymbol{K}_e$. The closed loop state transition matrix can be determined by using the following equation, Where:

$\boldsymbol{A_e}$ is the state transition matrix of the extended open loop system

$$\boldsymbol{A_e} = \begin{bmatrix} \boldsymbol{A} & \boldsymbol{0_{3\times3}} \\ -\boldsymbol{C} & \boldsymbol{0_{3\times3}} \end{bmatrix}, \boldsymbol{B}_e = \begin{bmatrix} \boldsymbol{B} \\ \boldsymbol{0_{3\times3}} \end{bmatrix}, \boldsymbol{K_e} = [\boldsymbol{K_{e1}}\ \ \boldsymbol{K_{e2}}]$$

By equating the elements of the left side matrix to the elements of the right side of the equation (3-23), we obtain eighteen linear equations. The solution of the eighteen linear equations are the values of the gain values of the matrix $\boldsymbol{K_e}$ (3-24):

$$\boldsymbol{K_e} = \begin{bmatrix} k_{11} & k_{12} & k_{13} & k_{14} & k_{15} & k_{16} \\ k_{21} & k_{22} & k_{23} & k_{24} & k_{25} & k_{26} \\ k_{31} & k_{32} & k_{33} & k_{34} & k_{35} & k_{36} \end{bmatrix} \tag{3-24}$$

$$\begin{bmatrix} a_{11} & 0 & 0 & a_{14} & 0 & 0 \\ 0 & a_{22} & 0 & 0 & a_{25} & 0 \\ 0 & 0 & a_{33} & 0 & 0 & a_{36} \\ -1 & 0 & 0 & 0 & 0 & 0 \\ 0 & -1 & 0 & 0 & 0 & 0 \\ 0 & 0 & -1 & 0 & 0 & 0 \end{bmatrix} = \begin{bmatrix} \boldsymbol{A} - \boldsymbol{B}.\boldsymbol{K_{e1}} & -\boldsymbol{B}.\boldsymbol{K_{e2}} \\ -\boldsymbol{Id_{3x3}} & \boldsymbol{0_{3x3}} \end{bmatrix} \tag{3-25}$$

3.4.3. Simulation results

3.4.3.1 Common mode response

For this trial, all current references have a similar 500 Hz square waveform with 2A as low level and 4A as high level. Figure 3-8 reports the corresponding results. As planned by the theory, the winding currents evolves simultaneously while satisfying the 500 µs time settling requirement.

To get this effect, the controller only slightly change the duty cycle amplitude as shown in Figure 3-8-b, which is consistent with the small common mode inductance value.

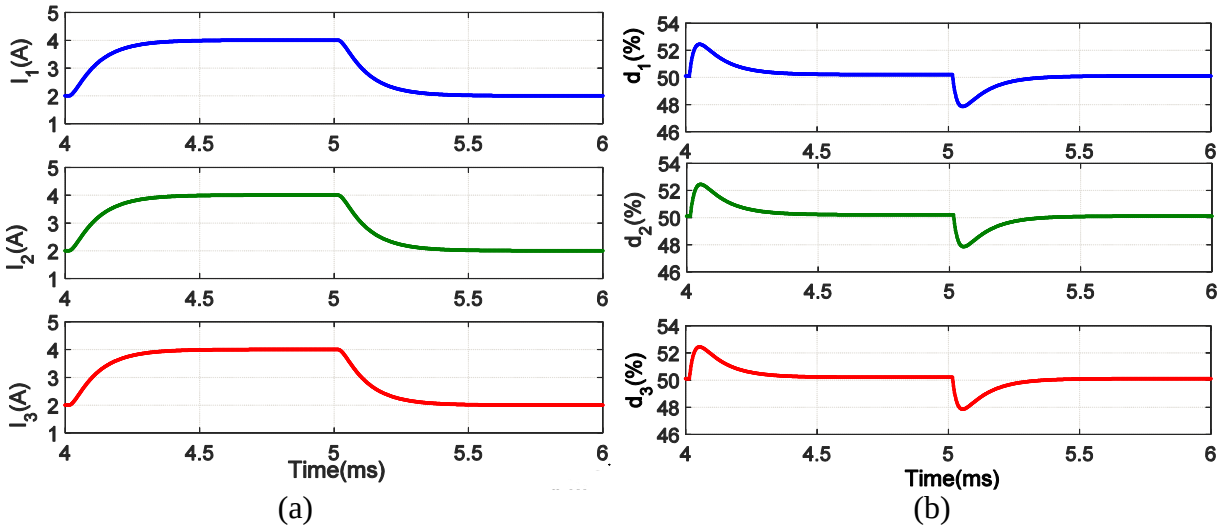

(a) (b)

Figure 3-8 closed loop behavior using state feedback criteria: common mode response

3.4.3.2 Differential mode response

Figure 3-9 shows the results in a situation where the first current reference $i_{1,ref}$ has a $2/3$ A ripple magnitude while the two others are set in opposite phase with half the magnitude, namely $1/3$ A. We notice that each current has the same dynamics as the common mode one. On the other hand, the duty cycles have a larger transient overshoot than in the previous results (see Figure 3-9-b). This is explained by the need to compensate the slow natural differential mode dynamics as the natural response time value is thirty times higher than the common mode one.

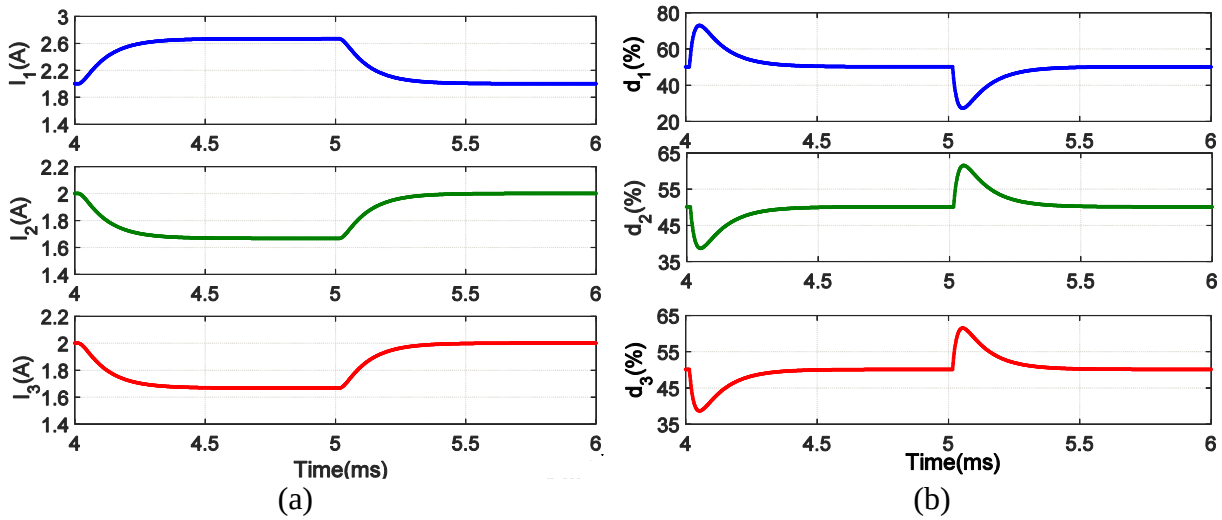

(a) (b)

Figure 3-9 closed loop behavior using state feedback criteria: differential mode response

3.4.3.3 Single current step response

Finally, Figure 3-10 depicts the results corresponding to the configuration where the supervision strategy needs to use unbalanced windings currents, for instance to take the pressure off a warmer cell. To get this configuration, only the first current reference $i_{1,ref}$ changes with a step magnitude of 2A (see Figure 3-10-a) and then $3A$ (see Figure 3-10-b). The first test shows input-output decoupling resulting from the fact that each natural mode behaves with similar time response. As this situation solicits two out of the three system modes, it is also not surprising to note that duty cycles reacts strongly. However Figure 3-10-b shows a very small coupling effect. This has been tied to the fact that one duty cycle tends transiently to exceed its limit value: the anti-windup apparatus operates and introduces a non-linearity which transiently cancels the decoupling effect(the system non-linearity is not compensated). This phenomenon disappears as soon as anti-windup function is useless.

It is important to underline that the anti-windup scheme has to be conservative by stopping all integral actions in case of any duty cycle reaching its low (0%) or high (100%) limits. Indeed, the controller behavior is completely coupled as the coefficients $\boldsymbol{K_{e1}}$ and $\boldsymbol{K_{e2}}$ of the equivalent state feedback computed using equation (3-25) reveals (Table 3-3).

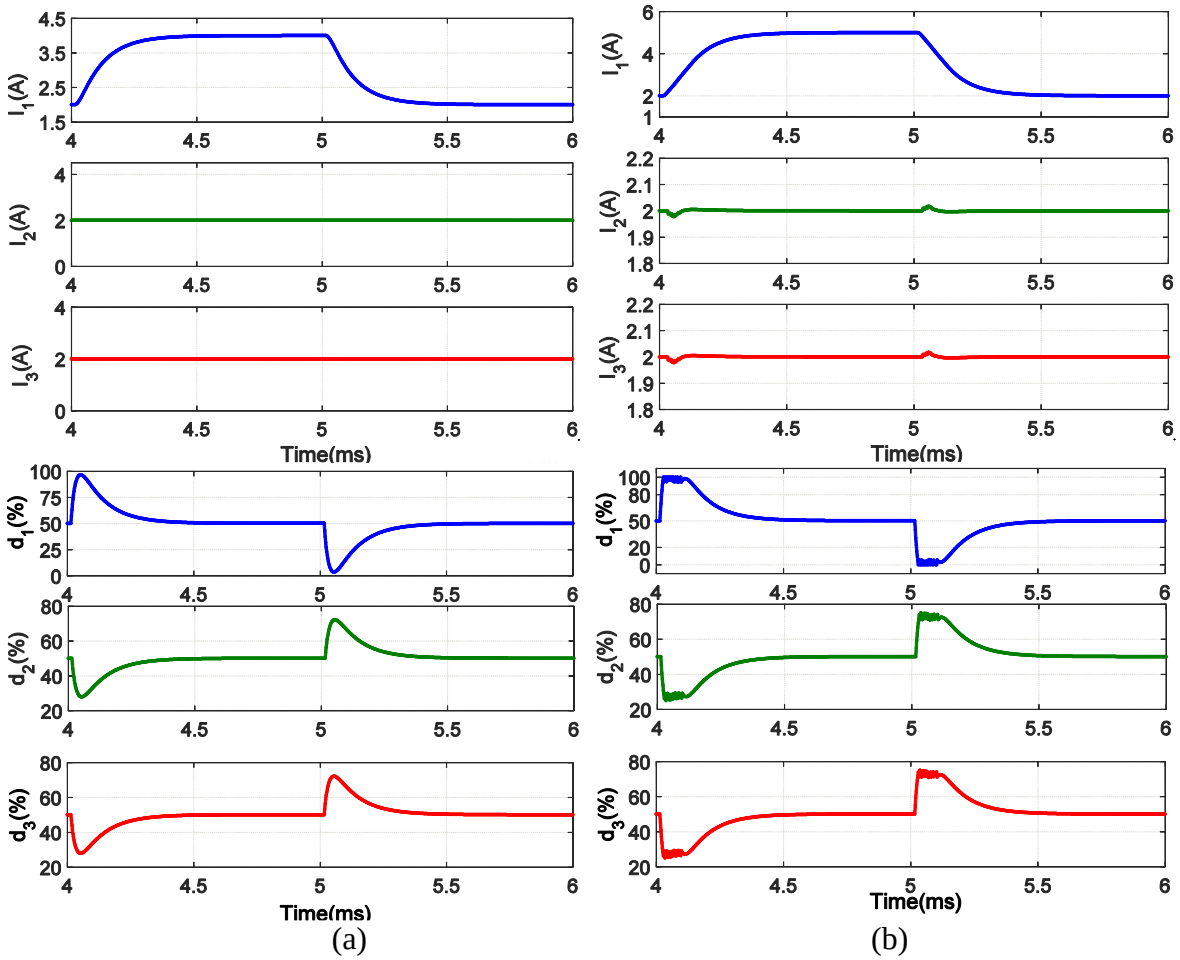

Figure 3-10 . closed loop behavior using state feedback criteria: a single current step response (a)small signal (b) large signal

Table 3-3 coefficients of the equivalent full state feedback

K_{e1}				K_{e2}		
1,999	-0,950	-0,950		-11550	5486	5486
-0,950	1,999	-0,950		5486	-11550	5486
-0,950	-0,950	1,999		5486	5486	-11550

3.4.3.4 Sensitivity analysis

This second step investigates the sensitivity of the state feedback design towards ICT parameters. Self-inductance and mutual inductance are studied among critical parameters important for assessing the control robustness. In fact, a better ICT coupling cancels the perfect coupling rejection as depicted in Figure 3-11-a where the actual values are $l = 19.8\text{mH}$ and $m = 9.7\text{mH}$. It induces a shift of the natural common mode dynamics (smaller time response) which finally also induces a modification of the closed loop common mode settling time. This change is mitigated by the controller but it induces a mismatch between the different modes dynamics which in turn produces this small coupling effect. In the case of an even better ICT coupling, the close loop behavior can also face instability as reported in Figure 3-11-b, where $l = 19.7\text{mH}$ and 9.8mH.

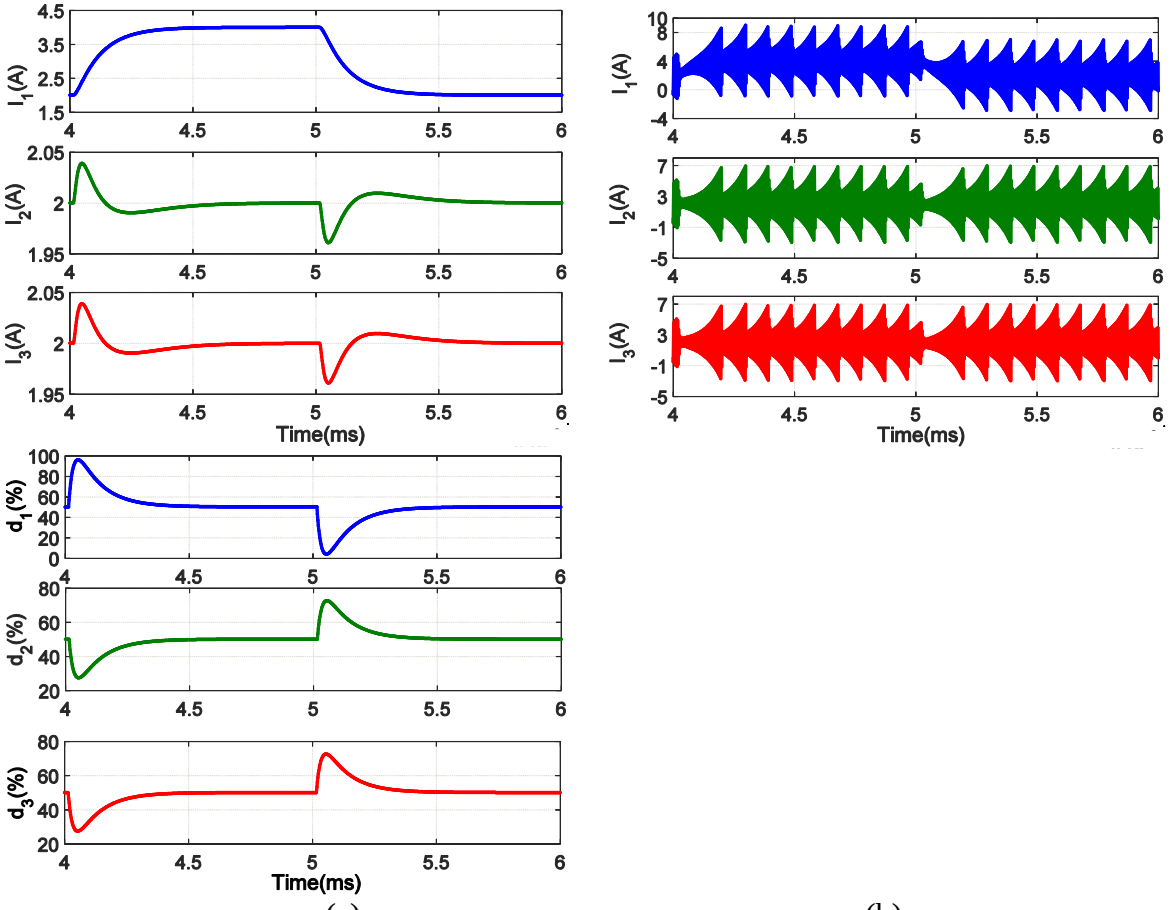

Figure 3-11 . closed loop behavior using state feedback criteria: ICT parameters l and m change(a) $l = 19.8mH$ and $m = 9.7mH$ (b) $l = 19.7mH$ and $m = 9.8mH$.

3.5. Decoupling strategy

The decoupling strategy principle is based on a proper linear transformation which turns the inductance matrix into a diagonal matrix. Controlling the system in the new frame given by this linear transformation leads to eliminate the coupling between the cells of the interleaved multicell buck DC-DC converter. When the decoupling is achieved it is possible to control each mode of the system with independent IP/PI.

3.5.1. Control structure degrees of freedom

Decoupling is obtained by using a transfer matrix $\boldsymbol{T}$ and its inverse $\boldsymbol{T^{-1}}$ that leads to transform the inductance matrix $\boldsymbol{T^{-1}LT}$ to diagonal form. Where the transfer matrix $\boldsymbol{T}$ is the eigenvector of the inductance matrix that is used in the system described in equation (3-10) the transfer matrix $\boldsymbol{T}$ and its inverse $\boldsymbol{T^{-1}}$ are formulated as:

$$\boldsymbol{T} = \frac{1}{3}\begin{bmatrix} 1 & 1 & 1 \\ 1 & -2 & 1 \\ 1 & 1 & -2 \end{bmatrix} \; and \; \boldsymbol{T^{-1}} = \begin{bmatrix} 1 & 1 & 1 \\ 1 & -1 & 0 \\ 1 & 0 & -1 \end{bmatrix} \tag{3-26}$$

The measured current (I_1, I_2 and I_3) will be transformed to the fictitious form (I_{com}, $I_{diff,1}$ and $I_{diff,2}$)by multiplying the measured current by the inverse of eigenvector ($\boldsymbol{T^{-1}}$) of the inductance matrix as in equations (3-27) and (3-28).

$$\boldsymbol{I_f} = \boldsymbol{T^{-1}} \times \boldsymbol{I} \tag{3-27}$$

$$\boldsymbol{D} = \boldsymbol{T} \times \boldsymbol{D_f} \tag{3-28}$$

Where: $\boldsymbol{I} = \begin{bmatrix} i_1 \\ i_2 \\ i_3 \end{bmatrix}$, $\boldsymbol{I_f} = \begin{bmatrix} i_{com} \\ i_{diff,1} \\ i_{diff,2} \end{bmatrix}$, $\boldsymbol{D} = \begin{bmatrix} d_1 \\ d_2 \\ d_3 \end{bmatrix}$ and $\boldsymbol{D_f} = \begin{bmatrix} d_{com} \\ d_{diff,1} \\ d_{diff,2} \end{bmatrix}$

The fictitious system satisfies the following relationship:

$$\frac{d}{dt}\boldsymbol{I_f} = (\boldsymbol{T^{-1}}.\boldsymbol{A}.\boldsymbol{T})\boldsymbol{I_f} + (\boldsymbol{T^{-1}}.\boldsymbol{B}.\boldsymbol{T})\boldsymbol{D_f} \tag{3-29}$$

This equation shows the three decoupled dynamics, the first diagonal term for the common mode and the two others for differential modes.

$$\frac{d}{dt}\boldsymbol{I_f} = -\begin{bmatrix} \frac{r}{l-2m} & 0 & 0 \\ 0 & \frac{r}{l+m} & 0 \\ 0 & 0 & \frac{r}{l+m} \end{bmatrix}\boldsymbol{I_f} + \begin{bmatrix} \frac{v_i}{l-2m} & 0 & 0 \\ 0 & \frac{v_i}{l+m} & 0 \\ 0 & 0 & \frac{v_i}{l+m} \end{bmatrix}\boldsymbol{D_f} \tag{3-30}$$

Consequently, each fictitious current can be independently controlled using its related fictitious duty cycle by three independent IP controllers. Figure 3-12 illustrates the proposed scheme where $\boldsymbol{K_p}$ and $\boldsymbol{K_i}$ are two diagonal matrices containing the proportional and integral terms

respectively.

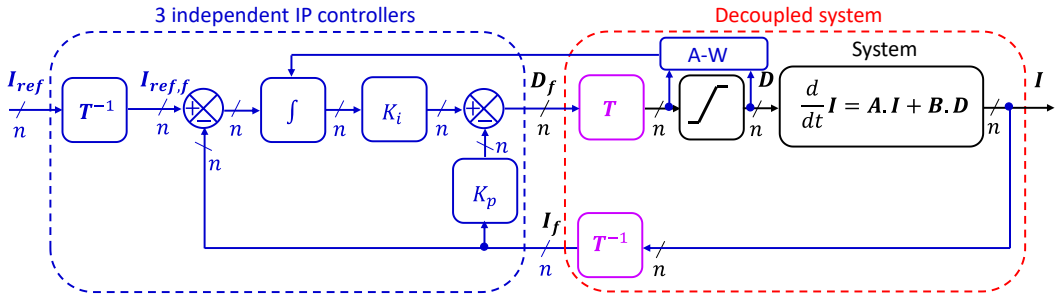

Figure 3-12 Control structure of the decoupling strategy

The controlled system is the fictitious one. This system is built by sandwiching the real system between the two linear transforms presented above. Thus, the fictitious inputs $\boldsymbol{D_f}$ are multiplied by matrix $\boldsymbol{T}$ to obtain the real duty-cycles $\boldsymbol{D}$. And the controlled fictitious currents are calculated from the real ones by multiplying them by inverse of transformation matrix $\boldsymbol{T^{-1}}$.

Assuming that there is no duty cycle saturation and using the identity matrix property and linearity of the control law, the closed loop equation can be expressed as:

$$\boldsymbol{D} = \left[-\boldsymbol{T}.\boldsymbol{K_p}.\boldsymbol{T^{-1}} \quad \boldsymbol{T}.\boldsymbol{K_i}.\boldsymbol{T^{-1}}\right].\begin{bmatrix}\boldsymbol{I}\\ \boldsymbol{Int_\varepsilon}\end{bmatrix} = -[\boldsymbol{K_{e1}} \ \boldsymbol{K_{e2}}]\begin{bmatrix}\boldsymbol{I}\\ \boldsymbol{Int_\varepsilon}\end{bmatrix} \qquad (3\text{-}31)$$

This expression is similar to that given by (3-16). Thus, the new control approach, based on modal system representation, is strictly similar to the previous one based on full state feedback of an extended system. By construction, this method provides a closed loop system controlling independently its three modes, namely the common and differential modes. The mathematical relationship between fictitious reference $\boldsymbol{I_{ref,f}}$ and fictitious output $\boldsymbol{I_f}$ is diagonal. Using the transform matrixes (3-26), the resulting relationship between the real currents and the corresponding references is given by:

$$\boldsymbol{I} = \boldsymbol{T}.\begin{bmatrix}\lambda_{CL,1} & 0 & 0\\ 0 & \lambda_{CL,2} & 0\\ 0 & 0 & \lambda_{CL,3}\end{bmatrix}.\boldsymbol{T^{-1}}.\boldsymbol{I_{ref}} \qquad (3\text{-}32)$$

Where $\lambda_{CL,k}$ are the required closed loop eigen values.

The previous equation yields:

$$\boldsymbol{I} = \frac{1}{3}.\begin{bmatrix}\lambda_{CL,1}+2\lambda_{CL,2} & \lambda_{CL,1}+\lambda_{CL,3}-2\lambda_{CL,2} & \lambda_{CL,1}-\lambda_{CL,3}\\ \lambda_{CL,1}-\lambda_{CL,2} & \lambda_{CL,1}+\lambda_{CL,2}+\lambda_{CL,3} & \lambda_{CL,1}-\lambda_{CL,3}\\ \lambda_{CL,1}-\lambda_{CL,3} & \lambda_{CL,1}+\lambda_{CL,2}-2\lambda_{CL,3} & \lambda_{CL,1}+2\lambda_{CL,3}\end{bmatrix}.\boldsymbol{I_{ref}} \qquad (3\text{-}33)$$

This means that the only way to obtain a decoupled behavior of the real system is to choose identical dynamics for each modes. This is possible, but in view of the strong disparity of open loop dynamics, this implies high gains for the differential modes to offset their low natural dynamics. Such a choice leads to high noise sensitivity and can lead to frequent transient duty cycles saturations.

Integral terms usually lead to large unexpected overshoot and possibly instability while saturation occurs. Indeed, saturation causes an open-loop behavior, especially for the integral terms. Anti-windup systems intend to maintain the system in closed loop. However, saturation is a non-linear phenomenon, and because of $\boldsymbol{T}$ matrix multiplication it is not possible to know which of the integral terms induce saturation. Hence in any saturation situation the anti-windup system clamps the three integral actions. This conservative option leads to a sub-optimal implementation of the controller.

In sum, the strict decoupling option has two theoretical drawbacks. It leads to unreasonably increase the differential mode dynamic which results in an inadequate anti-windup implementation.

3.5.2. Simulation results

3.5.2.1 Common mode response

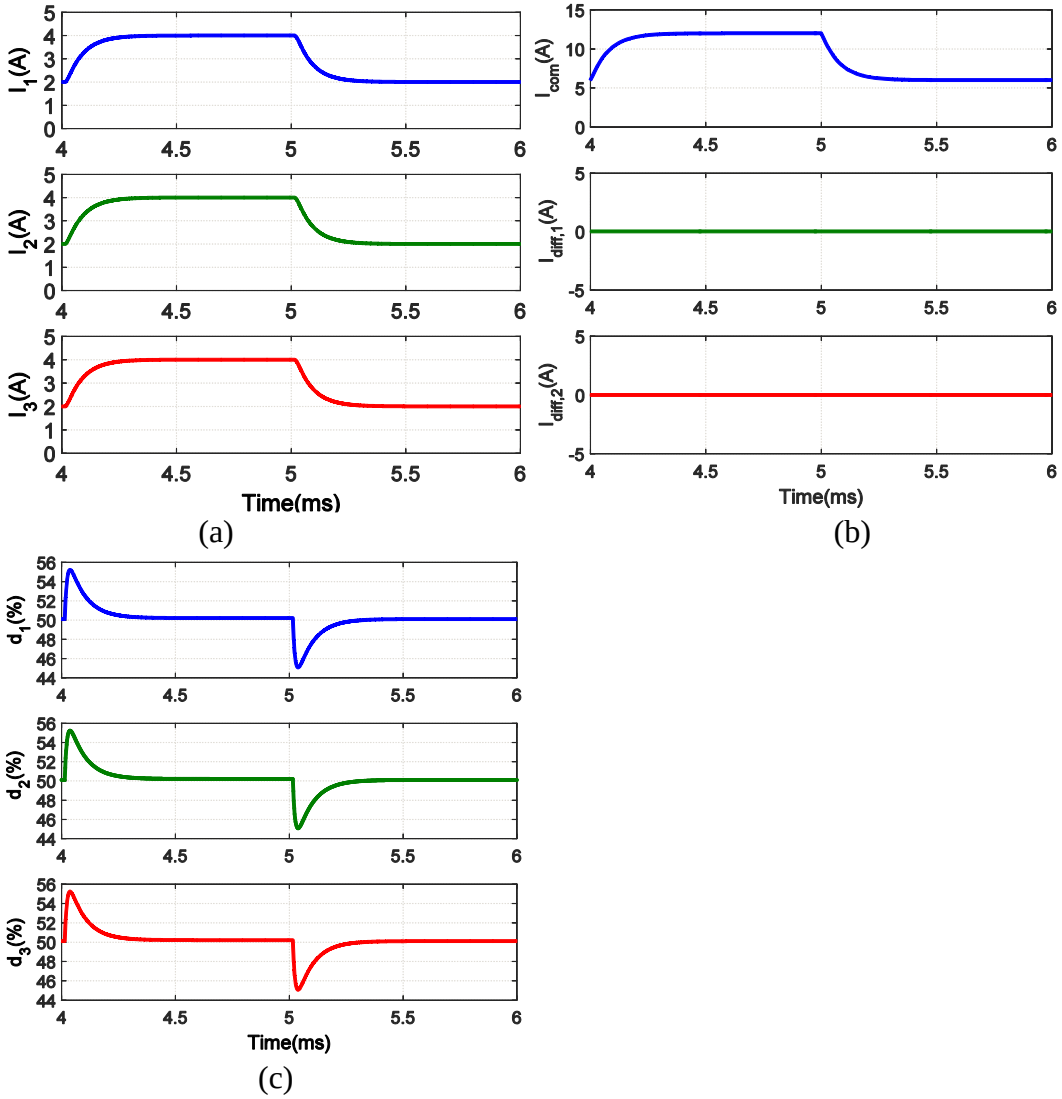

Figure 3-13 closed loop behavior using decoupling criteria: common mode response

For this trial, all current references have a similar 500 Hz square waveform with 2A as low level and 4A as high level. Figure 3-13 reports the corresponding results. As planned by the theory, the winding currents evolves simultaneously while satisfying the 500 µs time settling requirement. The three fictitious currents in Figure 3-13-b confirms this assessment by showing no response on the two differential mode channels ($i_{diff,1}$ & $i_{diff,2}$) To get this effect, the controller only slightly change the duty cycle amplitude as in Figure 3-13-c, which is consistent with the small common mode inductance value.

3.5.2.2 Differential mode response

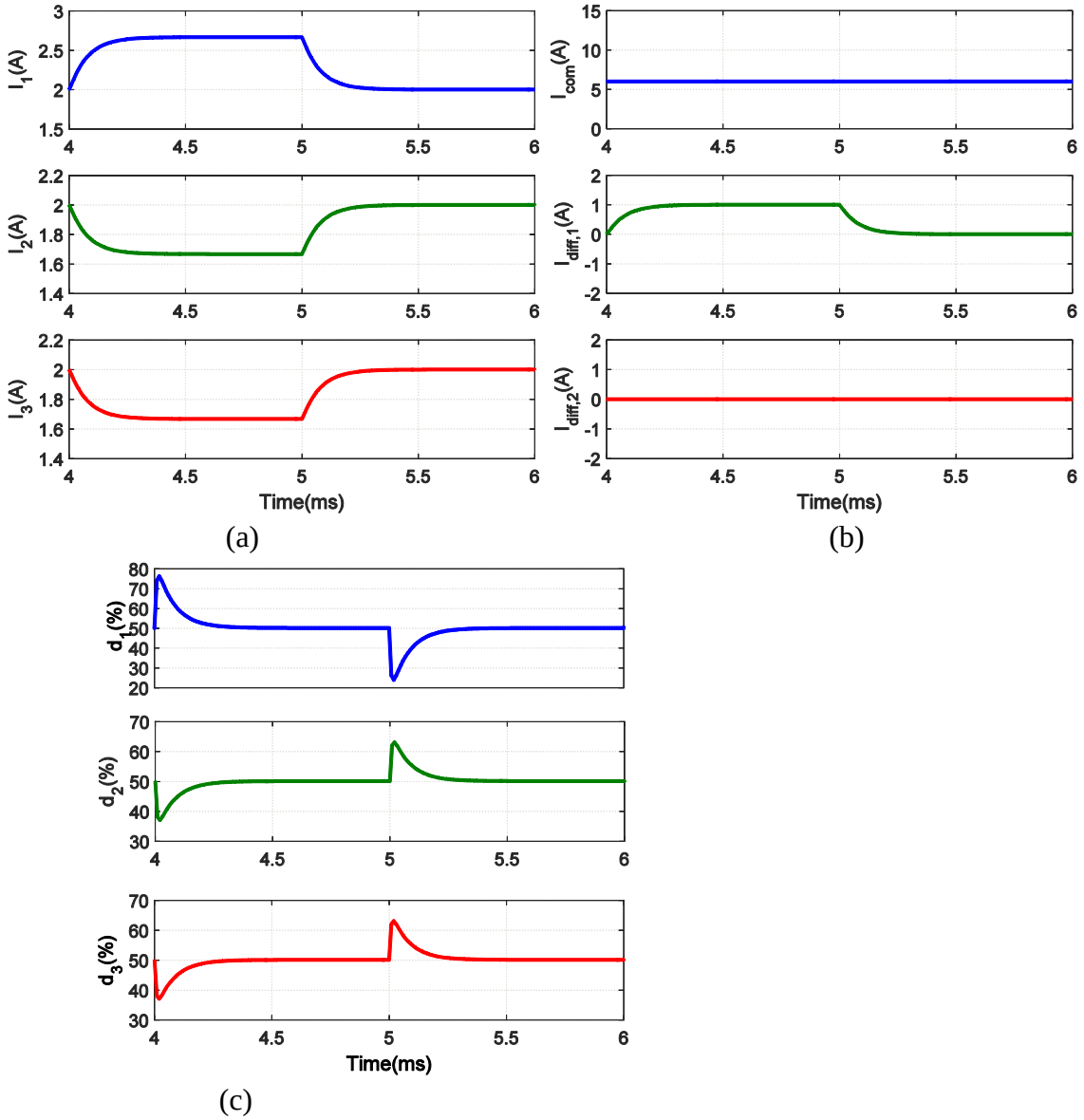

Figure 3-14 closed loop behavior using decoupling criteria: differential mode response

Figure 3-14 shows the results when the first current reference $i_{1,ref}$ has a $2/3$ A ripple magnitude while the two others are set in opposite phase with a half this magnitude, namely $1/3$ A. From this figure, we can see that controllers of differential modes are tuned to achieve the same dynamics as the common mode. In this configuration, the different duty cycles have a larger transient overshoot as shown in Figure 3-14-c, which is explained by the need to compensate the slow natural differential mode dynamics (thirty times higher than the common mode in this test). Anyway, as expected by the theoretical part, the fictitious currents shows a unique mode evolution (first differential mode) while the two other channels (i.e. common mode and second differential mode) have no reaction as in Figure 3-14-b.

3.5.2.3 Single current step response

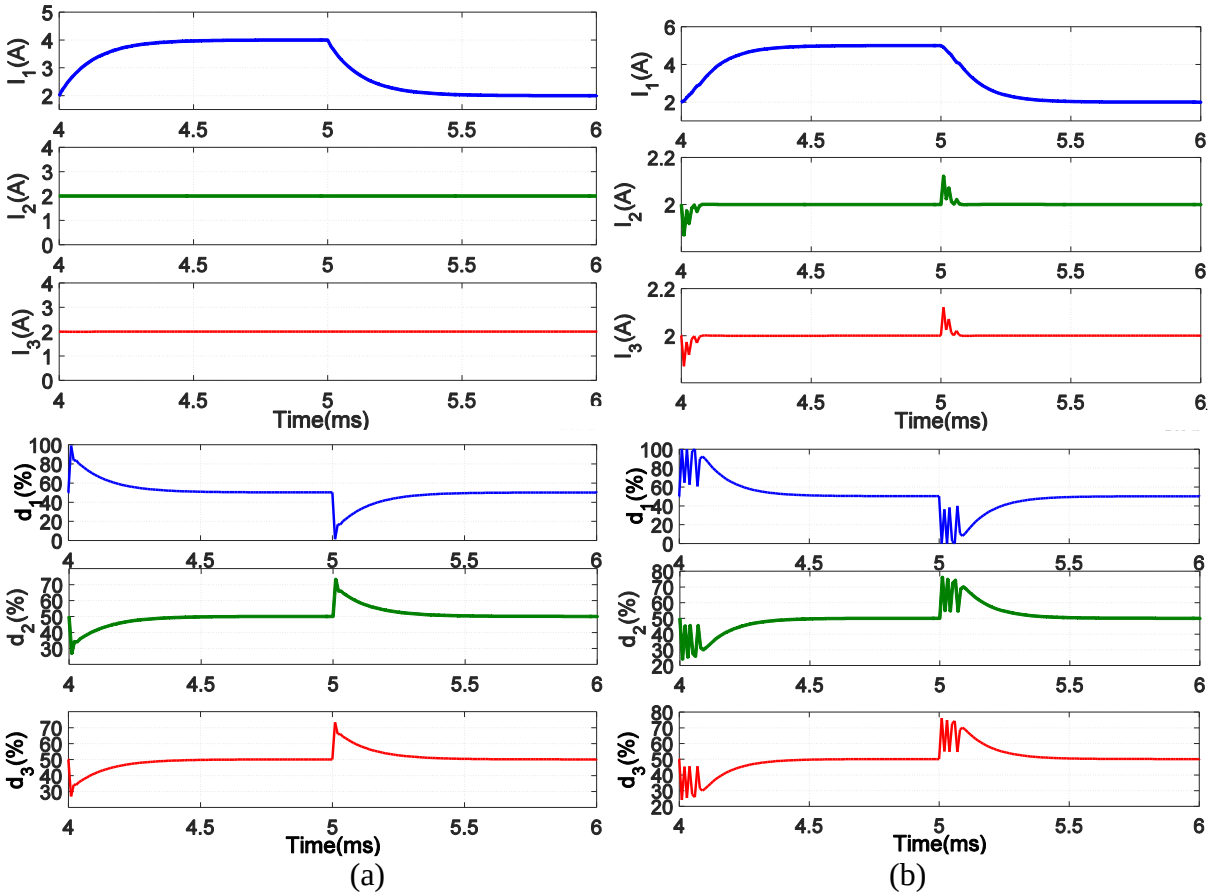

Figure 3-15 . closed loop behavior using decoupling criteria: a single current step response (a)small signal (b) large signal

Finally, Figure 3-15 depicts the results corresponding to the configuration where the supervision strategy needs to use unbalanced windings currents like in section 3.4.3.3. In this test, only the first current reference $i_{1,ref}$ changes with a step magnitude of 2A (see Figure 3-15-a) and then 3A (see Figure 3-15-b). The first trial shows input-output decoupling resulting from the fact that each natural mode behaves with similar time response. As this situation solicits two out of the three system modes, it is also not surprising to note that duty cycles reacts strongly. However, like

in section 3.4.3.3, Figure 3-15-b shows that a coupling effect may appear when one duty cycle tends transiently to exceed its limit value: the anti-windup apparatus operates and involves a non-linearity which locally cancels the decoupling effect. This phenomenon disappears as soon as anti-windup function is useless.

It is important to underline that, as in full state feedback of the extended system, the anti-windup scheme has to be conservative by stopping all integral actions in case of any duty cycle reaching its low (0%) or high (100%) limits. Indeed, in this situation, the controller behavior is completely coupled as the coefficients $\boldsymbol{K_{e1}}$ and $\boldsymbol{K_{e2}}$ of the equivalent state feedback computed using equation (3-31) reveals (see Table 3-4).

Table 3-4 coefficients of the equivalent full state feedback

$\boldsymbol{K_{e1} = T.K_p.T^{-1}}$			$\boldsymbol{K_{e2} = -T.K_i.T^{-1}}$		
2.033	-1.933	-0.967	-12 000	11 600	5 800
-0.967	1.067	-0.967	5 800	-6 400	5 800
0.000	0.000	3.000	0	0	-1 800

3.5.2.4 Sensitivity analysis

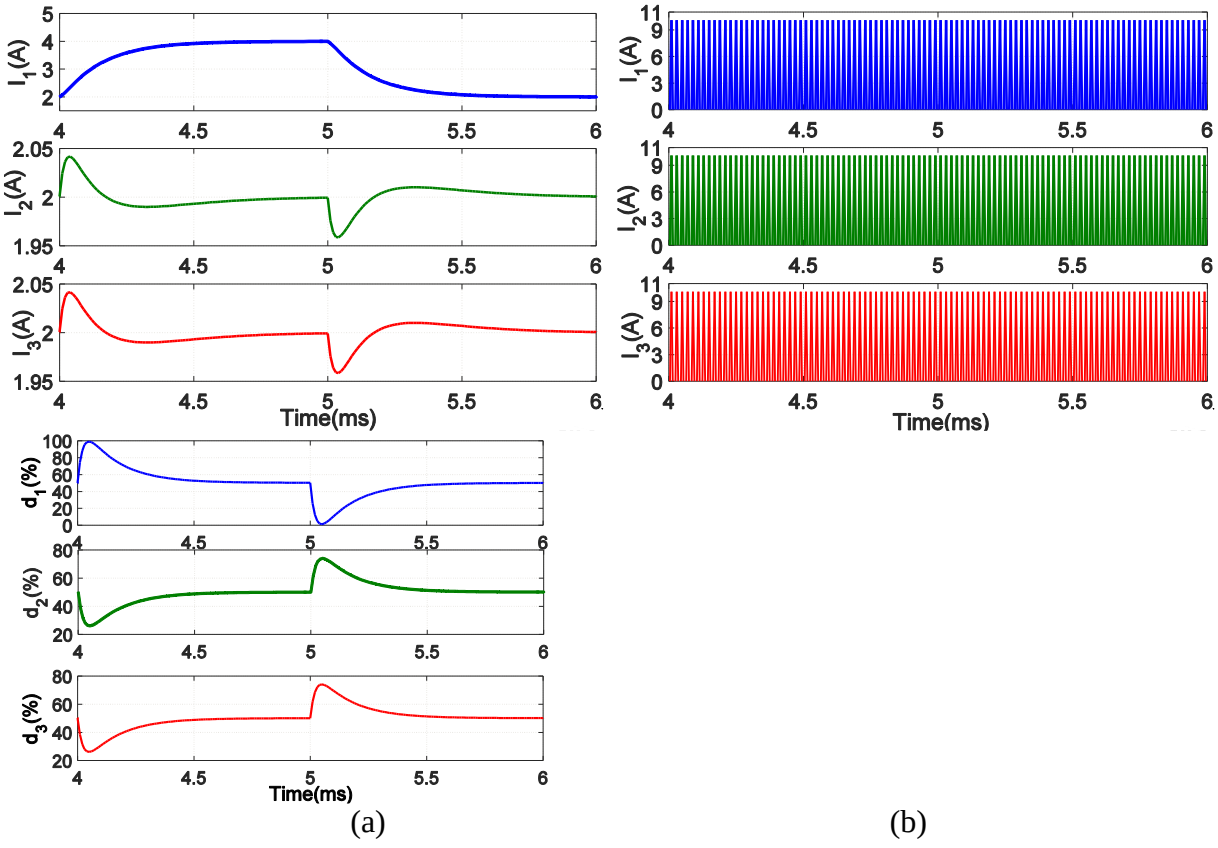

(a) (b)

Figure 3-16 . Closed loop behavior using decoupling criteria: ICT parameters l and m change(a) $l = 19.8mH$ and $m = 9.7mH$ (b) $l = 19.7mH$ and $m = 9.8mH$.

In this section, we study the sensitivity of the decoupling design towards ICT parameters. Self-inductance and mutual inductance are studied among critical parameters important for assessing the control robustness. In fact, a better ICT coupling cancels the perfect coupling rejection as depicted in Figure 3-16-a where the actual values are $l = 19.8\text{mH}$ and $m = 9.7\text{mH}$ instead of those used to tune the controllers namely $l = 20\text{mH}$ and $m = 9.5\text{mH}$. This difference induces a modification in the closed loop common mode settling time which induces a mismatch between the different modes dynamics. This difference produces in turn a channel coupling effect. Like in subsection 0, in the case of an even better ICT coupling, the close loop behavior can also face instability as reported in Figure 3-16-b, where $l = 19.7\text{mH}$ and $= 9.8\text{mH}$.

3.6. Linear quadratic regulator (LQR)

In previous sections, we have demonstrated that the current control of a multicell power converter may be done by using a full state feedback control of the extended system. We have seen that this strategy offers many degrees of freedom as the $n \times n_e$ feedback matrix $\boldsymbol{K_e} = [\boldsymbol{K_{e1}} \quad \boldsymbol{K_{e2}}]$ has $n \times n_e = 18$ independent real parameters in the 3-cell Buck-converter. The main objective to tune the controller may be to control the system's dynamics by adjusting the $n_e = 6$ poles of the closed loop system. It is thus evident that the $\boldsymbol{K_e}$ matrix meeting this pole criteria is not unique.

One of the possible solutions presented in previous sections was to design the closed loop system to be dynamically decoupled. This involves breaking the link between current references and current responses. This can be achieved by setting the closed loop transition matrix to be diagonal or by using a decoupling strategy based on a proper linear transformation. These two approaches are strictly equivalent.

Nevertheless, decoupling technics are model-dependent and therefore sensitive to fluctuations of the system parameters. In this section we are going to investigate another tuning strategy. To find the gain of the $n \times n_e$ feedback matrix of a MIMO system there are many possibilities. One of them is based on Linear Quadratic Regulator (LQR) theory which is an optimal multivariable feedback control approach that minimizes the excursion in state trajectories of a system while requiring minimum controller effort. Such approach is used to find the best gain matrix that makes the system optimal based on a specific cost function or a specific performance criterion[60][61] .

3.6.1. Objective function

In LQR approach, the parameters design issue of the full state feedback is managed by using a global performance index summarizing the closed loop behavior. It involves a functional, namely a time infinite-horizon Riemann integral based on a quadratic cost function:

$$\boldsymbol{J} = \int_0^{\infty} \left(\begin{bmatrix} \boldsymbol{I} \\ \boldsymbol{Int}_{\varepsilon} \end{bmatrix}^t . \boldsymbol{Q} . \begin{bmatrix} \boldsymbol{I} \\ \boldsymbol{Int}_{\varepsilon} \end{bmatrix} + \boldsymbol{D}^t . \boldsymbol{R} . \boldsymbol{D} \right) . dt \qquad (3\text{-}34)$$

Where $\boldsymbol{Q}$ and $\boldsymbol{R}$ are two positive semi-definite matrixes of weighting factors applied to the states and control variables, respectively. As in this case, all currents i_k play the same role and similarly all duty cycles d_k, $\boldsymbol{Q}$ and $\boldsymbol{R}$ can be simplified to $\boldsymbol{Q} = \begin{bmatrix} q_1 \boldsymbol{Id}_{3\times3} & \boldsymbol{0}_{3\times3} \\ \boldsymbol{0}_{3\times3} & q_2 \boldsymbol{Id}_{3\times3} \end{bmatrix}$ and $\boldsymbol{R} = \rho . \boldsymbol{Id}_{3\times3}$.

In conclusion, the objective is to find the (q, ρ) set of two scalar values that best meets specifications (given in Table 3-2). For this purpose, each (q, ρ) set permits to compute a full state feedback matrix $\boldsymbol{K_e}$ ($\boldsymbol{D} = -\boldsymbol{K_e}.[\boldsymbol{I} \quad \boldsymbol{Int}_\varepsilon]^t$) that minimizes the cost function:

$$\boldsymbol{J}(q,\rho) = \int_0^\infty \left(\begin{bmatrix} \boldsymbol{I} \\ \boldsymbol{Int}_\varepsilon \end{bmatrix}^t . \begin{bmatrix} q_1 \boldsymbol{Id}_{3\times3} & \boldsymbol{0}_{3\times3} \\ \boldsymbol{0}_{3\times3} & q_2 \boldsymbol{Id}_{3\times3} \end{bmatrix} . \begin{bmatrix} \boldsymbol{I} \\ \boldsymbol{Int}_\varepsilon \end{bmatrix} + \boldsymbol{D}^t . \rho . \boldsymbol{Id}_{3\times3} . \boldsymbol{D} \right) . dt \qquad (3\text{-}35)$$

$\boldsymbol{Q}$ and $\boldsymbol{R}$ are the design parameters that give a tradeoff between state variables and control signals. The more ratio of these matrices are increased the more the higher weighted signal is penalizes. In fact, selecting a large value of $\boldsymbol{R}$ and fixing $\boldsymbol{Q}$ means to put more weight on the control effort ($\boldsymbol{u}$) and try to stabilize the system with less control effort. It is called $expensive\ control\ strategy$ and this will slow down the response. Inversely, when smaller value of $\boldsymbol{R}$ is selected the system tries to stabilized regardless the control effort. It is called $cheap\ control\ strategy$ [62], the response will become faster. Correspondingly, when selecting a large value of $\boldsymbol{Q}$ and fixing $\boldsymbol{R}$ means to try to stabilize the system with less changes in states and put more concerns on states than on control effort. It is not easy to find good values for $\boldsymbol{Q}$ and $\boldsymbol{R}$. There are different ways to defined them. Many studies were done to tune them such as genetic algorithm [63], artificial neural networks [64] and quantum particle swarm optimization [65]. Also they can be defined by trail-and-error this method is time consuming. Nevertheless, we select this method, by setting random values for $q_1, q_2\ and\ \rho = 1$ from each set ($q_1$and q_2), we calculated the feedback gain matrix as in equation (3-36). By simulating the system and observe if the system response closed, the tuning parameters are changes and check again until the response becomes closed to the desired one.

The gain matrix $\boldsymbol{K_e}$ can be defined from the following equation

$$\boldsymbol{K_e} = \boldsymbol{R}^{-1}\boldsymbol{B}^T\boldsymbol{P} \qquad (3\text{-}36)$$

Where $\boldsymbol{P}$ is the unique positive definite solution of the matrix Algebraic Riccati Equation (ARE)

$$\boldsymbol{A}^T\boldsymbol{P} + \boldsymbol{P}\boldsymbol{A} - \boldsymbol{P}\boldsymbol{B}\boldsymbol{R}^{-1}\boldsymbol{B}^T\boldsymbol{P} + \boldsymbol{Q} = \boldsymbol{0} \qquad (3\text{-}37)$$

3.6.2. State feedback design by using LQR

By using LQR design approach and the tuning parameters $q_1 = 5, q_2 = 8 \times 10^8$ and $\rho = 100$, the global full state feedback matrix $\boldsymbol{K_e}$ is tuned. It leads to the parameters listed in Table 3-2 we can see that $\boldsymbol{K_{e2}}$ matrix related to the integral terms is strictly diagonal and that $\boldsymbol{K}_{e1}$ gain matrix related to the proportional terms has dominant values on its diagonal. This means that the controller almost acts as if there was three independent controllers acting independently on their dedicated duty cycle.

Table 3-5 LQR design of the full state feedback strategy setting parameters

K_{e1}			K_{e2}		
0.564	-0.154	-0.154	-3162	0	0
-0.154	0.564	-0.154	0	-3162	0
-0.154	-0.154	0.564	0	0	-3162

Such $\boldsymbol{K_e}$ matrix leads to a reduced number of multiplication, but also to a simpler and more efficient anti-windup scheme. Indeed, as $\boldsymbol{K_{e2}}$ matrix is diagonal, a duty cycle saturation can be

easily attributed to the related integral term. These properties are illustrated in the two next sections.

3.6.2.1 Common mode differential mode response

Figure 3-17 (a) and (b) shows the common mode and differential mode results, respectively. Conversely to the previous strategy, the LQR method derives a control that makes the dynamics of both modes different. As demanded by the specification, the differential mode satisfies the 500 µs time settling requirement, while the common mode has a faster dynamic. This result is not surprising given that LQR has a global approach combining both error and control magnitude issues. As differential mode is slow, it provides the minimum required gain values. These gains values make the common mode faster due to its intrinsic high dynamics. It can be observed in Figure 3-17-a representing the common mode response that the duty cycles overshoot are roughly 60% higher than in the decoupling case, whereas in Figure 3-17-b, showing the differential mode response, the duty cycles overshoot is roughly 15% lower than in the decoupling case.

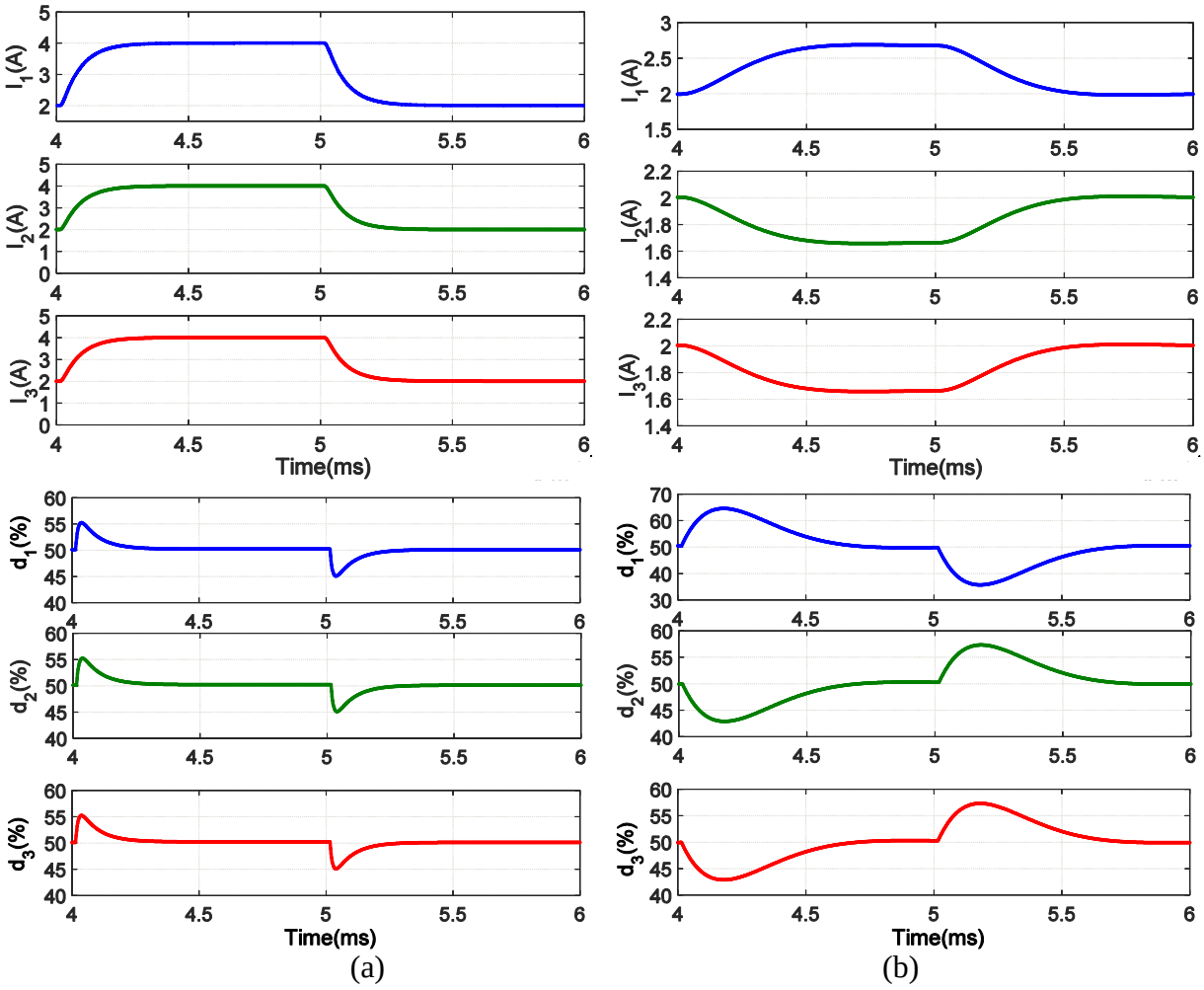

Figure 3-17 . Closed loop behavior using LQR design:(a) Common mode and (b)Differential mode response.

3.6.2.2 Single current step response

Finally, Figure 3-18 depicts the first current step response behavior. This trial solicits both the common mode and the first differential mode. Compared to Figure 3-15 a), the LQR design induces a much less aggressive control law which maintains the duty cycles much easily within its limits (see Figure 3-18-a). Conversely, the first current change impacts slightly the two others without exceeding the specifications. This coupling effect arises because the common mode and differential mode dynamics are different in this case.

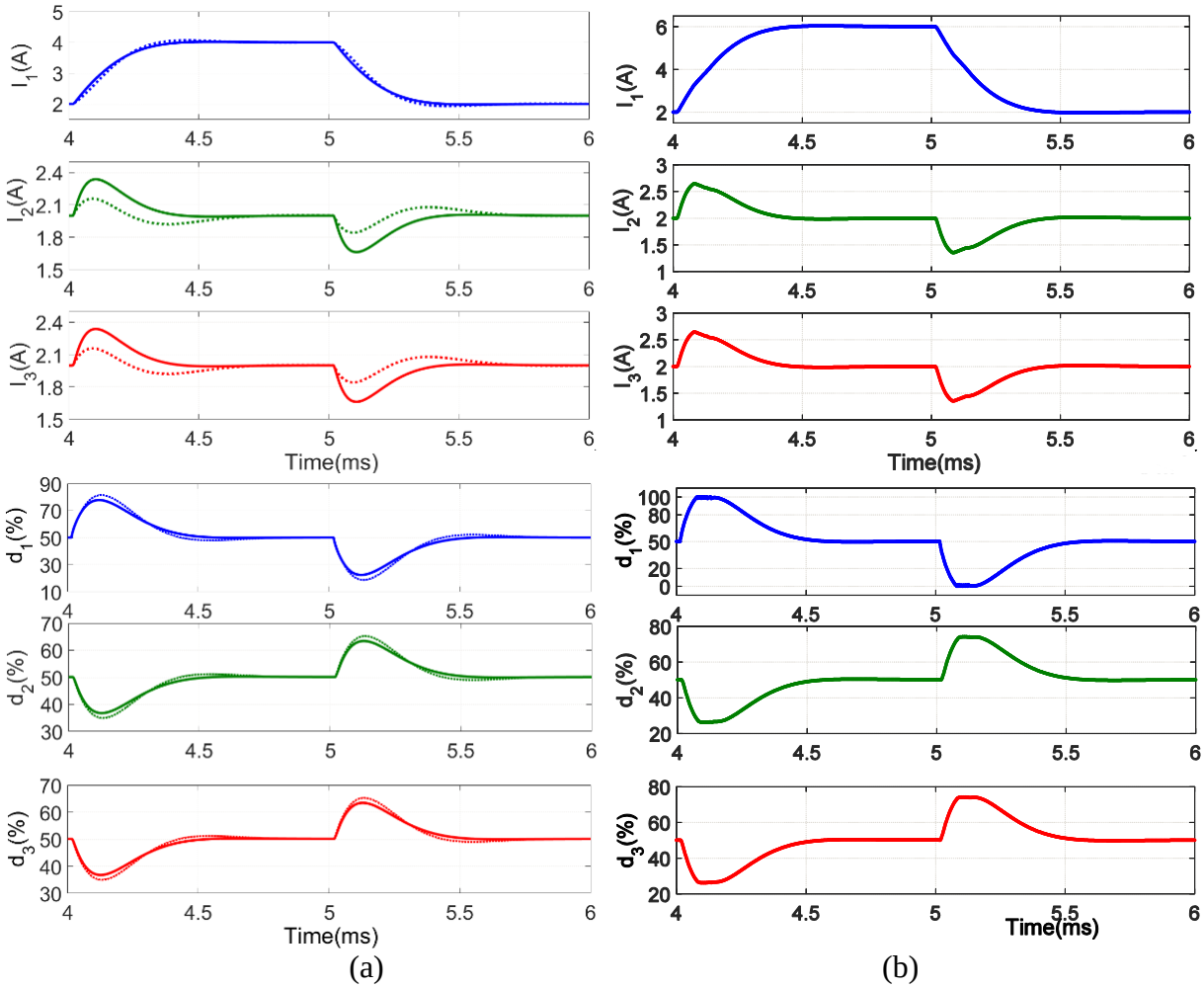

Figure 3-18 . Closed loop behavior using LQR design a single current step response :(a) Small signal (b) Large signal.

Figure 3-18-a also illustrates that the present controller may be almost considered as composed of three independent controllers. Indeed, Figure 3-18-a shows in dashed lines the same transient response in the case where all non-diagonal terms of K_{e1} are set to zero. Even if the control values are slightly higher, the behavior remains similar and totally acceptable while the coupling effects is even somewhat decreased. That is the reason why the anti-windup apparatus can be properly built by impacting solely the integral term corresponding to the control variable in saturation. Moreover, it leads to a very simple implementation similar to SISO systems. Figure 3-18-b depicts

the very good behavior of the system while d_1 saturate at 100%. It should be specified that the step magnitude has to be enlarged compared to Figure 3-15-b, in order to reach saturation mode. It is clearly due to the less aggressive behavior of this controller compared to the decoupling one. For information, in the present case, only the first duty cycle is saturated. The applied anti-windup strategy is built as follows: the integer is stopped as long as the duty cycle is clamped to 100% and the current error is positive, or the first duty cycle is clamped to 0% and the current error is negative.

3.6.2.3 Sensitivity analysis

Besides a smoother control action and a simpler implementation in a controller, the LQR design proves a better robustness regarding parameters uncertainty. Figure 3-19 shows that the controller remains stable even in the most demanding case of a higher actual ICT coupling than expected, namely when $l = 19.7mH$ and $m = 9.8mH$.

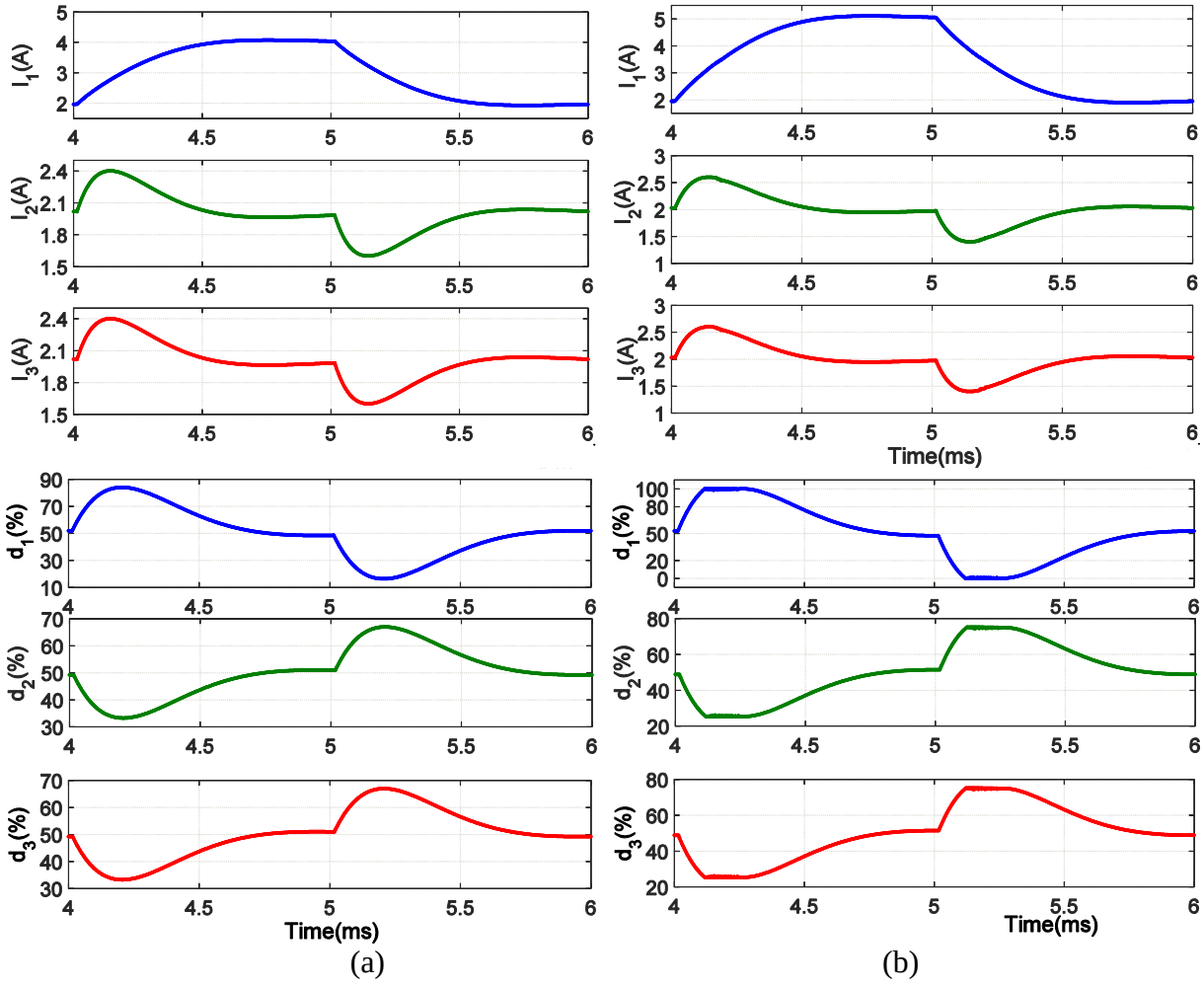

Figure 3-19 . Closed loop behavior using LQR design ICT parameters change ($l = 19.7mH$ and $m = 9.8mH$):(a) Small signal (b) Large signal.

3.7. Conclusion (Comparison)

The present study addresses the easier and more robust way to implement a controller scheme dedicated to control the current in an interleaved multi-cell converter using an ICT. This device clearly enables to significantly reduce both input and output currents ripples which permits using reliable capacitor technology. However, the control-oriented modeling part shows that it also creates a significant coupling between the different cells. This magnetic coupling induces to deal with a real MIMO system. To cope with this issue, different approaches are assessed.

The first one is based on classical PI controller. The PI controller is easy to implement and the anti-windup is easy to be used in this strategy. This controller gives good results when the current in the cells are balanced, but when there is variation in the currents or unbalance in converter the controller can't mitigate or eliminate that effect and the coupling appears strongly between the branches of the converter.

The second one based on a modal method is easy to understand for an engineering point of view. While operating in linear mode and with rated values, it permits a very good decoupling between the references inputs and the related outputs. However, an efficient anti-windup scheme cannot be implemented to optimally take the duty cycles saturation into account. In case of state feedback with decoupling closed loop system, the simulations show that the coupling is smaller than in the case of decoupling of inductance matrix and less aggressive regarding duty cycle variations. Moreover, the control design is somewhat sensitive to the ICT parameters which may be difficult to evaluate precisely. Finally, it uses high gains to offset the slow natural dynamics of the differential mode, possibly leading to noise sensitivity and more frequent saturated behavior.

The last methodology is based on a full state feedback of an extended model whose parameters are set using a quadratic cost time function. This so-called LQR technique enables to find a good trade-off between the different key points of the specification, which are stability, settling time, decoupling and robustness. Although a small but acceptable coupling remains, this second controller exhibits an almost internally decoupled structure permitting to implement a simple and efficient anti-windup technique. In addition, the controller acts smoothly during transient which reduces noise sensitivity. Finally, it is also more robust to ICT parameters changes, which is an important asset.

All these studies carried out in simulation show that the interleaved multi-cell converter is a very specific power converter. In this particular case, the full state feedback approach based on LQR method exhibits a very attractive trade-off between the different requirements of the control specifications while enabling a very easy implementation in a microcontroller or a FPGA device. These very positive results encourage to validate the study with an experiment on a laboratory test bench.

Chapter 4. Model Predictive Control

4.1. Introduction

Predictive control is widely used in many applications. It is recently used to control power converters and machine drives. These high computing-cost algorithms can todays be implemented in real-time for such applications as targets based on microcontroller and FPGA devices offered very affordable powerful digital solutions. Predictive control strategies are classified as shown in Figure 4-1 as proposed in [66].

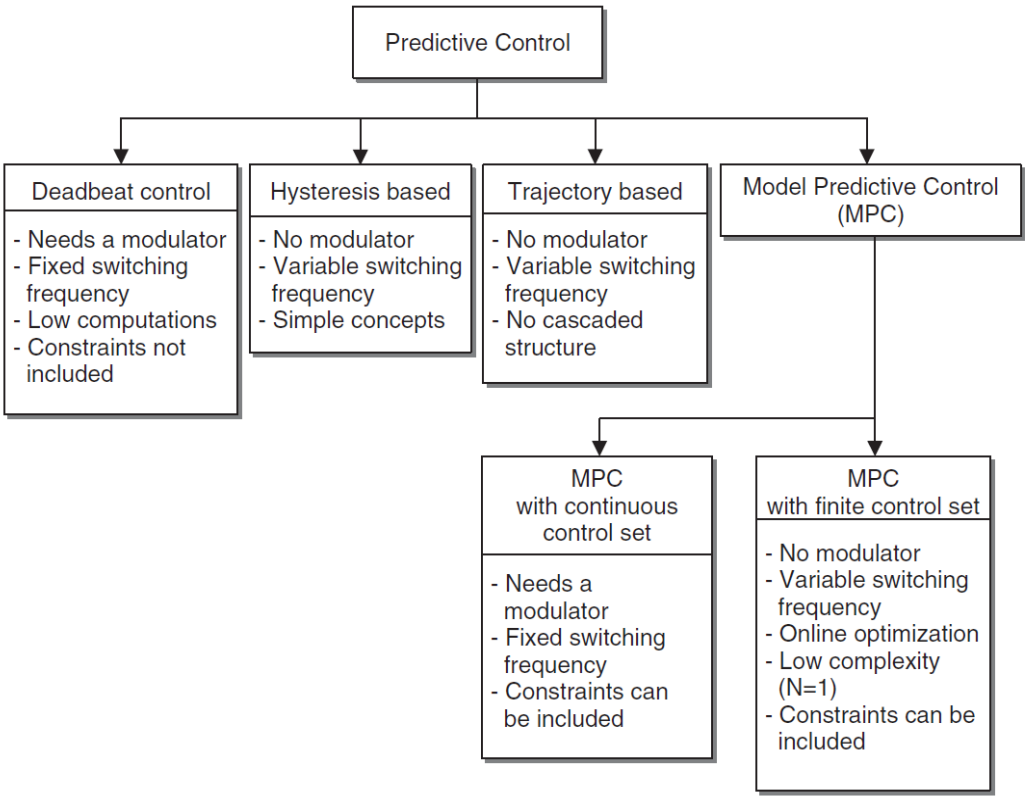

Figure 4-1 Classification of predictive control methods used in power electronics

Predictive control needs a model of the system to predict the future performance of the controlled variables, which means that a good model is needed and that the sensitivity to model should be tested. The controller uses this information to define the optimal actuating signal based on predefined optimization criteria. The optimization criterion can be, keeping the controlled variable within a boundary as in hysteresis-based predictive control [67]; or to force the controlled variable to follow some trajectory as in trajectory-based control [68], or to make the error equal to zero in the next sample as in deadbeat control [69], [70] ; or a more flexible optimization criterion that is used in model predictive control (MPC) which is expressed as a cost function that will be minimized [71].

The predictive control in previous classification is divided into two main categories. The first category needs a modulator to generate the PWM and in this case, the switching frequency will be fixed as in deadbeat control and MPC with continuous control set. In the second category, the switching signals can be directly generated for the converter and there are no needs for a modulator. This last strategy leads to a variable switching frequency.

The advantage of predictive control lie in its conceptual simplicity. Indeed, its implementation can be very simple for some method like deadbeat and finite control set MPC. But some implementations can also be more complex and need fast processing as in continuous control set. One very important point is that the system non-linearity can be included in the model and it does not require linearizing the model to tune the controller. This strategy can therefore be applied for all operating points with no modifications of the control parameters.

FCS-MPC does not need a modulator to generate the PWM, this means that the switching frequency is variable. However, when the switching frequency increases the switching losses increases as well. Some methods are proposed to minimize the switching frequency while requiring that the controlled variables follow their references [5], [66], [72]–[74]. Such methods like in [75] need a high computation time. Implementation of these algorithms in real time can be managed with off-line calculations and requires a sampling rate much higher than the switching frequency. In [22], [48], [76] authors propose a methodology to obtain a fixed switching frequency with direct power control.

This chapter has four sections. The first one presents the finite control set model predictive control (FCS-MPC) applied to power converters control and shows how to find the optimal switching vector ($SV\_optimal$) that leads to a minimum cost function. The second section explains how to generate FCS-MPC with fixed switching frequency by applying the general rules of sawtooth modulators to FCS-MPC. The next two sections deal with the use of FCS-MPC with fixed switching frequency to control interleaved multicell DC-DC Buck and Boost converters. In these structure FCS-MPC is used to control and balance the internal currents (branches' currents) and then to control the output voltage.

4.2. Finite control set MPC

As seen in the brief description of MPC in chapter 2, the main difference between Finite Control Set MPC (FCS-MPC) and continuous control MPC (CC-MPC) is that FCS-MPC has a finite number of input vectors. This involves less computational time and simplifies the implementation. This is obviously the case in Power Electronics applications where the number of power switches are finite and has only two states ON or OFF. For a power converter with S half-bridges and two states (*on-off*) the number of switching vectors are $N_{seq} = 2^S$. For example for a DC-DC buck converter with three branches for one-step prediction horizon ($H_p = 1$), there are eight different switching vectors from (000) to (111). For prediction horizon of more than one-step ($H_p > 1$) the number of switching vectors (N_{seq}) is given by equation (4-1). For example, for the same power converter with $H_p = 4$, the number of switching vectors will be $N_{seq} = 2^{4\times3} = 4096$. Therefore, the number of switching vectors increases exponentially with the number of switches and the size of the prediction horizon.

$$N_{seq} = 2^{H_p \times S} \qquad (4\text{-}1)$$

The FCS-MPC is evaluated at each time step, and applied at each time-step. This strategy leads

to a variable switching frequency. We can notice that there is no need for a PWM modulator in such controllers. In FCS-MPC, the maximum switching frequency will be the half of the sampling frequency (one sample on and one sample off) and there is no limit for the lower band frequency with this strategy. A variable switching frequency will affect the current and voltage ripples in a Power Converter and can leads to undesired resonance between some passive and filtering elements. That is the reason why, un-controlled switching frequencies are very often forbidden in Power Converters [77]

Figure 4-2 shows the FCS-MPC algorithm. At starting of the algorithm the optimal cost value (J_{star}) of the algorithm is initialized ($J_{star} = \infty$), and the weighting matrices ($\boldsymbol{g}, \boldsymbol{g_1}$) are defined. The weighting matrices $\boldsymbol{g}$ and $\boldsymbol{g_1}$ are used in the cost function to tradeoff between different objectives. Then, the currents in the converter's branches and the capacitors voltages are measured in order to identify the actual states. From these initial values, the cost function for each control sequence is evaluated in order to find the minimum one. This is done based on the following steps:

Counter (j) is a pointer that indicates the control sequence that has to be used in the calculation. This counter goes from 1 to N_{seq} where N_{seq} represents the number of sequences that can be applied on the prediction horizon

- Counter (n), is a pointer that indicates the actual step in the current calculation inside the prediction horizon. Indeed, the current is calculated step by step from the model over the prediction horizon using the previous current to calculate the next current. This counter goes from 1 to the end of the prediction horizon H_p
- The control vector at instance n of sequence j is applied to the state space model and the predicted currents on the prediction horizon are calculated
- The constraints on the output and on states variables are checked
    - If they are not satisfied, there are no need to continue the calculation, and the cost function is set to infinity for this control sequence j
    - If they are satisfied, the average value of each output and states as well as for example the maximum and minimum values along the prediction horizon ($n =$ 1 to H_p) are calculated.
- When the end of prediction horizon is reached ($n > H_p$), the cost function that is related to control sequence j is evaluated
- If cost function of sequence j is lower than the optimal one (J_{star}) this cost function replaces the previous one and the optimal index will be set to j
- Algorithm will continue for all possible control sequences (from $j = 1$ to $j = N_{seq}$)
- The next step (not shown in the flowchart) is to apply the entire sequence to the power converter and to repeat this algorithm at each switching instance

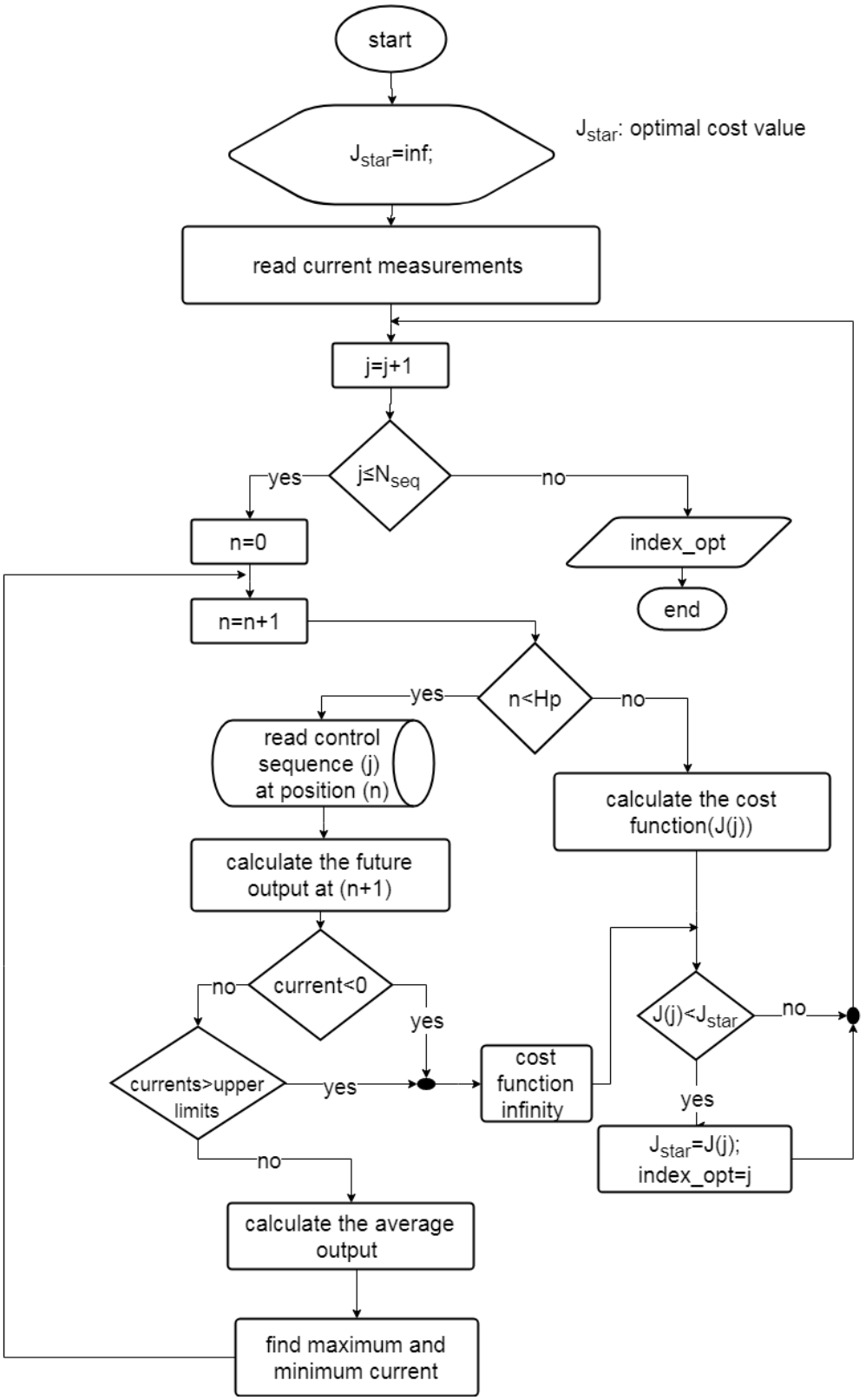

Figure 4-2 Flowchart of MPC algorithm

4.3. FCS-MPC with fixed switching frequency

The proposed methodology is inspired by classical Pulse Width Modulation (PWM) generation principles. To understand our proposal, we recall first the principle of interleaved PWM using sawtooth carriers.

4.3.1. PWM with sawtooth carriers

The principle of a PWM using a sawtooth carrier leads to one change from high to low during the switching period (T_{sw}) as shown in the Figure 4-3. When the reference value is greater than the carrier the PWM signal will be high until the reference value becomes lower than the carrier. By analogy, we define the time segment as the time period during which only one change from high to low or low to high is possible. In case of one carrier, the time segment is equal to the switching period (T_{sw}).

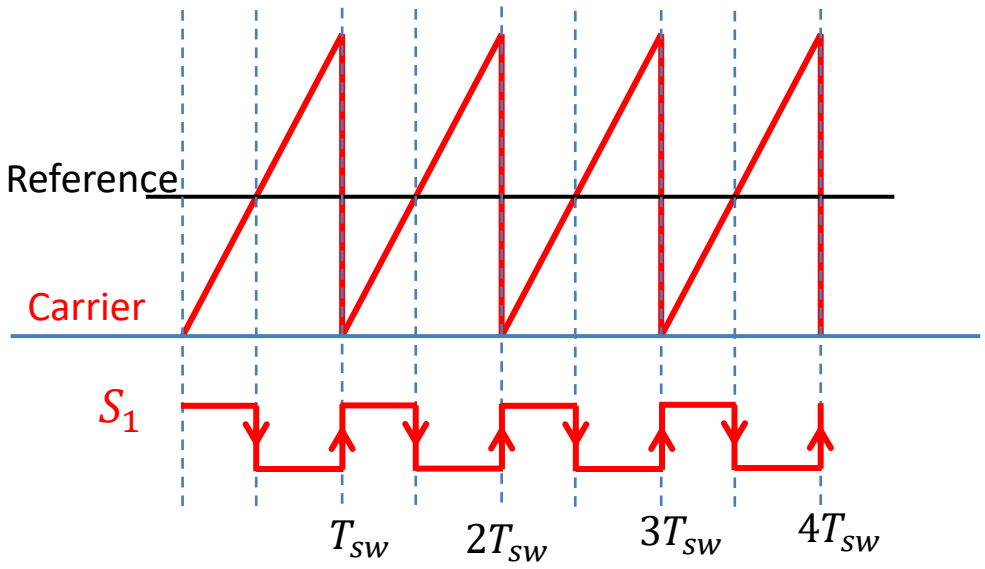

Figure 4-3 PWM with Sawtooth carrier

For several interleaved sawtooth carriers, the PWM modulator behavior will be different. The number of carrier (C_a) leads to a higher number of switching states (S) in a sawtooth period. For regular phase shifted carriers, we can define levels of the PWM modulator. The number of levels is equal to the number of carrier (three levels for three sawtooth carriers). The number of time segments during one switching period (one sawtooth period) for more than one sawtooth carrier is equal to the number of carriers (C_a). When the reference stays in the same level, there is only one switch state change in a time segment. This is no more true if the reference go from one level to another. The phase-shift angle, to be regular, can be calculated from the number of carriers (C_a):

$$\phi = \frac{2\pi}{C_a} \qquad (4\text{-}2)$$

Figure 4-4 shows the example of three sawtooth carriers defining three levels and three time

segments. The first PWM signal related to the first carrier (red) can change from high to low in the first time segment and the first level while the others PWMs remain low. This signal can also change from high to low in the second time segment for a reference located in the second level. Idem for segment three and level three. For the second PWM signal related to the second carrier (blue), the change from high to low arises respectively for the first segment and second level, the second segment and third level and the third segment and first level.

To obtain a fixed switching frequency with a regular phase shift the previous rules should be satisfied by any PWM generator.

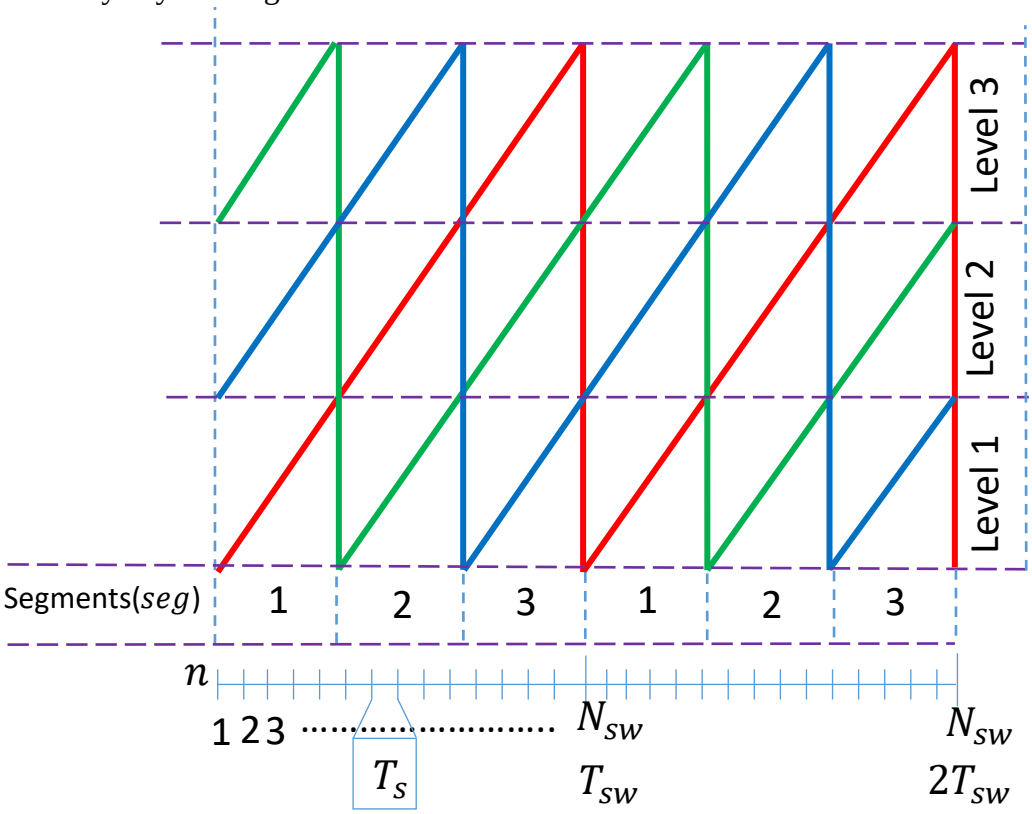

Figure 4-4 Three sawtooth carriers –two periods

4.3.2. Fixed switching frequency algorithm for FCS-MPC

The proposed idea for fixing the switching frequency is to apply the rules of sawtooth carriers to MPC. The switching period is divided in N_{sw} points with a constant time step equal to T_s. Index (n) is an internal pointer that indicates the position in the switching period. It varies from $n = 1$ to $n = N_{sw}$ as in Figure 4-4.

The proposed algorithm is presented in Figure 4-5. To obtain a fixed switching frequency in case of MPC algorithm, one can proceed as follow:

- The states of the power converter (currents and voltages) are measured or estimated at every switching instance ($k\ T_{sw}$)
- Switching vectors that match the PWM sawtooth carrier behavior are applied on the

prediction horizon (H_p: $H_p = N_{sw}$ in our study) to find the optimal switching vector among all this vectors collection.

- The optimal switching vector is applied to the power converter at each time position n.

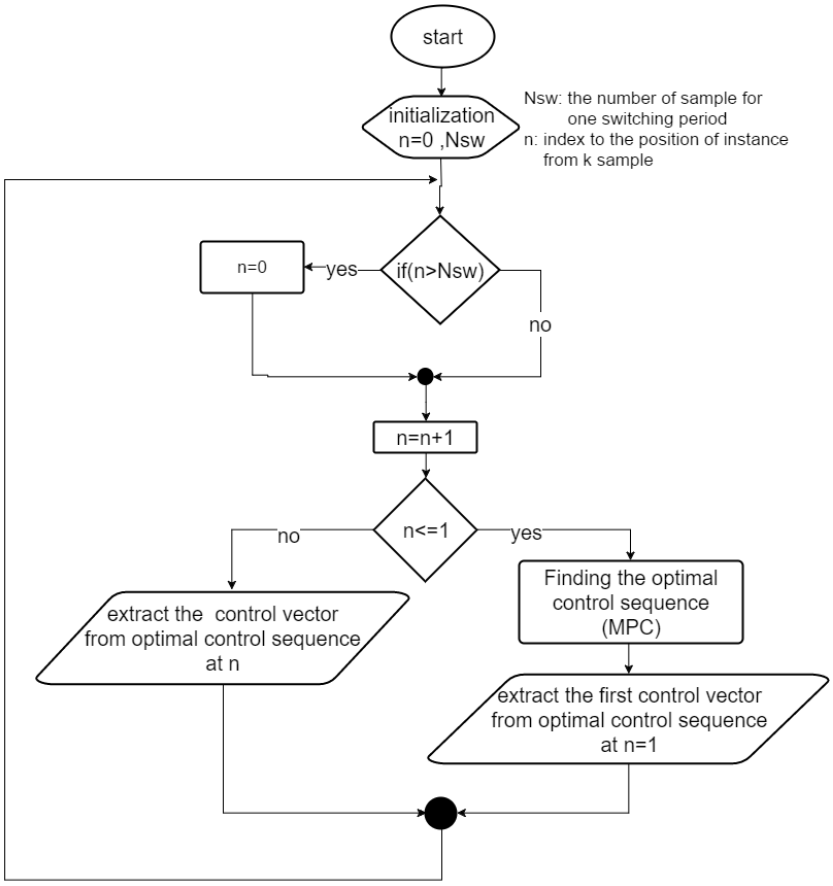

Figure 4-5 Flowchart for fixing the switching frequency

This methodology does not need a very high computational time compared to the methodology presented in [75]. In this algorithm measurements and estimations are done only one time per switching period T_{sw}.

The number of all possible switching vectors (N_{seq}) for $N_{sw} = 9$ and for 3 switching functions that can be in one of two states (a high state or a low state) is $N_{seq} = 2^{9\times3} = 134{,}217{,}728$. It is a huge number of possibilities which is not compatible with an on-line prediction realized at each switching time (T_{sw}). However, the number of switching sequences (N_{seq}) can be drastically reduced if we choose to implement an algorithm which imposed a sawtooth-like behavior.

There are two options to define the number of switching sequences (N_{seq}) that respect the behavior of PWM generated by sawtooth carriers.

1. First, the carrier level (level 1, 2 or 3 in our example) is defined at the beginning ($n = 1$) for all the switching period (for each carrier). In this case, the number of switching sequences N_{seq} is given by equation (4-3). For the same parameters as those of the

previous situation (N_{sw}= 9 and for 3 switching functions) the number of switching sequences is now N_{seq}= 1000 which is drastically lower than the number of all possible sequences.

$$N_{seq} = (N_{sw} + 1)^{Ca} \qquad (4\text{-}3)$$

Table 4-1 shows the set of possible switching vectors for three interleaved carriers along one switching period for all possible levels (3 levels) and for 9 sub-interval in the switching period $(N_{sw} = 9)$.

In this table, lines $S_{1,2,3}$ corresponds to the first level of the corresponding cell with duty cycles $(D_1, D_2\ or\ D_3)$ that can take only four values: $\left\{0; \frac{1}{9}; \frac{2}{9}; \frac{3}{9}\right\}$. Lines $S_{4,5,6}$ corresponds to the second level with 3 possible duty cycles, namely $\left\{\frac{4}{9}; \frac{5}{9}; \frac{6}{9}\right\}$ and lines $S_{7,8,9}$ are in the third level with also 3 possible duty cycles $\left\{\frac{7}{9}; \frac{8}{9}; 1\right\}$.

Table 4-1: Switching vectors satisfying the sawtooth carriers behavior

S	State of cell1									State of cell 2									State of cell 3									
	Seg_1 n= {1; 2; 3}			Seg_2 n= {4; 5; 6}			Seg_3 n= {7; 8; 9}			Seg_1 n= {1; 2; 3}			Seg_2 n= {4; 5; 6}			Seg_3 n= {7; 8; 9}			Seg_1 n= {1; 2; 3}			Seg_2 n= {4; 5; 6}			Seg_3 n= {7; 8; 9}			
0	0	0	0	0	0	0	0	0	0	0	0	0	0	0	0	0	0	0	0	0	0	0	0	0	0	0	0	
1	1	0	0	0	0	0	0	0	0	0	0	0	1	0	0	0	0	0	0	0	0	0	0	0	1	0	0	
2	1	1	0	0	0	0	0	0	0	0	0	0	1	1	0	0	0	0	0	0	0	0	0	0	1	1	0	Level 1
3	1	1	1	0	0	0	0	0	0	0	0	0	1	1	1	0	0	0	0	0	0	0	0	0	1	1	1	
4	1	1	1	1	0	0	0	0	0	0	0	0	1	1	1	1	0	0	1	0	0	0	0	0	1	1	1	
5	1	1	1	1	1	0	0	0	0	0	0	0	1	1	1	1	1	0	1	1	0	0	0	0	1	1	1	Level 2
6	1	1	1	1	1	1	0	0	0	0	0	0	1	1	1	1	1	1	1	1	1	0	0	0	1	1	1	
7	1	1	1	1	1	1	1	0	0	1	0	0	1	1	1	1	1	1	1	1	1	1	0	0	1	1	1	
8	1	1	1	1	1	1	1	1	0	1	1	0	1	1	1	1	1	1	1	1	1	1	1	0	1	1	1	Level 3
9	1	1	1	1	1	1	1	1	1	1	1	1	1	1	1	1	1	1	1	1	1	1	1	1	1	1	1	

We can note, for the vectors arrangement of table 4.1, that there is only one change of the cell states for each line along the switching period. Let us take an example:

- If line S_0 is chosen for Cell1, the successive states of the corresponding line will be played all other the switching period
- For Cell2, we can choose one line among the nine lines of table 4.1. As for the first cell, when the line is chosen, this line will be the same for the whole period
- For Cell3, it is exactly the same

As illustrated by Figure 4-6, the number of possible sequences is therefore $N_{seq} = 10 \times 10 \times 10 = 1000$ which is the same result than that of equation (4-3).

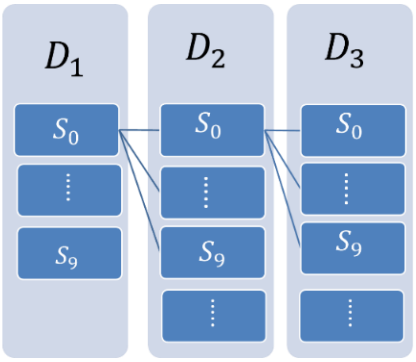

Figure 4-6 Illustration of possible sequences for 3 cells and one line (S) change per switching period

2. The carrier level can change at every time segment (seg) during the switching period (this mean three times for one switching period in our example). The number of switching sequences N_{seq} is given by equation (4-4). For N_{sw}= 9 and 3 switching functions, the number of switching sequences is now N_{seq} = 655360. This strategy has a much higher number of sequences and is not easy to implement on a FPGA.

$$N_{seq} = (N_{sw} + 1) \times \left(\frac{N_{sw}}{N_{seg}} + 1\right)^{C_a N_{seg} - 1} \qquad (4\text{-}4)$$

Where N_{seg} is the number of time segments.

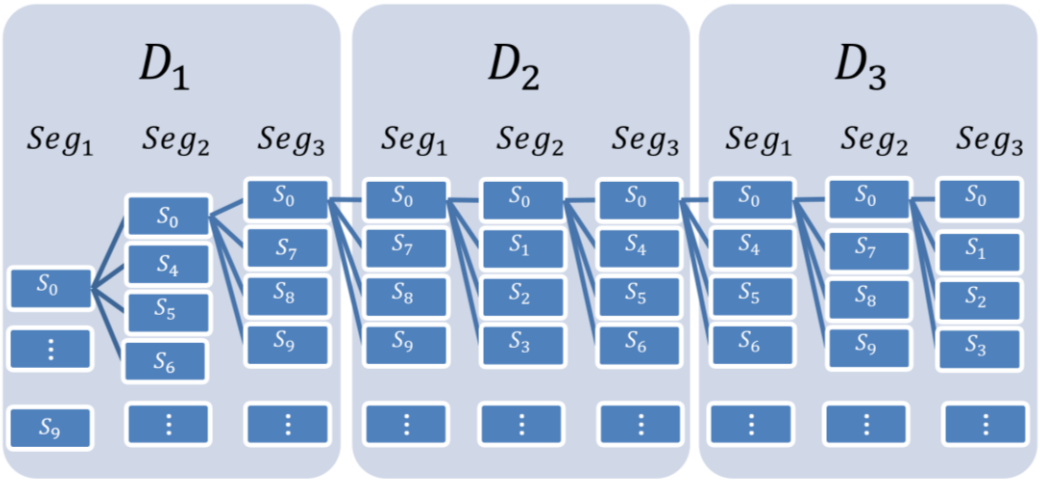

Figure 4-7 Illustration of possible sequences for 3 cells and 3 line (S) changes per switching period

In next sections, only solution 1 will be tested and implemented.

4.4. Model Predictive Control for multicell Buck Converter

4.4.1. Mathematical model of a 3-cells Buck converter

To predict the future output and states a discrete mathematical model is needed. The state-space model of the parallel multi-cell DC-DC buck converter derived from equation (3-8) with only a resistor as a load is:

$$\frac{d}{dt}\begin{bmatrix} i_1 \\ i_2 \\ i_3 \end{bmatrix} = -\begin{bmatrix} l & -m & -m \\ -m & l & -m \\ -m & -m & l \end{bmatrix}^{-1}\begin{bmatrix} r+r_L & r_L & r_L \\ r_L & r+r_L & r_L \\ r_L & r_L & r+r_L \end{bmatrix}\begin{bmatrix} i_1 \\ i_2 \\ i_3 \end{bmatrix} + \begin{bmatrix} l & -m & -m \\ -m & l & -m \\ -m & -m & l \end{bmatrix}^{-1}\left(\begin{bmatrix} S_1 \\ S_2 \\ S_3 \end{bmatrix} V_{dc}\right) \tag{4-5}$$

$$\dot{\boldsymbol{x}} = \boldsymbol{A}\boldsymbol{x} + \boldsymbol{B}\boldsymbol{u}$$
$$\boldsymbol{y}=\boldsymbol{C}\boldsymbol{x} \tag{4-6}$$

where:

$$\boldsymbol{A} = -\begin{bmatrix} l & -m & -m \\ -m & l & -m \\ -m & -m & l \end{bmatrix}^{-1}\begin{bmatrix} r+r_L & r_L & r_L \\ r_L & r+r_L & r_L \\ r_L & r_L & r+r_L \end{bmatrix}, \boldsymbol{B} = V_{dc}\begin{bmatrix} l & -m & -m \\ -m & l & -m \\ -m & -m & l \end{bmatrix}^{-1}$$

$$\boldsymbol{C} = \begin{bmatrix} 1 & 0 & 0 \\ 0 & 1 & 0 \\ 0 & 0 & 1 \end{bmatrix}, \quad \boldsymbol{x} = \begin{bmatrix} i_1 \\ i_2 \\ i_3 \end{bmatrix}, \boldsymbol{u} = \begin{bmatrix} S_1 \\ S_2 \\ S_3 \end{bmatrix}$$

and S_1, S_2, S_3 are the cell states. When $S_i = 1$ the output of $Cell_i$ is equal to V_{dc} and 0 otherwise.

The MPC controller needs a discrete space model to calculate the states and the outputs at the next sample $(k+1)$ time. To discretize the state space model, a simple Euler approximation [78] can be used. The small error due to this approximation over the switching period is compensated by measurements of states and outputs at the beginning of each switching period.

$$\dot{\boldsymbol{x}} \approx \frac{\boldsymbol{x}(n+1) - \boldsymbol{x}(n)}{T_s} \tag{4-7}$$

where T_s is the step time, $x(n+1)$ are the next predicted states values and $x(n)$ are the current states.
With Euler approximation, the discrete state space model of the converter is:

$$\boldsymbol{x}(n+1) = \boldsymbol{A}_d\boldsymbol{x}(n) + \boldsymbol{B}_d\boldsymbol{u}(n)$$
$$\boldsymbol{y} = \boldsymbol{C}_d\boldsymbol{x} \tag{4-8}$$

where matrices $\boldsymbol{A}_d$ and $\boldsymbol{B}_d$ are given in (4-9) and (4-10) respectively and $\boldsymbol{C}_d$ is the same as $\boldsymbol{C}$

$$\boldsymbol{A}_d = \boldsymbol{I}\boldsymbol{d}_{3x3} + T_s\boldsymbol{A} \tag{4-9}$$

$$\boldsymbol{B}_d = T_s\boldsymbol{B} \tag{4-10}$$

4.4.2. Current Control of multicell Buck converter

Figure 2-14 displays the proposed block diagram for MPC control of the 3 the currents of a 3 cells interleaved buck DC-DC converter. All currents are measured (these current are the states of the system as well as the controlled output) at each switching period defined by $t = k\,T_{sw}$. The previous model defined in equation (2-5) is used to calculate the currents at each step time T_s of the considered switching period. If the prediction horizon is chosen to be more than one switching period ($H_p > 1$), the model is used to calculate predicted currents at step $(n+1)$, $(n+2)$ and so on.

When all values are known, the cost function values are computed for all possible control sequences to find the optimal control vector. At the end the optimal control vectors (S) are applied to the real system.

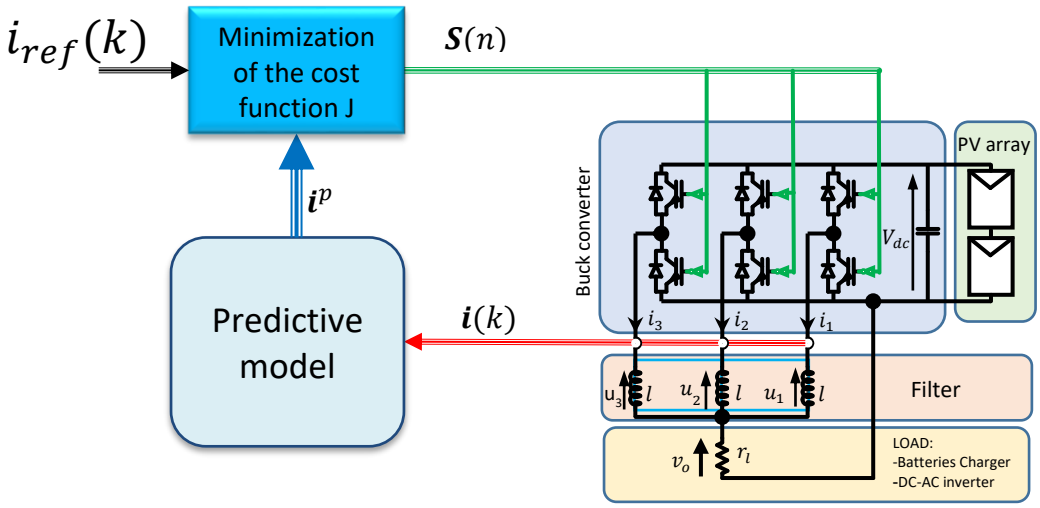

Figure 4-8 Block diagram of model predictive current control for interleaved multicell buck converter

4.4.2.1 Cost function for current control of Buck converter

The purpose of current control is to adapt and balance the currents flowing in the cells of the power converter (i_1, i_2, i_3 are shown in Figure 2-14). A quadratic form of the cost function is used as in equation (2-6). It consists of two parts: The role of the first part is to minimize the error on the mean value of the currents ($\boldsymbol{i_{av}}$) with respect to the references defined for the switching period (T_{sw}). The role of the second part is to minimize the maximum difference between the current references and the real currents along one switching period (T_{sw}).The weighting matrices $\boldsymbol{Q}$ and $\boldsymbol{g_1}$ are positive semi-definite matrices that can be used to tradeoff between the steady state error and the current ripple.

$$\begin{aligned} J = &\left(\boldsymbol{i}_{ref}(k) - \boldsymbol{i_{av}}(k)\right)' \boldsymbol{Q}\left(\boldsymbol{i}_{ref}(k) - \boldsymbol{i_{av}}(k)\right) \\ &+ \left(\boldsymbol{i}_{ref}(k) - \boldsymbol{i}_{max}(k)\right)' \boldsymbol{g_1}\left(\boldsymbol{i}_{ref}(k) - \boldsymbol{i}_{max}(k)\right) \\ &+ \left(\boldsymbol{i}_{ref}(k) - \boldsymbol{i}_{min}(k)\right)' \boldsymbol{g_1}\left(\boldsymbol{i}_{ref}(k) - \boldsymbol{i}_{min}(k)\right) \end{aligned} \qquad (4\text{-}11)$$

4.4.2.2 FCS-MPC for current control of Buck converter

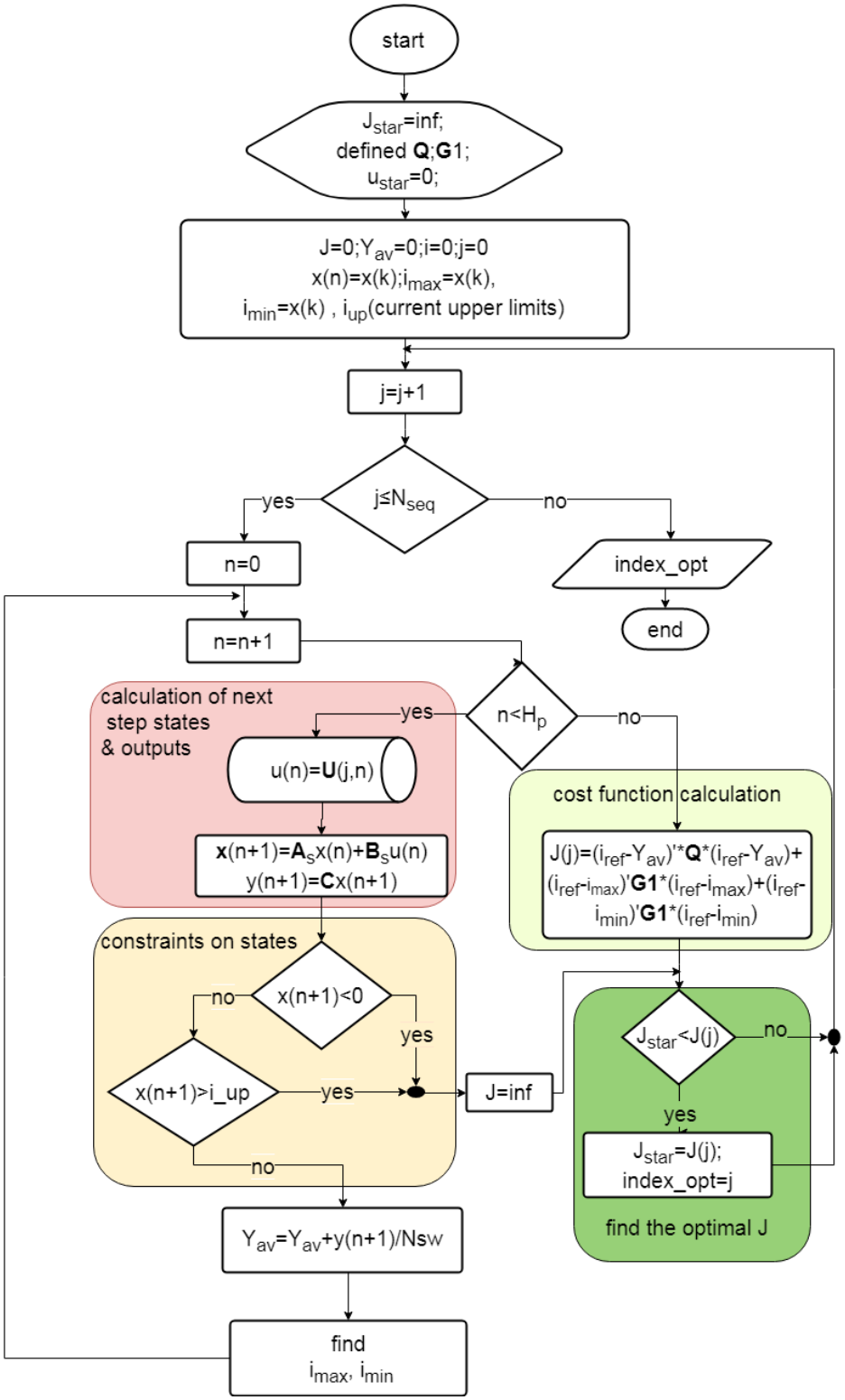

Figure 4-9 Flowchart of MPC :current control of multicell interleaved Buck DC-DC converter

The FCS-MPC algorithm aimed to find the optimal control sequence which minimizes the cost function depending on the dynamics of the system and the defined constraints on the currents (for example here to prohibit the currents to be higher than the values given in vector $\boldsymbol{i}_{up}$). This means to find the solution of (4-12)

$$\min_{u} \boldsymbol{J}$$

subjected to:

$$\begin{aligned} &\boldsymbol{x}(n+1) = \boldsymbol{A}_d \boldsymbol{x}(n) + \boldsymbol{B}_d \boldsymbol{u}(n) \\ &\boldsymbol{y}(n) = \boldsymbol{C}\, \boldsymbol{x}(n) \\ &\boldsymbol{0} \leq \boldsymbol{x}(n+1) \leq \boldsymbol{i}_{up} \\ &\boldsymbol{u} = [S_1, S_2, S_3]' \quad \text{with} \quad S_i = \{0\,;1\} \end{aligned} \qquad \textit{(4-12)}$$

The fixed switching period FCS-MPC algorithms dedicated to currents control of the multi-cell buck converter is depicted in Figure 4-9.

It first starts with the measurements of all states(currents) at $k\ T_{sw}$. Then, all possible switching vectors among the 1000 possibilities defined previously are applied to the model in order to calculate current mean values and their intermediate values along the switching period (N_{sw} evaluations). If one of this value do not meet the constraints, the cost function is set to infinity, and the next sequence is evaluated. When all sequences has been applied, each giving the corresponding average values of the currents as well as the maximum and minimum values reached over the switching period, the cost function is calculated. The sequence corresponding to the minimum cost function is pointed out by the index called "index_opt". Then, the controller apply this switching vector at each step n of the switching period until the end of the control sequence (Figure 4-5). This procedure is repeated for all switching periods.

4.4.2.3 Simulation results

All the following simulations are done with parameters in Table 2

Table 2 Simulation parameters for the 3-cell buck converter

Symbol	Quantity	Value
V_{dc}	The input voltage of buck converter	150 V
l	ICT inductance	15.4 mH
m	ICT mutual inductance	-7 mH
r	ICT resistance	5.36 Ω
r_l	Load resistance	5 Ω
i_{up}	Current upper limits	10 A
T_s	Sampling time	5 µS
T_{sw}	Switching time	45 µS
N_{sw}	Number of sample per switching time	9
C_a	Number of carrier	3
N_{seq}	Number of switching vectors	1000

(1) Common mode –uncoupled system

This trial is done to verify that the proposed method leads to obtain a fixed switching frequency as well as the interleaving of the PWM of the 3 cells. The simulation is done here for uncoupled inductance (no mutual inductance $m = 0$). In this situation, the current waveforms are independent, triangular and regularly interleaved. Figure 4-10 shows the current response with MPC controller for this uncoupled system while the reference are the same for each current. We can see in Figure 4-10-a that the currents follow their references with a high dynamic and no overshoot. Figure 4-10-b shows the phase shift of the three currents.

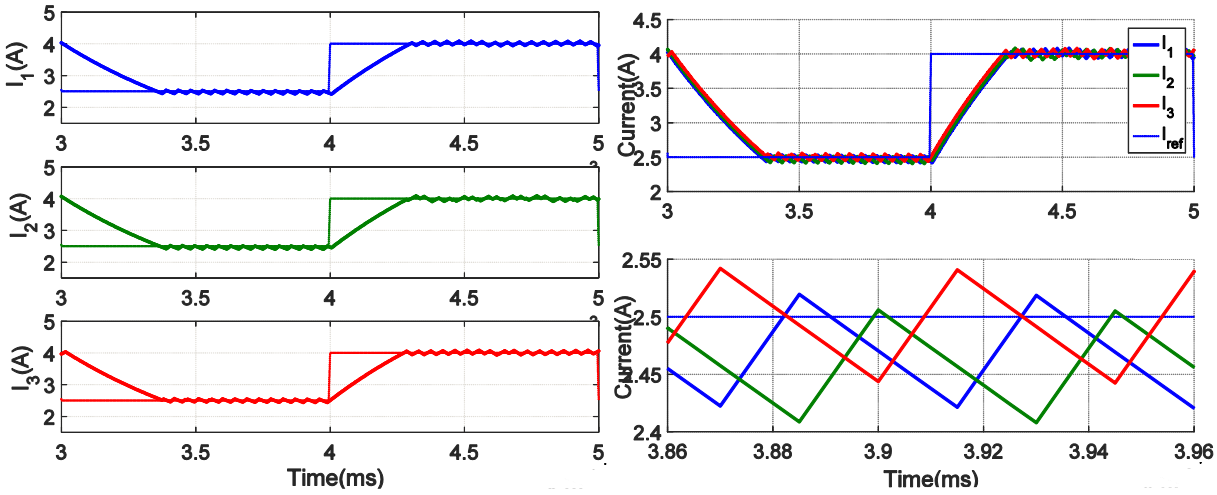

(a) (b)

Figure 4-10 Simulation result of Buck converter-MPC-Current response: common mode uncoupled system

Figure 4-11 shows the commands (S_1, S_2 and S_3) of the three cells. The switching period is divided in three time segments (Seg_1, Seg_2, Seg_3) and each time segment is divided in three sub-interval. The total number of points in one switching period is here equal to nine ($N_{sw} = 9$).

In this figure duty cycles of *Cell1*, *Cell2* and *Cell3* are $D_1 = 3/9$, $D_2 = 3/9$ and $D_3 = 3/9$ but S_1, S_2 and S_3 states change in different segment leading to a regular phase shift of 120°.

To verify that the switching frequency is constant, we perform an analysis of the spectral content of the currents. Figure 4-12-a shows a *hamming window FFT* of the first current for which the DC component has been removed. Figure 4-12b displays the half positive of this FFT. We can see that the fundamental frequency is 22 kHz equal to the designed switching frequency (4-13) with $T_{sw} = 45\mu s$.

$$F_{sw} = 1/T_{sw} \qquad (4\text{-}13)$$

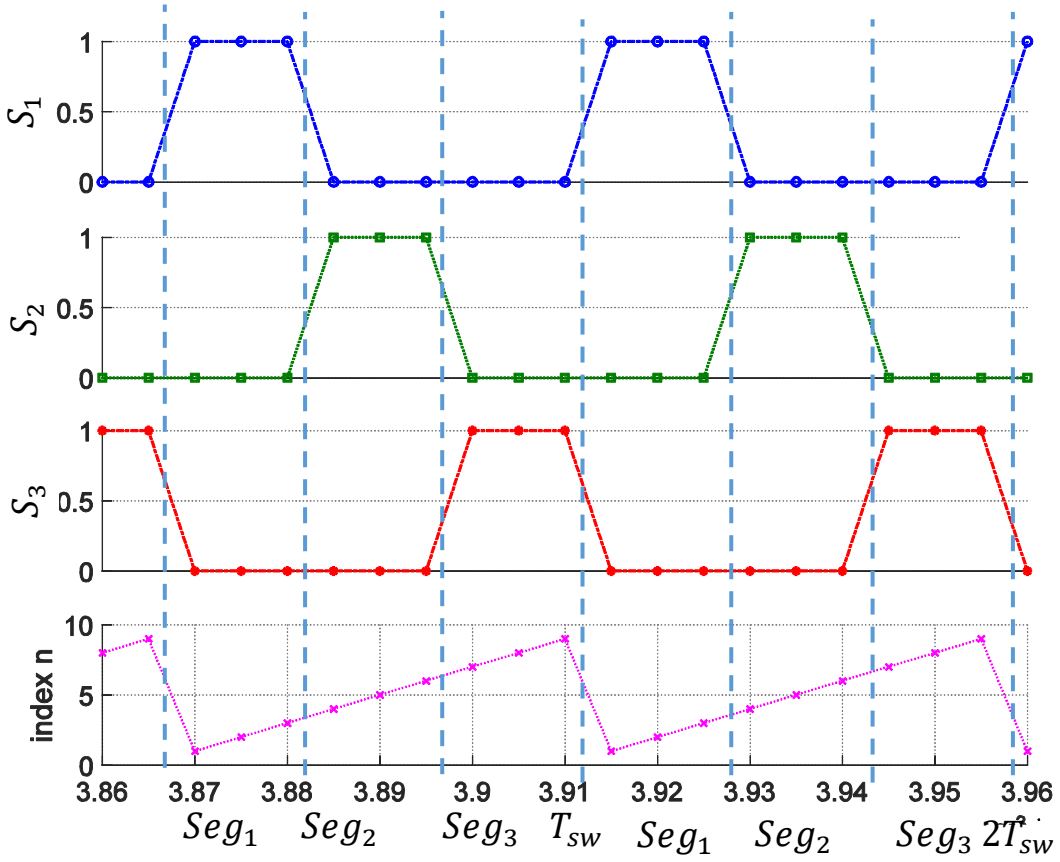

Figure 4-11 Command applied to each cell in steady state

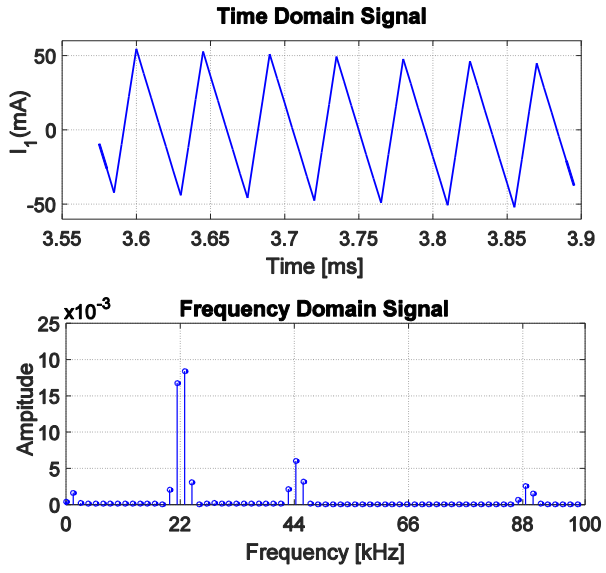

Figure 4-12 Current in Cell1 for a magnetically uncoupled system :(a) Time domain (b) Frequency domain

(2) Common mode response of the magnetically coupled system

For this trial, all current references have a similar 500 Hz square waveform with a 2A low level and a 4A high level. Figure 4-13 shows the currents in the three cells of the converter. When the current references are the same, the currents follow their references. The rising and falling times are very fast around 100µs. Note that there is an overshoot when the currents go from low to high level as shown in Figure 4-13-a, this phenomenon is attributable to the magnetic coupling between the cells of the power converter. A zoom on the currents behavior during steady state is shown in Figure 4-13-b. We can see here that the 3 currents do not show the interleaved behavior encountered previously. This is a pretty classic result for a multi-cell interleaved buck converter equipped with coupled output inductors. Nevertheless, a high ripple can be observed at the switching frequency and lower whereas such ripple is reduced to a lower value for classical interleaved strategies. This phenomenon is due to the low number of possible duty-cycles in this simulation and configuration (only 9 possible duty-cycles).

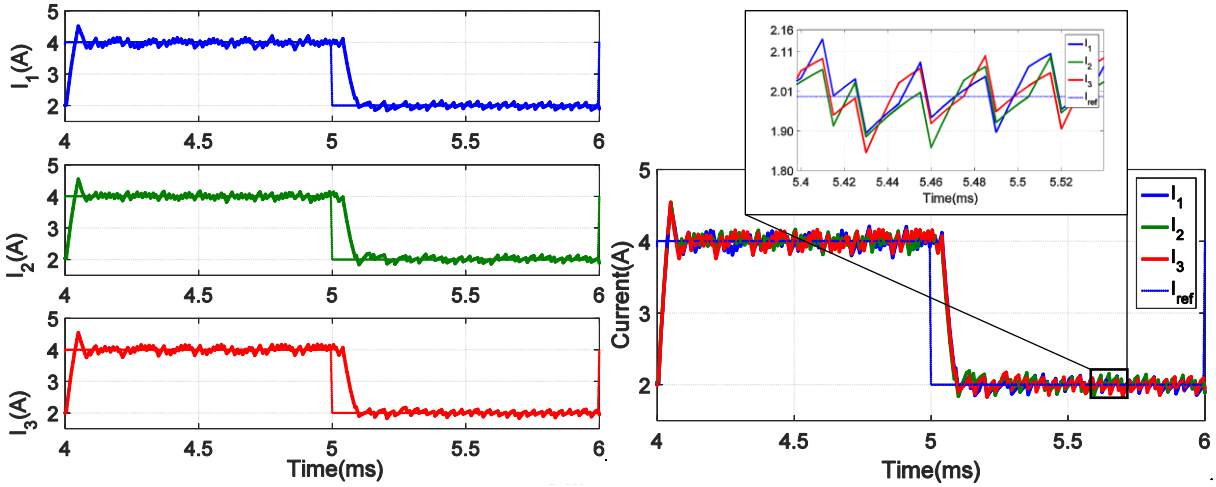

(a) (b)

Figure 4-13 Simulation results: Buck converter-MPC-Current response for common mode

This low frequency oscillation can be observed in Figure 4-14. In the first switching period the duty cycles of S_1, S_2 *and* S_3 are $D_1 = 8/9$, $D_2 = 2/9$ and $D_3 = 4/9$ while in the second switching period, the duty cycles are different $D_1 = 2/9$, $D_2 = 5/9$ and $D_3 = 8/9$.

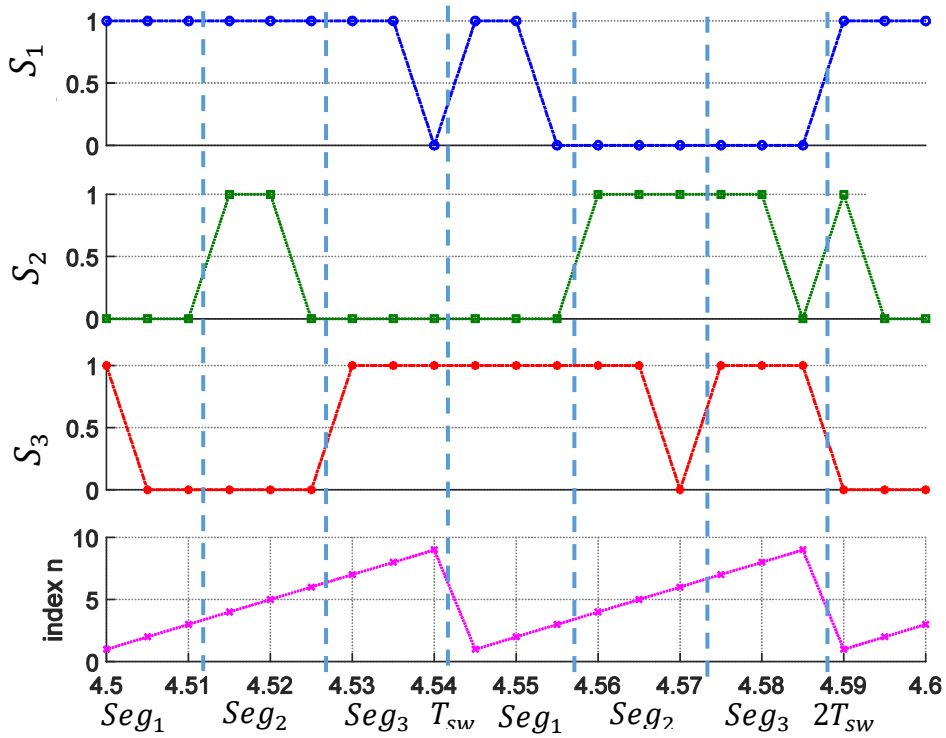

Figure 4-14 Command applied to each cell in steady state

(3) Differential mode response of the magnetically coupled system

Figure 4-15 shows the results while differential references are applied. The first current reference shows a $2/3$A magnitude square waveform while the two others are in opposite phase with a $1/3$A magnitude. We can see in this situation that the currents have the same dynamic but they are slower than previously when common mode references were applied. We can also note, because of the slower response in this mode, that there is no overshoot.

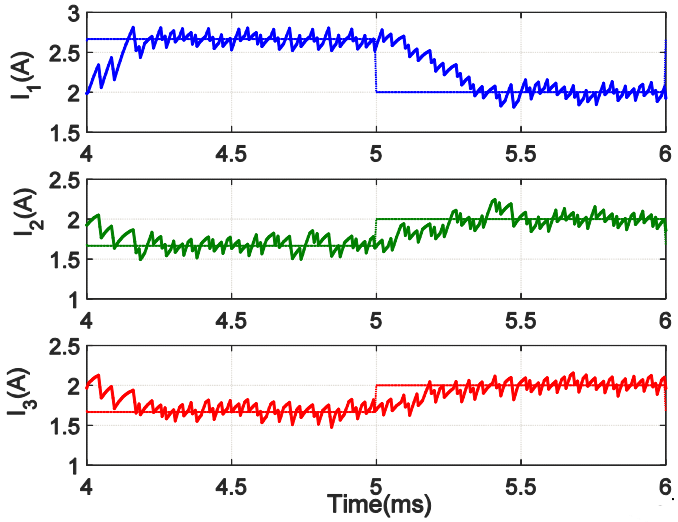

Figure 4-15 Simulation results: Buck converter-MPC-Current response for differential mode

(4) Single current step input of the magnetically coupled system

Finally, Figure 4-16 shows the simulation of the proposed current control while only one current reference change from 2A to 3A. We can see on the current responses that MPC control is able to manage the coupling effect between the cells. Indeed, effects on Cell2 and Cell3 are almost vanished after less than 250 µs.

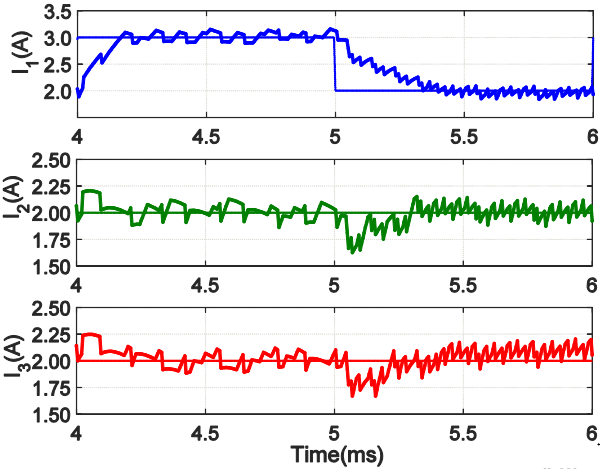

Figure 4-16 Simulation results: Buck converter-MPC-Current response in case of single current step

(5) Constraints on currents

MPC converts hard constraints to violation penalties. There is no need to add extra algorithms to manage saturation of some part of the controller (anti-wind up). It gives the optimal control value by minimizing the cost function while respecting the constraints on the states, output and control input. In the designed MPC controller, the implemented constraints defined two limits for the currents: the currents can't be negative (***i>0***) and must be lower than a defined value (***i<i_up***). Figure 4-17 shows the waveforms when the upper currents limit (here 3A) is reached while the references are 4A. We can see that MPC violations penalties are effective as no current go over 3A.

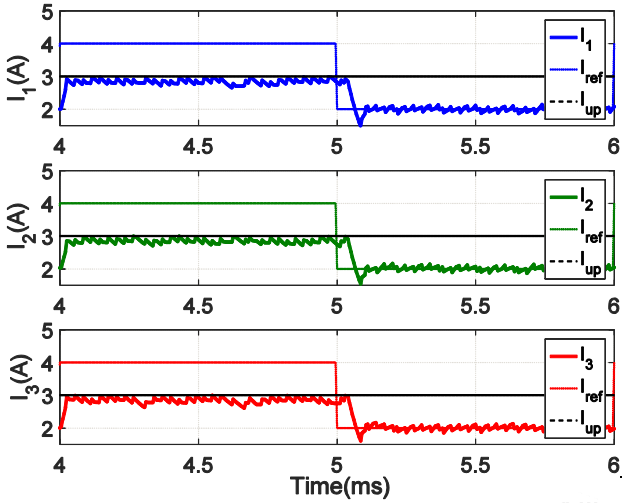

Figure 4-17 Simulation results: Buck converter-MPC-Current response with current saturation in common mode

(6) Sensitivity analysis

MPC is an advanced method of process control based on the knowledge of the system model. The sensitivity analysis of the system model for model predictive control must be done. In our system, variations of the load and the magnetic filtering device parameters (self-inductance and mutual inductance) may be critical.

a) Sensitivity due to changes of load

Regarding the load variation, the sensitivity of MPC controller is tested for three different load values, namely $r_l = 10\ \Omega$, $r_l = 2.5\ \Omega$ and short circuit $r_l = 0\ \Omega$ while the internal model used in MPC is unchanged ($r_l = 5\ \Omega$). Figure 4-20 shows the results. The main conclusion from these simulations is that the system remains stable even for such large variations of the model. We can note that MPC controller is able to control the current in short-circuit and that the current is closed to the reference even for this extreme condition. We can also remark that there is a DC shift when the load change and that the currents are higher than the reference when the load decreases, and lower when the load increases.

FCS-MPC is sensitive to the value of the load, but this sensitivity do not lead to instability but involves steady state error. If necessary, to overcome this sensitivity there is a simple solution, which is to build an observer to estimate the real value of the load.

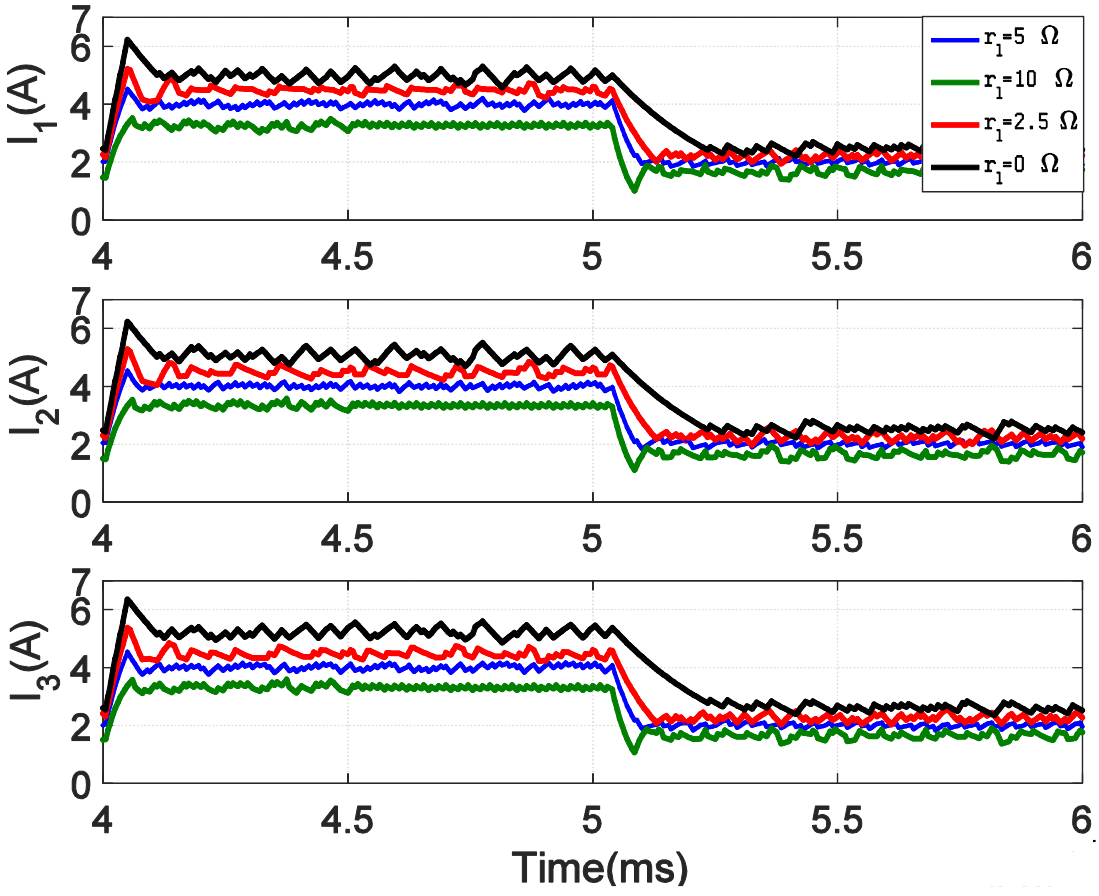

Figure 4-18 Simulation results: Buck converter-MPC-Current response ; Sensitivity to load variations

b) Sensitivity to the magnetic filtering device parameters

The self-inductance and mutual inductance of the output filtering device are among the main parameters of the studied converter and they greatly influence its dynamic as shown in equation (4-5). As these parameters are often badly defined (large tolerance of material permeability and dispersion of parameters in handmade inductors), the sensitivity to these parameters is important to be tested. In the following study, the values of inductances ($l = 15.4$ mH and $m = -7$ mH defined in Table 2) used in the MPC prediction model are not modified while the real values will be changed in the buck converter. Three configurations are tested, namely 120% ,80% and 70% of the MPC model self and mutual inductance ($l = 18.48$ mH - $m = -8.4$ mH , $l = 12.32$ mH and $m = -5.6$ mH and $l = 10.78$ mH and $m = -4.9$ mH).

Figure 4-19 shows the corresponding results. In these simulations, we can see that the system remains stable and that the cell-currents follow their references. We can also note that the system is more damped (the green dashed line) when inductances increase and vice versa (the red and black lines) when they decrease. So, the system dynamic is slightly changed but logically, no errors appear in steady state. We can therefore conclude that MPC has a low sensitivity to inductances variations.

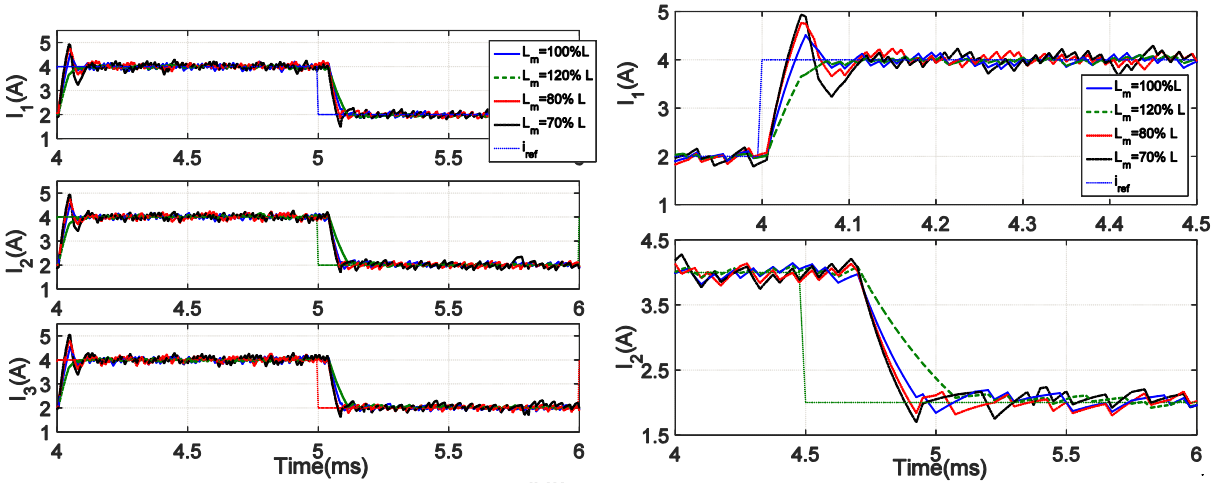

Figure 4-19 Simulation result: Buck converter-MPC-Current response; Sensitivity to change in the self-inductance and mutual inductance

4.4.3. Voltage Control of multicell Buck converter

When the load of power converter is a resistive load not associated to an output capacitor, it is not possible to control the output voltage of the interleaved multicell DC-DC converter with two control loops (a current loop and a voltage loop), because the dynamic of the inner loop (current control) is closed to that of the outer loop (voltage control) as shown in equation (4-14). The best way to do such control in this situation is to control the output voltage within a one control loop.

$$v_o = i_o r_l = (i_1 + i_2 + i_3) r_l \qquad (4\text{-}14)$$

The buck converter with three branches has three control inputs (D_1,D_2 and D_3). To control

the output voltage, there are two control inputs more than needed. To reduce the degree of freedom, two other outputs are added to the problem. These two outputs are the difference between the current of first and second branches ($i_1 - i_2$) and the difference between currents of the first and the third branches ($i_1 - i_3$) respectively. Controlling these values lead to control current balancing in the structure.

Here, FCS-MPC is used to control the output voltage to follow a specific trajectory and the other two outputs to be zero.

Equations of the system are the same than that defined in equation (2-5), except the output matrix $\boldsymbol{C}$ which is now:

$$\boldsymbol{C} = \begin{bmatrix} r_l & r_l & r_l \\ 1 & -1 & 0 \\ 1 & 0 & -1 \end{bmatrix} \qquad (4\text{-}15)$$

The first raw corresponds to the output voltage, the second to the current difference between the first and the second cells ($i_1 - i_2$) and the last raw to the current difference between the first and the third cells ($i_1 - i_3$).

MPC algorithm is the same as previously except for the cost function which must now integrate the constraints on the voltage.

4.4.3.1 Cost function for voltage control of Buck converter

The cost function has a quadratic form as in equation (4-16). As previously, the role of the first part is to minimize the error on the mean values defined by the references, namely the required average output voltage and zero for the current differences. The role of the second part is to minimize the maximum difference between the voltage reference and the real voltage along the switching period (T_{sw}).

$$J = \left([\boldsymbol{v}_{ref}\ 0\ \ 0]' - \boldsymbol{Y_{av}}\right)'\boldsymbol{Q}\left([\boldsymbol{v}_{ref}\ 0\ \ 0]' - \boldsymbol{Y_{av}}\right) + \left(\boldsymbol{v}_{ref} - \boldsymbol{v}_{max}\right)'\boldsymbol{g_1}\left(\boldsymbol{v}_{ref} - \boldsymbol{v}_{max}\right) + \left(\boldsymbol{v}_{ref} - \boldsymbol{v}_{min}\right)'\boldsymbol{g_1}\left(\boldsymbol{v}_{ref} - \boldsymbol{v}_{min}\right) \qquad (4\text{-}16)$$

4.4.3.2 Simulation results

Figure 4-20 shows the Simulink model of FCS-MPC dedicated to voltage control of the multicell buck converter. The block named "*buck converter*" is a discrete state space model of the interleaved multicell DC-DC converter. The block input is the switching sequence to apply to the three cells and its output is the three output currents. The green block "*MPC_Voltage*" is a Matlab function that contains the algorithm of FCS-MPC. Inputs of the FCS-MPC function are the currents limitations, the real currents differences, the converter output voltage and the three references which are the voltage reference and zero for the two current differences.

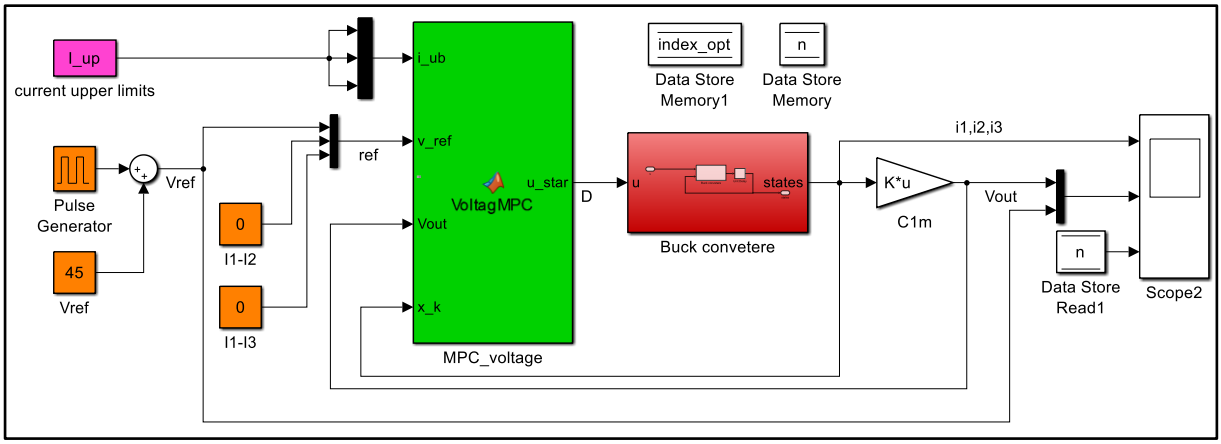

Figure 4-20 Simulink model of FCS-MPC –Voltage control

Figure 4-21 shows results for this voltage control configuration. In Figure 4-21-a we can see the controlled outputs. We can note that the output voltage is controlled and fluctuate around its reference with some variations due to the ripples of the currents. Furthermore, the change of the output voltage from high to low and vice versa is very fast as the currents do in common mode of the previous study. The other two outputs ($(i_1 - i_2)$ and $(i_1 - i_3)$) have an average close to zero, this means that currents of the power converter are balanced as shown in Figure 4-21b.

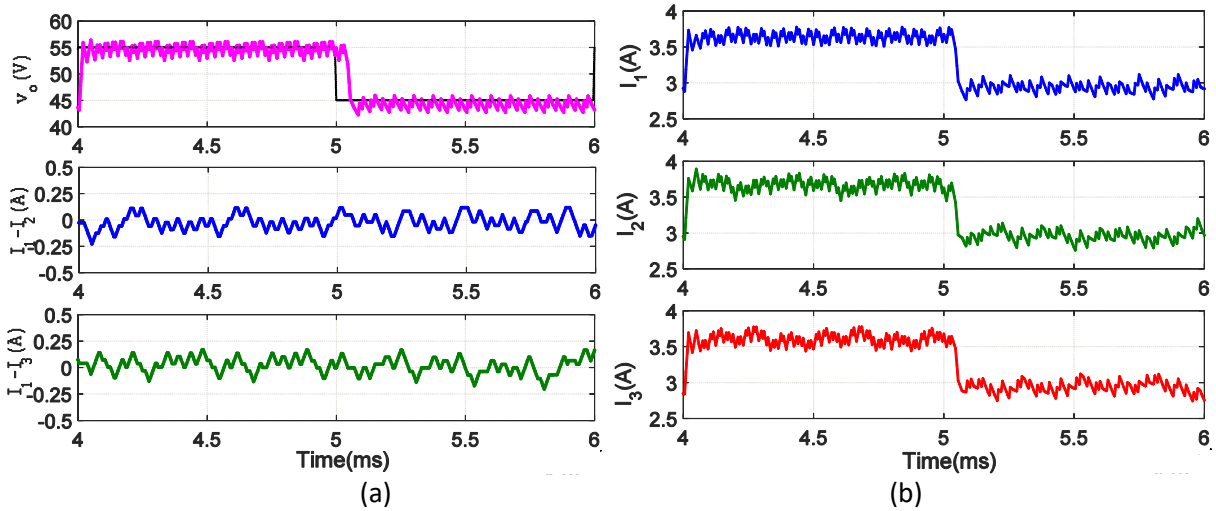

Figure 4-21 Simulation result: Control of the buck converter output voltage (a)Outputs response (b) Current response

4.5. Model Predictive Control for multicell Boost converter

Figure 4-22 shows the schematic of an interleaved multicell boost converter in parallel connection. Such converter can be used for many applications when output voltage higher than the input one is needed. We can find such converter as a first stage connected to a battery for example

or in some solar applications. The load might be very different depending on the application but we can say that this load is always connected in parallel with the output capacitor of the converter.

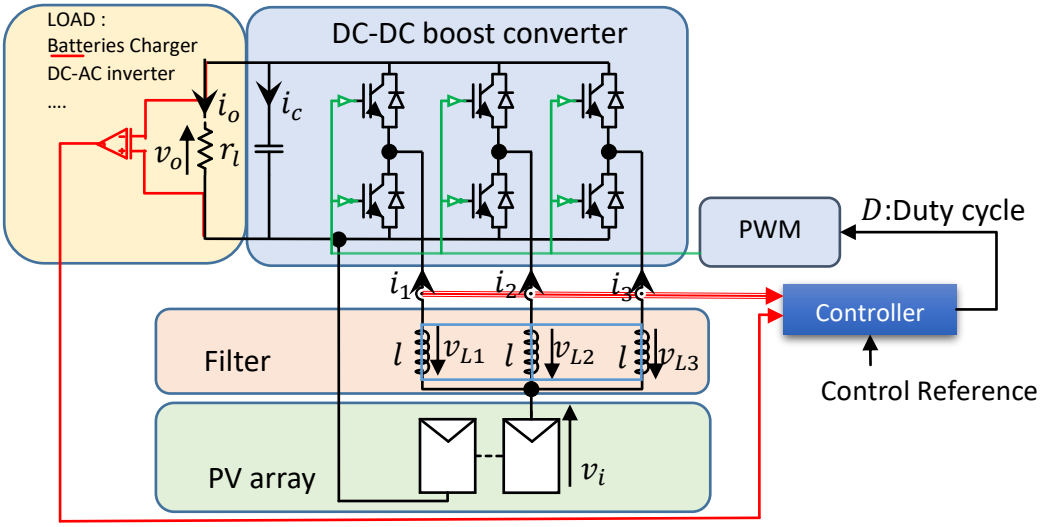

Figure 4-22 Interleaved Multicell Boost converter in parallel connection

4.5.1. Mathematical Modeling of multicell boost converter

Figure 4-23 shows the equivalent average model of the interleaved multicell DC-DC boost converter. This model uses two controlled sources. The first one is a voltage source which value is the product of the output capacitor voltage and the duty cycle of the cell. The second source is a current source equal to the product of current in the input inductor and the duty cycle.

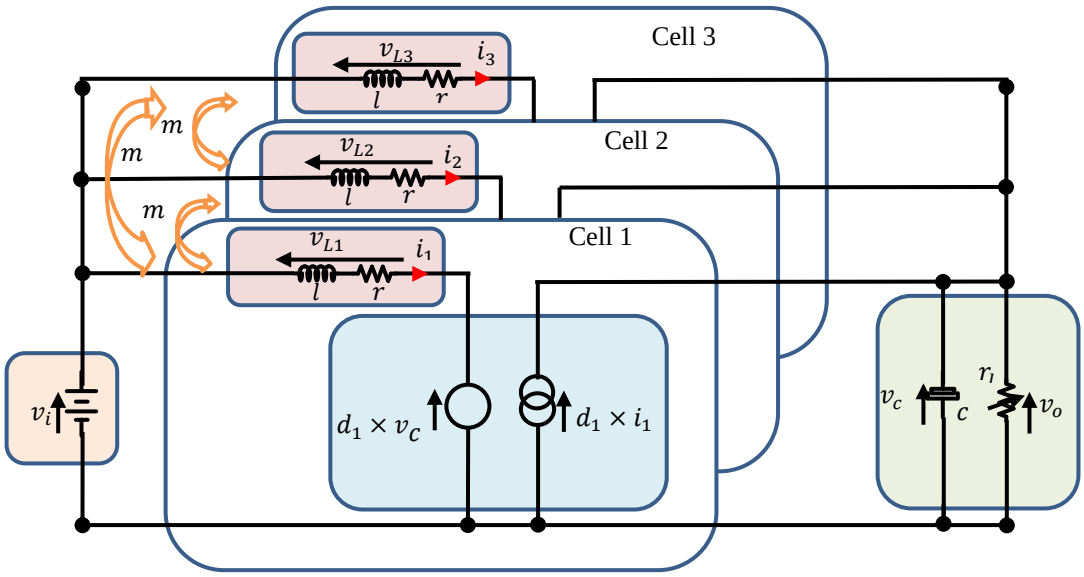

Figure 4-23 Equivalent average model of the interleaved multicell DC-DC boost converter

The state equation corresponding to this average equivalent model is:

$$l\frac{di_1}{dt} - m\frac{di_2}{dt} - m\frac{di_3}{dt} = v_i - d_1 v_c - i_1 r \qquad (4\text{-}17)$$

$$l\frac{di_2}{dt} - m\frac{di_1}{dt} - m\frac{di_3}{dt} = v_i - d_2 v_c - i_2 r \qquad (4\text{-}18)$$

$$l\frac{di_3}{dt} - m\frac{di_1}{dt} - m\frac{di_2}{dt} = v_i - d_3 v_c - i_3 r \qquad (4\text{-}19)$$

$$c\frac{dv_c}{dt} = d_1 i_1 + d_2 i_2 + d_3 i_3 - \frac{v_o}{r_l} \qquad (4\text{-}20)$$

The previous equations can be written in a matrix form:

$$\frac{d}{dt}\begin{bmatrix} i_1 \\ i_2 \\ i_3 \\ v_c \end{bmatrix} = \boldsymbol{L_n^{-1}} \begin{bmatrix} -r & 0 & 0 & -d_1 \\ 0 & -r & 0 & -d_2 \\ 0 & 0 & -r & -d_3 \\ d_1 & d_2 & d_3 & -\frac{1}{r_l} \end{bmatrix} \begin{bmatrix} i_1 \\ i_2 \\ i_3 \\ v_c \end{bmatrix} + \boldsymbol{L_n^{-1}} \begin{bmatrix} 1 \\ 1 \\ 1 \\ 0 \end{bmatrix} v_i \qquad (4\text{-}21)$$

Where:

$$L_n = \begin{bmatrix} l & -m & -m & 0 \\ -m & l & -m & 0 \\ -m & -m & l & 0 \\ 0 & 0 & 0 & c \end{bmatrix}$$

The system described in equation (4-21) is nonlinear as the control inputs d_i appear in matrix A_s as defined below in (4-22)

$$\dot{\boldsymbol{x}} = \boldsymbol{A}\boldsymbol{x} + \boldsymbol{B}\boldsymbol{u}_d \qquad (4\text{-}22)$$

Where:

$$\boldsymbol{A} = \boldsymbol{L_n^{-1}} \begin{bmatrix} -r & 0 & 0 & -d_1 \\ 0 & -r & 0 & -d_2 \\ 0 & 0 & -r & -d_3 \\ d_1 & d_2 & d_3 & -\frac{1}{r_l} \end{bmatrix}, \boldsymbol{B} = \boldsymbol{L_n^{-1}} \begin{bmatrix} 1 \\ 1 \\ 1 \\ 0 \end{bmatrix}, \boldsymbol{u}_d = v_i, \boldsymbol{x} = \begin{bmatrix} i_1 \\ i_2 \\ i_3 \\ v_c \end{bmatrix}$$

It is also possible to write the state equations which correspond to the different switching configurations of the power converter. For the boost converter with three cells, the number of switching configurations is 8. The state equations are then identical to that of (4-22) but $\boldsymbol{A}$ is now defined as a function of the switching state of each cell:

$$\boldsymbol{A} = \boldsymbol{L_n^{-1}} \begin{bmatrix} -r & 0 & 0 & -S_1 \\ 0 & -r & 0 & -S_2 \\ 0 & 0 & -r & -S_3 \\ S_1 & S_2 & S_3 & -\frac{1}{r_l} \end{bmatrix} \text{ with } S_i = \{0\,;\,1\}$$

So, there are eight linear dynamic equations for the 3-Cell boost converter. Table 3 shows all possibilities. By applying the switching vectors given in Table 3 to $\boldsymbol{A}$ we can define 8 matrixes A_s as shown from (4-23) to (4-30).

Table 3 Switching vector for multicell boost converter

S	Switching vector $[S_3\ S_2\ S_3]$
0	000
1	001
2	010
3	011
4	100
5	101
6	110
7	111

$$\boldsymbol{A_0 = L_n^{-1}}\begin{bmatrix} -r & 0 & 0 & 0 \\ 0 & -r & 0 & 0 \\ 0 & 0 & -r & 0 \\ 0 & 0 & 0 & -\frac{1}{r_l} \end{bmatrix} \quad (4\text{-}23)$$

$$\boldsymbol{A_1 = L_n^{-1}}\begin{bmatrix} -r & 0 & 0 & -1 \\ 0 & -r & 0 & 0 \\ 0 & 0 & -r & 0 \\ 1 & 0 & 0 & -\frac{1}{r_l} \end{bmatrix} \quad (4\text{-}24)$$

$$\boldsymbol{A_2 = L_n^{-1}}\begin{bmatrix} -r & 0 & 0 & 0 \\ 0 & -r & 0 & -1 \\ 0 & 0 & -r & 0 \\ 0 & 1 & 0 & -\frac{1}{R_L} \end{bmatrix} \quad (4\text{-}25)$$

$$\boldsymbol{A_3 = L_n^{-1}}\begin{bmatrix} -r & 0 & 0 & -1 \\ 0 & -r & 0 & -1 \\ 0 & 0 & -r & 0 \\ 1 & 1 & 0 & -\frac{1}{r_l} \end{bmatrix} \quad (4\text{-}26)$$

$$\boldsymbol{A_4 = L_n^{-1}}\begin{bmatrix} -r & 0 & 0 & 0 \\ 0 & -r & 0 & 0 \\ 0 & 0 & -r & -1 \\ 0 & 0 & 1 & -\frac{1}{r_l} \end{bmatrix} \quad (4\text{-}27)$$

$$\boldsymbol{A_5 = L_n^{-1}}\begin{bmatrix} -r & 0 & 0 & -1 \\ 0 & -r & 0 & 0 \\ 0 & 0 & -r & -1 \\ 1 & 0 & 1 & -\frac{1}{r_l} \end{bmatrix} \quad (4\text{-}28)$$

$$\boldsymbol{A_6 = L_n^{-1}}\begin{bmatrix} -r & 0 & 0 & 0 \\ 0 & -r & 0 & -1 \\ 0 & 0 & -r & -1 \\ 0 & 1 & 1 & -\frac{1}{r_l} \end{bmatrix} \quad (4\text{-}29)$$

$$A_7 = L_n^{-1}\begin{bmatrix} -r & 0 & 0 & -1 \\ 0 & -r & 0 & -1 \\ 0 & 0 & -r & -1 \\ 1 & 1 & 1 & -\frac{1}{r_l} \end{bmatrix} \quad (4\text{-}30)$$

Now, Euler forward method is used to discretize the continuous state space models leading to (4-31) which is the discrete form of equation (4-22).

$$\begin{aligned} x(k+1) &= A_{ds}x(k) + B_d u(k) \\ y &= Cx(k) \end{aligned} \quad (4\text{-}31)$$

Where :

$$A_{ds} = Id_{3x3} + T_s A_s \quad (4\text{-}32)$$

$$B_d = T_s B \quad (4\text{-}33)$$

4.5.2. Current Control of multicell Boost converter

Figure 4-24 displays the block diagram where MPC is used to control the currents of the interleaved multicell boost DC-DC converter. In this configuration, all currents are measured at discrete times (kT_{sw}) as well as the output capacitor voltage (the forth state). The predictive model of equation (4-31) is used to calculate the states ($i_1, i_2, i_3 and\ v_c$) at each step of the n sub-interval of the switching period. Later the cost function values are computed for all possible sequences in order to find the optimal one. At the end, the first best control sequence is applied to the power converter.

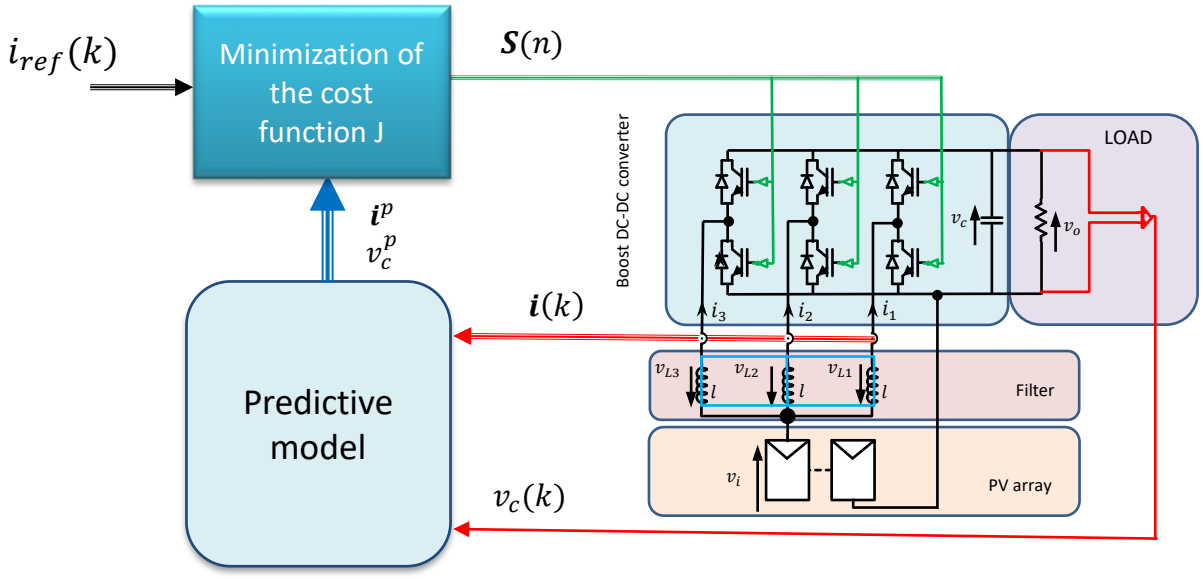

Figure 4-24 Block diagram of model predictive control applied to an interleaved multicell boost converter

4.5.2.1 Cost function for current control of Buck converter

In this section, the cost function is identical to that used for the multicell DC-DC buck-converter.

$$\begin{aligned} \boldsymbol{J} = &\left(\boldsymbol{i}_{ref}(k) - \boldsymbol{i}_{\boldsymbol{av}}(k)\right)' \boldsymbol{Q}\left(\boldsymbol{i}_{ref}(k) - \boldsymbol{i}_{\boldsymbol{av}}(k)\right) \\ &+ \left(\boldsymbol{i}_{ref}(k) - \boldsymbol{i}_{max}(k)\right)' \boldsymbol{g_1}\left(\boldsymbol{i}_{ref}(k) - \boldsymbol{i}_{max}(k)\right) \\ &+ \left(\boldsymbol{i}_{ref}(k) - \boldsymbol{i}_{min}(k)\right)' \boldsymbol{g_1}\left(\boldsymbol{i}_{ref}(k) - \boldsymbol{i}_{min}(k)\right) \end{aligned} \qquad (4\text{-}34)$$

As previously, FCS-MPC aims to minimize the cost function to find the optimal switching sequence by solving the problem (2-4)

$$\min_{u} \boldsymbol{J}$$

with:

$$\begin{aligned} &\boldsymbol{x}(n+1) = \boldsymbol{A}_{ds}\boldsymbol{x}(n) + \boldsymbol{B}_d\boldsymbol{u}(n) \\ &\boldsymbol{y}(n) = \boldsymbol{C}\,\boldsymbol{x}(n) \\ &\boldsymbol{0} \le \boldsymbol{x}(n+1) \le \boldsymbol{i}_{up} \\ &\boldsymbol{A}_{ds} = \boldsymbol{Id}_{3x3} + T_s\boldsymbol{A}_s \\ &\boldsymbol{A}_s = \boldsymbol{L_n^{-1}} \begin{bmatrix} -r & 0 & 0 & -S_1 \\ 0 & -r & 0 & -S_2 \\ 0 & 0 & -r & -S_3 \\ S_1 & S_2 & S_3 & -\frac{1}{r_l} \end{bmatrix} \text{ with } \; S_i = \{0\,;1\} \end{aligned} \qquad (4\text{-}35)$$

4.5.2.2 Simulation results

All simulations of boost converter are done with specifications of Table 4.

Table 4 Simulation parameters for boost converter

Symbol	Quantity	Value
v_i	The input voltage of buck converter	100 V
l	ICT inductance	15.4 mH
m	ICT mutual inductance	-7 mH
c	The output filter capacitor	1560 µF
r	ICT resistance	5.36 Ω
r_l	Load resistance	15 Ω
i_{up}	Current upper limits	12A
T_s	Sampling time	5 µS
T_{sw}	Switching time	45 µS
N_{sw}	Number of sample per switching time	9
C_a	Number of carrier	3
N_{seq}	Number of switching vectors	1000

(1) Common mode response

For this trial, all current references have a similar 500 Hz square waveform varying from 5.5A to 7A. Figure 4-25 shows the currents in each cells. When the current references are the same, the output currents follow their references. In this common mode configuration, currents rises very fast in few switching periods. There is no overshoot when the currents change as shown in Figure 4-25-a. Figure 4-25-b shows the three currents during steady state. The phase shift between currents imposed by the chosen MPC strategy does not appears in the figure, because the coupling.

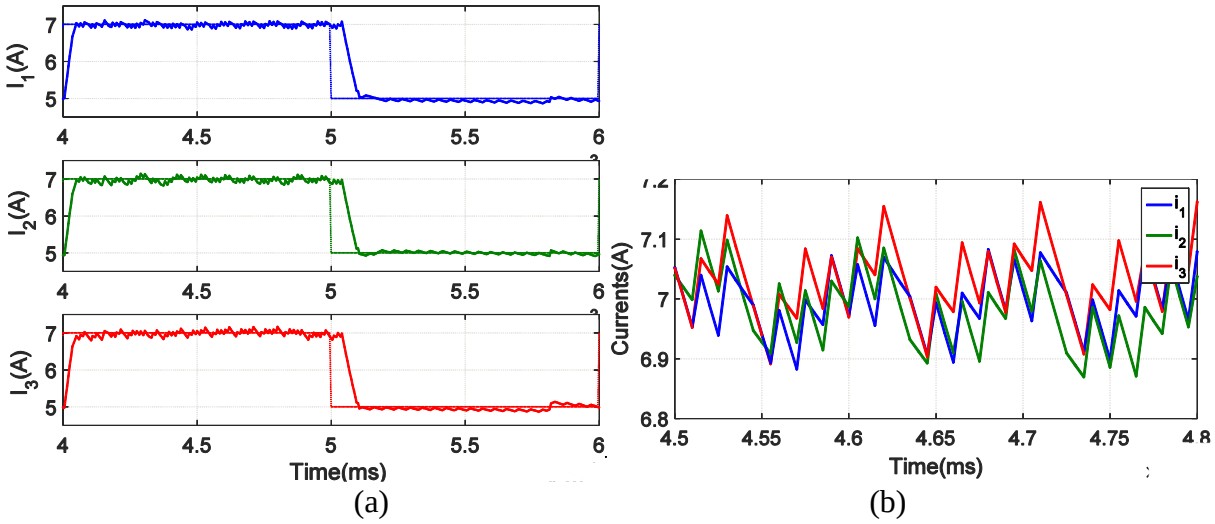

Figure 4-25 Simulation result: Boost converter-MPC-Current response for common mode

(2) Differential mode response

Figure 4-26 shows the simulation result in case of differential mode steps, where the first current reference has a square waveform with a $2/3$A step amplitude while the two others are in the opposite phase with $1/3$A step amplitude. We can see that all currents show an identical dynamic slower than that of common response.

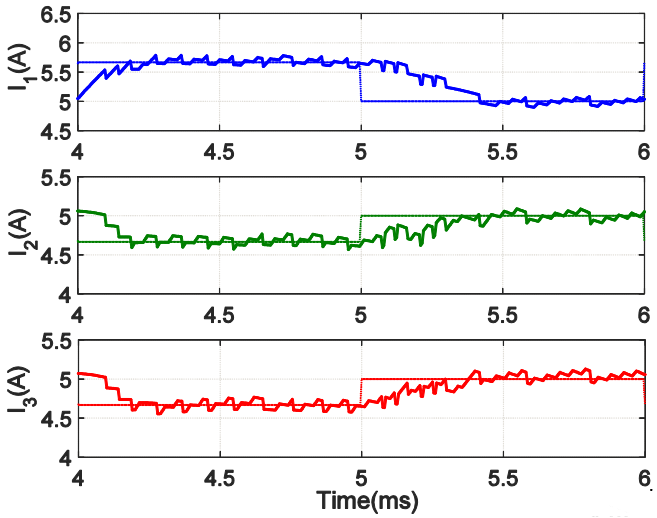

Figure 4-26 Simulation result of Boost converter-MPC-Current response: differential mode

(3) Single current step input

Figure 4-27 shows results in case of single current command. We can see here as for buck that MPC correctly manage the magnetic coupling between the cells. Effects of coupling disappear here in less than 500 µs.

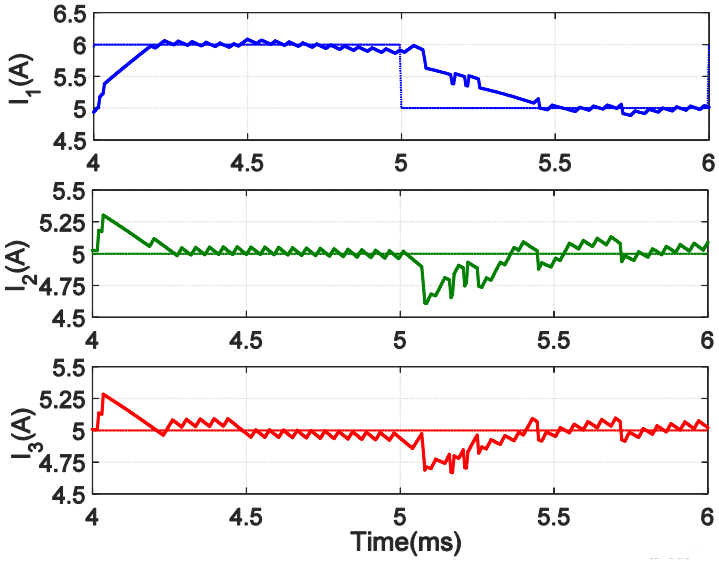

Figure 4-27 Simulation result of Boost converter-MPC-Current response: single current step mode

(4) Constraints on currents

Figure 4-17 shows that MPC also correctly manage current limitations (by applying hard violation penalties) in case of boost topology.

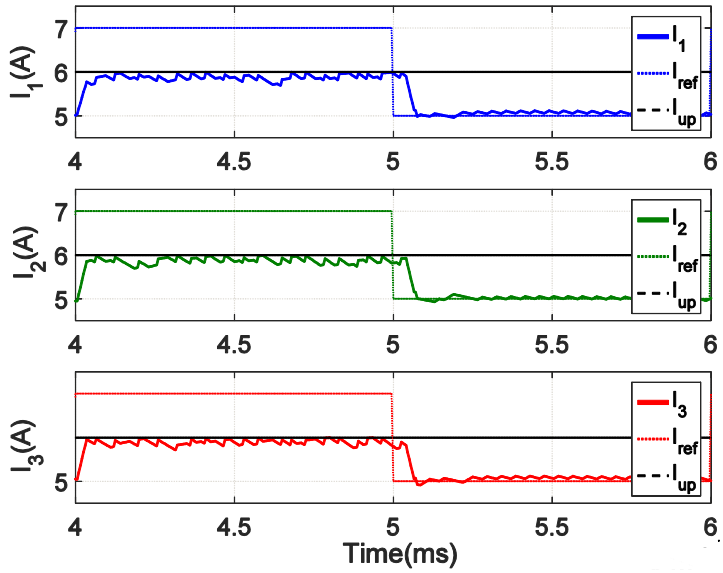

Figure 4-28 Simulation result: Boost converter-MPC-Current response; Current saturation in common mode

(5) Sensitivity analysis

The sensitivity analysis is done by varying either the load resistor or the magnetic device parameters.

a) Sensitivity to load variations

In the following simulations, the load takes three different values, namely $r_l = 30\ \Omega$, $r_l = 7.5\ \Omega$ and the minimum load possible resistance for the given reference current $r_l = 4\ \Omega$ while the internal model used in MPC is unchanged ($r_l = 15\ \Omega$). Figure 4-29 shows the results. We can conclude from these simulations that the system remains stable and that FCS-MPC is less sensitive to load variations than in the previous multicell buck converter. Indeed, current dynamics, when going from lower to upper level (there are no duty cycle saturations in this configuration) are the same. This property is not due to the converter topology but is inherent to the large output capacitor, which is equivalent to a short circuit during transients.

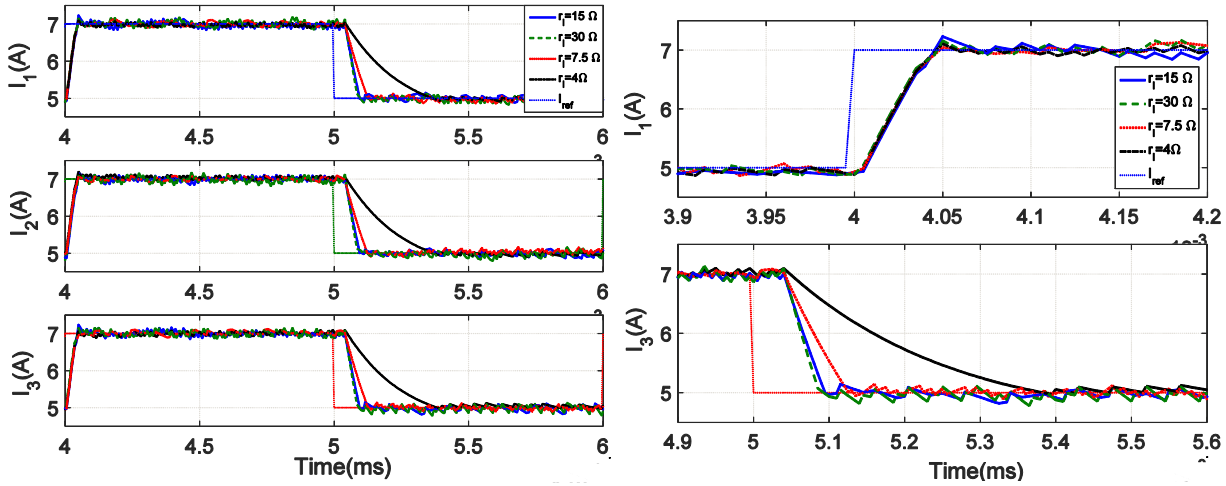

(a) (b)

Figure 4-29 Simulation result of Boost converter-MPC-Current response: sensitivity to the change in the load

b) Sensitivity to the magnetic filtering device parameters

In the following study, the values of inductances ($l = 15.4$ mH and $m = -7$ mH) used in the MPC prediction model are changed in the boost converter. Three configurations are tested, namely 120%, 90% and 80% of the MPC model self and mutual inductance ($l = 18.48$ mH - $m = -8.4$ mH, $l = 13.86$ mH - $m = -6.3$mH , and $l = 12.32$ mH - $m = -5.6$ mH).

Figure 4-30 shows the corresponding results. The simulations show that the system remains stable, but we can also observe a steady state error. When inductances increase the real current become higher than the reference (the green dashed line) and vice versa (the red and black lines) when inductances are lower. We can also note that model errors have no real impact on the system dynamic.

We can conclude that the MPC based proposed strategy is sensitive to inductance values in this boost configuration and leads to significant steady state errors. This behavior, different of that seen in the previous Buck topology, is due to the nature of the sources at both side of the magnetic

device. In the previous configuration, one side of the filtering device was connected to a load resistor, whereas it is now connected to a voltage input source. As this magnetic device has now a voltage source at its both sides (one constituted by the input voltage source and the other by the voltages imposed by the power converter), command errors and thus voltage errors are now integrated, due to the inductive nature of this device, and lead to this steady state deviation.

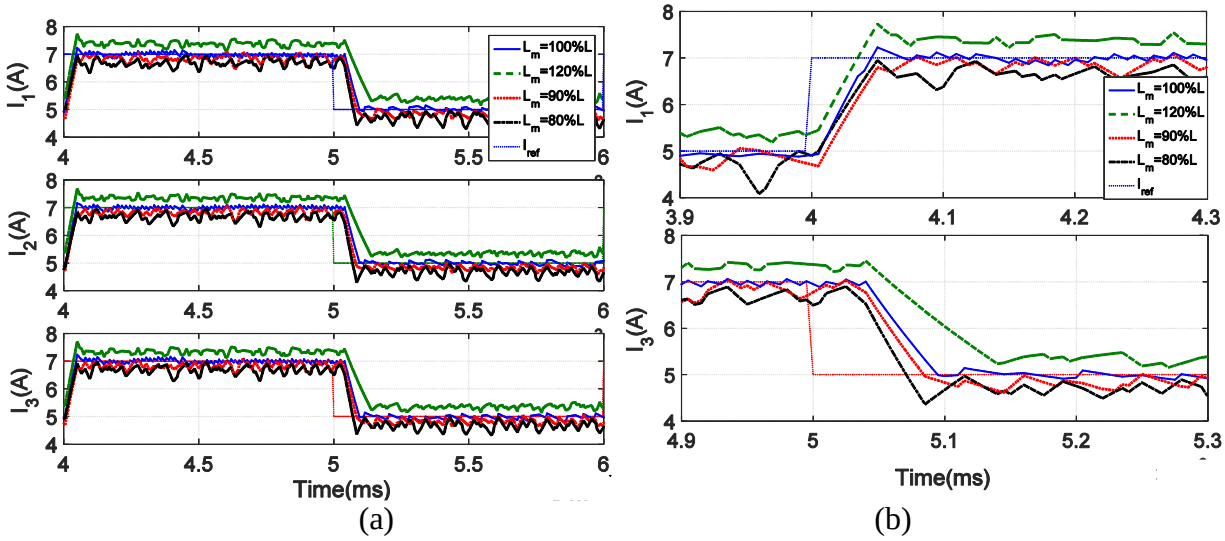

Figure 4-30 Simulation result: Boost converter-MPC-Current response; sensitivity to the magnetic filtering device parameters

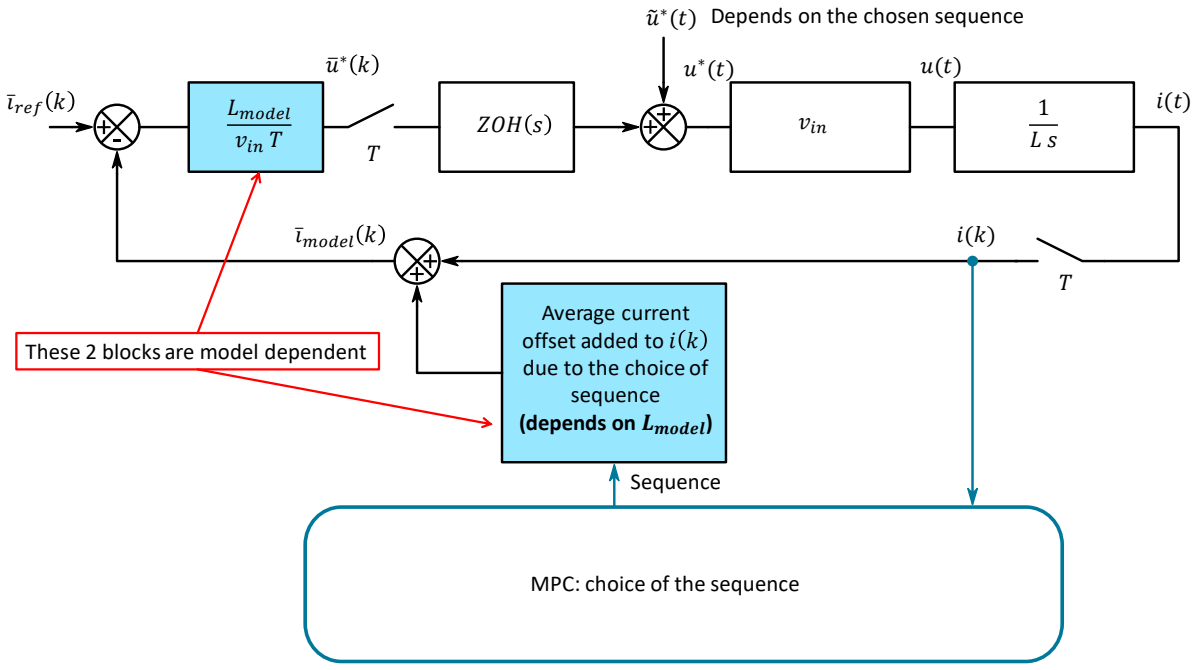

Figure 4-31 Impact of the magnetic filtering device parameters

The previous behavior can be basically explained by considering the Figure 4-31. This block diagram represent the situation where a predictive model is used to control the average current in a single inductance driven by a pure voltage source obtain from a switching power supply which output voltage is denoted u. In this figure u^* is the dimensionless output voltage calculated from the power supply input voltage v_{in}: $u^* = u/v_{in}$ and variables denoted $\overline{x}$ represent the average of $x(t)$ over the switching period T.

From this model we can conclude that the steady state error is zero due to the integration behavior of inductor. This mean that $\bar{\imath}_{model}(k) = \bar{\imath}_{ref}(k)$. Nevertheless, blue blocks in this diagram are model dependent, as $L_{model} \neq L$ the average value which is added in the model to $i(k)$ is wrong. This lead to obtain a systematic error such as $\bar{\imath}_{ref}(k) = \bar{\imath}_{model}(k) \neq \overline{i}(k)$.

4.5.3. Voltage Control of Boost converter

4.5.3.1 FCS-MPC voltage control

It not feasible to use the proposed method to control the output voltage of the multicell interleaved boost converter. Indeed, the output dynamic of this voltage is slow due to the output filter (capacitor). To use the MPC strategy in such problem, it is necessary that the minimum prediction horizon H_p covers a significant part of the transient region to be efficient [79] which means that the predication horizon should be much more than a switching period in this case.

4.5.3.2 Two loops voltage control

However, in this configuration, it is possible to design two control loops as the current dynamics are faster than that of the output voltage. The proposed strategy is to use FCS-MPC to control the currents in an inner loop and a classical PI controller for the voltage in a second control loop.

Figure 4-32 shows the Simulink model of the two loops voltage control of the multicell boost converter. The block named "$boost\ converter\ 3cells$" is the discrete state space model of the interleaved multicell DC-DC boost converter. The green block "$MPC\_Current$" is the Matlab function which contains the algorithm of the FCS-MPC. This part represents the inner loop of the control strategy. One of the input of the FCS-MPC function is the current reference for the three cells of the converter ($i_{ref1} = i_{ref2} = i_{ref3} = i_{ref}$). This reference is delivered by the PI controller. This controller is named "$PI\ controller$" in the figure and is defined by equation (4-36).

$$i_{ref} = \left[K_p\left(V_{ref}(t) - v_c(t)\right) + K_i\frac{d}{dt}\left(V_{ref}(t) - v_c(t)\right)\right]/3 \qquad (4\text{-}36)$$

Figure 4-33 shows the results of the voltage control. Figure 4-33-b shows the currents in each cell. It is clear that these currents are balanced. In Figure 4-33-a, the first two graphs show the output voltage of the converter. We can see that this voltage follows its reference with a very low ripple. The third graph of Figure 4-33-a shows a closed view of the currents. We can see here some oscillations already observed in previous simulations and due to magnetic coupling between the cells and to the low number of possible duty-cycles provided by the MPC controller.

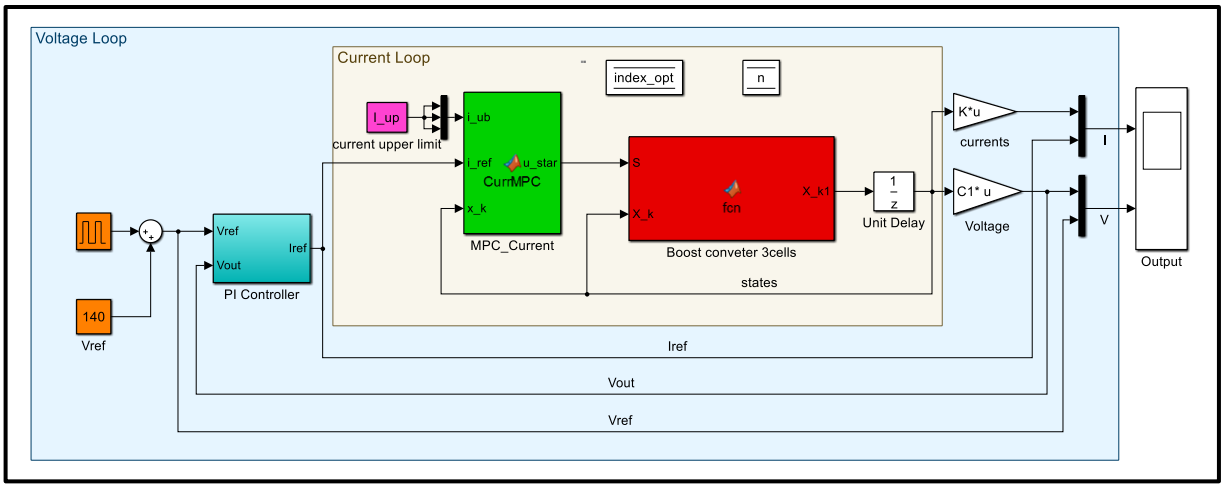

Figure 4-32 Simulink model of boost converter-Two loops Voltage Control

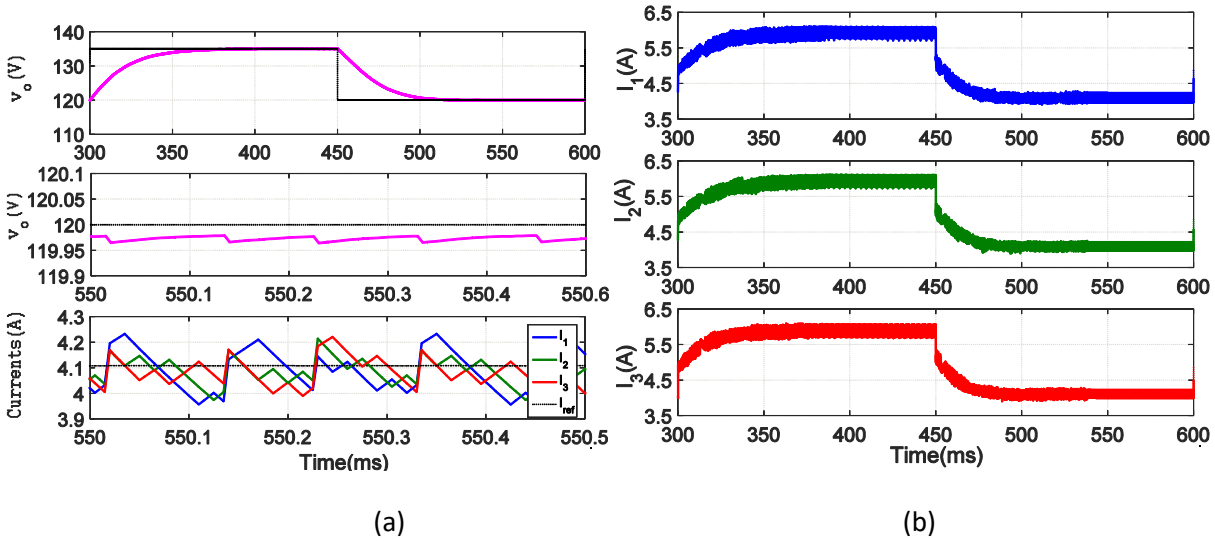

(a) (b)

Figure 4-33 Simulation of the controlling output voltage of boost converter (a)Outputs response (b) Current response

4.6. Conclusion

The FCS-MPC can be used to control a multi-cell interleaved and magnetically coupled DC-DC converter. It offers the possibility to balance the current and control the global current of such power converter even if there is a strong coupling between the cells. In this chapter, we propose a method for fixing the switching frequency while using FCS-MPC to control the converter. The benefits of the proposed method beyond the fixed frequency are:

- The reduction of the number of sequences to be evaluated which allow an implementation

in real-time with a FPGA target.

- No need for offline calculation.
- No need for high speed measurements (the measurements are done at the beginning of the switching period).
- Can be implemented for high number of switches or for multi-level converters.

But FCS-MPC method has also many limitations:

- The number of possible duty cycles (duty cycle resolution) depends on the number of points which divides the switching period N_{sw} and gives the number of sequences to be tested
- A very fast hardware is needed to test in real-time all possible switching sequences and find the optimal solution.
- Model predictive control is sensitive to model's parameters, it needs extra addition to compensate some deviations, such as observers to estimate some parameters.

Due to these limitations, the previous MPC method is not really satisfactory. We are going to propose in the next chapter a new methodology also based on the converter model but with much less limitations.

Chapter 5. Space vector placement based on model Predictive Control

5.1. Introduction

There are different control techniques dedicated to power converters. For such systems, the so-called direct and indirect control principles can be used.

In indirect control, a modulator dedicated to the PWM generation is designed and the controller provides a reference voltage to the PWM which generates the turn-on and turn-off times of the power converter's switches. Among all indirect control methods we can mentioned the Voltage Oriented Control (VOC) [80]–[82] or the Virtual flux (VF) control[83], [84]. Indirect control techniques, mostly have a fixed switching frequency.

Conversely, in direct control strategies, there is a direct link between the controller and the state of converter's switches. The Direct Power control (DPC) is commonly used to control grid connected converters [85]–[87]. DPC is similar to Direct Torque Control (DTC) developed in case of machine control. DPC does not need a modulator, internal loops and any specific transformation. At switching times, the direct controller selects from a look-up table the best switching sequence that sends the controlled quantities close to the references. This principle is also applied in VF control as in VF-DPC [83], [84]. But DPC involves a variable switching frequency, this means that unwanted harmonics will appear leading to high difficulties in designing the output filter. This is the main disadvantage of this technic. To overcome the variable switching frequency, predictive approached can be applied with DPC. This kind of approach is used for example to control AC-machines like in [76], [88], [89]. This is done by selecting a set of voltage vectors along a defined switching period and by computing for each vector its duration of application in order to reach the references. Many authors developed such strategies for multilevel converters like in [48].

The proposed control technic developed in this chapter uses two principles. A classical linear control is implemented to control the common mode (global current and voltage output), whereas a space vector placement strategy is used to control the differential currents. For this purpose, a model inversion is applied to calculate the duration of application of vectors for different set of switching vectors (different sequences) in order to obtain, if possible, a zero average differential value of the currents in the multicell converter. For each sequence, the currents along a switching period are estimated and different derived values such as the maximum and minimum currents or the average currents along the switching period can be predetermined. These values can be used in a Finite control set model predictive control algorithm (FCS-MPC) to select the optimal sequence of vectors that minimizes a defined cost function. This method can be seen as a direct control technique as it does not need a modulator.

This chapter is organized as follow. The first section gives the model equations of a 3-cell parallel Buck converter used in this chapter. In a second section, we recall the main physical implications of common and differential modes on the coupled inductors of such topologies. It is shown that controlling the magnetic behavior of such devices implies to control three currents modes for a 3-cell converter via its 3 voltage modes. The next section shows how the duration of applications of the vectors of a given sequence can be calculated from the model. It is shown that

the current waveforms along the switching period depends on the sequence. In order to choose the sequence, a MPC strategy is used to select the best one regarding a given cost function.

5.2. Model of a 3-Cell parallel Buck converter

Figure 3-1 shows a 3-cell buck converter built with three half-bridges, each one controlled by a switching function S_i $(i = 1,2,3)$. These 3 switching functions can be merged to form a vector (a space vector). The space vectors are numbered from 0 to 7. During a switching period, different space vectors can be applied to form a space vector sequence ($SV_{sequence}$). In the following we will use 6 space vectors within one switching period. The space vector sequence is a $[6 \times 1]$ vector which contains the vector numbers to apply successively. The durations of application of each space vector are merged in one vector denoted $t_{sequence}$ with a dimension $[6 \times 1]$.

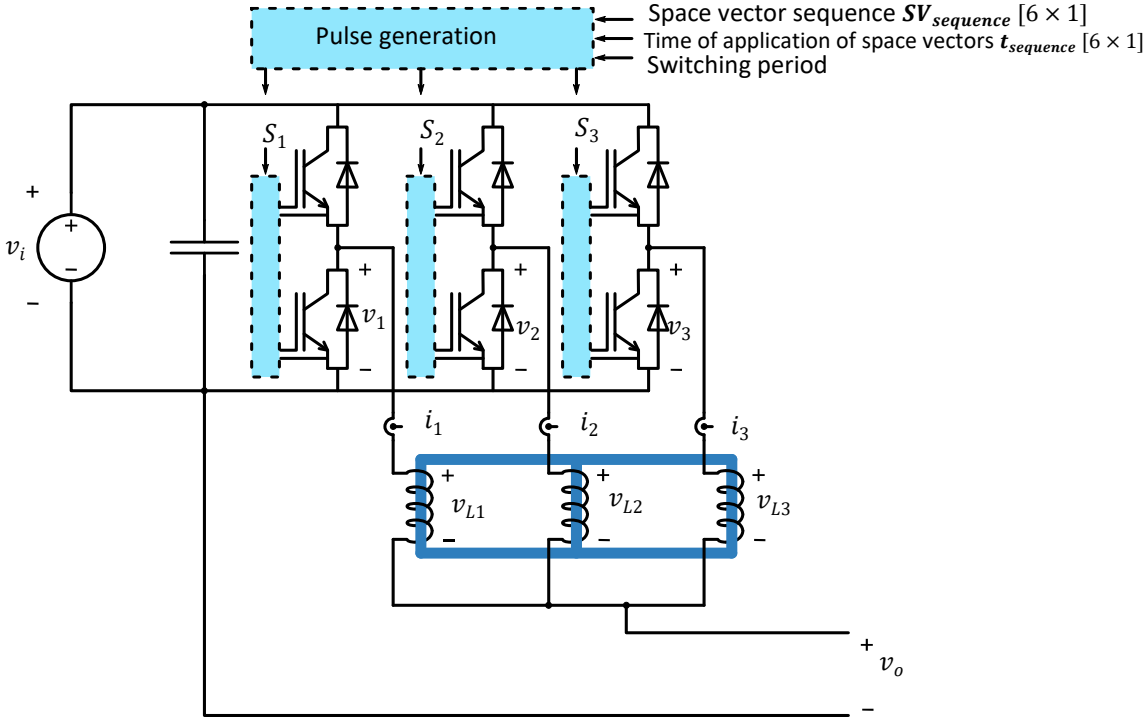

Figure 5-1 3-Cell parallel Buck converter

All simulations of the 3-cell buck converter are done with the parameters defined in Table 5-1

Table 5-1 Parameters used for the 3-Cell buck converter

Symbol	Quantity	Value
v_i	The input voltage of buck converter	150 V
l	ICT inductance	15.4 mH
M	ICT mutual inductance	-7 mH
r	ICT resistance	5.36 Ω
r_l	Load resistance	5 Ω
T	Switching time	50 µS

There are only a finite number of possible space-vectors for a multi-cell power converter (8 for a 3-cell converter [90]). All the possible combinations are given in the following table. Each one defines a voltage space vector denoted SV_x.

Table 5-2 Switch combinations for a multi-cell power converter: cell-voltages and cell-states

Space vector	v_1	v_2	v_3	Cell 1 state S_1	Cell 2 state S_2	Cell 3 state S_3
SV_0	0	0	0	0	0	0
SV_1	0	0	v_{in}	0	0	1
SV_2	0	v_{in}	0	0	1	0
SV_3	v_{in}	0	0	1	0	0
SV_4	0	v_{in}	v_{in}	0	1	1
SV_5	v_{in}	v_{in}	0	1	1	0
SV_6	v_{in}	0	v_{in}	1	0	1
SV_7	v_{in}	v_{in}	v_{in}	1	1	1

It is now well known that performances of a multi-cell power converter can be improved by using coupled inductors instead of individual inductors.

As shown in previous chapters, control of currents in such coupled devices are not easy to implement if the control is performed on v_L voltages. This control is easier if it is performed on each independent mode of the passive device. This modes (fictitious voltages and currents) are defined so that it provides a system equation in which each mode is independent of each other.

For a 3-cell converter, there are three independent modes characterized by the following voltages and currents:

$$\begin{bmatrix} u_{cm} \\ u_{diff_\alpha} \\ u_{diff_\beta} \end{bmatrix} \quad ; \quad \begin{bmatrix} i_{cm} \\ i_{diff_\alpha} \\ i_{diff_\beta} \end{bmatrix}$$

Fictitious currents can be calculated from real one by using a linear transformation defined by matrix in equation (3-26)and will be:

$$\begin{bmatrix} x_{cm} \\ x_{diff_\alpha} \\ x_{diff_\beta} \end{bmatrix} = T^{-1} \begin{bmatrix} x_1 \\ x_2 \\ x_3 \end{bmatrix} \quad \Leftrightarrow \quad \begin{bmatrix} x_{cm} \\ x_{diff_\alpha} \\ x_{diff_\beta} \end{bmatrix} = \begin{bmatrix} x_1 + x_2 + x_3 \\ x_1 - x_2 \\ x_2 - x_3 \end{bmatrix} \tag{5-1}$$

The first mode is the common mode of the coupled inductor. The two others are two different differential modes.

The coupled inductor modes equations (3-3)are derived from the previous transform:

$$\begin{bmatrix} v_{Lcm} \\ v_{Ldiff_\alpha} \\ v_{Ldiff_\beta} \end{bmatrix} = s \begin{bmatrix} L + 2M & 0 & 0 \\ 0 & L - M & 0 \\ 0 & 0 & L - M \end{bmatrix} \begin{bmatrix} i_{cm} \\ i_{diff_\alpha} \\ i_{diff_\beta} \end{bmatrix} + r \begin{bmatrix} i_{cm} \\ i_{diff_\alpha} \\ i_{diff_\beta} \end{bmatrix} \tag{5-2}$$

We can notice that such transform leads to an effective decoupling of system equations.

5.3. Physical impact of common and differential modes of the currents on output coupled inductors

The simplest way to fabricate the output coupled inductor consist in using the cyclic cascade topology in which the converter cells are coupled 2 by 2 by a 2 windings inductor. This configuration is illustrated in the Figure 5-2.

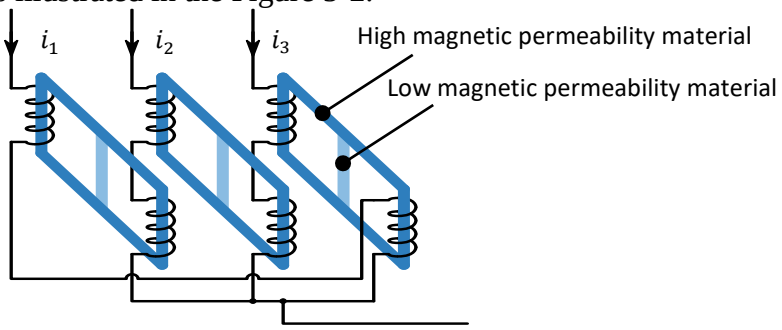

Figure 5-2 Cyclic cascade coupling inductor topology

In this arrangement, three identical two-winding coupled inductor are used. In the following the physical impact of common mode and differential mode currents on fluxes in one two-winding inductor is studied. The Physical behavior of such a device can be built from the reluctance model of the device as in Figure 5-3:

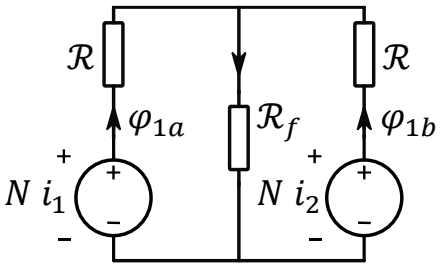

Figure 5-3 reluctance model of the multicell interleaved power converter

From this model, the fluxes in the different part of the magnetic core are:

$$\begin{bmatrix}\varphi_{1a}\\ \varphi_{1b}\end{bmatrix} = N\begin{bmatrix}\dfrac{\mathcal{R}+\mathcal{R}_f}{\mathcal{R}^2+2\mathcal{R}\mathcal{R}_f} & -\dfrac{\mathcal{R}_f}{\mathcal{R}^2+2\mathcal{R}\mathcal{R}_f}\\ -\dfrac{\mathcal{R}_f}{\mathcal{R}^2+2\mathcal{R}\mathcal{R}_f} & \dfrac{\mathcal{R}+\mathcal{R}_f}{\mathcal{R}^2+2\mathcal{R}\mathcal{R}_f}\end{bmatrix}\begin{bmatrix}i_1\\ i_2\end{bmatrix} \qquad (5\text{-}3)$$

Considering the local common mode current and the differential current mode, we can rewrite the equation (5-3):

$$\begin{bmatrix}\varphi_{1a}\\ \varphi_{1b}\end{bmatrix} = \frac{N}{2}\begin{bmatrix}\dfrac{\mathcal{R}}{\mathcal{R}^2+2\mathcal{R}\mathcal{R}_f} & \dfrac{1}{\mathcal{R}}\\ \dfrac{\mathcal{R}}{\mathcal{R}^2+2\mathcal{R}\mathcal{R}_f} & -\dfrac{1}{\mathcal{R}}\end{bmatrix}\begin{bmatrix}i_1+i_2\\ i_1-i_2\end{bmatrix} \qquad (5\text{-}4)$$

From this system, we can note that the core magnetic operating point depends on the two current modes. Nevertheless, the reluctance $\mathcal{R}_f$ is much larger than that of the high permeability path of the core represented by $2\mathcal{R}$.

The two fluxes can thus be approximated by:

$$\begin{bmatrix}\varphi_{1a}\\ \varphi_{1b}\end{bmatrix} = \frac{N}{2}\begin{bmatrix}\frac{1}{2\mathcal{R}_f} & \frac{1}{\mathcal{R}}\\ \frac{1}{2\mathcal{R}_f} & -\frac{1}{\mathcal{R}}\end{bmatrix}\begin{bmatrix}i_1+i_2\\ i_1-i_2\end{bmatrix} \quad \Leftrightarrow \tag{5-5}$$

$$\begin{bmatrix}\varphi_{1a}\\ \varphi_{1b}\end{bmatrix} = \frac{N}{2}\begin{bmatrix}\frac{1}{2\mathcal{R}_f}(i_1+i_2)+\frac{1}{\mathcal{R}}i_{diff_\alpha}\\ \frac{1}{2\mathcal{R}_f}(i_1+i_2)-\frac{1}{\mathcal{R}}i_{diff_\alpha}\end{bmatrix} \approx \frac{N}{2\mathcal{R}}\begin{bmatrix}i_{diff_\alpha}\\ -i_{diff_\alpha}\end{bmatrix} \tag{5-6}$$

The magnetic operating point of the core is therefore mainly defined by the differential mode of the cells currents whereas the output current equal to the summation of all the cells' currents as in equation (5-7) and it is only defined by the common mode current.

$$i_o = i_1 + i_2 + i_3 = i_{mc} \tag{5-7}$$

Using the definitions and notations used for the three modes of three coupled inductors, the magnetic operating points of the three cores in the previous 3-cell cyclic cascade topology are given by:

$$\varphi_{inductor1} \approx \frac{N}{2\mathcal{R}} i_{diff_\alpha} \tag{5-8}$$

$$\varphi_{inductor2} \approx \frac{N}{2\mathcal{R}} i_{diff_\beta} \tag{5-9}$$

$$\varphi_{inductor3} \approx \frac{N}{2\mathcal{R}}\left(i_{diff_\alpha} - i_{diff_\beta}\right) \tag{5-10}$$

It is worth to notice that to avoid magnetic saturation, the differential modes of the currents must be controlled. One possible strategy is to use a controller to maintain the average value of these differential modes over a switching period equal to zero. By doing this, the average value of the three cores fluxes will be zero.

5.4. Control of the three current modes

The control of the three current modes is facilitated when controlling the three voltage modes of the output voltages instead of each output voltage v_1, v_2 and v_3. This can be easily demonstrated from the electrical system equations:

$$\begin{bmatrix}v_1\\ v_2\\ v_3\end{bmatrix} = \begin{bmatrix}v_{L1}\\ v_{L2}\\ v_{L3}\end{bmatrix} + v_o\begin{bmatrix}1\\ 1\\ 1\end{bmatrix} = s\begin{bmatrix}L & M & M\\ M & L & M\\ M & M & L\end{bmatrix}\begin{bmatrix}i_1\\ i_2\\ i_3\end{bmatrix} + r\begin{bmatrix}i_1\\ i_2\\ i_3\end{bmatrix} + v_o\begin{bmatrix}1\\ 1\\ 1\end{bmatrix} \tag{5-11}$$

$$\begin{bmatrix} v_{cm} \\ v_{diff_\alpha} \\ v_{diff_\beta} \end{bmatrix} = s \begin{bmatrix} L+2M & 0 & 0 \\ 0 & L-M & 0 \\ 0 & 0 & L-M \end{bmatrix} \begin{bmatrix} i_{cm} \\ i_{diff_\alpha} \\ i_{diff_\beta} \end{bmatrix} + r \begin{bmatrix} i_{cm} \\ i_{diff_\alpha} \\ i_{diff_\beta} \end{bmatrix} + v_o \begin{bmatrix} 3 \\ 0 \\ 0 \end{bmatrix} \quad (5\text{-}12)$$

$$\begin{bmatrix} i_{cm} \\ i_{diff_\alpha} \\ i_{diff_\beta} \end{bmatrix} = \begin{bmatrix} \frac{1}{r+(L+2M)s} & 0 & 0 \\ 0 & \frac{1}{r+(L-M)s} & 0 \\ 0 & 0 & \frac{1}{r+(L-M)s} \end{bmatrix} \begin{bmatrix} v_{mc}-3v_o \\ v_{diff_\alpha} \\ v_{diff_\beta} \end{bmatrix} \quad (5\text{-}13)$$

Indeed, this last set of equation shows that each current mode can be independently controlled by each voltage mode.

5.4.1. Control of the three voltage modes

The output voltage of a multi-cell power converter has a finite number of possible switch combinations, so do the three voltage modes. The different possible values for these modes are shown in the Table 5-3:

Table 5-3 Switch combinations for a multi-cell power converter: fictitious voltage

Space vector	v_{cm}	v_{diff_α}	v_{diff_β}	Cell 1 state S_1	Cell 2 state S_2	Cell 3 state S_3
SV_0	0	0	0	0	0	0
SV_1	v_{in}	0	$-v_{in}$	0	0	1
SV_2	v_{in}	$-v_{in}$	v_{in}	0	1	0
SV_3	v_{in}	v_{in}	0	1	0	0
SV_4	$2v_{in}$	$-v_{in}$	0	0	1	1
SV_5	$2v_{in}$	0	v_{in}	1	1	0
SV_6	$2v_{in}$	v_{in}	$-v_{in}$	1	0	1
SV_7	$3v_{in}$	0	0	1	1	1

The main goal assigned to the controller is to insure that the power converter delivers the proper current and voltage at its output. Therefore, common mode current and voltage are the main system quantities to control. Differential modes are secondary controlled variables that allow to define the magnetic state of the cores. It can be noticed that the dynamic of common and differential modes are not the same. Indeed, maximum dI/dt is equal to $\tilde{v}_{mc}/(L+2M)$ for the common mode and $\tilde{v}_{diff_{\alpha,\beta}}/(L-M)$ for the two differential modes. As $M=-k\frac{L}{2}$ in which k is the coupling factor (in usual design $k>0.95$), the common mode current has a much higher dynamic than that of differential currents.

To avoid high common mode current ripple, the common mode voltage must be controlled at a high speed (at the switching period scale). Moreover, it is possible to use the multi-cell character of the power converter to "over-sample" the output voltage. For a 3-cell structure, it is possible to multiply by three the frequency of the common mode voltage v_{cm}.The plurality of vectors giving the same common mode voltage can be used to perform such apparent frequency increase.

In the following, the required common voltage is defined by a dimensionless variable denoted

$v_{cm}^{*} = v_{cm}/v_i$. The possible space vectors gives three discrete values for the dimensionless common mode voltage, namely {0,1,2,3} called $level$. Dimensionless variables can also be used for the two differential modes, they are denoted $v_{diff_\alpha}^{*}$ et $v_{diff_\beta}^{*}$. These values are shown in Table 5-4

During each switching period, we apply a sequence of six space vectors. In this sequence, successive space vectors are chosen in such a way that the levels associated to these space vectors alternate on either side of the desired common mode level. Each vectors are applied during a duration that can be defined by dimensionless duty cycles.

Table 5-4 Switch combinations for a multi-cell power converter: dimensionless output voltage

Space vector	$v_{cm}^{*} = level$	$v_{diff_\alpha}^{*}$	$v_{diff_\beta}^{*}$
SV_0	0	0	0
SV_1	1	0	−1
SV_2	1	−1	1
SV_3	1	1	0
SV_4	2	−1	0
SV_5	2	0	1
SV_6	2	1	−1
SV_7	3	0	0

The sequence of space vectors is defined by the 6 successive space vector:$(SV_{seq1},\ SV_{seq2},\ SV_{seq3},\ SV_{seq4},\ SV_{seq5},\ SV_{seq6})$. The duration of application of each vector is given by: $(d_{seq1},\ d_{seq2},\ d_{seq3},\ d_{seq4},\ d_{seq5},\ d_{seq6}) \times T$, where T is the switching period of each cell. The Figure 5-4 shows an example of sequence and the corresponding dimensionless voltage modes.

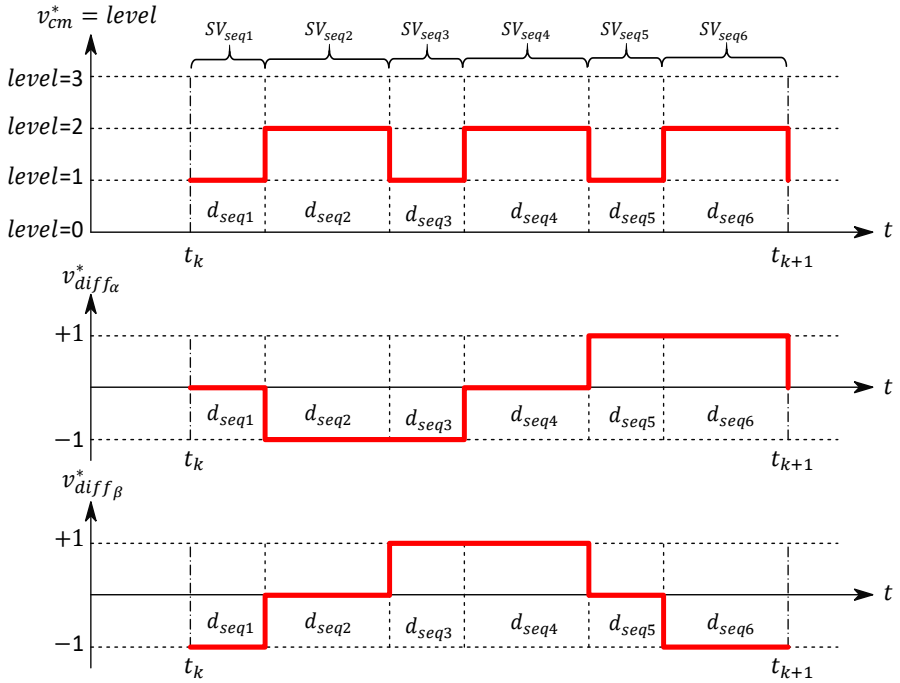

Figure 5-4 An example of sequence and the corresponding dimensionless voltage modes

From this figure, we can observe that if space vectors corresponding to the lower level are applied during the same duration as the space vectors corresponding to the higher level:

- The apparent frequency of the common mode voltage is three times the switching frequency of each cell [91].
- The average value of the two differential voltages is zero

The average values of the voltage modes over the switching period are given by:

$$\begin{bmatrix} \bar{v}^*_{cm}(k) \\ \bar{v}^*_{diff_\alpha}(k) \\ \bar{v}^*_{diff_\beta}(k) \end{bmatrix} = \begin{bmatrix} v^*_{cm_{seq1}} & v^*_{cm_{seq2}} & v^*_{cm_{seq3}} & v^*_{cm_{seq4}} & v^*_{cm_{seq5}} & v^*_{cm_{seq6}} \\ v^*_{diff\alpha_{seq1}} & v^*_{diff\alpha_{seq2}} & v^*_{diff\alpha_{seq3}} & v^*_{diff\alpha_{seq4}} & v^*_{diff\alpha_{seq5}} & v^*_{diff\alpha_{seq6}} \\ v^*_{diff\beta_{seq1}} & v^*_{diff\beta_{seq2}} & v^*_{diff\beta_{seq3}} & v^*_{diff\beta_{seq4}} & v^*_{diff\beta_{seq5}} & v^*_{diff\beta_{seq6}} \end{bmatrix} \begin{bmatrix} d_{seq1}(k) \\ d_{seq2}(k) \\ d_{seq3}(k) \\ d_{seq4}(k) \\ d_{seq5}(k) \\ d_{seq6}(k) \end{bmatrix} \quad (5\text{-}14)$$

5.4.2. Determination of the duty-cycles

The relationships giving the voltage modes show six unknowns (six duty-cycles). The duty cycle determination has a unique solution if we add three more equations to (5-14). One of them is obvious: the summation of all duty cycles must be equal to one. The two others must be built by adding some more constraints to the solution. For this purpose, the common mode voltage interval (from 0 to 3 in our study) is divided in four intervals. We suppose in the following that the sequence is chosen in such a way to alternate a low $v_{cm}(t)$ value at sequence seq_{2n+1} and a high value at seq_{2n+2} with $n = \{0,1,2\}$.

- Interval 1: For $0 \leq \bar{v}^*_{cm}(k) < 1$: space vector duty-cycles of seq_2, seq_4 and seq_6 (at $level$ 1) are calculated and the rest of the switching period is evenly distributed to seq_1, seq_3 and seq_5 (at $level$ 0). In this interval, space vector in seq_1, seq_3 and seq_5 is SV_0 and space vectors in seq_2, seq_4 and seq_6 must be SV_1, SV_2 and SV_3
- Interval 2: For $1 \leq \bar{v}^*_{cm}(k) < 1.5$: space vector duty-cycles of seq_1, seq_3 and seq_5 (at $level$ 1) are calculated and the rest of the switching period is evenly distributed to seq_2, seq_4 and seq_6 (at $level$ 2).
- Interval 3: For $1.5 \leq \bar{v}^*_{cm}(k) < 2$: space vector duty-cycles of seq_2, seq_4 and seq_6 (at $level$ 2) are calculated and the rest of the switching period is evenly distributed to seq_1, seq_3 and seq_5 (at $level$ 1). In interval 2 and 3, space vectors in seq_1, seq_3 and seq_5 must be SV_1, SV_2 and SV_3 and space vectors in seq_2, seq_4 and seq_6 must be SV_4, SV_5 and SV_6
- Interval 4: For $2 \leq \bar{v}^*_{cm}(k) \leq 3$: space vector duty-cycles of seq_1, seq_3 and seq_5 (at $level$ 2) are calculated and the rest of the switching period is evenly distributed to seq_2, seq_4 and seq_6 (at $level$ 3). In this interval, space vectors in seq_1, seq_3 and seq_5 must be SV_4, SV_5 and SV_6 and space vector in seq_2, seq_4 and seq_6 is SV_7

Including the previous constraints in the system of equation, we obtain the following system:

- For odd intervals:

$$\begin{bmatrix} \bar{v}^*_{cm}(k) \\ \bar{v}^*_{diff_\alpha}(k) \\ \bar{v}^*_{diff_\beta}(k) \\ 1 \\ 1 \\ 1 \end{bmatrix} = \begin{bmatrix} v^*_{cm_{seq1}} & v^*_{cm_{seq2}} & v^*_{cm_{seq3}} & v^*_{cm_{seq4}} & v^*_{cm_{seq5}} & v^*_{cm_{seq6}} \\ v^*_{diff\alpha_{seq1}} & v^*_{diff\alpha_{seq2}} & v^*_{diff\alpha_{seq3}} & v^*_{diff\alpha_{seq4}} & v^*_{diff\alpha_{seq5}} & v^*_{diff\alpha_{seq6}} \\ v^*_{diff\beta_{seq1}} & v^*_{diff\beta_{seq2}} & v^*_{diff\beta_{seq3}} & v^*_{diff\beta_{seq4}} & v^*_{diff\beta_{seq5}} & v^*_{diff\beta_{seq6}} \\ 3 & 1 & 0 & 1 & 0 & 1 \\ 0 & 1 & 3 & 1 & 0 & 1 \\ 1 & 1 & 1 & 1 & 1 & 1 \end{bmatrix} \begin{bmatrix} d_{seq1}(k) \\ d_{seq2}(k) \\ d_{seq3}(k) \\ d_{seq4}(k) \\ d_{seq5}(k) \\ d_{seq6}(k) \end{bmatrix} \quad (5\text{-}15)$$

- For even intervals:

$$\begin{bmatrix} \bar{v}^*_{cm}(k) \\ \bar{v}^*_{diff_\alpha}(k) \\ \bar{v}^*_{diff_\beta}(k) \\ 1 \\ 1 \\ 1 \end{bmatrix} = \begin{bmatrix} v^*_{cm_{seq1}} & v^*_{cm_{seq2}} & v^*_{cm_{seq3}} & v^*_{cm_{seq4}} & v^*_{cm_{seq5}} & v^*_{cm_{seq6}} \\ v^*_{diff\alpha_{seq1}} & v^*_{diff\alpha_{seq2}} & v^*_{diff\alpha_{seq3}} & v^*_{diff\alpha_{seq4}} & v^*_{diff\alpha_{seq5}} & v^*_{diff\alpha_{seq6}} \\ v^*_{diff\beta_{seq1}} & v^*_{diff\beta_{seq2}} & v^*_{diff\beta_{seq3}} & v^*_{diff\beta_{seq4}} & v^*_{diff\beta_{seq5}} & v^*_{diff\beta_{seq6}} \\ 1 & 3 & 1 & 0 & 1 & 0 \\ 1 & 0 & 1 & 3 & 1 & 0 \\ 1 & 1 & 1 & 1 & 1 & 1 \end{bmatrix} \begin{bmatrix} d_{seq1}(k) \\ d_{seq2}(k) \\ d_{seq3}(k) \\ d_{seq4}(k) \\ d_{seq5}(k) \\ d_{seq6}(k) \end{bmatrix} \quad (5\text{-}16)$$

To be more general, we can synthesize the previous results as follows: the calculation of the duty cycles can be done by using one of the two expressions below:

- For intervals for which seq_1, seq_3 and seq_5 are imposed evenly distributed

$$\begin{bmatrix} d_{seq1}(k) \\ d_{seq2}(k) \\ d_{seq3}(k) \\ d_{seq4}(k) \\ d_{seq5}(k) \\ d_{seq6}(k) \end{bmatrix} = \begin{bmatrix} v^*_{cm_{seq1}} & v^*_{cm_{seq2}} & v^*_{cm_{seq3}} & v^*_{cm_{seq4}} & v^*_{cm_{seq5}} & v^*_{cm_{seq6}} \\ v^*_{diff\alpha_{seq1}} & v^*_{diff\alpha_{seq2}} & v^*_{diff\alpha_{seq3}} & v^*_{diff\alpha_{seq4}} & v^*_{diff\alpha_{seq5}} & v^*_{diff\alpha_{seq6}} \\ v^*_{diff\beta_{seq1}} & v^*_{diff\beta_{seq2}} & v^*_{diff\beta_{seq3}} & v^*_{diff\beta_{seq4}} & v^*_{diff\beta_{seq5}} & v^*_{diff\beta_{seq6}} \\ 3 & 1 & 0 & 1 & 0 & 1 \\ 0 & 1 & 3 & 1 & 0 & 1 \\ 1 & 1 & 1 & 1 & 1 & 1 \end{bmatrix}^{-1} \begin{bmatrix} \bar{v}^*_{cm}(k) \\ \bar{v}^*_{diff_\alpha}(k) \\ \bar{v}^*_{diff_\beta}(k) \\ 1 \\ 1 \\ 1 \end{bmatrix} \quad (5\text{-}17)$$

- For intervals for which seq_2, seq_4 and seq_6 are imposed evenly distributed

$$\begin{bmatrix} d_{seq1}(k) \\ d_{seq2}(k) \\ d_{seq3}(k) \\ d_{seq4}(k) \\ d_{seq5}(k) \\ d_{seq6}(k) \end{bmatrix} = \begin{bmatrix} v^*_{cm_{seq1}} & v^*_{cm_{seq2}} & v^*_{cm_{seq3}} & v^*_{cm_{seq4}} & v^*_{cm_{seq5}} & v^*_{cm_{seq6}} \\ v^*_{diff\alpha_{seq1}} & v^*_{diff\alpha_{seq2}} & v^*_{diff\alpha_{seq3}} & v^*_{diff\alpha_{seq4}} & v^*_{diff\alpha_{seq5}} & v^*_{diff\alpha_{seq6}} \\ v^*_{diff\beta_{seq1}} & v^*_{diff\beta_{seq2}} & v^*_{diff\beta_{seq3}} & v^*_{diff\beta_{seq4}} & v^*_{diff\beta_{seq5}} & v^*_{diff\beta_{seq6}} \\ 1 & 3 & 1 & 0 & 1 & 0 \\ 1 & 0 & 1 & 3 & 1 & 0 \\ 1 & 1 & 1 & 1 & 1 & 1 \end{bmatrix}^{-1} \begin{bmatrix} \bar{v}^*_{cm}(k) \\ \bar{v}^*_{diff_\alpha}(k) \\ \bar{v}^*_{diff_\beta}(k) \\ 1 \\ 1 \\ 1 \end{bmatrix} \quad (5\text{-}18)$$

5.4.3. Direct control of differential currents

It is supposed in this section that the main controller of the power converter calculates the average common mode voltage to apply to the load at time t_k, $\bar{v}^*_{cm}(k)$ is thus externally imposed. A secondary controller must now define the proper differential voltage that must be applied at the converter outputs in order to control the average value of the differential currents i_{diff_α} and i_{diff_β} over the switching period denoted $\bar{i}_{diff_\alpha}$ and $\bar{i}_{diff_\beta}$.

It can be noted, as shown previously, that balanced duty cycles in a sequence lead to zero average differential mode voltages. This situation is identical to that encountered in an interleaved multi-cell power converter in case a constant imposed duty-cycle. Conversely if zero average values are imposed for $\bar{v}^*_{diff_\alpha}(k)$ and $\bar{v}^*_{diff_\beta}(k)$, the duty cycles of each vectors are well balanced

within the sequence. Nevertheless, this configuration can lead to a non-zero value of $\bar{i}_{diff_\alpha}$ and $\bar{i}_{diff_\beta}$ and thus to unwanted magnetic states in the cores of the coupled inductors. This mean that $\bar{v}^*_{diff_\alpha}(k)$ and $\bar{v}^*_{diff_\beta}(k)$ must be modified to bring the average value of the two currents toward zero.

There are two possible strategies that can be implemented to obtain this result in one switching period:

- First, we can impose the average currents to be zero over the switching period and calculate the proper average differential voltage to apply for this purpose. But this strategy is difficult to implement due to voltage saturations to which it can lead as the differential inductances are high
- Secondly, we can use a less dynamic strategy for which the differential currents final values at $t = t_{k+1}$ are imposed in order to insure a zero average value for the next switching period (if the imposed common mode voltage stays the same)

We are going to explain the last strategy. The principle is as follows:

1) Initial values of differential currents must be measured at t_k: $i_{diff_\alpha}(k)$ and $i_{diff_\beta}(k)$
2) Duty cycles of each sequences are first calculated using zero references for $\bar{v}^*_{diff_\alpha}(k)$ and $\bar{v}^*_{diff_\beta}(k)$

$$\begin{bmatrix} d_{seq1}(k) \\ d_{seq2}(k) \\ d_{seq3}(k) \\ d_{seq4}(k) \\ d_{seq5}(k) \\ d_{seq6}(k) \end{bmatrix} = \boldsymbol{A}^{-1} \begin{bmatrix} \bar{v}^*_{cm}(k) \\ 0 \\ 0 \\ 1 \\ 1 \\ 1 \end{bmatrix} \qquad (5\text{-}19)$$

For intervals for which seq_1, seq_3 and seq_5 are imposed evenly distributed:

$$\mathbf{A} = \begin{bmatrix} v^*_{cm_{seq1}} & v^*_{cm_{seq2}} & v^*_{cm_{seq3}} & v^*_{cm_{seq4}} & v^*_{cm_{seq5}} & v^*_{cm_{seq6}} \\ v^*_{diff\alpha_{seq1}} & v^*_{diff\alpha_{seq2}} & v^*_{diff\alpha_{seq3}} & v^*_{diff\alpha_{seq4}} & v^*_{diff\alpha_{seq5}} & v^*_{diff\alpha_{seq6}} \\ v^*_{diff\beta_{seq1}} & v^*_{diff\beta_{seq2}} & v^*_{diff\beta_{seq3}} & v^*_{diff\beta_{seq4}} & v^*_{diff\beta_{seq5}} & v^*_{diff\beta_{seq6}} \\ 3 & 1 & 0 & 1 & 0 & 1 \\ 0 & 1 & 3 & 1 & 0 & 1 \\ 1 & 1 & 1 & 1 & 1 & 1 \end{bmatrix}$$

For intervals for which seq_2, seq_4 and seq_6 are imposed evenly distributed:

$$\mathbf{A} = \begin{bmatrix} v^*_{cm_{seq1}} & v^*_{cm_{seq2}} & v^*_{cm_{seq3}} & v^*_{cm_{seq4}} & v^*_{cm_{seq5}} & v^*_{cm_{seq6}} \\ v^*_{diff\alpha_{seq1}} & v^*_{diff\alpha_{seq2}} & v^*_{diff\alpha_{seq3}} & v^*_{diff\alpha_{seq4}} & v^*_{diff\alpha_{seq5}} & v^*_{diff\alpha_{seq6}} \\ v^*_{diff\beta_{seq1}} & v^*_{diff\beta_{seq2}} & v^*_{diff\beta_{seq3}} & v^*_{diff\beta_{seq4}} & v^*_{diff\beta_{seq5}} & v^*_{diff\beta_{seq6}} \\ 1 & 3 & 1 & 0 & 1 & 0 \\ 1 & 0 & 1 & 3 & 1 & 0 \\ 1 & 1 & 1 & 1 & 1 & 1 \end{bmatrix}$$

3) From the duty cycles values, the chosen order for the sequence of space vector and the currents initial values, we can use the model equation (5-13) to calculate the average of each differential

currents arising from these conditions. The model equation gives the instantaneous currents.

It can be noted that the dynamic during the short time of application of the voltages is mainly defined by the integral part only. The resistive term leads to a long time effect. For fast transient study, we can consider that the resistive term can be neglected and equation (5-13) becomes:

$$\begin{bmatrix} i_{diff_\alpha} \\ i_{diff_\beta} \end{bmatrix} \approx \begin{bmatrix} \frac{1}{(L-M)s} & 0 \\ 0 & \frac{1}{(L-M)s} \end{bmatrix} \begin{bmatrix} v_{diff_\alpha} \\ v_{diff_\beta} \end{bmatrix} \qquad (5\text{-}20)$$

From this model, the trajectories of the currents can be calculated as well as their mean values:

$$\begin{bmatrix} i_{diff_\alpha}(t_k + d_{seq1}T) \\ i_{diff_\alpha}(t_k + (d_{seq1} + d_{seq2})T) \\ i_{diff_\alpha}(t_k + (d_{seq1} + d_{seq2} + d_{seq3})T) \\ i_{diff_\alpha}(t_k + (d_{seq1} + d_{seq2} + d_{seq3} + d_{seq4})T) \\ i_{diff_\alpha}(t_k + (d_{seq1} + d_{seq2} + d_{seq3} + d_{seq4} + d_{seq5})T) \\ i_{diff_\alpha}(t_k + T) \end{bmatrix} = \begin{bmatrix} i_{diff_\alpha}(k) \\ i_{diff_\alpha}(k) \\ i_{diff_\alpha}(k) \\ i_{diff_\alpha}(k) \\ i_{diff_\alpha}(k) \\ i_{diff_\alpha}(k) \end{bmatrix} + \frac{v_i\, T}{(L-M)} \boldsymbol{v}_{diff\alpha_p} \begin{bmatrix} d_{seq1}(k) \\ d_{seq2}(k) \\ d_{seq3}(k) \\ d_{seq4}(k) \\ d_{seq5}(k) \\ d_{seq6}(k) \end{bmatrix} \qquad (5\text{-}21)$$

Where

$$\boldsymbol{v}_{diff\alpha_p} = \begin{bmatrix} v^*_{diff\alpha_{seq1}} & 0 & 0 & 0 & 0 & 0 \\ v^*_{diff\alpha_{seq1}} & v^*_{diff\alpha_{seq2}} & 0 & 0 & 0 & 0 \\ v^*_{diff\alpha_{seq1}} & v^*_{diff\alpha_{seq2}} & v^*_{diff\alpha_{seq3}} & 0 & 0 & 0 \\ v^*_{diff\alpha_{seq1}} & v^*_{diff\alpha_{seq2}} & v^*_{diff\alpha_{seq3}} & v^*_{diff\alpha_{seq4}} & 0 & 0 \\ v^*_{diff\alpha_{seq1}} & v^*_{diff\alpha_{seq2}} & v^*_{diff\alpha_{seq3}} & v^*_{diff\alpha_{seq4}} & v^*_{diff\alpha_{seq5}} & 0 \\ v^*_{diff\alpha_{seq1}} & v^*_{diff\alpha_{seq2}} & v^*_{diff\alpha_{seq3}} & v^*_{diff\alpha_{seq4}} & v^*_{diff\alpha_{seq5}} & v^*_{diff\alpha_{seq6}} \end{bmatrix}$$

$$\begin{bmatrix} i_{diff_\beta}(t_k + d_{seq1}T) \\ i_{diff_\beta}(t_k + (d_{seq1} + d_{seq2})T) \\ i_{diff_\beta}(t_k + (d_{seq1} + d_{seq2} + d_{seq3})T) \\ i_{diff_\beta}(t_k + (d_{seq1} + d_{seq2} + d_{seq3} + d_{seq4})T) \\ i_{diff_\beta}(t_k + (d_{seq1} + d_{seq2} + d_{seq3} + d_{seq4} + d_{seq5})T) \\ i_{diff_\beta}(t_k + T) \end{bmatrix} = \begin{bmatrix} i_{diff_\beta}(k) \\ i_{diff_\beta}(k) \\ i_{diff_\beta}(k) \\ i_{diff_\beta}(k) \\ i_{diff_\beta}(k) \\ i_{diff_\beta}(k) \end{bmatrix} + \frac{v_i\, T}{(L-M)} \boldsymbol{v}_{diff\beta_p} \begin{bmatrix} d_{seq1}(k) \\ d_{seq2}(k) \\ d_{seq3}(k) \\ d_{seq4}(k) \\ d_{seq5}(k) \\ d_{seq6}(k) \end{bmatrix} \quad (5\text{-}22)$$

Where

$$\boldsymbol{v}_{diff\beta_p} = \begin{bmatrix} v^*_{diff\beta_{seq1}} & 0 & 0 & 0 & 0 & 0 \\ v^*_{diff\beta_{seq1}} & v^*_{diff\beta_{seq2}} & 0 & 0 & 0 & 0 \\ v^*_{diff\beta_{seq1}} & v^*_{diff\beta_{seq2}} & v^*_{diff\beta_{seq3}} & 0 & 0 & 0 \\ v^*_{diff\beta_{seq1}} & v^*_{diff\beta_{seq2}} & v^*_{diff\beta_{seq3}} & v^*_{diff\beta_{seq4}} & 0 & 0 \\ v^*_{diff\beta_{seq1}} & v^*_{diff\beta_{seq2}} & v^*_{diff\beta_{seq3}} & v^*_{diff\beta_{seq4}} & v^*_{diff\beta_{seq5}} & 0 \\ v^*_{diff\beta_{seq1}} & v^*_{diff\beta_{seq2}} & v^*_{diff\beta_{seq3}} & v^*_{diff\beta_{seq4}} & v^*_{diff\beta_{seq5}} & v^*_{diff\beta_{seq6}} \end{bmatrix}$$

At this point, it can be noted that $i_{diff_\alpha}(t_k + T) = i_{diff_\alpha}(k+1) = i_{diff_\alpha}(k)$ and $i_{diff_\beta}(t_k + T) = i_{diff_\beta}(k+1) = i_{diff_\beta}(k)$ as shown by equations (5-23) and (5-24):

$$i_{diff_\alpha}(t_k + T) = i_{diff_\alpha}(t_k) + \frac{v_i\, T}{(L-M)} \bar{v}^*_{diff_\alpha}(k) = i_{diff_\alpha}(t_k) \text{ for } \bar{v}^*_{diff_\alpha}(k) = 0 \quad (5\text{-}23)$$

$$i_{diff_\beta}(t_k + T) = i_{diff_\beta}(t_k) + \frac{v_i\, T}{(L-M)} \bar{v}^*_{diff_\beta}(k) = i_{diff_\beta}(t_k) \text{ for } \bar{v}^*_{diff_\beta}(k) = 0 \quad (5\text{-}24)$$

The mean values of the differential current are calculated from (5-21) and (5-22):

$$\bar{i}_{diff_\alpha}(k) = \frac{1}{2} \begin{bmatrix} 1 \\ 1 \\ 1 \\ 1 \\ 1 \\ 1 \end{bmatrix}^t \boldsymbol{d}_p \begin{bmatrix} i_{diff_\alpha}(t_k) \\ i_{diff_\alpha}(t_k + d_{seq1}T) \\ i_{diff_\alpha}(t_k + (d_{seq1} + d_{seq2})T) \\ i_{diff_\alpha}(t_k + (d_{seq1} + d_{seq2} + d_{seq3})T) \\ i_{diff_\alpha}(t_k + (d_{seq1} + d_{seq2} + d_{seq3} + d_{seq4})T) \\ i_{diff_\alpha}(t_k + (d_{seq1} + d_{seq2} + d_{seq3} + d_{seq4} + d_{seq5})T) \\ i_{diff_\alpha}(t_k + T) \end{bmatrix} \quad (5\text{-}25)$$

$$\bar{i}_{diff_\beta}(k) = \frac{1}{2}\begin{bmatrix}1\\1\\1\\1\\1\\1\end{bmatrix}^t \boldsymbol{d}_p \begin{bmatrix} i_{diff_\beta}(t_k) \\ i_{diff_\beta}(t_k + d_{seq1}T) \\ i_{diff_\beta}(t_k + (d_{seq1} + d_{seq2})T) \\ i_{diff_\beta}(t_k + (d_{seq1} + d_{seq2} + d_{seq3})T) \\ i_{diff_\beta}(t_k + (d_{seq1} + d_{seq2} + d_{seq3} + d_{seq4})T) \\ i_{diff_\beta}(t_k + (d_{seq1} + d_{seq2} + d_{seq3} + d_{seq4} + d_{seq5})T) \\ i_{diff_\beta}(t_k + T) \end{bmatrix} \qquad (5\text{-}26)$$

Where :

$$\boldsymbol{d}_p = \begin{bmatrix} d_{seq1}(k) & d_{seq1}(k) & 0 & 0 & 0 & 0 & 0 \\ 0 & d_{seq2}(k) & d_{seq2}(k) & 0 & 0 & 0 & 0 \\ 0 & 0 & d_{seq3}(k) & d_{seq3}(k) & 0 & 0 & 0 \\ 0 & 0 & 0 & d_{seq4}(k) & d_{seq4}(k) & 0 & 0 \\ 0 & 0 & 0 & 0 & d_{seq5}(k) & d_{seq5}(k) & 0 \\ 0 & 0 & 0 & 0 & 0 & d_{seq6}(k) & d_{seq6}(k) \end{bmatrix}$$

4) The strategy consist now to impose the correct average differential voltages ($\bar{v}^*_{diff_\alpha}(k)$ and $\bar{v}^*_{diff_\beta}(k)$) in order to reach the final differential currents at t_{k+1} that will lead to a zero average differential current for the next period $[t_{k+1}, t_{k+2}]$ while $\bar{v}^*_{diff_\alpha}(k+1) = 0$ and $\bar{v}^*_{diff_\beta}(k+1) = 0$ as shown in Figure 5-5.

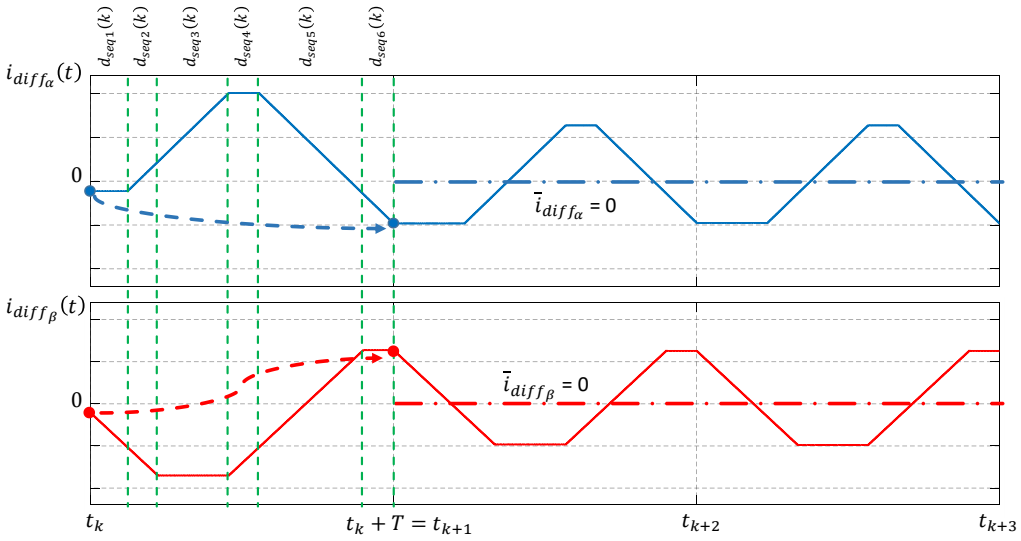

Figure 5-5 Direct control of differential currents in one switching period

This result is obtained if $i_{diff_\alpha}(t_k + T)$ and $i_{diff_\beta}(t_k + T)$ are equal to:

$$i_{diff_\alpha}(t_k + T) = i_{diff_\alpha}(k+1) = i_{diff_\alpha}(k) - \bar{i}_{diff_\alpha}(k) \qquad (5\text{-}27)$$

The

$$i_{diff_\beta}(t_k + T) = i_{diff_\beta}(k+1) = i_{diff_\beta}(k) - \bar{i}_{diff_\beta}(k) \quad (5\text{-}28)$$

differential voltages leading to the proper final values are given by combination of the equations (5-23) and (5-27), (5-24) and (5-28) the results will be:

$$\bar{v}^*_{diff_\alpha}(k) = -\bar{i}_{diff_\alpha}(k)\,\frac{(L-M)}{v_i\,T} \quad (5\text{-}29)$$

$$\bar{v}^*_{diff_\beta}(k) = -\bar{i}_{diff_\beta}(k)\,\frac{(L-M)}{v_i\,T} \quad (5\text{-}30)$$

5) The duty-cycles of each space vector imposed to the power converter can now be calculated as in equation (5-31):

$$\begin{bmatrix} d_{seq1}(k) \\ d_{seq2}(k) \\ d_{seq3}(k) \\ d_{seq4}(k) \\ d_{seq5}(k) \\ d_{seq6}(k) \end{bmatrix} = \boldsymbol{A}^{-1} \begin{bmatrix} \bar{v}^*_{cm}(k) \\ \bar{v}^*_{diff_\alpha}(k) \\ \bar{v}^*_{diff_\beta}(k) \\ 1 \\ 1 \\ 1 \end{bmatrix} \quad (5\text{-}31)$$

Figure 5-6 shows the flowchart summarizing the previous proposed method.

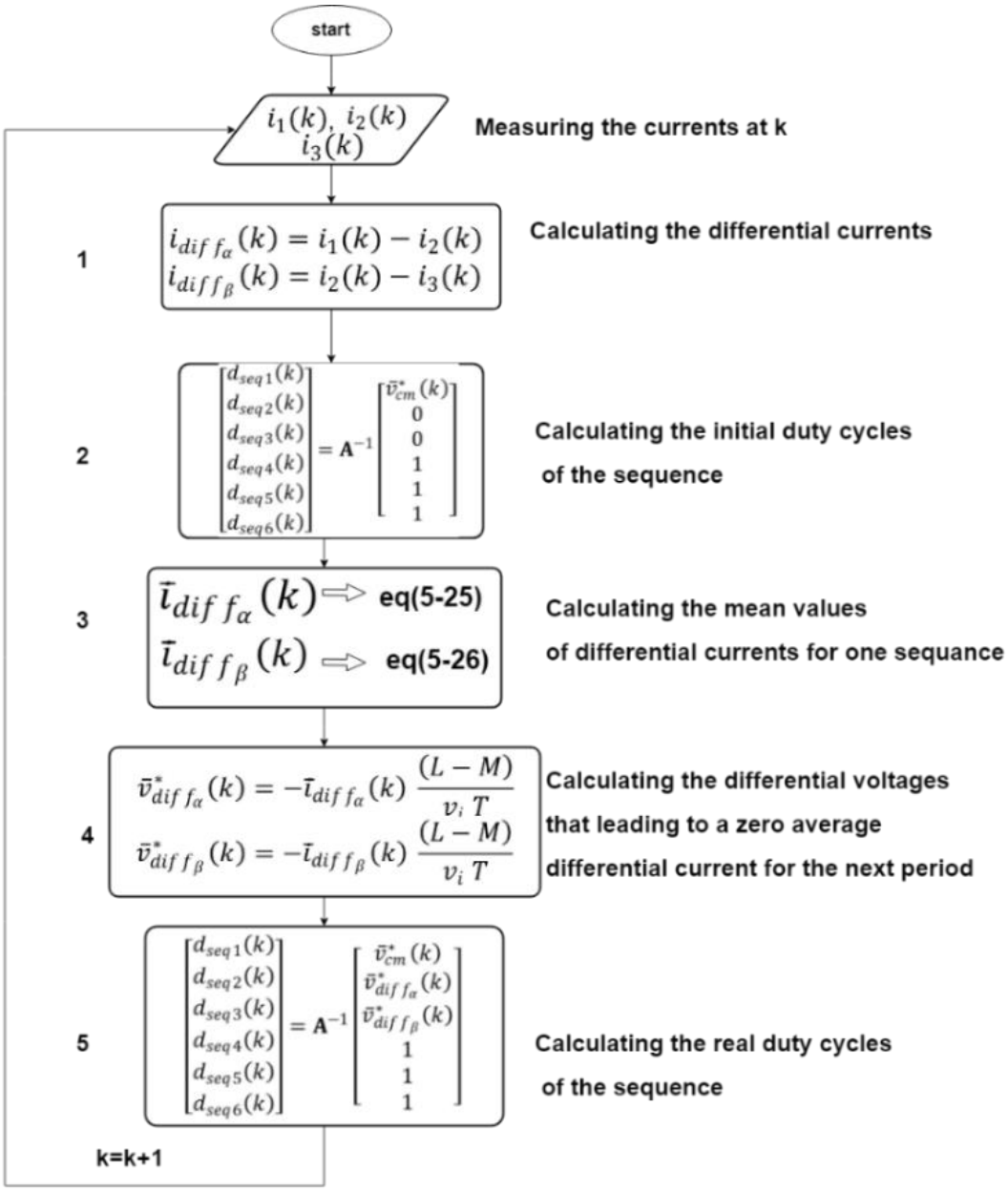

Figure 5-6 Flowchart of the proposed method for the direct control of differential currents

5.4.4. Choice of the space vector sequence

First, a sequence must be chosen so that there is only one switching cell at each space vector change. This mean that we can choose only 12 possible sequences as in Table 5-5, Table 5-6 and Table 5-7.

All these sequences can be obtained from the Figure 5-7 by reading the successive states from a chosen starting space vector and turning clockwise or counterclockwise.

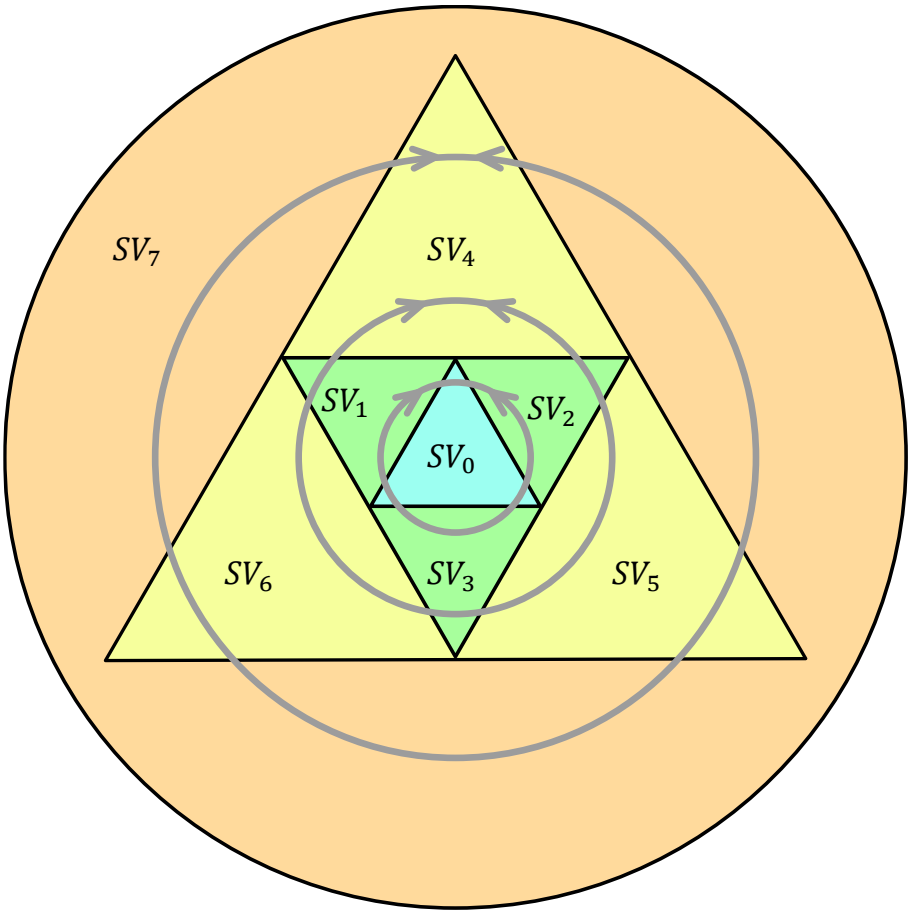

Figure 5-7 Figure helping to select a proper sequence

Important observation: more possibilities can be added. For example, we can divide the starting vector duration by half and add the removed half time at the end of the sequence.

Table 5-5 Valid sequences for level 0 to 1

Sequence	SV_{seq1}	SV_{seq2}	SV_{seq3}	SV_{seq4}	SV_{seq5}	SV_{seq6}
1	SV_0	SV_1	SV_0	SV_2	SV_0	SV_3
2	SV_3	SV_0	SV_1	SV_0	SV_2	SV_0
3	SV_0	SV_3	SV_0	SV_1	SV_0	SV_2
4	SV_2	SV_0	SV_3	SV_0	SV_1	SV_0
5	SV_0	SV_2	SV_0	SV_3	SV_0	SV_1
6	SV_1	SV_0	SV_2	SV_0	SV_3	SV_0
7	SV_0	SV_3	SV_0	SV_2	SV_0	SV_1
8	SV_1	SV_0	SV_3	SV_0	SV_2	SV_0
9	SV_0	SV_1	SV_0	SV_3	SV_0	SV_2
10	SV_2	SV_0	SV_1	SV_0	SV_3	SV_0
11	SV_0	SV_2	SV_0	SV_1	SV_0	SV_3
12	SV_3	SV_0	SV_2	SV_0	SV_1	SV_0

Table 5-6 Valid sequences for level 1 to 2

Sequence	SV_{seq1}	SV_{seq2}	SV_{seq3}	SV_{seq4}	SV_{seq5}	SV_{seq6}
1	SV_1	SV_4	SV_2	SV_5	SV_3	SV_6
2	SV_6	SV_1	SV_4	SV_2	SV_5	SV_3
3	SV_3	SV_6	SV_1	SV_4	SV_2	SV_5
4	SV_5	SV_3	SV_6	SV_1	SV_4	SV_2
5	SV_2	SV_5	SV_3	SV_6	SV_1	SV_4
6	SV_4	SV_2	SV_5	SV_3	SV_6	SV_1
7	SV_1	SV_6	SV_3	SV_5	SV_2	SV_4
8	SV_4	SV_1	SV_6	SV_3	SV_5	SV_2
9	SV_2	SV_4	SV_1	SV_6	SV_3	SV_5
10	SV_5	SV_2	SV_4	SV_1	SV_6	SV_3
11	SV_3	SV_5	SV_2	SV_4	SV_1	SV_6
12	SV_6	SV_3	SV_5	SV_2	SV_4	SV_1

Table 5-7 Valid sequences for level 2 to 3

Sequence	SV_{seq1}	SV_{seq2}	SV_{seq3}	SV_{seq4}	SV_{seq5}	SV_{seq6}
1	SV_4	SV_7	SV_5	SV_7	SV_6	SV_7
2	SV_7	SV_4	SV_7	SV_5	SV_7	SV_6
3	SV_6	SV_7	SV_4	SV_7	SV_5	SV_7
4	SV_7	SV_6	SV_7	SV_4	SV_7	SV_5
5	SV_5	SV_7	SV_6	SV_7	SV_4	SV_7
6	SV_7	SV_5	SV_7	SV_6	SV_7	SV_4
7	SV_4	SV_7	SV_6	SV_7	SV_5	SV_7
8	SV_7	SV_4	SV_7	SV_6	SV_7	SV_5
9	SV_5	SV_7	SV_4	SV_7	SV_6	SV_7
10	SV_7	SV_5	SV_7	SV_4	SV_7	SV_6
11	SV_6	SV_7	SV_5	SV_7	SV_4	SV_7
12	SV_7	SV_6	SV_7	SV_5	SV_7	SV_4

5.4.5. Impact of the choice of a sequence

All the sequences are not equivalent. Indeed, if we apply the required duty cycles to obtain the same $\vec{v}^*_{cm}(k)$ to each sequence while using zero references for $\vec{v}^*_{diff_\alpha}(k)$ and $\vec{v}^*_{diff_\beta}(k)$, we do not obtain the same mean differential currents $\bar{\imath}_{diff_\alpha}(k)$ and $\bar{\imath}_{diff_\beta}(k)$ as in equation (5-19).

To illustrate this fact, we draw in the figures below the value of the mean value of $\bar{i}_{diff_\alpha}(k)\frac{(L-M)}{v_i\,T}$ and $\bar{i}_{diff_\beta}(k)\frac{(L-M)}{v_i\,T}$ (for starting points $i_{diff_\alpha}(t_k)=0$ and $i_{diff_\beta}(t_k)=0$) for $\vec{v}^*_{cm}(k)$ varying from 0 to 3.

- For $\vec{v}^*_{cm}(k) \in [0,1]$:

It can be noted from Figure 5-8 that sequences are equivalent 2 by 2. The following sequences are equivalent:

Sequences 1 and 6	Sequences 4 and 5	Sequences 8 and 9
Sequences 2 and 3	Sequences 7 and 12	Sequences 10 and 11

This mean that starting for the first space vector with $v_{cm}^{*} = 0$ or $v_{cm}^{*} = 1$ has no impact on the mean value of the differential currents. In these graphs, the maximum values of $\left|\bar{i}_{diff_{\alpha,\beta}}(k)\frac{(L-M)}{v_i\,T}\right|$ are either $1/9$ or $2/9$ and these values are zero for $\bar{v}_{cm}^{*}(k) = 0$.

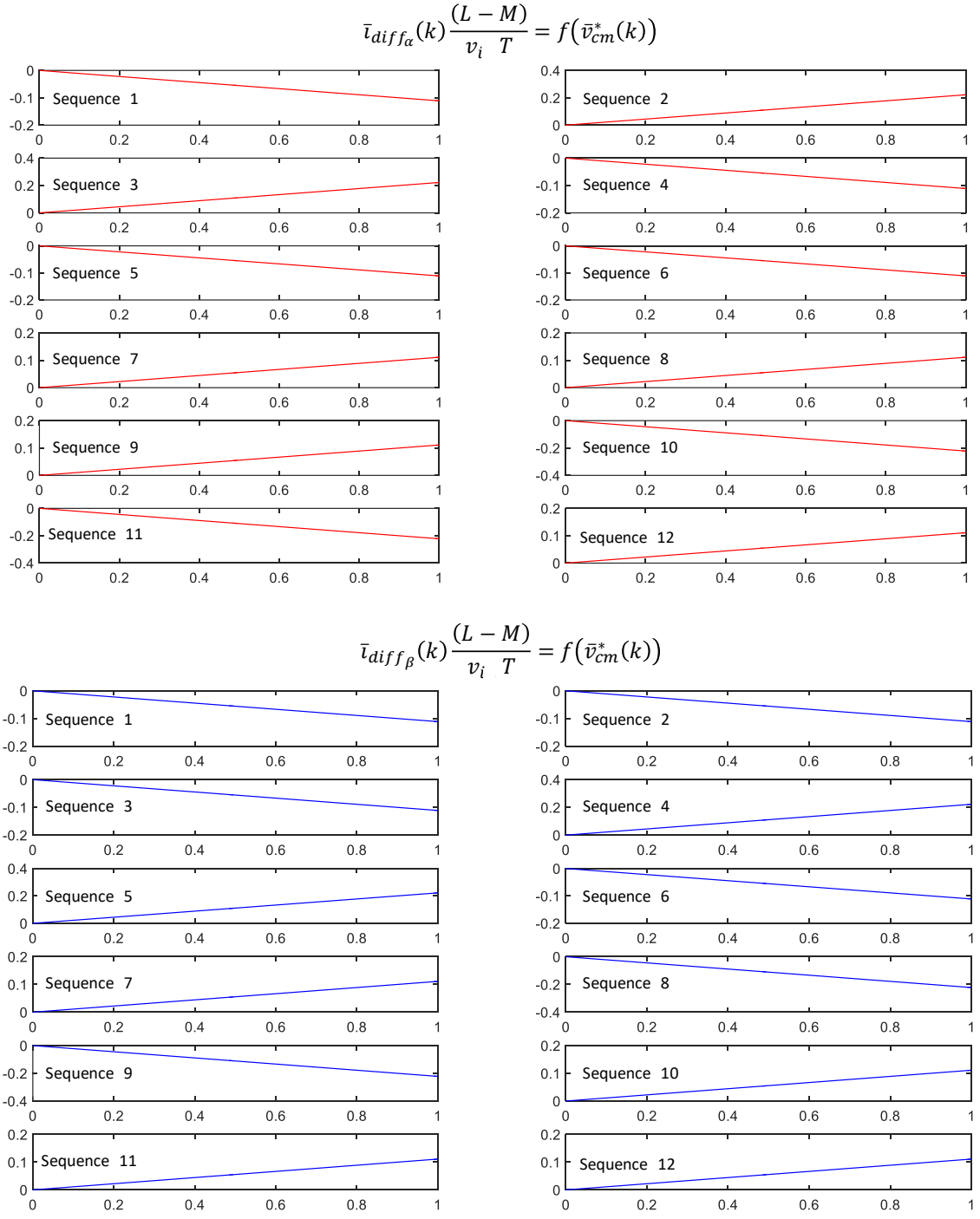

Figure 5-8 Impact of sequences on the average differential currents when $\bar{v}_{cm}^{*}(k) \in [0,1]$

- For $\bar{v}_{cm}^{*}(k) \in [1,2]$:

For this interval, the sequences have all a different impact on both $\bar{i}_{diff_\alpha}(k)$ and $\bar{i}_{diff_\beta}(k)$. In these graphs, the maximum values of $\left|\bar{i}_{diff_{\alpha,\beta}}(k)\frac{(L-M)}{v_i\,T}\right|$ are either $1/9$ or $2/9$.

$$\bar{\imath}_{diff_\alpha}(k)\frac{(L-M)}{v_i\ T} = f\left(\bar{v}_{cm}^{*}(k)\right)$$

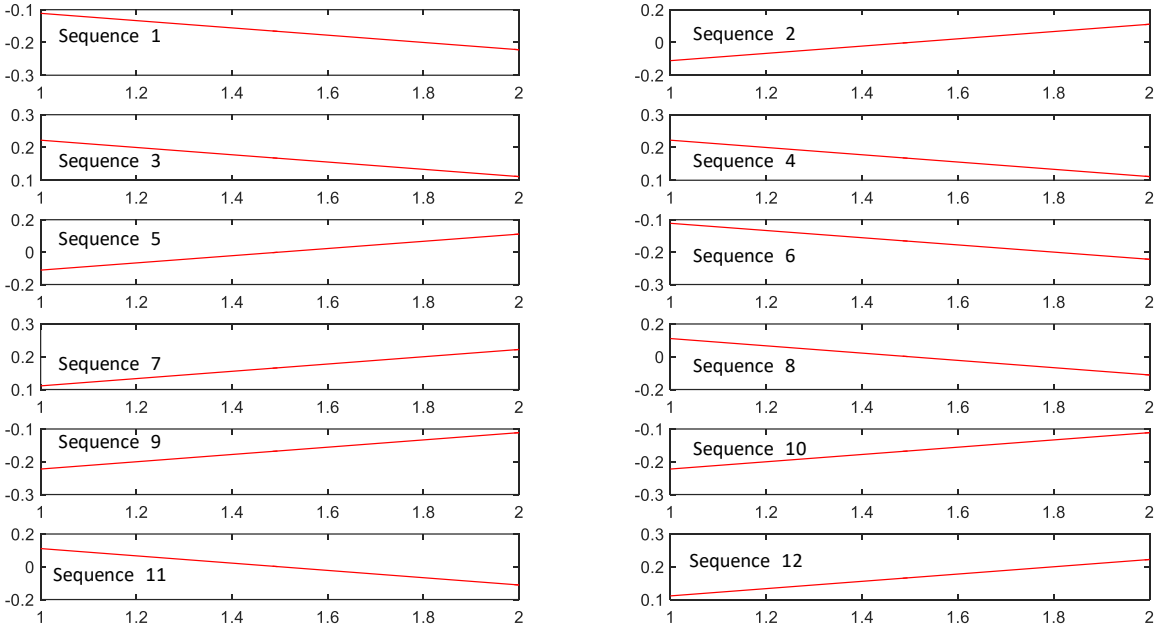

$$\bar{\imath}_{diff_\beta}(k)\frac{(L-M)}{v_i\ T} = f\left(\bar{v}_{cm}^{*}(k)\right)$$

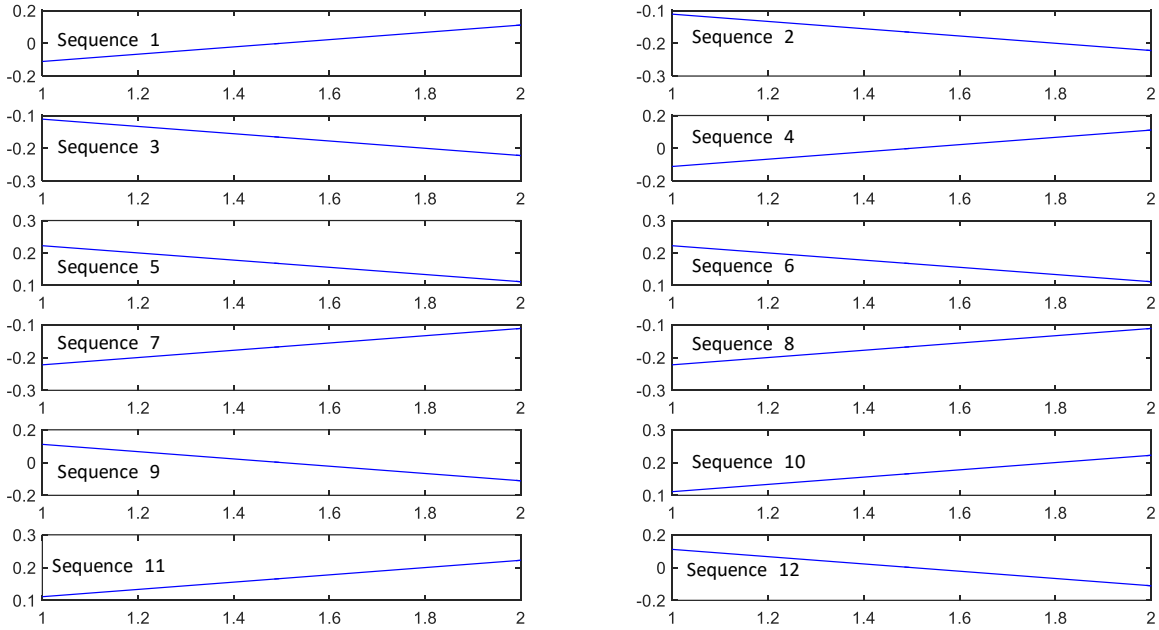

Figure 5-9 Impact of sequences on the average differential currents when $\bar{v}_{cm}^{*}(k) \in [1,2]$

- For $\bar{v}_{cm}^{*}(k) \in [2,3]$:

We can note as in first interval that the sequences are equivalent 2 by 2. The following sequences are equivalent:

Sequences 1 and 2	Sequences 5 and 6	Sequences 9 and 10
Sequences 3 and 4	Sequences 7 and 8	Sequences 11 and 12

In these graphs, the maximum values of $\left|\bar{\imath}_{diff_{\alpha,\beta}}(k)\frac{(L-M)}{v_i\,T}\right|$ are either $1/9$ or $2/9$ and these values are zero for $\bar{v}_{cm}^{*}(k) = 3$.

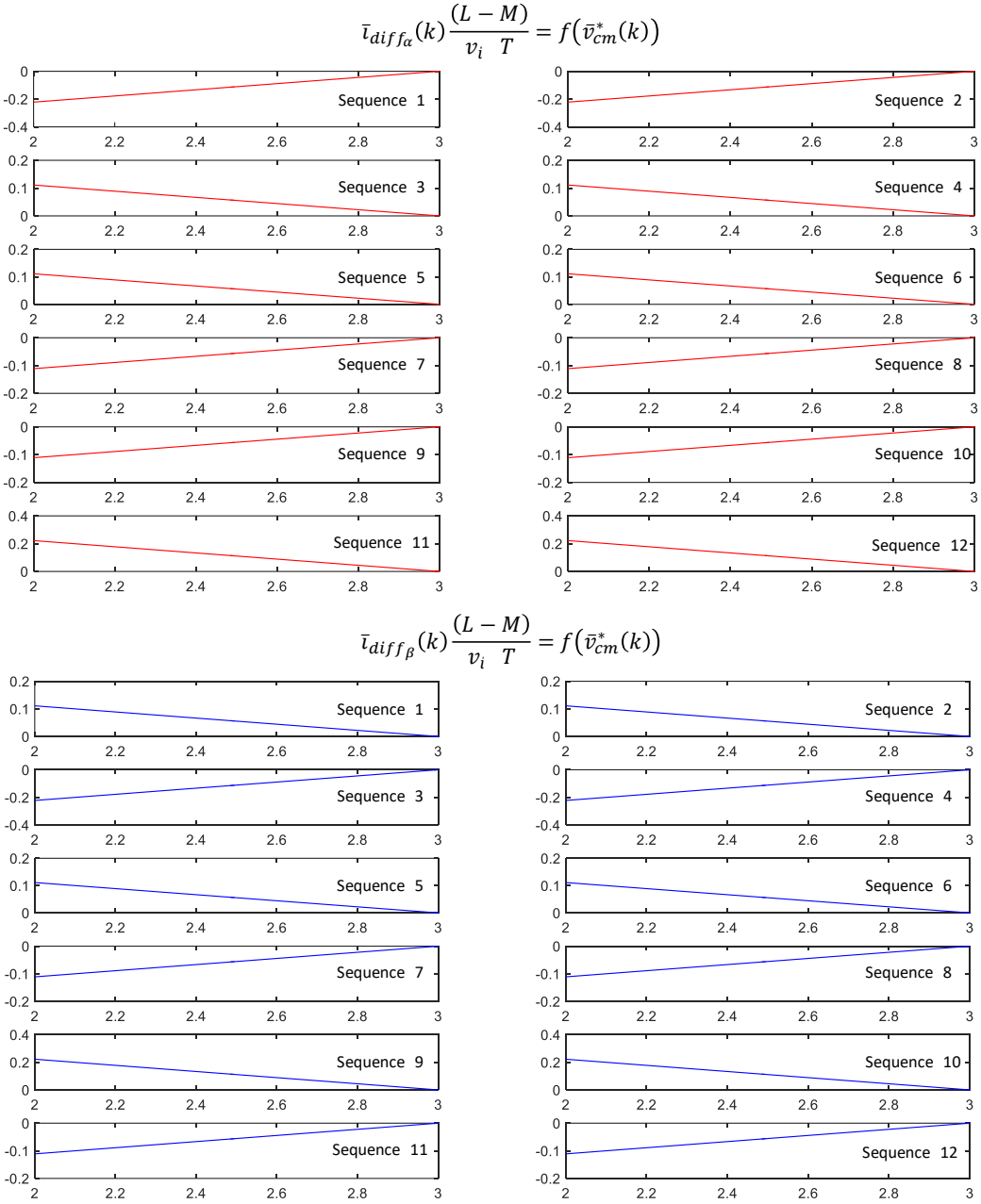

Figure 5-10 Impact of sequences on the average differential currents when $\bar{v}_{cm}^{*}(k) \in [2,3]$

5.4.6. Levels transitions

We have demonstrated in the previous section that the choice of the sequence influences the behavior of the structure regarding the differential currents. If all the sequences are possible at each level, the PWM generator must nevertheless insure a correct transition between each switching period. This means that the space vectors should be adjacent (only one cell switching between two successive space vectors) or identical at both sides of the switching period boundary (at $k\,T$).

When $\bar{v}_{cm}^{*}(k)$ stays in the same level interval [0,1], [1,2] or [2,3], this can be done by repeating the same sequence. Indeed, the last space vector of the sequence is adjacent to the first one.

When $\bar{v}_{cm}^{*}(k)$ go from an interval to another, only few sequences can insure that the space vectors at both sides are adjacent. For *Sequence n°1* in the level interval [0,1], the next sequences can be *Sequences n°2, 3, 4, 10,11 or 12* in the level interval [1,2]. Nevertheless, it can be interesting for the control process (to avoid steps in $\bar{\imath}_{diff_\alpha}$ and $\bar{\imath}_{diff_\beta}$) to insure a continuity of $\bar{\imath}_{diff_\alpha}$ and $\bar{\imath}_{diff_\beta}$ at level change. This property is only verified by *Sequence n°2* in the level interval [1,2] then by *Sequence n°3* in the level interval [2,3].

There are therefore few sets of sequences verifying the two conditions:

- Sequence n°1 in [0,1], Sequence n°2 in [1,2], Sequence n°3 in [2,3]
- Sequence n°3 in [0,1], Sequence n°4 in [1,2], Sequence n°5 in [2,3]
- Sequence n°5 in [0,1], Sequence n°6 in [1,2], Sequence n°1 in [2,3]

The last set of sequences leads to a symmetrical response for $\bar{i}_{diff_\alpha}$ and $\bar{i}_{diff_\beta}$. This one is used in the following developments. The corresponding values for $\bar{i}_{diff_\alpha}$ and $\bar{i}_{diff_\beta}$ for all levels from 0 to 3 are given in the Figure 5-11.

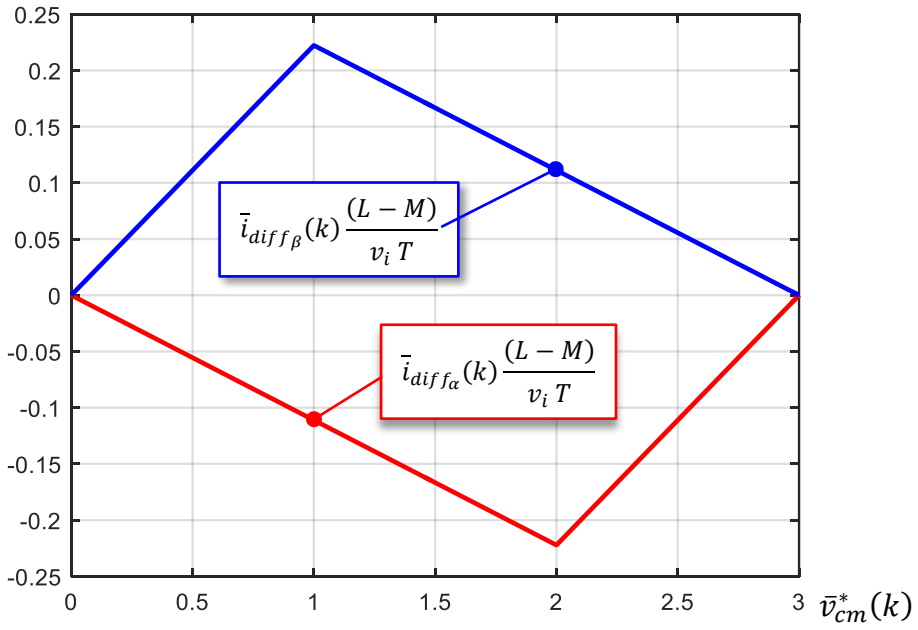

Figure 5-11 The average differential currents when of sequences 5,6,1 and $\bar{v}_{cm}^{*}(k) \in [0,3]$

5.4.7. Control point of view of the proposed strategy

The discrete control model of the direct differential currents control method is presented in Figure 5-12. In this model, effects of $\bar{v}^*_{cm}(k)$ imposed by the main controller are seen has perturbations as well as those due to instantaneous variations of space vector sequence on $v_{diff_{\alpha,\beta}}(t)$ denoted $\tilde{v}^*_{diff_{\alpha,\beta}}(t)$ in the schematic. From a control point of view, $\tilde{v}^*_{diff_{\alpha,\beta}}(t)$ has no impact on the control as the average value of this perturbation is zero over the switching period and as the differential currents are sampled at the same frequency.

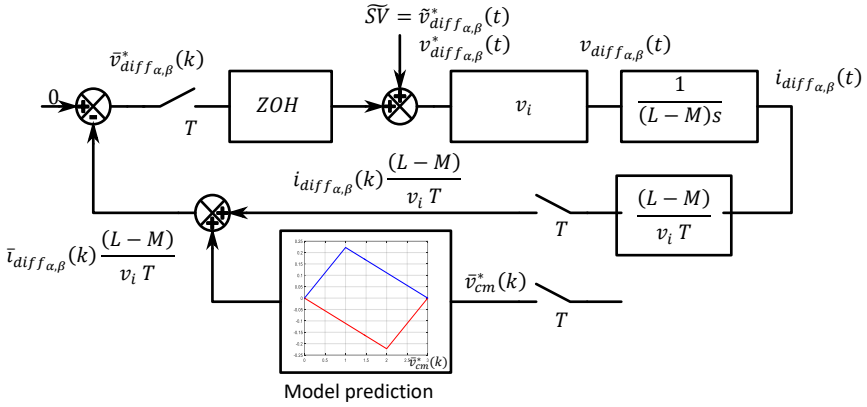

Figure 5-12 The block diagram of controlling differential currents

The z model of the whole system is shown in Figure 5-13. From the perturbation point of view due to variation of $\bar{v}^*_{cm}(k)$ the closed loop transfer function is

$$H_p(z) = 1 - z^{-1}. \qquad (5\text{-}32)$$

This means that the impact of a perturbation on $\bar{\imath}_{diff_{\alpha,\beta}}$ is eliminated in one switching period for a step variation of $\bar{v}^*_{cm}(k)$.

From the reference point of view (set to 0 in the figure), the closed loop transfer function is

$$H_r(z) = z^{-1} \qquad (5\text{-}33)$$

Thus $\bar{i}_{diff_{\alpha,\beta}}$ is sent to zero in one period.

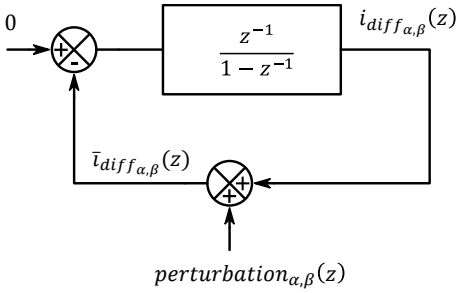

Figure 5-13 The z model of the control system

5.4.8. Simulation

The following simulations are done based on the parameters listed in Table 5-1 for variations of $\bar{v}_{cm}^{*}$ within a level interval or for transitions going from one level interval to another. Figure 5-14 shows i_{cm}, $i_{diff_{\alpha}}$ and $i_{diff_{\beta}}$ waveforms. Figure 5-14-a are the results obtained when the reference average common mode voltage $\bar{v}_{cm}^{*}$ change from 0.3 to 0.7, Figure 5-14-b when $\bar{v}_{cm}^{*}$ change from 1.3 to 1.7 and Figure 5-14-c when $\bar{v}_{cm}^{*}$ change from 2.3 to 2.7.

In all these figures we can note that the differential mode currents show oscillations around zero and that their average values are near zero as shown in Figure 5-14-d giving the moving average of differential currents over a switching period duration. In this figures, $\bar{v}_{cm}^{*}$ is imposed, the common mode current is thus uncontrolled. This current shows a small overshoot in the transient region due to interactions between the equivalent common mode inductance and the load elements (resistance in parallel with capacitor). This mode will be controlled in the next section.

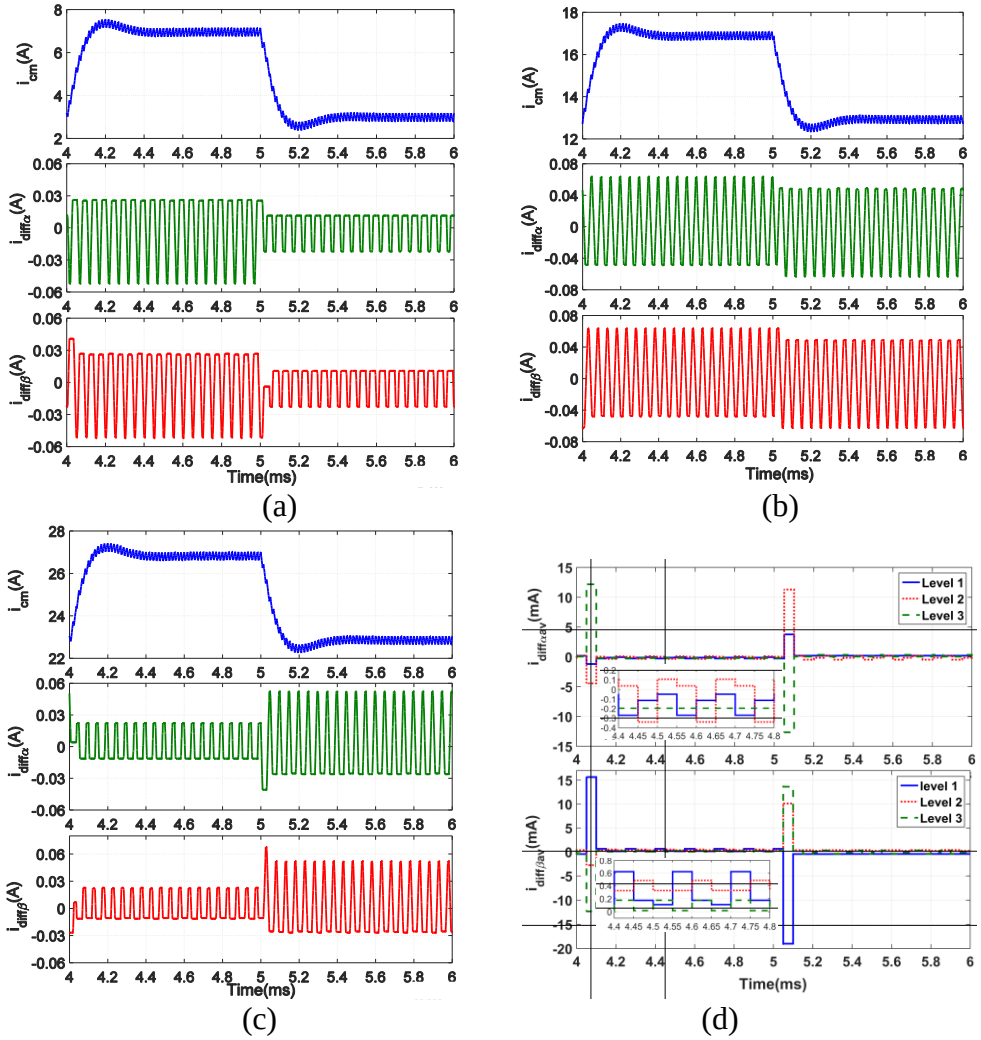

Figure 5-14 Simulation results for $\bar{v}_{cm}^{*}$ steps within one level interval:(a) when $\bar{v}_{cm}^{*} \in [0,1]$ (b) when $\bar{v}_{cm}^{*} \in [1,2]$ (c) when $\bar{v}_{cm}^{*} \in [2,3]$ (d) moving average of differential currents

Figure 5-15 shows the simulation results when the imposed common mode voltage $\bar{v}_{cm}^{*}$ jumps from one level interval to another. Figure 5-15-a are the results obtained when the reference average common mode voltage $\bar{v}_{cm}^{*}$ change from 0.7 to 1.7, Figure 5-15-b when $\bar{v}_{cm}^{*}$ change from 1.7 to 2.7 and Figure 5-15-c when $\bar{v}_{cm}^{*}$ change from 0.7 to 2.7.

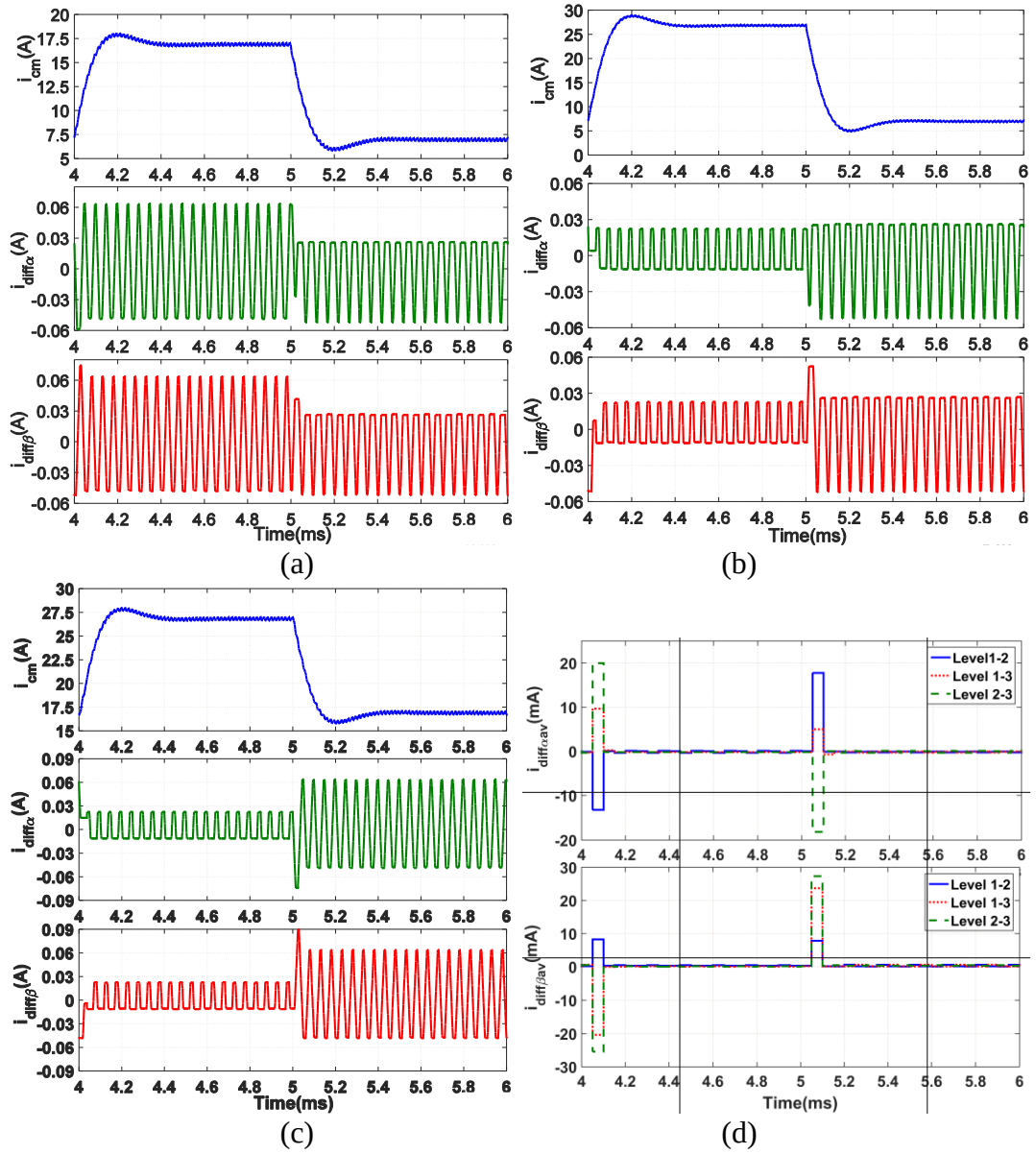

Figure 5-15 Simulation results for $\bar{v}_{cm}^{*}$ steps variation from one level interval to another: (a) when $\bar{v}_{cm}^{*} \in [0,1] \leftrightarrow \bar{v}_{cm}^{*} \in [1,2]$, (b) when $\bar{v}_{cm}^{*} \in [1,2] \leftrightarrow \bar{v}_{cm}^{*} \in [2,3]$ (c) when $\bar{v}_{cm}^{*} \in [0,1] \leftrightarrow \bar{v}_{cm}^{*} \in [2,3]$ (d) moving average of differential currents

These last results are similar to those obtained when $\bar{v}_{cm}^{*}$ vary within the same level interval. The main difference is here a higher overshoot of differential currents during one switching period after the transient. Nevertheless, differential mode currents are still well controlled with a zero average value after one switching period.

5.5. MPC with space vector placement

We have seen that the choice of the space vector sequence influences the behavior of the structure regarding the differential currents waveforms during one switching period. The choice of the best sequence can be done by implementing a MPC strategy. Figure 3-1 shows a possible block diagram of a possible implementation of the control of the whole system. In this diagram, the main controller (here PI controller) is designed to control the common mode current ($i_{cm} = i_o$). The output of this controller gives the common mode average voltage $\overline{v}^*_{cm}(k)$ that has to be generated by the converter. A level limitation prevents $\overline{v}^*_{cm}(k)$ from exiting interval [0,3]. The secondary direct controller (MPC with vector placement) determines the best space vector sequence and calculates the duty cycles for each space vectors in order to obtain the proper $\bar{v}^*_{cm}(k)$, $\bar{v}^*_{diff_\alpha}(k)$ and $\bar{v}^*_{diff_\beta}(k)$ while minimizing a given cost function depending on the currents waveforms.

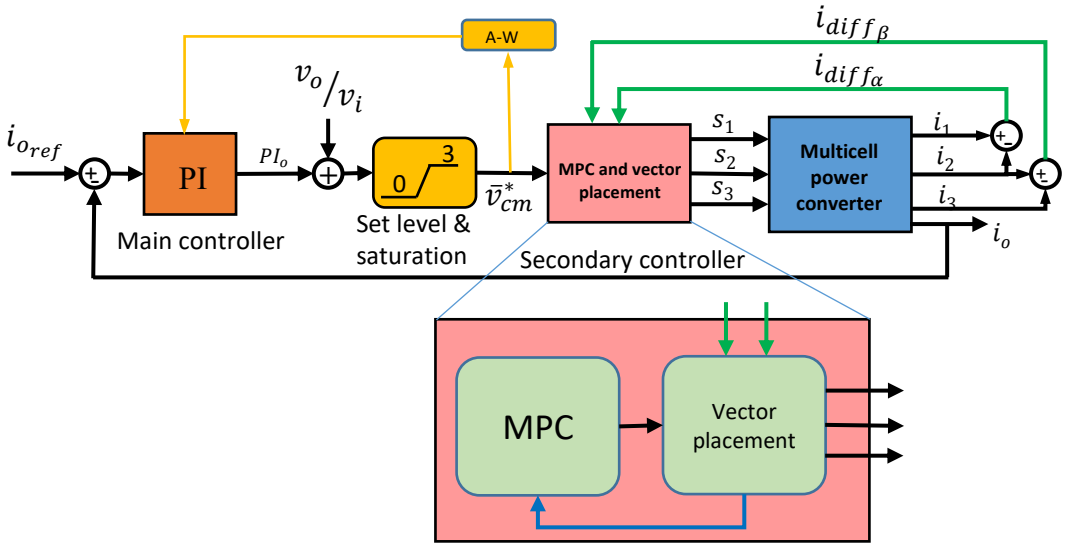

Figure 5-16 Block diagram of the whole control system

5.5.1. Main controller

The PI controller is used to regulate or track the common mode current. The output of the controller (PI_o) is used to calculate the common mode average voltage ($\bar{v}^*_{cm}$) used as common mode reference level by the secondary controller. $\bar{v}^*_{cm}$ is given by:

$$\bar{v}^*_{cm} = PI_o + \frac{v_o}{v_i} \qquad (5\text{-}34)$$

The anti-windup ($A-W$) algorithm is used to stop the integral part of the PI-controller when the common mode average voltage is out of the saturation range $\bar{v}^*_{cm}(k) \in [0,3]$. The PI-controller is a single input single output system, the tuning of the PI-parameters (K_p and K_i) can be done by root locus methodology.

5.5.2. Secondary controller

The secondary controller consists from two parts, the first part corresponds to the previous proposed control algorithm described in section 5.4.3 and the second part consists in the optimization algorithm implemented to find the optimal sequence via a FCS-MPC principle.

5.5.2.1 The cost function

The quadratic form of the cost function takes the form given in equation (2-6). It consists of two parts. The first part gives the deviation of average differential currents from the zero reference during the switching period (T). The last part gives a value depending on the maximum and minimum values reached by the differential currents during the switching period (T) .The weighting matrices $\boldsymbol{Q}$ and $\boldsymbol{g}_1$ are positive semi-definite matrices that can be used to tradeoff between the steady state error and the currents ripple. So, (q, ρ) is a set of two scalar values that are used to tune the objective function to have the desired behavior.

$$\boldsymbol{J} = \left(\bar{\boldsymbol{\imath}}_{diff}\right)' \boldsymbol{Q} \left(\bar{\boldsymbol{\imath}}_{diff}\right) + \left(\boldsymbol{i}_{diff_{\alpha,\beta\_max}}\right)' \boldsymbol{g_1} \left(\boldsymbol{i}_{diff_{\alpha,\beta\_max}}\right) + \left(\boldsymbol{i}_{diff_{\alpha,\beta\_min}}\right)' \boldsymbol{g_1} \left(\boldsymbol{i}_{diff_{\alpha,\beta\_min}}\right) \qquad (5\text{-}35)$$

Where

$$\bar{\boldsymbol{\imath}}_{diff} = \begin{bmatrix} i_{diff_\alpha} \\ i_{diff_\beta} \end{bmatrix}, \mathbf{i}_{diff_{\alpha,\beta\_max}} = \begin{bmatrix} i_{diff_{\alpha\_max}} \\ i_{diff_{\beta\_max}} \end{bmatrix}, \mathbf{i}_{diff_{\alpha,\beta\_min}} = \begin{bmatrix} i_{diff_{\alpha\_min}} \\ i_{diff_{\beta\_min}} \end{bmatrix}$$

$$\boldsymbol{Q} = q \begin{bmatrix} 1 & 0 \\ 0 & 1 \end{bmatrix}, \ \boldsymbol{g_1} = \rho \begin{bmatrix} 1 & 0 \\ 0 & 1 \end{bmatrix}$$

5.5.2.2 FCS-MPC with space vector placement

Figure 5-17 shows the flowchart of the proposed secondary control algorithm. This algorithm is played at each switching instance (k). First, $i_{diff_\alpha}(k)$ and $i_{diff_\beta}(k)$ are calculated from $i_1(k), i_2(k)$ and $i_3(k)$. Then the 6 duty cycles of the space vectors corresponding to the level interval defined by the required $\bar{v}^*_{cm}$ are calculated while considering for this initial calculation that $\bar{v}^*_{diff_\alpha} = 0$ and $\bar{v}^*_{diff_\beta} = 0$. Next, the algorithm evaluates the differential currents waveforms for the 12 possible space vector sequences (12 different possible ordering of the space vectors verifying level alternate conditions over the switching interval). From model equations given by (5-25) and (5-26), $\bar{i}_{diff_\alpha}$ and $\bar{i}_{diff_\beta}$ are evaluated and the derived $\bar{v}^*_{diff_\alpha}$ and $\bar{v}^*_{diff_\beta}$ are calculated. From $\bar{v}^*_{cm}$, $\bar{v}^*_{diff_\alpha}$ and $\bar{v}^*_{diff_\beta}$ the real duty cycle $d = [d_{seq1}\ d_{seq2}\ d_{seq3}\ d_{seq4}\ d_{seq5}\ d_{seq6}]$ corresponding to each selected sequence are obtained. If no duty cycle in the sequence is negative, the maximum and minimum of the differential currents are derived. From all these values, the cost function is evaluated. After 12 evaluations (12 space vector sequences), the sequence corresponding to the minimum cost function is selected and is applied to the power converter.

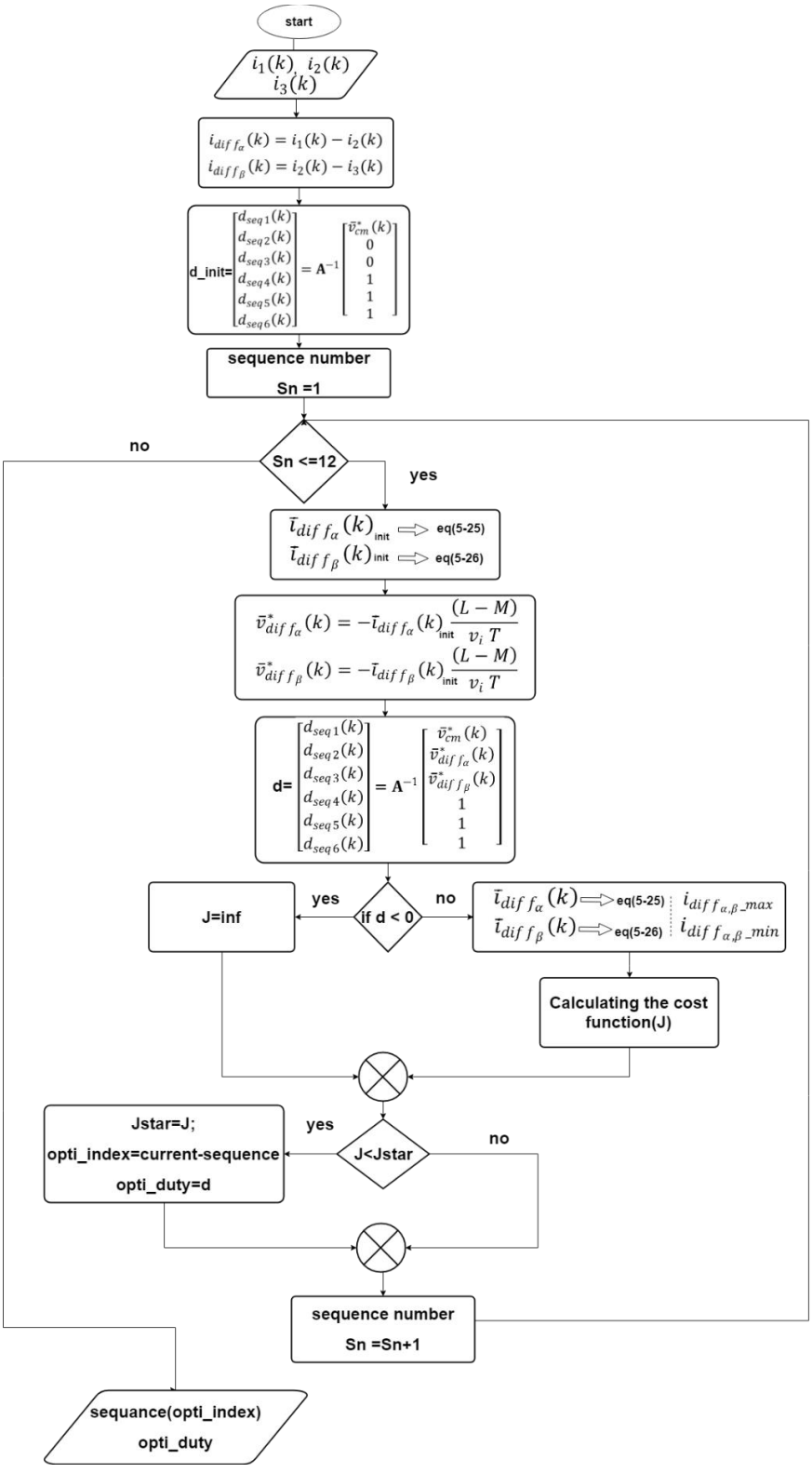

Figure 5-17 Flowchart of the secondary controller(MPC with space vector placement)

5.5.3. Simulation

(1) Common mode response

For this trial, the common mode current reference $i_{cm_{ref}}$ (i_{cm} is the output current i_o of the 3-Cell power converter) is a 500 Hz square waveform going from 6A to 12A. When the system is well balanced, the corresponding cell currents are the third of this global current. Figure 5-18 shows the simulation results obtained with the proposed strategy. It can be observe from Figure 5-18-a that the common mode current follows the reference with a transient time of less than 300 µs and no overshoot. This system response fulfill the requirements listed in Table 3-2. We can also note that the two differential modes are well controlled with a zero average values. Figure 5-18-b shows the current in the three cells. These currents are well balanced and have the same dynamic.

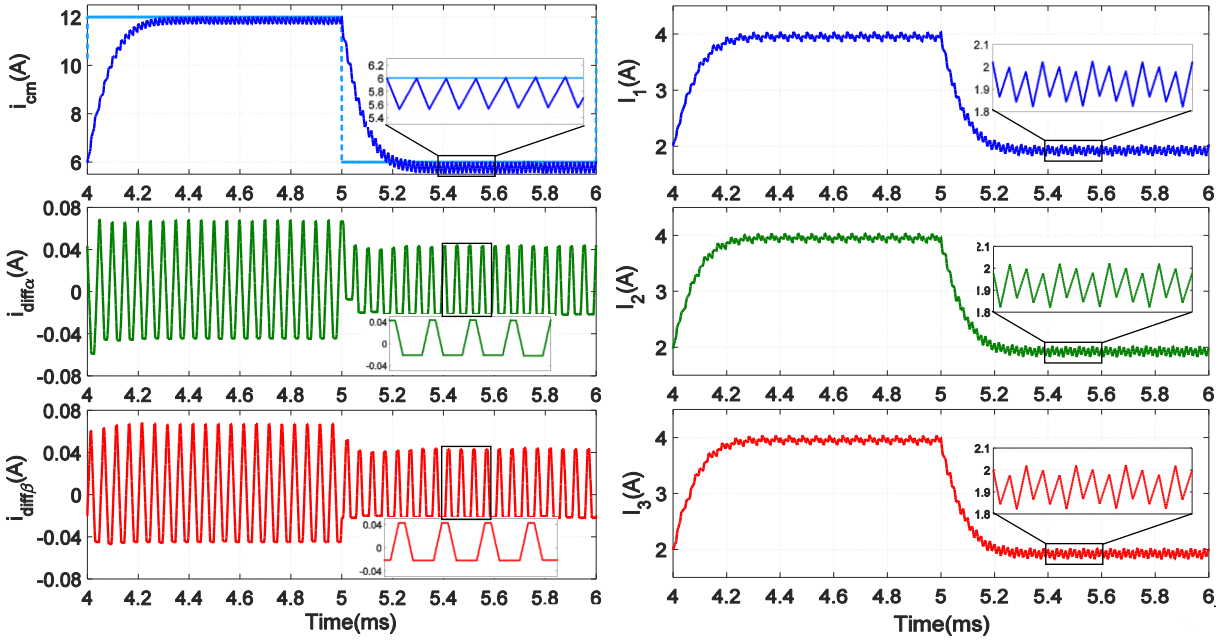

(a) (b)

Figure 5-18 Simulation results of the 3-Cell Buck converter controlled with the proposed MPC-Space vector placement

(2) Sensitivity analysis

The following two parts will discuss the sensitivity of the proposed method, based on model knowledge, to some converter's parameters changes. The most variable parameters in the proposed power converter is indubitably the magnetic device parameters, namely, the inductance and mutual inductance but also the load of the converter.

(a) Sensitivity to load change

The global control process defined above is designed from the converter's parameters as listed in Table 5-1. In the following simulations, the load value is changed with no modifications of the main controller and the secondary controller. The following results are given for 3 load values:

10 Ω, 2.5 Ω and 1 Ω to check the controller sensitivity to load change.

Figure 5-19 shows the corresponding simulation results. In Figure 5-19-a the three currents mode are shown. We can see that the common mode transient response is slightly affected by the load change. This result was predictable as the load value influence the common mode open-loop transfer functions. We can also note that the differential currents seem to be modified. This in fact an artefact because the values of $\bar{v}_{cm}^{*}$ calculated by the main controller change to compensate the load variation, the differential current ripple depending on the value of $\bar{v}_{cm}^{*}$ change accordingly but the average remain perfectly controlled as shown in Figure 5-19-b.

Impact of the load change on the main controller could be reduced by designing this controller with different techniques more robust to load change. For this purpose, state feedback using LQR could be used.

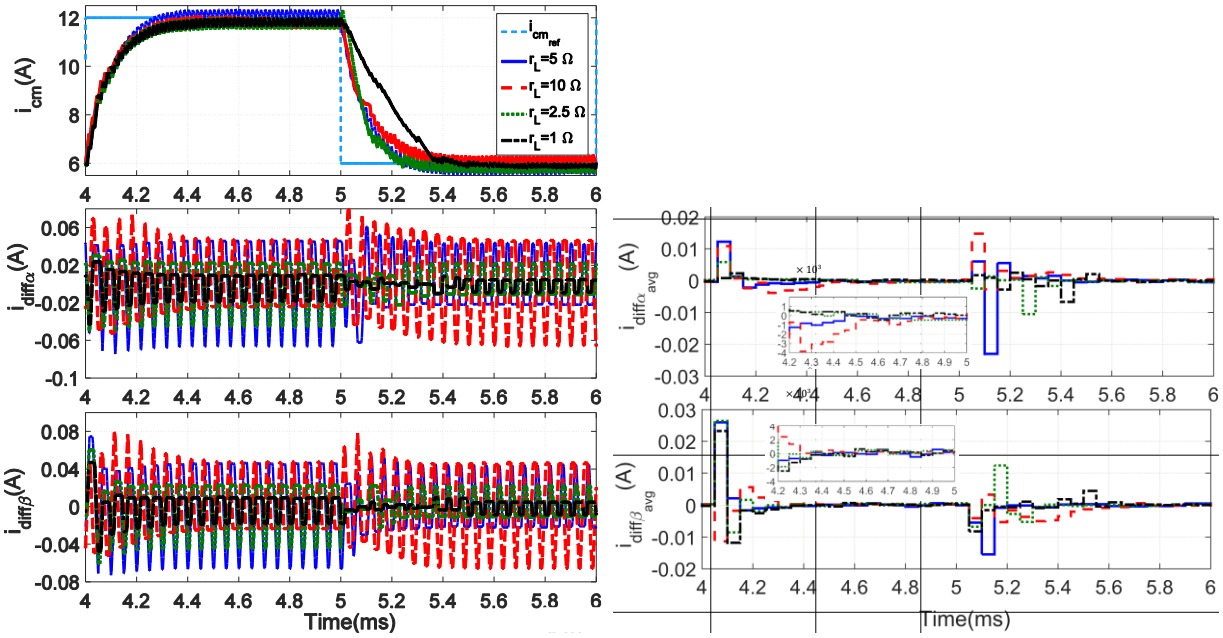

(a) (b)

Figure 5-19 Simulation result of 3-Cell Buck converter using MPC- Space vector placement: sensitivity to load change,(a)three mode currents (b)moving average of the differential currents

(b) Sensitivity to Inductance change

The second main parameter that may affected the response of the closed loop system is the output filter inductances. In this section, the inductance matrix is kept unchanged in the model used by the secondary controller as the main controller parameters. In the following graphs, inductances are successively increased by 20% ($L_{new} = L * 120\%$), decreased by 10% and by 20%.

Figure 5-20 shows the simulation results corresponding to these three values. In Figure 5-20-a we can see that the common mode current dynamic is not affected by the inductance variation. In fact, the dynamic in this mode is mainly imposed by the main controller for the controller tuning used in this simulation.

But from Figure 5-20-b, it can be observed that inductances errors in the prediction model leads to systematic DC shifts of the average differential mode currents. When the inductances are increased a positive DC shift appears for the first differential current (i_{diff_α}) whereas that of the second differential current (i_{diff_β}) is negative. Note that the two DC shifts are symmetrical around zero. When the inductances are decreased the DC shifts also exists but the shift is now positive for i_{diff_β} and negative for i_{diff_α}.

This behavior is due to systematic prevision errors of the prediction model implemented in the secondary controller. This problem could be solved by building an observer to calculate and correct the differential inductances used in the model.

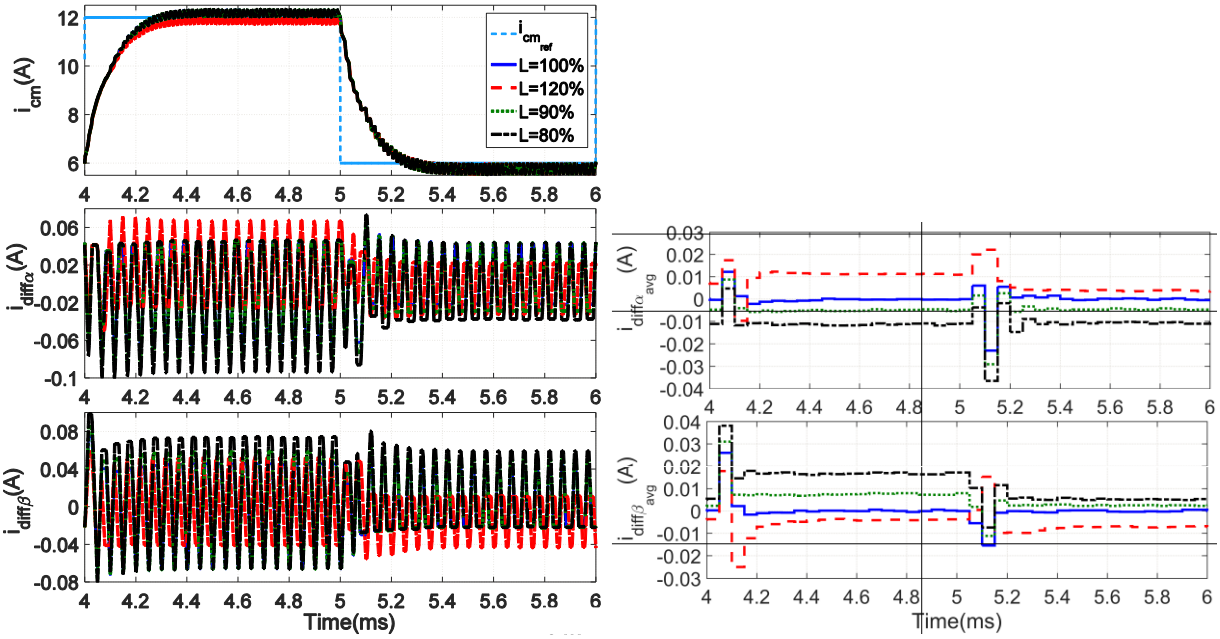

Figure 5-20 Simulation result of 3-Cell Buck converter using MPC- Space vector placement: sensitivity to inductance change,(a)three mode currents (b)moving average differential currents

5.6. Conclusion

The Space vector placement based on model Predictive Control is a real improvement over the FCS-MPC presented in chapter 4. Indeed the previous method designed to obtain a fix switching frequency has several limitations. The main one is the low resolution of the duty cycle to avoid a two large number of prediction points.

The proposed space vector placement (SVP) solves this problem by using the model equations to directly calculate the duration of application of the 6 space vectors of a sequence with a high possible resolution. So the previous limitation disappears and this method also ensures a constant switching frequency and a regular cell interleaving operation in steady state. MPC applied in this

methodology aims to define the best sequence to apply to the power converter. This leads to evaluate a cost function for only 12 different sequences compared to the previous FCS-MPC leading to evaluate 1000 possibilities for only 9 prediction points. FCS-MPC with SVP gives much better results for a lower computing cost.

In the last part of this chapter, we analyze the robustness of the method with respect to errors in the knowledge of the parameters of the model. The simulations show that the converter remains stable even for significant model errors. Nevertheless, model error on inductance causes significant DC shift of differential current average value, which can lead to saturation of the magnetic component. This sensitivity to inductance needs more investigation to manage this problem.

Further improvements can also be made regarding the management of duty cycle saturations. This problem arise especially when the average common mode is close to level 0 or level 3 because some duty cycles are very small or very large. But this problem can also arise in case of large and fast variation of the common mode voltage. This kind of problem is not implemented yet in the proposed control algorithm.

Chapter 6. Experimental Results

6.1. Introduction

The test bench consists of two parts. One is the power converter which can be configured either like a Buck or a Boost multicell topology. The second part is the control system which achieves the proper global behavior and the current balancing in the multicell converter.

Before the great development in digital systems, implementation of controllers was based on analog and passive components made with capacitors, resistors and operational amplifiers (Op-Amp). With such components only simple controllers such as PI, PID and filters could be easily realized. Even though they may have good performance this technology suffers from a number of disadvantages. Indeed, the characteristics of analog components change throughout time and the global designed function is sensitive to thermal variations and electromagnetic interferences. Nowadays, the complexity, the size of implementation and the cost of analog controllers lead the designer to replace this technology with its digital equivalent.

The great developments of digital systems offer a large range of real-time implementation solutions and today digital controllers are very widely used. With such controllers, it is now possible to implement more complex control strategies with less sensitivity to components ageing, thermal variations and electromagnetic disturbances.

In such controllers, Analog to Digital Converters (ADC) are needed. ADC play an important role in digital control and are critical parts of the controller due to their latencies and their quantization noise.

Implementation of digital controllers can be done in three ways. Firstly, this can be done by using a software implementation (sequentially executed) in a Microcontrollers (µC) or a Digital Signal Processor (DSP). This technological solution is preferred by many designers due to its easy implementation and the reduced development time it requires [92]. The second way is closed to a hardware digital solution and uses Field-Programmable Gate Array (FPGA) or Applied-Specific Integrated Circuit (ASIC) targets. Such hardware digital solutions leads to a parallel management of input signals. So these solutions are used for high speed calculations and can support very complex systems. The last way is based on a mixed software and hardware implementation. Such kind of solutions can be used when the control process can be divided in two parts, a fast one (in the range of the switching frequency) and a slower one. In the following, we will use this last mixed solution. In our experiment, FPGA is used to implement the critical computing time loops like those dedicated to the currents control and the PWM generation and software programing in a Microcontroller is used for the output voltage control.

This chapter is divided in three parts. In the first part the experimental test bench is presented with details on its components and limitations. The second part shows implementation of the classical control and the corresponding experimental results. The last part is dedicated to FCS-MPC implementation in FPGA target.

6.2. Experimental test bench

The general structure of the test bench is shown in Figure 3-1. The test bench is built around a 3-cell power converter ant its output coupled inductor. We can also see on this figure, the controller using a mixed implementation: the currents management and the PWM elaborations are built in a Field-Programmable Gate Array (Xilinx® Kintex® -7 XC7K325T FPGA) and the output voltage controller is built in a microcontroller (Real-time processor : Freescale QorlQ P5020, dual-core, 2 GHz 32 KB L1 data cache per core, 32 KB L1 instruction cache per core, 512 KB L2 cache per core, 2 MB L3 cache total, Freescale QorlQ P1011 800 MHz for communication with host PC). All these devices are included in a Dspace MicroLabbox. The last part is the Controldesk software (installed on personal computer PC) dedicated to the control of the test bench and providing monitoring facilities.

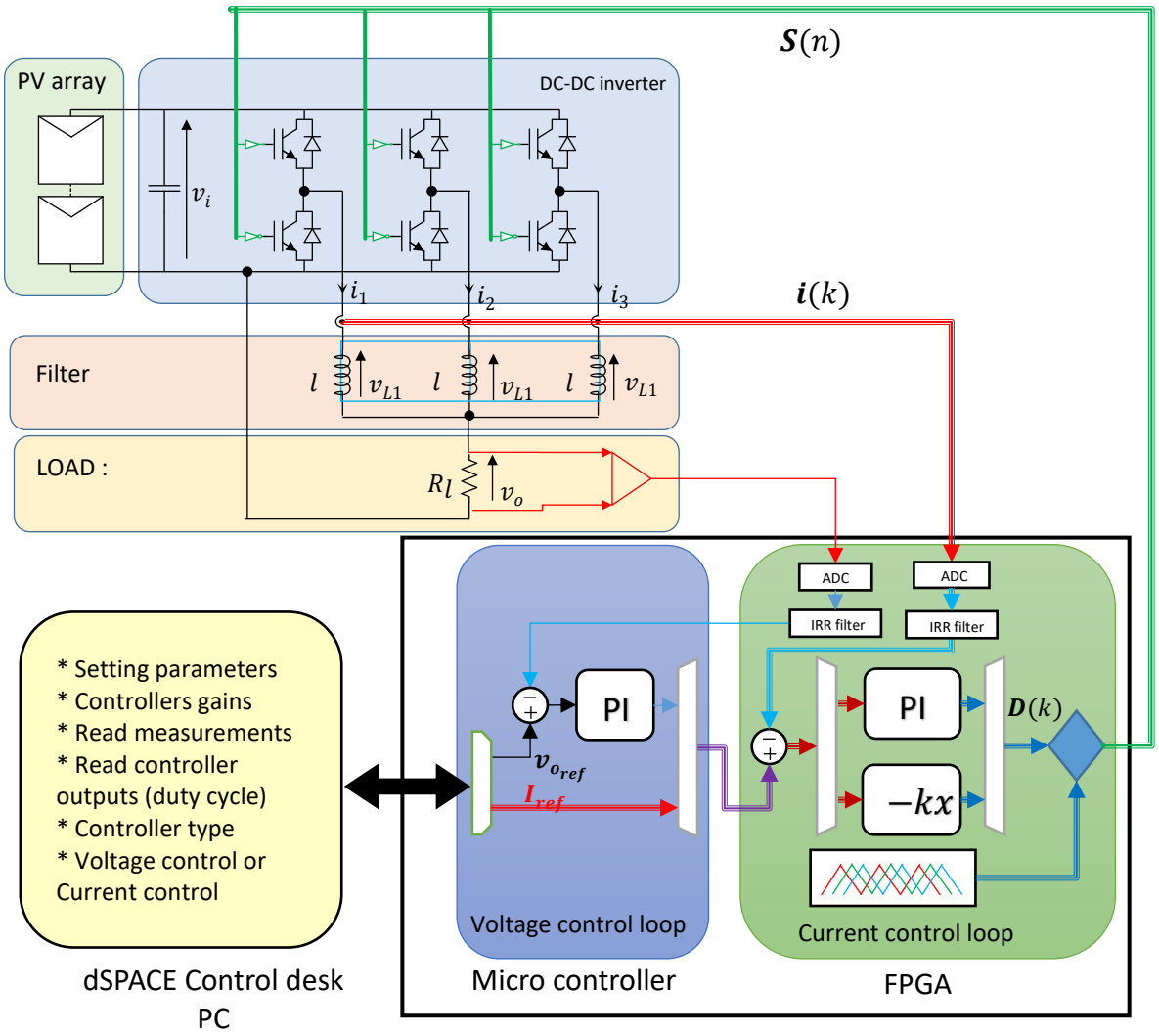

Figure 6-1 Block diagram of the test bench

Currents in each cells and the output voltage are converted from analog to digital values by the Analog to Digital Converter (ADC) of the MicroLabBox (14-bit channels, 10 Msps, differential; functionality: free running mode). The corresponding digital data are filtered by digital filter type Infinite Impulse Response (IIR) implemented in the FPGA target.

6.2.1. Power supply

In our experiments, string of solar panels are replaced by a 3300W DC power supply. The controlled output voltage is up to 300V and the controlled output current up to 11A. The output ripple and noise are peak to peak is 300 mV, and 100mV, rms [93].

6.2.2. The inductance elements

The input filter is made of two electrochemical capacitors wired in series connection ($c_i = 1100$ µF) to avoid the input ripples. The output filter is made of a coupled inductance. In order to simply realize the monolithic coupled inductor, we used the stator of an electrical machine. This stator belongs to a three phase machine which has twelve windings wound on its twelve teeth. These windings are connected in parallel two by two to form six windings and then each group is connected in series with another to form three equivalent coupled inductors (Figure 6-2). These coupled inductors has the following properties: inductance $l = 15.4mH$ and mutual inductance $m = -7$mH. The three windings are star connected and the common point is connected to the load. The three remaining connections are feed by three half-bridges as shown in Figure 3-1. The power rating of the machine is 15kW and the maximum currents in each winding is 10.6A. The total resistance of each winding is a little bit high and is equal to $r = 5.36\Omega$. We can note that magnetic saturation due to differential currents mismatch can be avoided or limited in this magnetic device because of the air gap between the stator and the rotor.

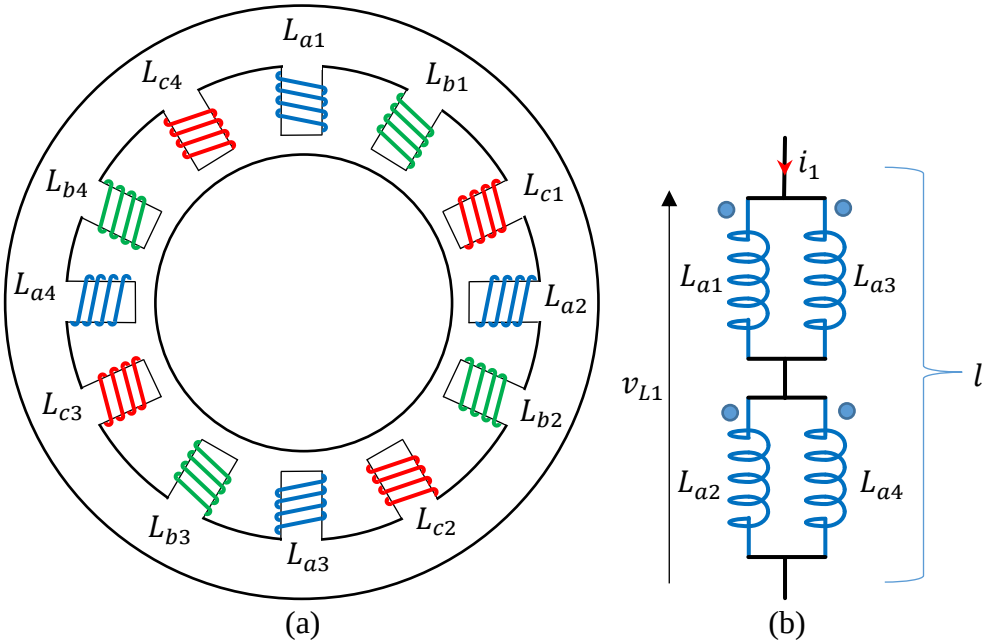

Figure 6-2 Configuration of electrical machine inductance (a) the stator winding (b) the connection configuration

6.2.3. The converter

The power converter consists from three IGBT half bridge from $Semikron$ with two capacitors ($2200\mu F$) wired in series connection and connected in parallel with the DC busbar. The rated voltages of IGBTs are $1200V$ and the maximum currents are $81A$ at $25°C$. They are placed on a heat sink equipped with a fan. The dead time of the converter cells are around $327ns$. This delay time is managed by the SKHI22 driver [94] which also insure a role of protection against over currents and temperature.

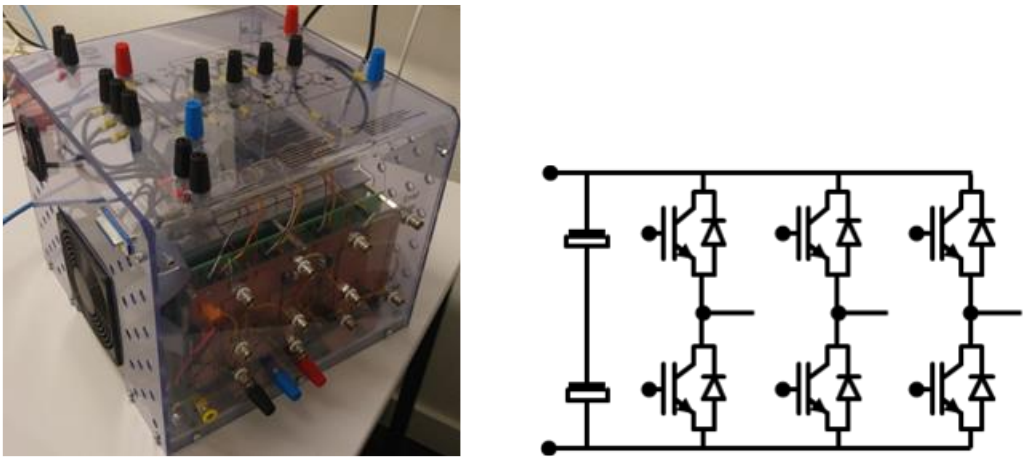

Figure 6-3 The structure of power converter for test bench

6.2.4. Measurements sensors

The sensors are very important for the control system and the sensitivity of the controller is very high with respect to the quality of measurement signals.

In our application, we need current and voltage sensors:

- Hall effect current sensors are used for the 3-cell currents as shown in Figure 6-4. For these sensors, the range of the measured current can go from $I_p = 0$ to $\pm\ 100A$. The primary to secondary current conversion ratio of the sensors is $K_N = 1:2000$. To increase the sensitivity of the measurement and avoid quantization problems for our quite low currents, we wounded five turns in the sensor window rather than one. For this configuration the conversion ratio becomes $K_N = 1:400$. A measurement resistance $R_M = 50\Omega$ is added at the end of the coaxial cable just before the ADC to convert current to voltage. The relation between the output voltage of the sensor and the measured currents is therefore $K_{iv} = 125\ \mathrm{mV/A}$ [95].
- For the output voltage, a differential voltage probe is used. The conversion ratio of the probe is $K_{vv} = 100\ \mathrm{mV/V}$.

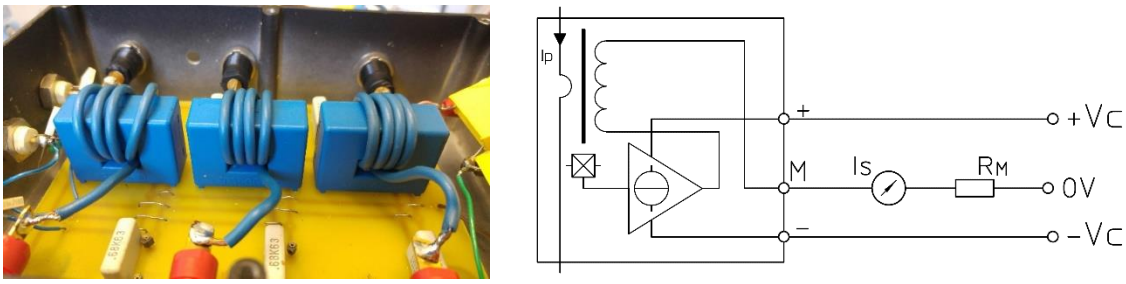

Figure 6-4 The hall effect current sensors

6.2.5. Hardware for implementation of the controller

The MicroLabBox is manufactured by dSPACE. This development system for the laboratory includes a processor and a FPGA boards. High computation power combined with very low I/O latencies provide great real-time performances. The programmable FPGA gives a high degree of flexibility and allows to run extremely fast control loops. In our application the MicroLabBox is used to implement the currents and the voltage loops. The voltage loop which is much slower than the switching frequency is implemented in the microcontroller part and the currents controllers are implemented in the FPGA part.

6.2.5.1 Microcontroller Card

The real time processor is a *Freescale Q P*5020, dual-core, 2 GHz. The processor is part of the Dspace board called *DS*1202. The block diagram of this board is shown in Figure 6-5 [96]. The real time processor is connected to input/output I/O through the FPGA and the local bus.

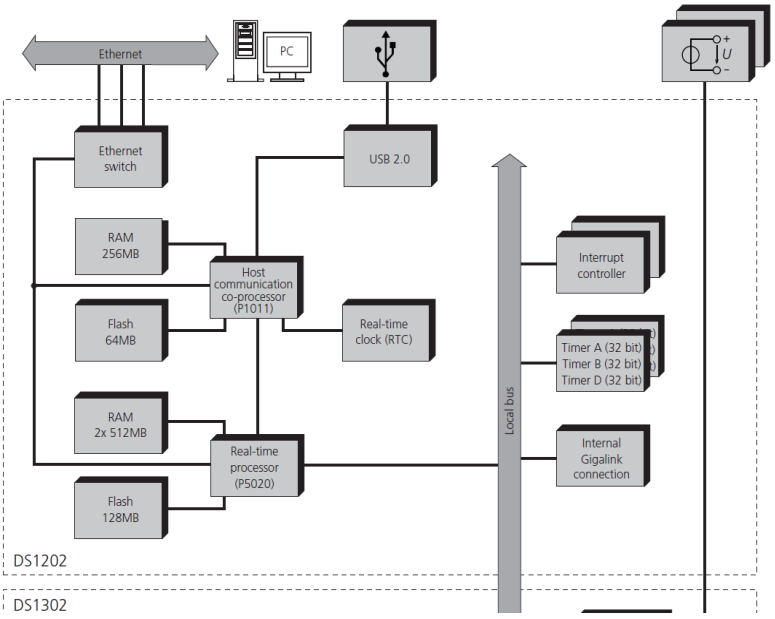

Figure 6-5 Block diagram of the DS1202 card

6.2.5.2 FPGA card

Figure 6-6 shows the block diagram of the $DS1302$ board [96]. A FPGA type Xilinx® Kintex®-7 XC7K325T is installed on this board. It has 326,080 programmable logic cells. Its clock frequency can raised 100MHz. This board is equipped with 24 analog inputs $Class\ 1$ (16 Bits resolution, 1 $MSPS$ sampling rate and $\pm 10V$ input range), 8 analog inputs $Class\ 2$ (14 Bits resolution , 10 $MSPS$ sampling rate and $\pm 10V$ input range), 16 analog *Class 1* outputs, 48 digital *Class 1* bidirectional channels and 12 digital *Class 2* bidirectional channels [97].

For FPGA programming, we used the Simulink Block Set Xilinx System Generator (XSG). This is carried out in two steps. Firstly, FPGA blocks in Simulink interface are used to design the required functions. At this step, a functional simulation can be performed. The second step is the conversion of the Simulink block diagram to Verilog language by using the Matlab Simulink tools. Then, Xilinx System Generator takes over and - Translates (merges the incoming netlists and constraints into a Xilinx® design file); - Maps (fits the design into the available resources on the target device); - Places and routes the design to the timing constraints; Generates the programming file (creates a bitstream file that can be downloaded to the device).

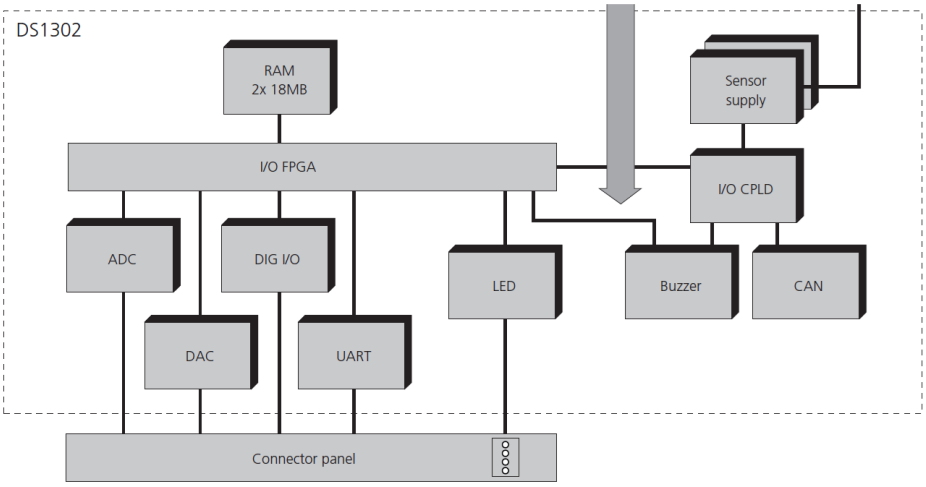

Figure 6-6 Block diagram of the DS1302 card

6.3. Implementation of classical controller

The current and voltage control of the interleaved DC-DC buck power converter which is described in Chapter 3 is implemented in the MicroLabBox. There are two ways to design the digital controller. In the first method, when the closed loop performances requirements are much slower than the sampling frequency, the controller can be designed in s-domain and then transformed in its discrete form (z-domain). The second method is based on a direct control synthesis in z-domain. For this last, the continuous transfer function of the physical system must be first converted to a discrete form [62], [98]. In the following, we will choose the first method.

6.3.1. Controller implementation

Figure 6-7 shows the block diagram of the proposed control structure for the 3-Cell buck converter. The model of the buck converter given by equation (3-8) is shown in the orange block. The current controller is built on the FPGA board. All the inductors currents are measured by current sensors which convert the measured current to a voltage in (mV) with ratio $K_{iv} = 125\ \mathrm{mV/A}$. This voltage is converted by an Analog to Digital Converter (ADC) which give a numerical value in the range$(\pm 2^{15}, it\ is\ a\ 16\ bit\ ADC)$ but we convert the numerical valued to (mV) by the gain factor equal to 0.3052). In the FPGA, the deviations (called *error*) between the reference currents $(i_{ref(mV)})$ and the measured currents are calculated. These errors are processed in the current controller (C_i) to determine each cell duty cycle.

The performance requirement of the voltage control loop is much slower than that of the current loops. It can be built in the processor board. The output voltage is measured using a differential voltage probe with a transformation ratio $K_{vv} = 10\ \mathrm{mV/V}$. After conversion by an ADC, we apply a scaling factor such that the digital data processed in the micro-controller corresponds to the value of the analog voltage in mV. The difference between the reference voltage (V_{oref}) and the actual output voltage $(v_o(mV))$ is calculated and the voltage controller (C_v) evaluates the proper global reference output current. This value is divided in thee equal parts which become the reference for the three current controllers. These references are sent to the FPGA through the internal data bus.

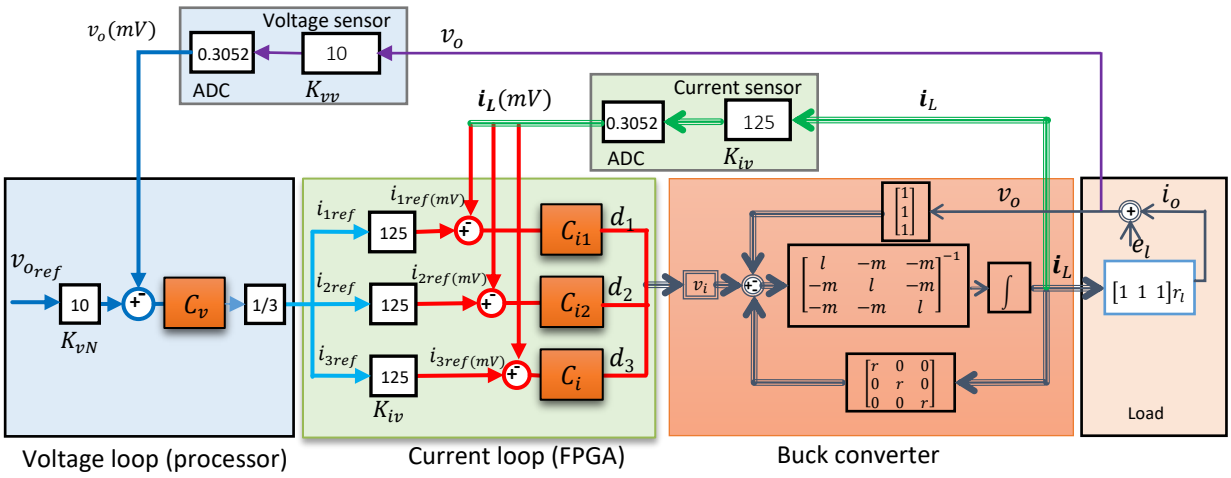

Figure 6-7 The block diagram of buck converter control structure

6.3.2. Current controllers

6.3.2.1 Independent PI/IP controller

The proportional integral controller (PI) is designed in s-domain as described in chapter 3. To implement the controllers in the FPGA we need first to convert the controllers to their discrete form (z-domain).

The continuous transfer function of the PI controllers is given by equation (6-1). Where d is

the cell duty cycle which is the output of the current controller (C_i), e is the error (the difference between the current reference and the measured one), K_p is the proportional gain and K_i is the integral gain.

$$\frac{d}{e} = K_p + \frac{K_i}{s} \qquad (6\text{-}1)$$

To convert the transfer function of the PI controller from s-domain to z-domain the Back-ward difference method is used. The transformation is done by substituting s by the value given in equation (6-2), where T_s is the sampling time.

$$s = \frac{1 - z^{-1}}{T_s} \qquad (6\text{-}2)$$

With this transformation, the discrete form of a PI controller is:

$$\frac{d}{e} = K_p + \frac{T_s K_i}{1 - z^{-1}} \qquad (6\text{-}3)$$

This controller equation is separated in two parts, the proportional term (d_p) and the integral term (d_I) given in equation (6-4).

$$d_p = eK_p \qquad (6\text{-}4)a$$

$$d_I = e\frac{T_s K_i}{1 - z^{-1}} \qquad (6\text{-}4)b$$

Equation (6-4)*b* can be expressed in a computation form given in (6-5).

$$d_I = eT_s K_i + d_I z^{-1} \qquad (6\text{-}5)$$

6.3.2.2 Decoupling strategy (PI)

Figure 6-8 shows the block diagram which correspond to the decoupling strategy applied to the 3-Cell converter currents control. As explained in chapter 3, the controllers acts on the fictitious system for which there are no coupling effects. The real currents are measured and converted to integer numbers which are scaled to mV. Then, these values are transformed to the fictitious ones by multiplying them by the inverse of the transformation matrix (see chapter 3). In the same way the reference currents are transformed into fictitious references ($i_{cm_{ref}}$, $i_{diff1_{ref}}$ *and* $i_{diff2_{ref}}$). From error calculated on these fictitious values, independent *PI* controllers are applied and give the proper fictitious duty cycle. Then, the real duty cycles are calculated from the fictitious ones.

The synthesis of the *PI* controllers are done from their continuous form as explained in section 6.3.2.1. Note that there is no matrix multiplication blocks in Simulink dedicated to the FPGA. The matrix multiplications used in this strategy must therefore be explicitly written.

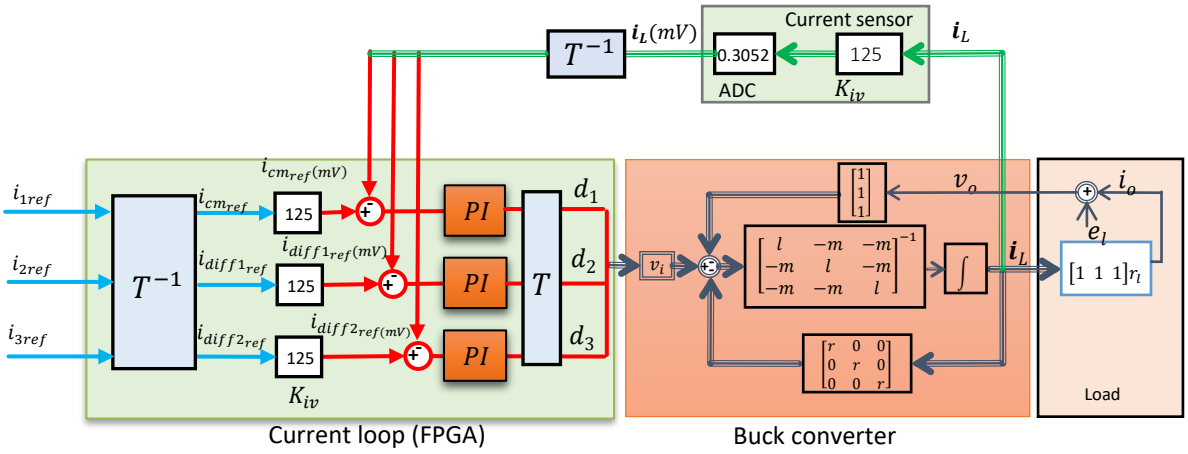

Figure 6-8 Block diagram of the currents control: decoupling strategy

The equation (6-6) show the relations between real reference currents and fictitious reference currents.

$$i_{cm_{ref}} = i_{1_{ref}} + i_{2_{ref}} + i_{3_{ref}} \qquad (6\text{-}6)\ a$$

$$i_{diff1_{ref}} = i_{1_{ref}} - i_{2_{ref}} \qquad (6\text{-}6)\ b$$

$$i_{diff2_{ref}} = i_{1_{ref}} - i_{3_{ref}} \qquad (6\text{-}6)\ c$$

The equation (6-7) show the relations between real measured currents and fictitious measured currents.

$$i_{cm_{mes}} = i_{1_{mes}} + i_{2_{mes}} + i_{3_{mes}} \qquad (6\text{-}7)\ a$$

$$i_{diff1_{mes}} = i_{1_{mes}} - i_{2_{mes}} \qquad (6\text{-}7)\ b$$

$$i_{diff2_{mes}} = i_{1_{mes}} - i_{3_{mes}} \qquad (6\text{-}7)\ c$$

The equation (6-8) show the relations between real duty cycles and fictitious duty cycles.

$$d_1 = \frac{1}{3}(d_{cm} + d_{diff1} + d_{diff2}) \qquad (6\text{-}8)\ a$$

$$d_2 = \frac{1}{3}(d_{cm} - 2d_{diff1} + d_{diff2}) \qquad (6\text{-}8)\ b$$

$$d_3 = \frac{1}{3}(d_{cm} + d_{diff1} - 2d_{diff2}) \qquad (6\text{-}8)\ c$$

6.3.2.3 LQR strategy

Figure 6-9 shows the block diagram corresponding to LQR implementation. It was shown in table 3-5 that $\boldsymbol{k}_{e2}$ used in this strategy is diagonal. This means that there is no coupling effects for the integral parts of the extended state feedback controller. In this structure $\boldsymbol{k}_{e1}$ is, on the other hand, not diagonal leading to coupling effects for the proportional parts of the controller. The LQR implementation is, therefore, similar to that of an IP controller except for the coupling on the proportional part.

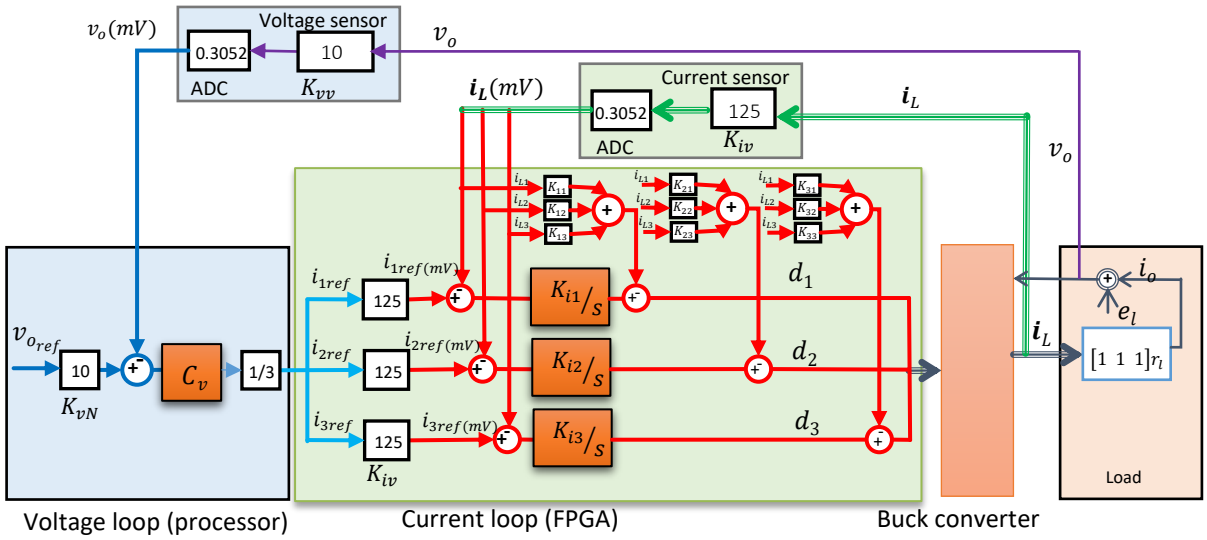

Figure 6-9 Block diagram of the currents control: LQR strategy

In this controller, the gain matrices are defined as follow

$$\boldsymbol{k}_{e1} = \begin{bmatrix} K_{11} & K_{12} & K_{13} \\ K_{21} & K_{22} & K_{23} \\ K_{31} & K_{32} & K_{33} \end{bmatrix} \qquad (6\text{-}9)\ a$$

$$\boldsymbol{k}_{e2} = \begin{bmatrix} K_{i1} & 0 & 0 \\ 0 & K_{i2} & 0 \\ 0 & 0 & K_{i3} \end{bmatrix} \qquad (6\text{-}9)\ b$$

Note that an anti-windup algorithm can be easily implement for this LQR strategy, because there are no coupling between the integrals terms of the controller. In our algorithm, the implemented anti-windup algorithm is defined as follows: when the duty cycle exceeds the upper limit ($d \geq d_{up}$) while the error is negative ($i_{ref} - i_{mes} < 0$) or if the duty cycle is exceeds the lower limit ($d \leq 0$) while the error is positive ($i_{ref} - i_{mes} > 0$) the corresponding integration should be stopped.

6.3.3. Voltage controller

The voltage controller is implemented on the processor board. The sampling time of

corresponding voltage loop is $Ts = 0.1$ ms. The PI controller is built by mean of Simulink blocks as in Figure 6-10. Note that the integrator is only started when the voltage control mode and enabling the PWM signal signals are true. The output of the controller is saturated to the maximum output current allowed. The proportional gain (K_{pv}) and integral gain (K_{iv}) are found by classical design methods such as root-locus.

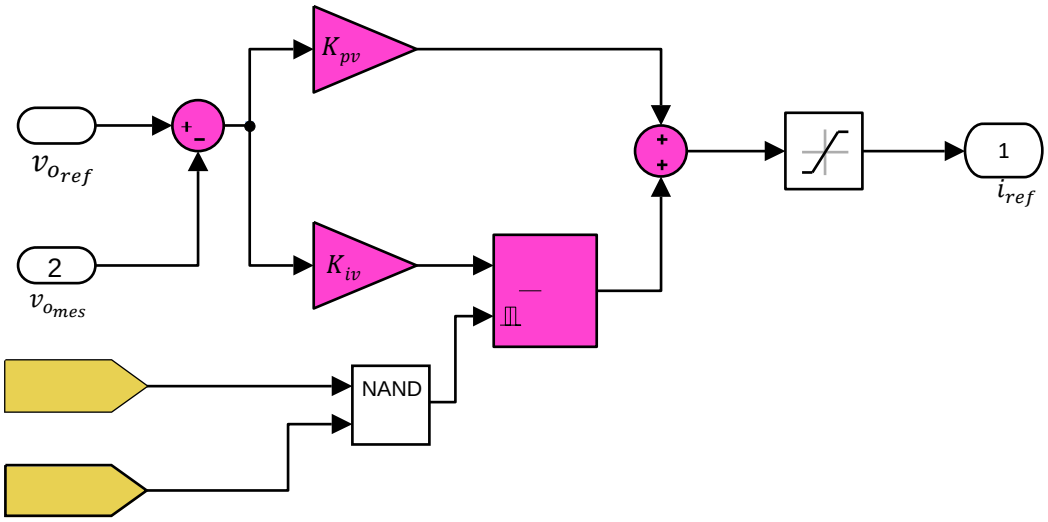

Figure 6-10 Simulink implementation of voltage controller: PI controller

6.3.4. Controllers implementation

Analog signals acquisition and current controllers are implemented in the FPGA. In FPGA only fixed-point representations can be used. So all the blocks should be converted from floating point to fixed point. A wrong sizing for fixed point will lead to quantization error and a loss of information. For this purpose, all blocks are changed to fixed-point format and simulated in Matlab Simulink to verify the sizing and the decimal point fixed position.

In order to avoid the recompilation of the FPGA program for each control strategy we developed an all in one scheme including all possible strategies which can be externally selected via $dSPACE\ Control\ desk$ through the processor board.

6.3.4.1 Data acquisition

MicroLabBox ADC class 1 with 16-bit resolution are used to acquire the currents as show in Figure 6-11. As explained previously, ADC convert the hall effect sensor voltage to numerical value ($i_{L_k}(N)$) then, this value is scaled to a number giving the voltage level in (mV). Via a selector which can be externally configured, it is possible to pass this data through a digital low pass filter.

The digital filter is a 3rd order low pass IIR filter. It is used to remove the high frequency signals from the current measurements. The parameters of IIR filter are as follows: $F_{pass} = 100\ kHz, F_{stop} = 1\ MHz$, $F_{sampling} = 10MHz$. To decrease the filter complexity, it is split in two stages (1st order + 2nd order).

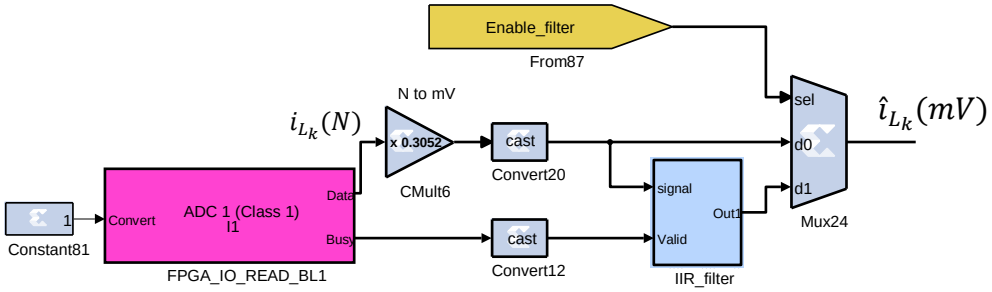

Figure 6-11 Implementation of the external data acquisition with XSG blocks

The transfer function of the IIR filter is given in equation (6-10)

$$\frac{out1}{signal} = \underbrace{k * \left(\frac{b_{1_0} + b_{1_1}Z^{-1}}{a_{1_0} + a_{1_1}Z^{-1}}\right)}_{1^{st}\ stage} * \underbrace{\left(\frac{b_{2_0} + b_{2_1}Z^{-1} + b_{2_2}Z^{-2}}{a_{2_0} + a_{2_1}Z^{-1} + a_{2_2}Z^{-2}}\right)}_{2^{nd}\ stage} \qquad (6\text{-}10)$$

Where:

$k = 2.9826 \times 10^{-4}$

$b1 = [1 \quad 0.99999]$, $a1 = [1 \quad -0.8692]$

$b2 = [1 \quad 2 \quad 1]$, $a2 = [1 \quad -1.852 \quad 0.8698]$

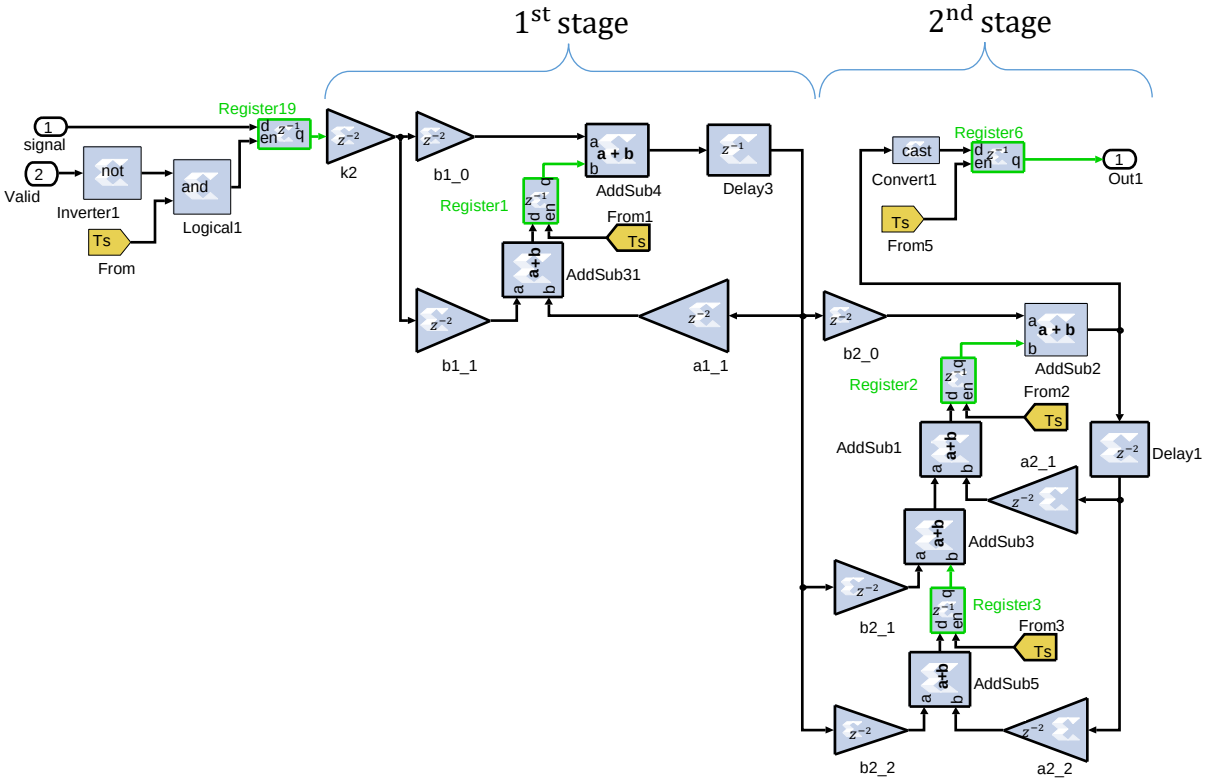

Figure 6-12 Implementation of the IIR filter with XSG blocks

After this first block, the signal is sampled and held using a "regular sampled" PWM strategy, where the waveforms are sampled and then held constant during each PWM triangular carrier interval. The sampled signal can change value at either the positive or positive/negative peaks of the carrier waveform, depending on the sampling strategy.

This means, in our experiment, that the sampling frequency can be either 20kHz or 40kHz. In the two samples (top and bottom) configuration, the output is the average of two samples as shown on Figure 6-13. This strategy was chosen to limit impact of switching noises which appear near the top or the bottom of triangular carrier according to the value of the duty-cycle.

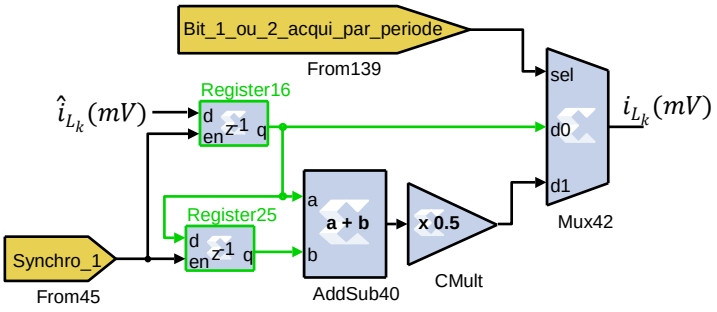

Figure 6-13 Synchronization and averaging of data acquisitions with XSG blocks

6.3.4.2 Implementation of PI/IP controller

Figure 6-14 shows the implementation of PI and IP controllers with anti-windup. In this implementation current error is integrated by the I-element of the block diagram and multiplied by the proportional gain in the P-element. Then, the results of both I-element and P-element are summed. The selector "$Mux7$" is used to select one of three controller types. The possible controller types are PI (selected by setting the selector to $d0$), IP (selected by setting the selector to $d1$) and LQR (selected by setting the selector to $d2$). In case of PI the output is directly the result of I-element and P-element. For IP, $K_p\ i_{ref}$ is subtracted to the previous value.

Note that the anti-windup can stop the integral part by setting "$mux1$" input to 1. When this input is 0 the integral part works normally.

The discrete PI/IP controller is sampled at $F_s = 20kHz$. The proportional gain K_p of the discrete version of the controller is equal to the gain K_p of its continuous equivalent as shown by equation (6-4)a. However, for the integral part, K_i gain is equal to $T_s \times K_{i_{cont}}$ where $T_s = \frac{1}{20\times10^3}$ for one pulse sampling and $T_s = \frac{1}{40\times10^3}$ for two pluses per PWM period as shown in equation (6-4)b.

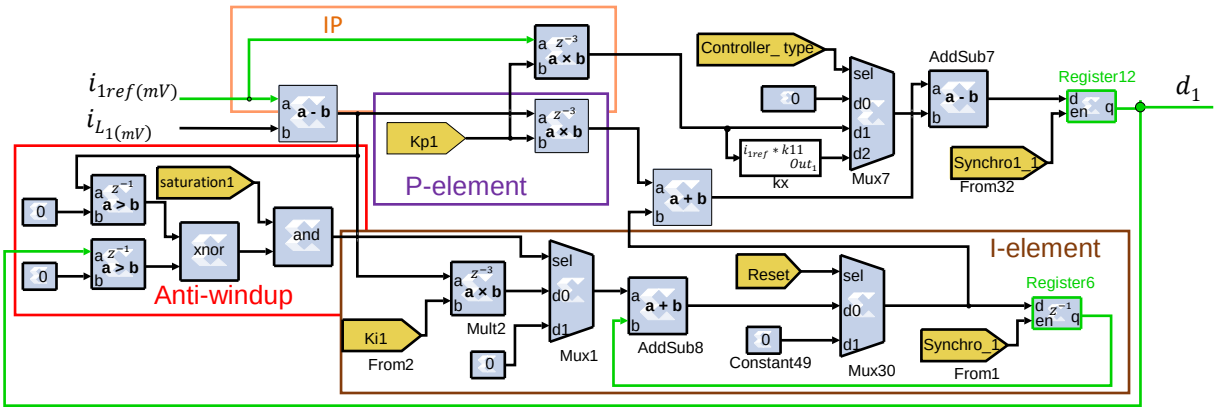

Figure 6-14 Implementation of PI and IP controllers with anti-windup with XSG blocks

6.3.4.3 Implementation of the decoupled strategy

Implementation of the decoupled strategy is shown in Figure 6-15. Figure 6-15-a shows how the transformation from real currents to fictitious currents is performed. Figure 6-15-b shows the inverse transformation applied here to fictitious duty cycles.

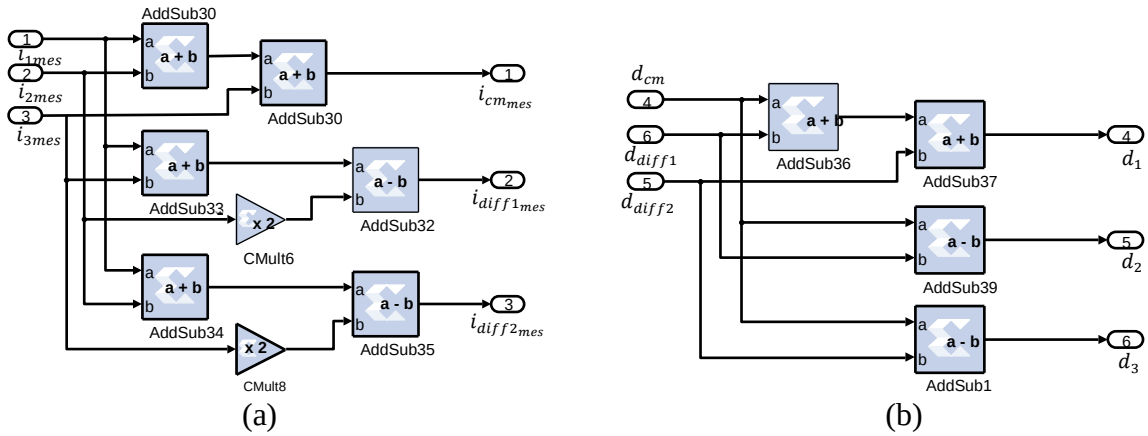

Figure 6-15 Implementation of the decoupling strategy with XSG blocks(a) current transformation (b) duty cycles transformation

6.3.4.4 Implementation of LQR

LQR strategy looks like the *IP* strategy except for its proportional part. As for *IP*, the integral parts of the controller are decoupled (section 6.3.2.3). The proportional part can be implemented as depicted in Figure 6-16. This figure describes the content of the block named "*kx*" in Figure 6-14. Figure (a), figure (b) and figure (c) are given respectively for the first, the second and the third current controller.

No change on the integral part is needed as there are no coupling between the integrals terms of the controller. The anti-windup is applied on each integrator of this structure.

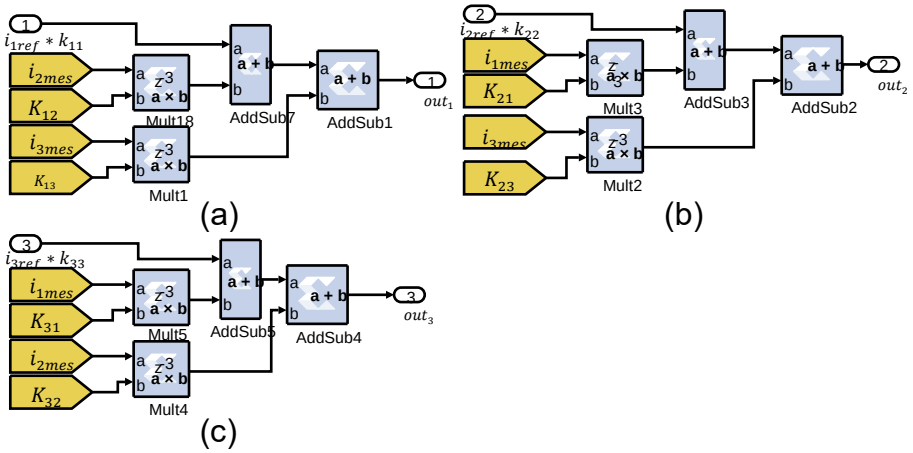

Figure 6-16 Programing the LQR strategy by XSG blocks

6.3.5. Experimental results

Experiments are done under the same conditions and with the same parameters as those used in simulations of chapter 3.

6.3.5.1 Experimental results for independent PI/IP controllers

Figure 3-6 shows experimental current waveforms for PI controllers. Experimental results and simulation results of figure 3-6 are consistent. In Figure 3-6-a where the three current references are the same, which corresponds to a common mode solicitation, it is clear that the response of the PI controller is acceptable and the behavior meet the design criteria. However, in Figure 3-6-b which corresponds to a pure differential response, the system is not stable. We can, thus verify that independent PI controllers are not suitable to properly control our coupled system.

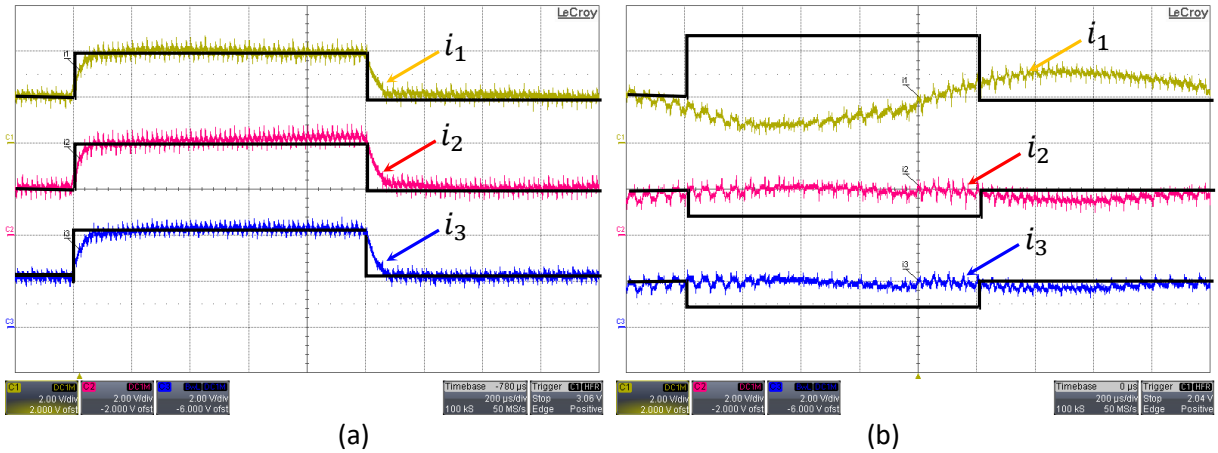

Figure 6-17 experimental results for PI controllers: (a) for the same current references , (b) in case of differential solicitations

6.3.5.2 Experimental result in case of decoupling strategy and IP controllers

Figure 3-13 shows the experimental result when the decoupling strategy is applied. The three figures show different current modes. Figure 3-13-a shows the common mode response, Figure 3-13-b the differential mode response and Figure 3-13-c a mix of both (in order to highlight effects due to coupling).

Here again, experimental and simulation results are consistent. In Figure 3-13-a the currents follow their references. Current dynamics in each cell are the same with a rise time of about 20µs and no overshoot as defined in the specifications. Figure 3-13-b shows the well-controlled behavior in case of differential mode and Figure 3-13-c demonstrates that the decoupling strategy is efficient as the step of current in phase 1 as almost no impacts on other phases.

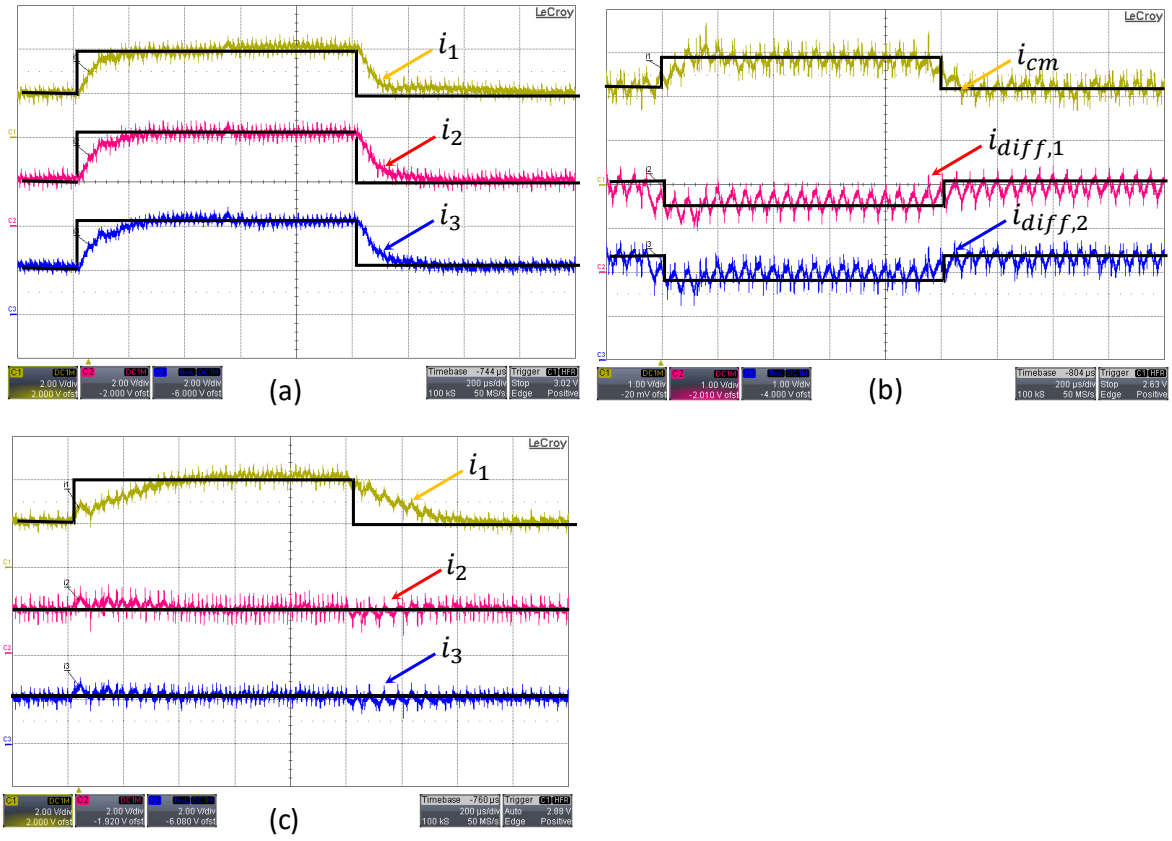

Figure 6-18 experimental result of closed loop behavior using the decoupling strategy: a) common mode response b) differential mode response c) single current step response

6.3.5.3 Experimental result for LQR

Figure 3-17 shows the experimental results when an extended state feedback control strategy tuned by LQR is applied. Figure 3-17-a shows the common mode response, the dynamic behavior of the current are the same and gives the same results than those obtain in the previous experiments. Figure 3-17-b shows the differential mode which is slower than previously for the decoupling strategy. We have seen in chapter 3 that this result is not surprising given that LQR has a global approach combining both error and control magnitude issues. As differential mode is slow, it

provides the minimum required gain values. The LQR gains make the common mode faster due to its intrinsic high dynamics.

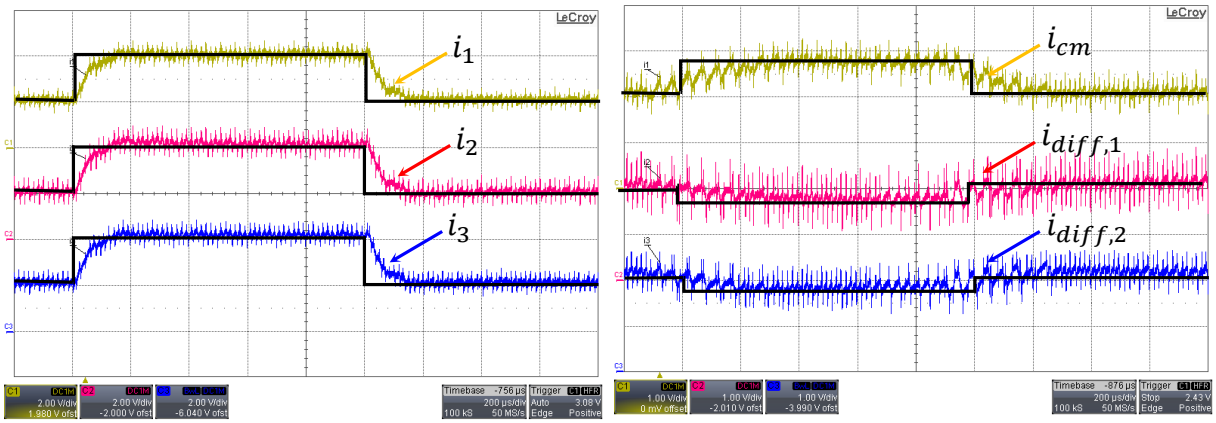

(a) (b)

Figure 6-19 . Experimental result of closed loop behavior using LQR design: a) Common mode b)Differential mode response.

Figure 3-18 shows the experimental results in case of a single current step response. The first figure shows the response when the current step is small (no duty cycles saturations in this case) and the second one when the current step is large enough to saturate the duty cycles.

Even if this control strategy is not dedicated to remove the system coupling effects, we can note that there are almost no impacts (in both figures) of the current variation in phase 1 on the two other currents. The response of the step current in case of large step response is slower than for the small step response. This behavior is due to saturation of the duty cycles and thus to voltage limitations but the controller still works properly. All these experimental results are consistent with the simulations shown in chapter 3.

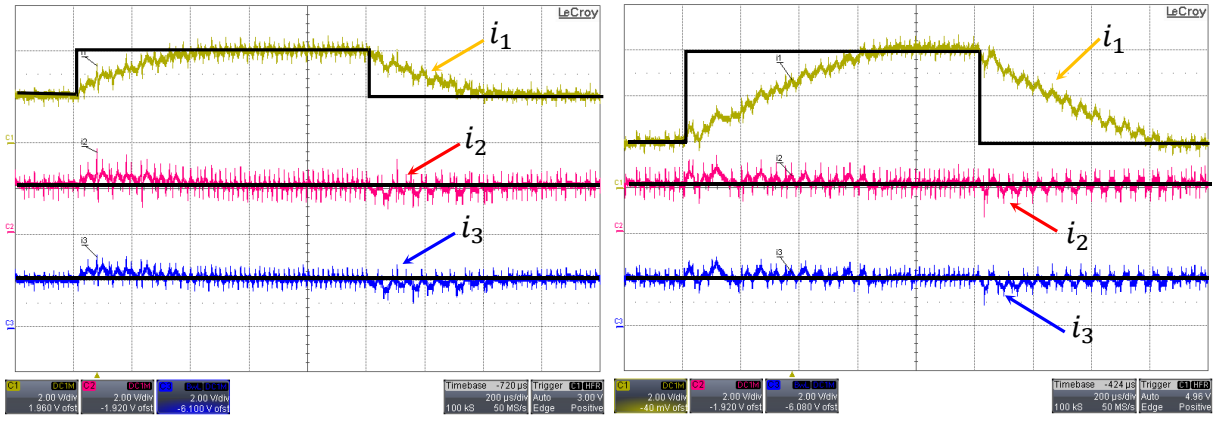

(a) (b)

Figure 6-20 . Experimental result of closed loop behavior using LQR design a single current step response :(a) Small signal (b) Large signal.

6.4. Implementation of FCS-MPC

This part shows how FCS-MPC dedicated to current control of a multicell DC-DC buck converter (described in chapter 4) can be implemented on the FPGA board. The design flow chart for FCS-MPC is shown in figure 4-9. Such kind of algorithm using program loops and sequential tests is badly adapted to a FPGA implementation. Indeed, such devices are dedicated to very fast parallel execution and not for sequential algorithms. However, as very short execution time are required to guaranty the required switching frequency, we will try in this section to implement such algorithm in the MicroLabBox FPGA.

6.4.1. Synthesis of the controller

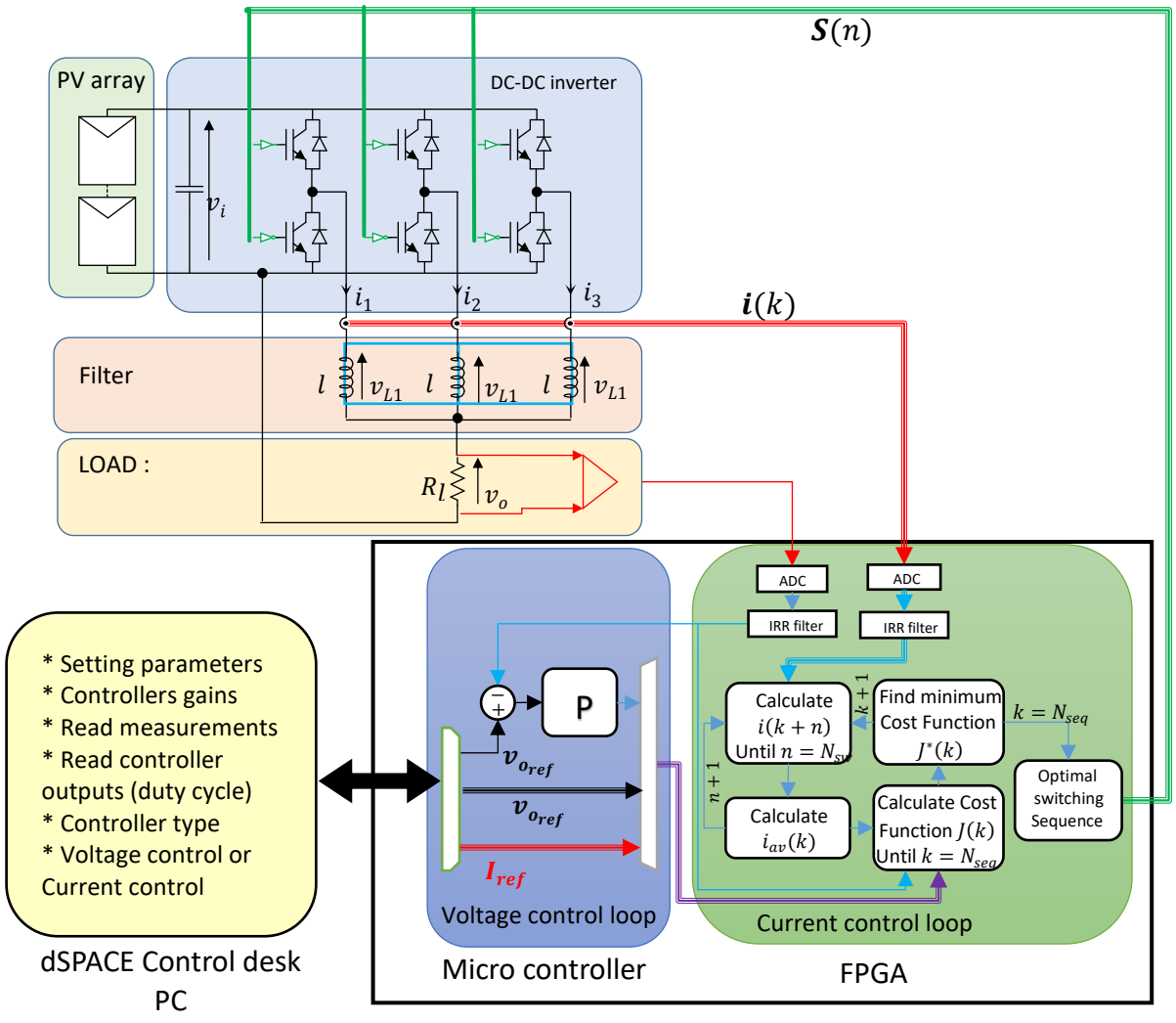

Figure 6-21 Block diagram for implementation of FCS-MPC on FPGA

Figure 6-21 shows the block diagram corresponding to the FCS-MPC control strategy of the cell currents. The program is divided in six steps. The first one is the current measurements. This

is done exactly as in previous section. The second step aims to calculate the future currents over the prediction horizon for each possible switching sequences ($i(k+n)$, Until $n = N_{sw}$). The third one consists in calculating the average current along the prediction horizon ($i_{av}(k)$). In the fourth step, the cost function of each sequence can be calculated ($J(k)$). The fifth step objective is to find the minimum cost function and the corresponding switching sequence (optimal sequence) through all the sequences ($k = 1\ to\ N_{seq}$). In the last step, the optimal sequence is applied to the power converter.

As previously, the voltage control loop is a PI-controller implemented in the processor board of the MicroLabBox. The settings of the MPC controller are defined in dSPACE control desk and passed to the FPGA through the processor and the internal bus.

6.4.2. Current loop

FCS-MPC is defined in a discrete form, so it is well adapted to digital programing. Equation (4-8) with a sampling rate T_s is used to calculate the future currents along the prediction horizon ($H_p = N_{sw}$). The cost function can be evaluated by using equation (4-11). Constraints defined by equation (4-12)are used in the implementation of the FCS-MPC.

For implementation in a FPGA, matrix multiplications must be explicitly developed. Equations derived from (4-8) are given below:

$$i_{1_k}(n+1) = a_{11}i_{1_k}(n) + a_{12}i_{2_k}(n) + a_{13}i_{3_k}(n) + b_{11}s_1 + b_{12}s_2 + b_{13}s_3 \qquad \textit{(6-11) a}$$

$$i_{2_k}(n+1) = a_{21}i_{1_k}(n) + a_{22}i_{2_k}(n) + a_{23}i_{3_k}(n) + b_{21}s_1 + b_{22}s_2 + b_{23}s_3 \qquad \textit{(6-11) b}$$

$$i_{3_k}(n+1) = a_{31}i_{1_k}(n) + a_{32}i_{2_k}(n) + a_{33}i_{3_k}(n) + b_{31}s_1 + b_{32}s_2 + b_{33}s_3 \qquad \textit{(6-11) c}$$

Where

$n = 1,2,3, \ldots\ldots, N_{sw}$

$$\begin{bmatrix} a_{11} & a_{12} & a_{13} \\ a_{21} & a_{21} & a_{21} \\ a_{31} & a_{31} & a_{31} \end{bmatrix} = \boldsymbol{A}_d\ , \begin{bmatrix} b_{11} & b_{12} & b_{13} \\ b_{21} & b_{21} & b_{21} \\ b_{31} & b_{31} & b_{31} \end{bmatrix} = \boldsymbol{B}_d\ , \begin{bmatrix} i_{1_k}(n+1) \\ i_{2_k}(n+1) \\ i_{3_k}(n+1) \end{bmatrix} = x_k(n+1)$$

$$\begin{bmatrix} i_{1_k}(n) \\ i_{2_k}(n) \\ i_{3_k}(n) \end{bmatrix} = x_k(n),\ k = 1,2,3\ \ldots.(\text{is the switching instance})$$

For a given switching sequence, the currents at each step ($\boldsymbol{i}_k(n+1)$) are compared with the current limitations ($0 \leq \boldsymbol{i}_k(n+1) \leq \boldsymbol{i}_{up}$). If they are out of the range, the cost function of this sequence is set to infinity ($J_k = \infty$) and there is no need to continue the prediction to the end of prediction horizon (H_p). If they are in the range, the current prediction algorithm continue until the end of the prediction horizon is reached. When the currents are known at all steps, the summation of these currents are accumulated and divided by the number of samples (H_p) to find the average of the currents corresponding to the tested sequence (j).

The cost function defined in (4-11)is converted to the form given by (6-12). The cost function of the current sequence ($J(j)$) is computed and compared to the lowest value of the previously

calculated cost functions ($J_{star} < [J(1) to\ J(j-1)]$.

$$J(j) = q_{11}\left(i_{ref_1}(k) - i_{av_1}(j)\right)^2 + q_{22}\left(i_{ref_2}(k) - i_{av_2}(j)\right)^2 + q_{33}\left(i_{ref_3}(k) - i_{av_3}(j)\right)^2 + g_1\left(i_{ref_1}(k) - i_{max_1}(j)\right)^2 + g_1\left(i_{ref_2}(k) - i_{max_2}(j)\right)^2 + g_1\left(i_{ref_3}(k) - i_{max_3}(j)\right)^2 + g_1\left(i_{ref_1}(k) - i_{min_1}(j)\right)^2 + g_1\left(i_{ref_2}(k) - i_{min_2}(j)\right)^2 + g_1\left(i_{ref_3}(k) - i_{min_3}(j)\right)^2 \quad (6\text{-}12)$$

Where

$$\begin{bmatrix} q_{11} & 0 & 0 \\ 0 & q_{22} & 0 \\ 0 & 0 & q_{33} \end{bmatrix} = \boldsymbol{Q}$$

6.4.3. Controller implementation

The execution in the FPGA is intrinsically parallel. To realize a sequential algorithm we need to synchronize each part of the program with a proper timing clock as shown in Figure 6-22.

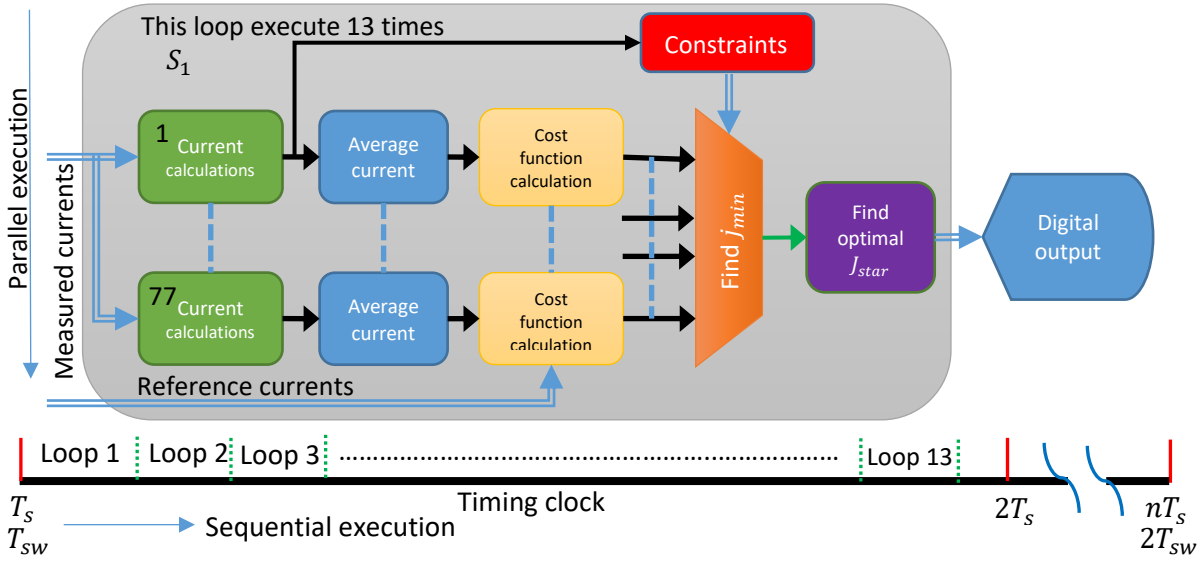

Figure 6-22 Block diagram for the FPGA program of FCS-MPC

The implemented program is divided in six stages:

- The first stage is dedicated to the currents calculations. There are 77 parallel blocks which are designed to calculate the predicted currents on the horizon. Each block is triggered n times to calculate the currents from $n = 1\ to\ n = H_p$
- The second step is dedicated to the calculation of the average current for the n-prediction currents and at the same time it is designed to give the maximum and minimum currents within the prediction region
- After that the cost function is calculated. 77 cost functions are evaluated taking into account the constraints.

- The minimum one is identified and stored in J_{star} for the first loop
- All the previous steps are repeated and executed sequentially 13 times
- At the end of each loop the J_{star} is compared with the result of j_{min} to find the minimum cost function from all 13 loops. All the calculations (13 loops) are done in a time duration lower than the sampling period T_s
- The digital outputs give the optimal switching vector to apply to the power converter at each sampling instance (T_s).

The calculations of the predicted currents given by equation (6-11) are implemented with Xilinx blocks as shown in Figure 6-23. This subsystem is repeated three times to calculate the predicted currents of the three cells ($i_1, i_2, and\ i_3$).

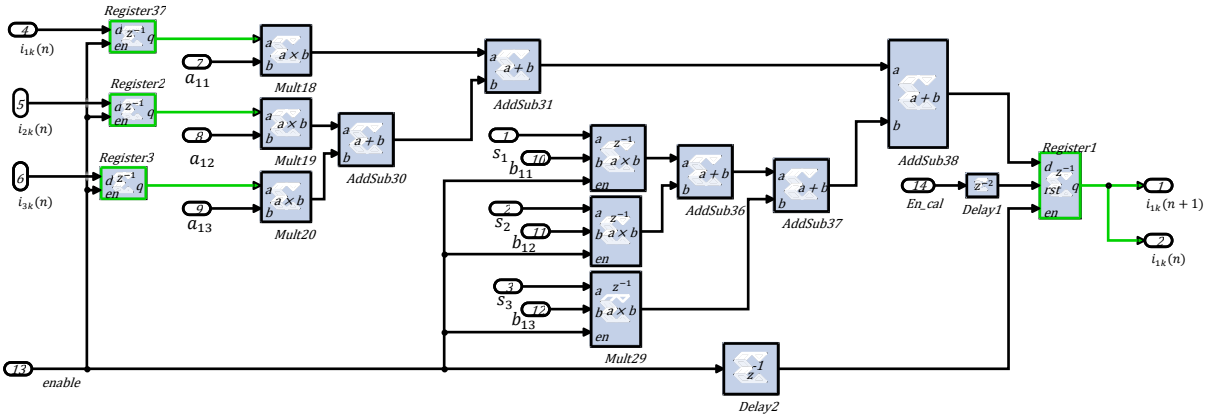

Figure 6-23 Implementation of the predicted currents with XSG blocks

Figure 6-24 shows the implementation of the average current calculation. The predicted currents $i(n+1)$ is multiplied by $(1/H_p)$) then accumulated to the end of the prediction by the addition block ($AddSub31$) and the register ($Register2$). At the end of prediction the average current ($i_{1_{av}}$) is held by the register ($Register37$) until the execution of the next loop starts. This subsystem is repeated three time to calculate the three average current.

Figure 6-25 shows the implementation of the cost function given by equation (6-12). This block consists of three parts.

- The first part is dedicated to calculate the difference between the reference currents (I_{1ref}, I_{2ref} and I_{3ref}) and the predicted average current values (i_{1av}, i_{2av} and i_{3av}).
- The second and third parts give the difference between the reference currents and the maximum and minimum predicted currents respectively (the third part is not shown in the figure).

Then all three parts are summed and stored in the register "$register1$". This register is preloaded with a high value after the end of calculation of the control sequence

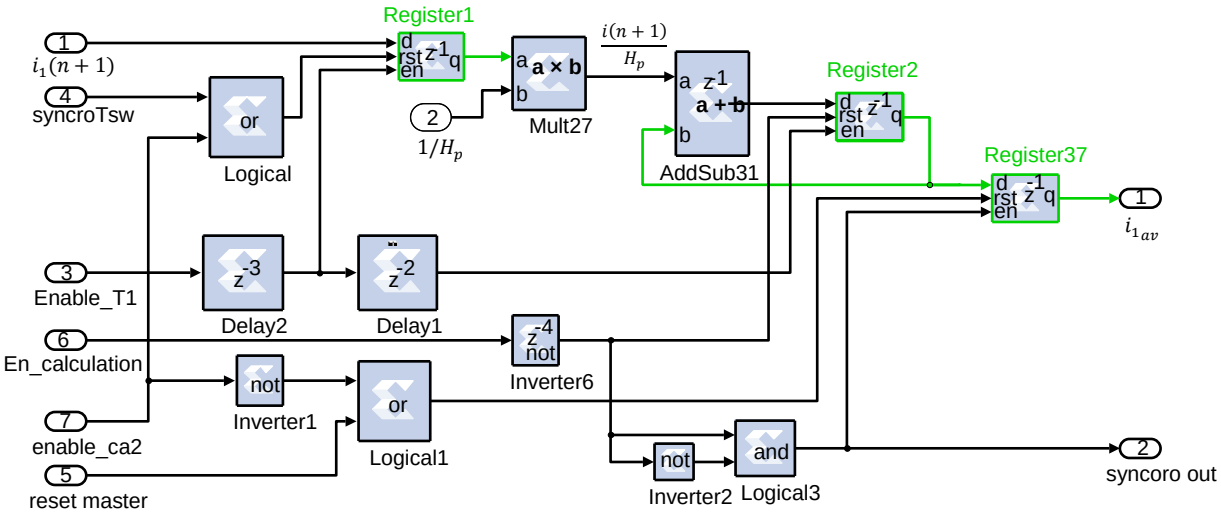

Figure 6-24 Programing the average currents calculations by XSG blocks

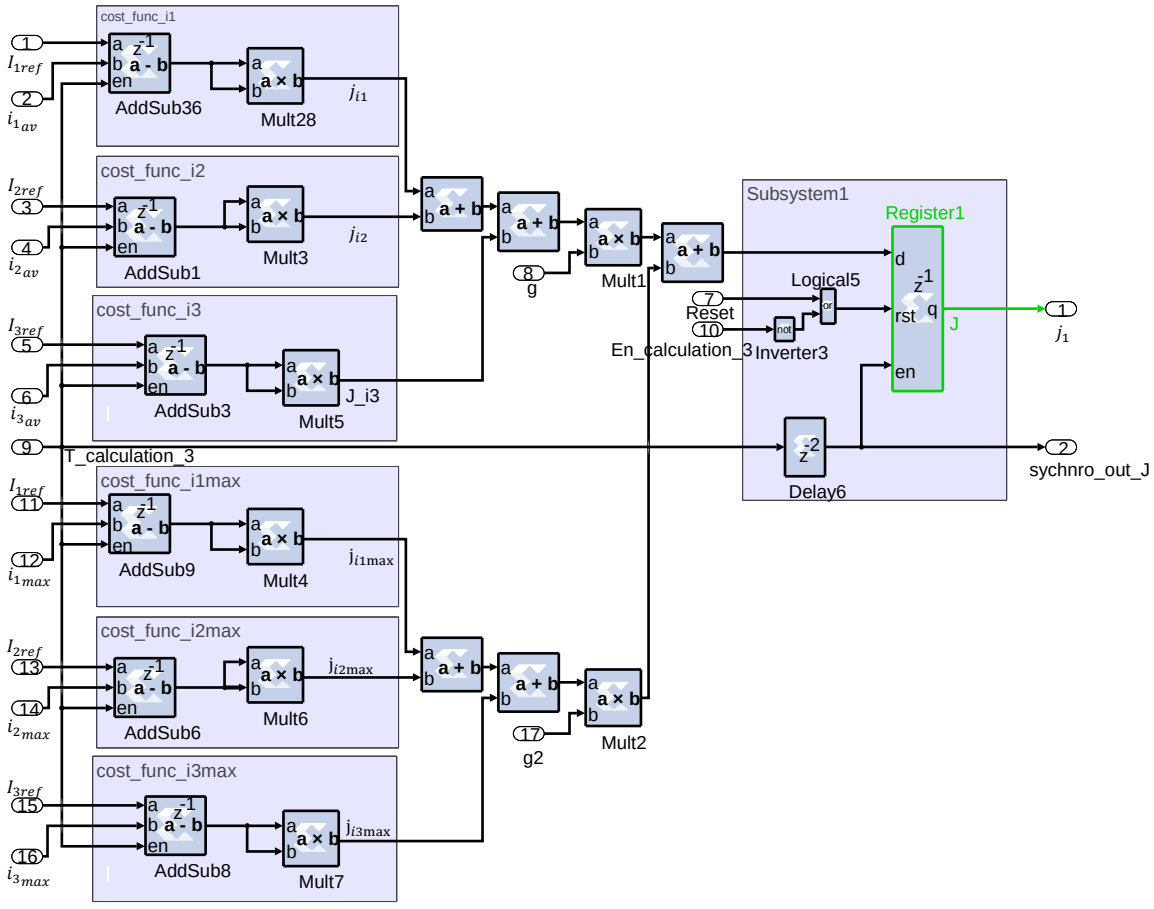

Figure 6-25 Implementation of the cost function calculations with XSG blocks

Implementation of the constraints is shown in Figure 6-26. The constraints concern the predictive currents $(i_1(n+1), i_2(n+1)$ and $i_3(n+1))$. Indeed, the currents are limited in the range $(0 \leq \boldsymbol{i}_k(n+1) \leq \boldsymbol{i}_{up})$. If the predicted currents are within the limits, the register "out_limit" will be set to one. The flag "out_limits" is used to set the dedicated cost function to a high value when the predicted currents exceed the limits. The flag "out_limits" is reset to zero at the beginning of the switching period, when there is a reset of the command and at the beginning of each loop calculation.

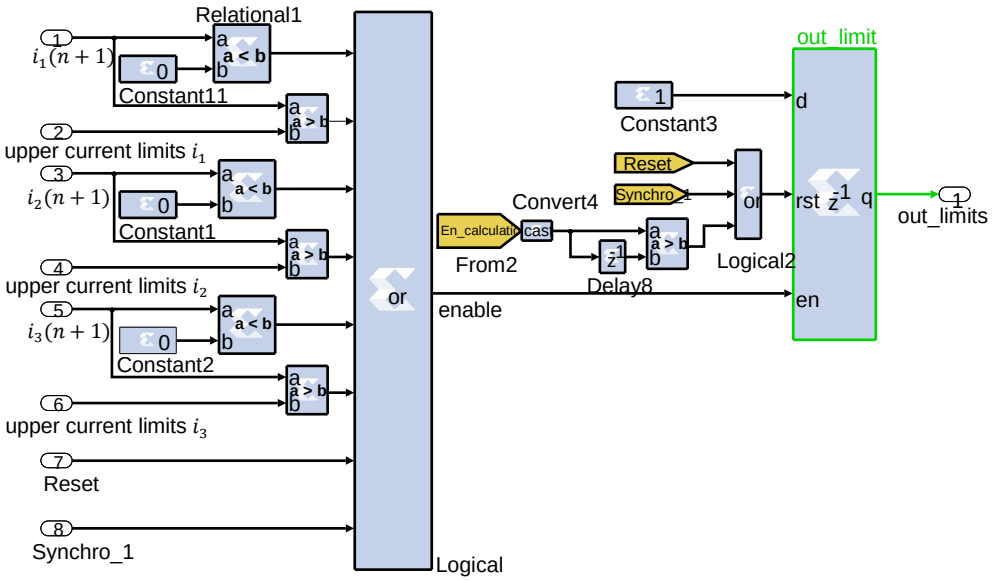

Figure 6-26 Programing the constraints by XSG blocks

Figure 6-27 shows the FPGA program designed to find the optimal cost function. The program compares the optimal value of J_{star} which is stored in the register "Jstar_reg" with the minimum cost function value J of the 76 switching sequences calculated in parallel (see Figure 6-22). If J is less than the J_{star}, J is stored in the register "Jstar_reg" as well as the related indices stored as optimal indices ($opti\_index$ and $opti\_J\_index$). $opti\_index$ is related to the switching sequence for the sequential execution of the loop (1 to 13). The $opti\_J\_index$ is related to the switching sequence during the parallel execution (1 to 76)

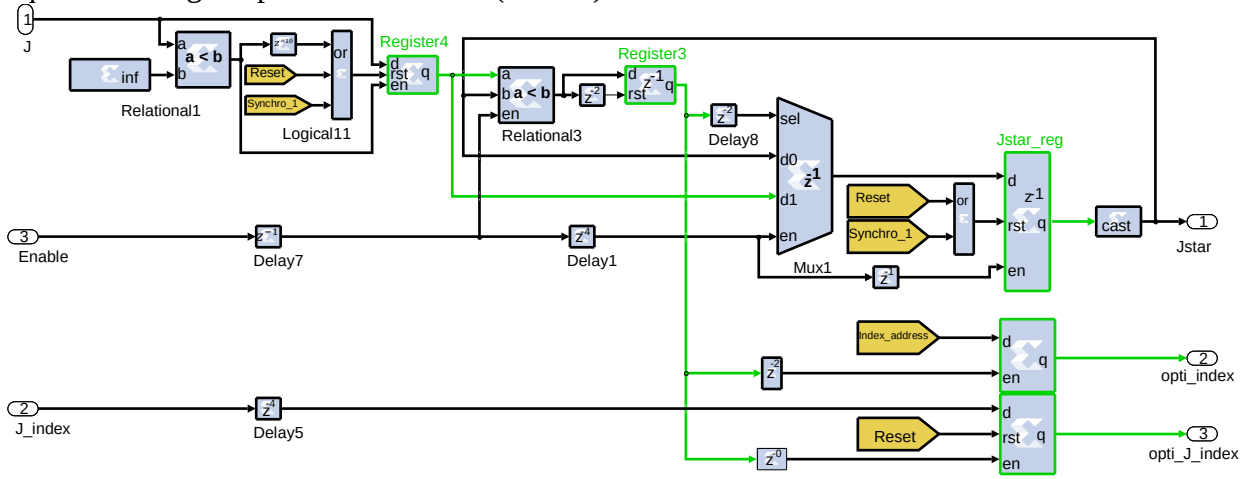

Figure 6-27 Implementation of the optimal cost function with XSG blocks

6.5. Conclusion

In this chapter, we have endeavored to describe the implementation of the control strategies developed in this thesis. We have seen that experimental results, obtained on a developed test bench, validate the theoretical results and the analyzes of the previous chapters for independent PI controller, decoupled strategy and state feedback with LQR. All these control methods have been easily implemented on a FPGA target. However, implantation of FCS-MPC on FPGA has been challenging and not easy even if we proposed in this work partial descriptions of its implementation. At the time of writing this document, there are no experimental results for FCS-MPC due to the unsolved difficulty to place and root the whole FPGA program. The proposed implementation of FCS-MPC needs a FPGA with a larger number of cells or an implementation in a different way by using specific development tools allowing the implementation of DSP cores within the FPGA in order to optimize the size of implemented program.

Chapter 7. Conclusion

The main objective of this thesis was to design a control able to manage the complexity of coupled interleaved multicell DC-DC converters. The main addressed questions were about the effects of coupling on the current balancing, the converter parameters variations on the stability and the implementation of the real time controllers.

On these different subjects, we have shown that independent PI controllers applied to the direct control of the currents in each converter cells can't mitigate or overcome the effect of coupling effects. Implementation of a modal control offering decoupling properties overcomes the coupling effect, but it can't be easily implemented with an efficient anti-windup scheme. Furthermore, such controller is very sensitive to model knowledge uncertainties such as that on inductances of the coupled inductors but also to load variations. Robustness is thus a critical issue for such controllers. We also demonstrated that state feedback with LQR is an attractive controller which is able to reduce impacts of coupling effects while being more robust than the previous one. In addition, we showed that it allows an easy implementation in a FPGA target of an efficient anti-windup. All the previous linear controllers are unconstrained controllers which makes them behave non-linearly when the anti-windup is activated.

We have also shown that FCS-MPC is also able to control a coupled interleaved multicell DC-DC converter. Such control strategy mitigates the effect of strong coupling and do not require anti-windup management or extra algorithms as it is a constrained controller (it is possible to add the limitation as a constraint). We showed that FCS-MPC is sensitive to system parameters knowledge because it is a model based controller. We proposed a method for setting the switching frequency and limiting the number of evaluations of the cost function over the switching period. This last property makes the implementation of FCS-MPC easier and allow with restrictions an implementation in a FPGA target. However, restrictions concern the limitation of the duty cycle resolution as the set of evaluated predictions over one switching period increase exponentially with the number of prediction points.

In this work, we also proposed and analyzed a space vector placement strategy based on model Predictive Control. The proposed method is based on a modal control of the cell currents and is thus able to manage the coupling effects between the cells. But this strategy, based on a modal representation of the system is, as in previous methods sensitive to model knowledge uncertainties. Control of saturations is also an issue and still needs more investigations.

The work conducted in this thesis answers number of questions, but there are still several fields of investigation:

- For modal based control, and the main issue regarding robustness to model parameters knowledge, the proposed control strategy should be completed by the implementation of observers allowing to correct model parameters errors
- Real time implementation, especially in a mixed digital system, namely a FPGA and a Microcontroller needs more works. We used in this work development tools offered by Dspace but there are many limitations. Indeed, with the proposed hardware, there are many difficulties to synchronize in a good way, the Microcontroller tasks and those in the FPGA. This is a real issue that should be more easily managed by using a Microcontroller core

within the FPGA target rather than an external Microcontroller board

- As explained previously, the space vector placement strategy is very interesting and offer many possibilities of improvement as for example the management of saturations. These aspects are currently under investigation

References

[1] C. Mahamat, M. Petit, R. Marquant, C. Gautier, A. Mami, and F. Costa, “Decoupled PQ control applied to a multicellular parallel inverter for grid-connected photovoltaic system,” in *2016 17th International Conference on Sciences and Techniques of Automatic Control and Computer Engineering (STA)*, 2016, pp. 455–460.

[2] C. Gautier, F. Adam, E. Laboure, B. Revol, and D. Labrousse, “Control for the currents balancing of a multicell interleaved converter with ICT,” in *2013 15th European Conference on Power Electronics and Applications (EPE)*, 2013, pp. 1–9.

[3] M. Le Bolloch, M. Cousineau, and T. Meynard, “Current-sharing control technique for interleaving VRMs using intercell transformers,” *Epe 2009 13th Eur. Conf. Power Electron. Appl. Vols 1-9*, pp. 1379–1388, 2009.

[4] S. Alepuz, S. Busquets-Monge, J. Bordonau, J. Gago, D. Gonzalez, and J. Balcells, “Interfacing renewable energy sources to the utility grid using a three-level inverter,” *Ieee Trans. Ind. Electron.*, vol. 53, no. 5, pp. 1504–1511, 2006.

[5] J. Rodriguez and P. Cortes, *Predictive Control of Power Converters and Electrical Drives*. Wiley, 2012.

[6] J. Rodriguez *et al.*, “State of the Art of Finite Control Set Model Predictive Control in Power Electronics,” *IEEE Trans. Ind. Informatics*, vol. 9, no. 2, pp. 1003–1016, 2013.

[7] J. Rubinic, V. Yaramasu, B. Wu, and N. Zargari, “Model Predictive Control of Neutral-Point Clamped Inverter with Harmonic Spectrum Shaping,” *2015 Ieee Energy Convers. Congr. Expo.*, pp. 717–722, 2015.

[8] R. O. Ramirez, J. R. Espinoza, F. Villarroel, E. Maurelia, and M. E. Reyes, “A Novel Hybrid Finite Control Set Model Predictive Control Scheme With Reduced Switching,” *Ieee Trans. Ind. Electron.*, vol. 61, no. 11, pp. 5912–5920, 2014.

[9] P. Cortes, J. Rodriguez, D. E. Quevedo, and C. Silva, “Predictive current control strategy with imposed load current spectrum,” *Ieee Trans. Power Electron.*, vol. 23, no. 2, pp. 612–618, 2008.

[10] M. Tomlinson, T. Mouton, R. Kennel, and P. Stolze, “A generic approach to implementing finite-set model predictive control with a fixed switching frequency,” *2014 Ieee 23rd Int. Symp. Ind. Electron.*, pp. 330–335, 2014.

[11] M. Tomlinson, T. Mouton, R. Kennel, and P. Stolze, “Model Predictive Control with a Fixed Switching Frequency for an AC-to-AC Converter,” *2013 Ieee Int. Conf. Ind. Technol.*, pp. 570–575, 2013.

[12] M. Tomlinson, T. Mouton, R. Kennel, and P. Stolze, “Model Predictive Control with a Fixed Switching Frequency for a 5-level Flying Capacitor Converter,” *2013 Ieee Ecce Asia Downunder (Ecce Asia)*, pp. 1208–1214, 2013.

[13] L. Tarisciotti, P. Zanchetta, A. Watson, J. Clare, M. Degano, and S. Bifaretti, “Modulated model predictve control (M2PC) for a 3-phase active front-end,” in *2013 IEEE Energy Conversion Congress and Exposition*, 2013, pp. 1062–1069.

[14] J. Rodriguez *et al.*, “Predictive current control of a voltage source inverter,” *Ieee Trans. Ind. Electron.*, vol. 54, no. 1, pp. 495–503, 2007.

[15] L. Malesani, P. Mattavelli, and S. Buso, “Robust dead-beat current control for PWM rectifiers and active filters,” *Ieee Trans. Ind. Appl.*, vol. 35, no. 3, pp. 613–620, 1999.

[16] Q. R. Zeng and L. C. Chang, “An advanced SVPWM-based predictive current controller for three-phase inverters in distributed generation systems,” *Ieee Trans. Ind. Electron.*, vol. 55, no. 3, pp. 1235–1246, 2008.

[17] R. Vargas, P. Cortes, U. Ammann, J. Rodriguez, and J. Pontt, “Predictive control of a three-phase neutral-point-clamped inverter,” *Ieee Trans. Ind. Electron.*, vol. 54, no. 5, pp. 2697–2705, 2007.

[18] P. A. and M. P. Kazmierkowski, “Predictive direct power control of three-phase boost rectifier,” *Bull. Polish Acad. Sci.*, vol. 54, no. 3, pp. 287–292, 2006.

[19] J. Rodríguez, J. Pontt, P. Correa, P. Lezana, and P. Cortés, “Predictive power control of an AC/DC/AC converter,” in *Conference Record - IAS Annual Meeting (IEEE Industry Applications Society)*, 2005, vol. 2, pp. 934–939.

[20] P. Antoniewicz, M. P. Kazmierkowski, and M. Jasinski, “Comparative study of two Direct Power Control algorithms for AC/DC converters,” in *2008 IEEE Region 8 International Conference on Computational Technologies in Electrical and Electronics Engineering*, 2008, pp. 159–163.

[21] P. Cortés, J. Rodríguez, P. Antoniewicz, and M. Kazmierkowski, “Direct power control of an AFE using predictive control,” *IEEE Trans. Power Electron.*, vol. 23, no. 5, pp. 2516–2523, 2008.

[22] S. A. Larrinaga, M. A. R. Vidal, E. Oyarbide, and J. R. T. Apraiz, “Predictive control strategy for DC/AC converters based on direct power control,” *Ieee Trans. Ind. Electron.*, vol. 54, no. 3, pp. 1261–1271, 2007.

[23] T. Nussbaumer, M. L. Heldwein, G. Gong, S. D. Round, and J. W. Kolar, “Comparison of prediction techniques to compensate time delays caused by digital control of a three-phase buck-type PWM rectifier system,” *IEEE Trans. Ind. Electron.*, vol. 55, no. 2, pp. 791–799, 2008.

[24] T. Meynard, *chapter 2: Analysis and Design of Multicell DCDC Converters Using Vectorized Models*. Wiley, 2015.

[25] H. E. Helmut L. , Votzi, “Cell Balancing of a Multi-Cell Battery Storage System for Renewable DC Micro-Grids,” in *pcim europe 2018*, 2012.

[26] H. Ertl, J. Kolar, and F. C. Zach, “A Novel Multi-Cell DC-AC Converter for Applications in Renewable Energy Systems,” *Ind. Electron. IEEE Trans.*, vol. 49, 2002.

[27] L. Kerachev, Y. Lembeye, and J. C. Cr�bier, “Analysis and prototyping of distributed series connected DC/AC converters integrated in PV panels,” in *2017 19th European Conference on Power Electronics and Applications (EPE’17 ECCE Europe)*, 2017, p. P.1-P.10.

[28] A. De Bernardinis, “Synthesis on power electronics for large fuel cells: From power conditioning to potentiodynamic analysis technique,” *Energy Convers. Manag.*, vol. 84, pp. 174–185, Aug. 2014.

[29] T. A. Meynard and H. Foch, “Multi-Level Choppers for High Voltage Applications,” *EPE J.*, vol. 2, no. 1, pp. 45–50, 1992.

[30] T. A. Meynard and H. Foch, “Imbricated Cells Multi-Level Voltage-Source Inverters for High Voltage Applications,” *EPE J.*, vol. 3, no. 2, pp. 99–106, 1993.

[31] T. A. M. E. LEFEUVRE, “Fast line voltage conditioners using new PWM AC chopper opologies,” *European Power Electronics Conference*. Graz, pp. 27–29, 2001.

[32] T. Meynard, *Chapter 2: Analysis and Design of Multicell DC/DC Converters Using Vectorized Models*. Wiley, 2015.

[33] S. Sanchez, F. Richardeau, and D. Risaletto, “Design and fault-operation analysis of a modular cyclic cascade inter-cell transformer (ICT) for parallel multicell converters,” *Math. Comput. Simul.*, vol. 131, pp. 190–199, 2017.

[34] T. Meynard, B. C. Laplace, F. Forest, and E. Labouré, “Parallel multicell converters for high current: Design of intercell transformers,” in *2010 IEEE International Conference on Industrial Technology*, 2010, pp. 1359–1364.

[35] Y. Cho, “Dual-buck residential photovoltaic inverter with a high-accuracy repetitive current controller,” *Renew. Energy*, vol. 101, pp. 168–181, 2017.

[36] D. Guilbert, A. Gaillard, A. N’Diaye, and A. Djerdir, “Power switch failures tolerance and remedial strategies of a 4-leg floating interleaved DC/DC boost converter for photovoltaic/fuel cell applications,” *Renew. Energy*, vol. 90, pp. 14–27, 2016.

[37] N. Zhang, D. Sutanto, and K. M. Muttaqi, “A review of topologies of three-port DC-DC converters for the integration of renewable energy and energy storage system,” *Renew. Sustain. Energy Rev.*, vol. 56, pp. 388–401, 2016.

[38] D. Guilbert, A. N’Diaye, A. Gaillard, and A. Djerdir, “Fuel cell systems reliability and availability enhancement by developing a fast and efficient power switch open-circuit fault detection algorithm in interleaved DC/DC boost converter topologies,” *Int. J. Hydrogen Energy*, vol. 41, no. 34, pp. 15505–15517, 2016.

[39] M. Elsied, A. Oukaour, H. Chaoui, H. Gualous, R. Hassan, and A. Amin, “Real-time implementation of four-phase interleaved DC-DC boost converter for electric vehicle power system,” *Electr. Power Syst. Res.*, vol. 141, pp. 210–220, 2016.

[40] H. R. E. Mamede, W. M. dos Santos, R. F. Coelho, and D. C. Martins, “A multicell Dual-Active Bridge converter for increasing the reliability of power supply in a DC microgrid,” *2015 IEEE First Int. Conf. DC Microgrids*, pp. 274–279, 2015.

[41] T. Ohnishi, “Three phase PWM converter/inverter by means of instantaneous active and reactive power control,” in *Industrial Electronics, Control and Instrumentation, 1991. Proceedings. IECON ’91., 1991 International Conference on*, 1991, pp. 819–824 vol.1.

[42] G. Goodwin, M. M. Seron, and J. A. de Doná, *Constrained Control and Estimation: An Optimisation Approach*. Springer London, 2006.

[43] L. Grüne and J. Pannek, *Nonlinear Model Predictive Control: Theory and Algorithms*. Springer International Publishing, 2016.

[44] S. J. Qin and T. A. Badgwell, “A survey of industrial model predictive control technology,” *Control Eng. Pract.*, vol. 11, no. 7, pp. 733–764, 2003.

[45] J. B. Rawlings and D. Q. Mayne, *Model Predictive Control: Theory and Design*. Nob Hill Pub., 2009.

[46] J. Rodriguez *et al.*, "State of the Art of Finite Control Set Model Predictive Control in Power Electronics," *Ieee Trans. Ind. Informatics*, vol. 9, no. 2, pp. 1003–1016, 2013.

[47] J. Rodriguez and P. Cortes, *Chapter 5:Predictive Control of Power Converters and Electrical Drives*. 2012.

[48] S. Aurtenechea, M. A. Rodriguez, E. Oyarbide, and J. R. Torrealday, "Predictive direct power control - A new control strategy for DC/AC converters," *Iecon 2006 - 32nd Annu. Conf. Ieee Ind. Electron. Vols 1-11*, p. 1710–+, 2006.

[49] P. Antoniewicz and M. P. Kazmierkowski, "Virtual-Flux-Based Predictive Direct Power Control of AC/DC Converters With Online Inductance Estimation," *IEEE Trans. Ind. Electron.*, vol. 55, no. 12, pp. 4381–4390, 2008.

[50] E. Laboure, A. Cuniere, T. A. Meynard, F. Forest, and E. Sarraute, "A theoretical approach to InterCell Transformers, application to interleaved converters," *Ieee Trans. Power Electron.*, vol. 23, no. 1, pp. 464–474, 2008.

[51] B. Amghar, M. Darcherif, J.-P. Barbot, and P. Gauthier, "Modeling and control of parallel multicell chopper using Petri nets," *IFAC Proc. Vol.*, vol. 45, no. 21, pp. 633–638, 2012.

[52] F. K. J. W. Kolar Y. Lobsiger, J. Muhlethaler, T. Nussbaumer and J. Minibock, "Extreme efficiency power electronics," *7th International Conference on Integrated Power Electronics Systems (CIPS)*. Nuremberg, pp. 1–22, 2012.

[53] O. Bethoux, E. Laboure, G. Remy, and E. Berthelot, "Real-Time Optimal Control of a 3-Phase PMSM in 2-Phase Degraded Mode," *Ieee Trans. Veh. Technol.*, vol. 66, no. 3, pp. 2044–2052, 2017.

[54] W. H. Li, Y. J. Gu, H. Z. Luo, W. F. Cui, X. N. He, and C. L. Xia, "Topology Review and Derivation Methodology of Single-Phase Transformerless Photovoltaic Inverters for Leakage Current Suppression," *Ieee Trans. Ind. Electron.*, vol. 62, no. 7, pp. 4537–4551, 2015.

[55] Q. Li and P. Wolfs, "A review of the single phase photovoltaic module integrated converter topologies with three different dc link configurations," *Ieee Trans. Power Electron.*, vol. 23, no. 3, pp. 1320–1333, 2008.

[56] L. L. Chen, L. Xiao, W. B. Hu, and Y. G. Yan, "Application of coupled inductors in parallel inverter system," *Icems 2003 Proc. Sixth Int. Conf. Electr. Mach. Syst. Vols 1 2*, pp. 398–401, 2003.

[57] D. Maksimovic, A. M. Stankovic, V. J. Thottuvelil, and G. C. Verghese, "Modeling and simulation of power electronic converters," *Proc. IEEE*, vol. 89, no. 6, pp. 898–912, 2001.

[58] A. G. O. Mutambara, *Chapter 4:Design and Analysis of Control Systems*. CRC Press, 2017.

[59] E. Ostertag, *Mono- and Multivariable Control and Estimation: Linear, Quadratic and LMI Methods*. Springer Publishing Company, Incorporated, 2011.

[60] T. Kailath, *chapter 7 : Linear Systems*. Prentice-Hall, 1980.

[61] E. Lavretsky and K. Wise, *Chapter 2: Robust and Adaptive Control: With Aerospace Applications*. Springer London, 2012.

[62] D. Xue, Y. Q. Chen, and D. P. Atherton, *Chapter 5 : Linear Feedback Control: Analysis and Design with MATLAB*. Society for Industrial and Applied Mathematics, 2007.

[63] C. Wongsathan and C. Sirima, "Application of GA to Design LQR Controller for an Inverted Pendulum System," *2008 Ieee Int. Conf. Robot. Biomimetics, Vols 1-4*, pp. 951–954, 2009.

[64] L. Wiklendt, S. Chalup, and R. Middleton, "A small spiking neural network with LQR control applied to the acrobot," *Neural Comput. Appl.*, vol. 18, no. 4, pp. 369–375, 2009.

[65] K. Hassani and W. Lee, "Optimal Tuning of Linear Quadratic Regulators Using Quantum Particle Swarm Optimization," 2014.

[66] P. Cortes, M. P. Kazmierkowski, R. M. Kennel, D. E. Quevedo, and J. Rodriguez, "Predictive Control in Power Electronics and Drives," *Ieee Trans. Ind. Electron.*, vol. 55, no. 12, pp. 4312–4324, 2008.

[67] J. H. and S. Stadtfeld, "A predictive controller for the stator current vector of AC machines fed from a switched voltage source," *International Power Electronics Conference, IPEC*. Tokyo, pp. 1665–1675, 1983.

[68] P. Mutschler, "A new speed-control method for induction motors." 1998.

[69] T. Kawabata, T. Miyashita, and Y. Yamamoto, "Dead Beat Control of Three Phase PWM Inverter," *Ieee Trans. Power Electron.*, vol. 5, no. 1, pp. 21–28, 1990.

[70] O. Kukrer, "Discrete-time current control of voltage-fed three-phase PWM inverters," *Ieee Trans. Power Electron.*, vol. 11, no. 2, pp. 260–269, 1996.

[71] S. Kouro, P. Cortes, R. Vargas, U. Ammann, and J. Rodriguez, "Model Predictive Control-A Simple and Powerful Method to Control Power Converters," *Ieee Trans. Ind. Electron.*, vol. 56, no. 6, pp. 1826–1838, 2009.

[72] P. Stolze, M. Kramkowski, T. Mouton, M. Tomlinson, and R. Kennel, *Increasing the performance of Finite-Set Model Predictive Control by oversampling*. 2013.

[73] S. Vazquez *et al.*, "Model Predictive Control with Constant Switching Frequency Using a Discrete Space Vector Modulation with Virtual State Vectors," *2009 Ieee Int. Conf. Ind. Technol. Vols 1-3*, p. 1389–+, 2009.

[74] M. Tomlinson, T. Mouton, R. Kennel, and P. Stolze, "Model Predictive Control of an AC-to-AC Converter with Input and Output LC Filter," *2011 6th Ieee Conf. Ind. Electron. Appl.*, pp. 1233–1238, 2011.

[75] M. Tomlinson, H. D. Mouton, R. Kennel, and P. Stolze, "A Fixed Switching Frequency Scheme for Finite-Control-Set Model Predictive Control-Concept and Algorithm," *Ieee Trans. Ind. Electron.*, vol. 63, no. 12, pp. 7662–7670, 2016.

[76] M. Pacas and J. Weber, "Predictive direct torque control for the PM synchronous machine," *Ieee Trans. Ind. Electron.*, vol. 52, no. 5, pp. 1350–1356, 2005.

[77] W. S. Levine, *Control System Applications*. Taylor & Francis, 1999.

[78] D. G. Zill and M. R. Cullen, *Advanced Engineering Mathematics*, no. vol. 1. Jones and Bartlett Publishers, 2006.

[79] L. Wang, *Model Predictive Control System Design and Implementation Using MATLAB®*. Springer

London, 2009.

[80] R. Rocha and L. D. S. M. Filho, “A discrete current control for PWM rectifier,” *ISIE 2005 Proc. IEEE Int. Symp. Ind. Electron. 2005, Vols 1- 4*, pp. 681–686, 2005.

[81] J. Lira, V. Cardenas, and C. Nunez, “Analysis and design of a PWM rectifier using the DQ theory and a digital control based in a DSP,” *2004 IEEE 9th Int. Power Electron. Congr. Tech. Proc.*, pp. 52–57, 2004.

[82] A. C. S. L. / N. Guimaraes F. A. S. / Carvalho, M. A. / Cavalcanti, M. C. / Lins, Z. D., “DOUBLY FED INDUCTION GENERATORS ACTIVE AND REACTIVE POWER CONTROL,” *11TH, International power electronics and motion control conference:; EPE-PEMC 2004*. Riga Technical Univ., Riga, pp. 5–64, 2004.

[83] M. Malinowski, “Sensorless Control Strategies for Three - Phase PWM Rectifiers,” Warsaw university of technology, Warsaw, Poland, 2001.

[84] M. Malinowski, M. P. Kazmierkowski, and A. M. Trzynadlowski, *A Comparative Study of Control Techniques for PWM Rectifiers in AC Adjustable Speed Drives*, vol. 18. 2003.

[85] G. Escobar, A. M. Stankovic, J. M. Carrasco, E. Galvan, and R. Ortega, “Analysis and design of direct power control (DPC) for a three phase synchronous rectifier via output regulation subspaces,” *Ieee Trans. Power Electron.*, vol. 18, no. 3, pp. 823–830, 2003.

[86] T. Noguchi, H. Tomiki, S. Kondo, and I. Takahashi, “Direct power control of PWM converter without power-source voltage sensors,” *Ieee Trans. Ind. Appl.*, vol. 34, no. 3, pp. 473–479, 1998.

[87] B. S. Chen and G. Joos, “Direct Power Control of Active Filters With Averaged Switching Frequency Regulation,” *Ieee Trans. Power Electron.*, vol. 23, no. 6, pp. 2729–2737, 2008.

[88] A. Linder and R. Kennel, *Direct model predictive control-a new direct predictive control strategy for electrical drives*. 2005.

[89] A. BenAbdelghani, C. A. Martins, X. Roboam, and T. A. Meynard, “Use of extra degrees of freedom in multilevel drives,” *Ieee Trans. Ind. Electron.*, vol. 49, no. 5, pp. 965–977, 2002.

[90] J. Rodriguez and P. Cortes, *Chapter 3: Predictive Control of Power Converters and Electrical Drives*. Wiley, 2012.

[91] E. Monmasson, *Chapter 16: Power Electronic Converters: PWM Strategies and Current Control Techniques*. Wiley, 2013.

[92] W. Na, R. Kohl, P. Burrmann, and M. Daly, “Control design of DSP based a bi-directional converter for electric vehicles applications,” in *IEEE International Conference on Electro Information Technology*, 2014, pp. 427–431.

[93] “Manual Agilent N8700 Series System DC Power Supplies.” Agilent Technologies, USA, 2009.

[94] SEMIKRON, “SEMIKRON_DataSheet_SKM50GB12T4_22892000.” 2013.

[95] LEM, “Current Transducer LA 55-P/SP1.” 2013.

[96] dSPACE GmbH, “MicroLabBox Features.” Paderborn, 2014.

[97] dSPACE GmbH, “MicroLabBox Hardware Installation and Configuration.” Paderborn, 2016.

[98] M. S. Fadali, A. Visioli, M. S. Fadali, and A. Visioli, “Chapter 6 – Digital Control System Design,” in *Digital Control Engineering*, 2013, pp. 165–234.